Ruthenium picolinates for photosensitisation of heterogeneous water oxidation

Graham Steel

2016

Thesis submitted to the Department of Pure and Applied Chemistry, University of Strathclyde, in the requirement for degree in Doctor of Philosophy.

This thesis is the result of the author's original research. It has been composed by the author and has not been previously submitted for examination which has led to the award of a degree.

The copyright of this thesis belongs to the author under the terms of the United Kingdom Copyright Acts as qualified by University of Strathclyde Regulation 3.50. Due acknowledgement must always be made of the use of any material contained in, or derived from, this thesis.

Signed:

Date:

Abstract

Catalytic photochemical water oxidation is one of the key problems in the development of both the generation of solar fuels and renewable chemical feed stocks. One of the leading proposals is to use heterogeneous semiconductors, which, when under irradiation, generate a large enough voltage to electrolyse water molecules in situ. To the effectiveness of this process, dye sensitisers are employed to harvest more of the high intensity visible spectrum. The purpose of this thesis is to gain a better understanding of how these dyes behave in combination with selected substrates, and to examine how, with minor alterations to existing dyes, their effectiveness could be improved. Chapter I consists of a survey of various different water oxidation methods found in both nature and in the lab, to build an understanding of both homogenous and heterogeneous water oxidation pathways and how they are connected. Chapter II details the synthesis, characterisation and catalytic testing of a series of ruthenium (IV) based dyes, deriving from ethylcarboxylate-substituted picolinic acid. The investigation determined that significant shifts in the redox couples could be achieved via the simple variation of the substitution pattern of the ethylcarboxylates. What was also discovered was the reduced form of the dyes and the subsequent exchange of charge-carrying ligands for neutral aqua groups. In chapter III, DFT and TDDFT calculations were performed in order to gain a more fundamental understanding of the behaviour of these dyes at a molecular level. The results show that the complexes are reducing upon contact with water, as the experimental UV-Vis spectra match those of the reduced species rather than the original ruthenium (IV) dyes. This reduction is attributed to the complexes acting as water-oxidation agents due to the high oxidation potential of their $Ru^{III/IV}$ couples in comparison with that of the water oxidation reaction. Attempts to develop similar ruthenium-amide based dyes are discussed in chapter IV. What was discovered was that, while the ligands could be synthesised easily, the complexes proved to be unstable and unsuitable for the water oxidation reaction. Overall these studies show that small changes in ligand design, such as variation in anchoring position, can have pronounced effects on the characteristics of those dyes and highlight the need for systematic exploration of ruthenium based dye sensitisers if improvements to the heterogeneous water oxidation reaction are going to occur.

Acknowledgements

Contents

Chapter I

A background on chemical water oxidation

Introduction

Traditional solar energy generation is in either the form of what is termed solar thermal or solar voltaic. Solar thermal is the simplest form of solar energy generation and acts to raise the average temperature of a volume of water to reduce the energy requirements of heating that water for domestic use. The warming is usually achieved by passing cooler water through pipes of broad-spectrum absorbing material (black) under direct solar irradiation. While this is mainly a small scale domestic form of solar energy generation, the use of concentrating technologies allows for scale-up to industrial levels by heating the water enough to vaporise it and drive steam turbines, as in the case at Solar Energy Generating Systems (SEGS) in California or Solnova in Spain.

Solar voltaic is the direct conversion of solar energy into electrical energy via the generation of an electrical potential. These systems have been used for both small- and large-scale electricity production. Combining photovoltaics with solar concentrating technologies for large scale production increases the potential output, but has not yet achieved the same level of development as solar thermal. This is due to efficiency limitations making such practices economically unviable at the current level of technology.

In a traditional solar voltaic cell, electron-rich elements (n-type) are doped onto one side of a very fine semiconductor layer, while electron-poor elements (p-type) are doped onto the opposite side of the semiconductor layer. At the junction between the n-type and p-type sides of the semiconductor assembly, electrons will flow from the electron-rich n-type to the electron-poor p-type.[1] The migration of the electron-hole pairs across the p-n junction is however diffusion-limited, as the migration is dependent on the concentration of dopant species in each layer - which typically differ by approximately a factor of 10.[2] This results in a build-up of electrical charge at the interface between the layers. The charge build-up retards the migration of electron-hole pairs towards the p-n junction. The zone where the fixed electrical charge counterbalances the movement of free charge carriers is termed the depletion region or space charge region. The migration of charges slows until the net movement of electron-hole pairs reaches zero. It is the electrical field generated by the fixed charges on either side of the junction which will force any electron in a higher energy

environment to return to its ground state by an alternate path, such as an external circuit, rather than by diffusion against the electrical field.

Upon exposure to light, a photon of sufficient energy is absorbed by the p-type semiconductor and an electron is promoted from the valence band of the semiconductor into the conduction band. This will only occur if the incident photon is of equal or greater energy than the energy gap between the valence and conduction band. Due to the electron being delocalised within the conduction band rather than tightly bound in the valence band, it will move more freely within the semiconductor. When the electron is promoted, it leaves behind a positively charged region of the semiconductor, normally called a "hole". This electron-hole pair will eventually recombine and emit radiation equivalent to the band gap of the semiconductor. However, the electrical field at the p-n junction drives the electron to the n-type region of the semiconductor and the hole to the p-type. If an external circuit is attached the electrons will flow around it from the n-type and recombine with the electron holes in the p-type (Figure 1.1). The flow of the electrons around this circuit is the current and the electrical field at the n-p junction is the voltage. The voltage is dependent on the number of promoted electrons, which is in turn dependent on the number of the incident photons - i.e. the intensity of the light hitting the semiconductor.
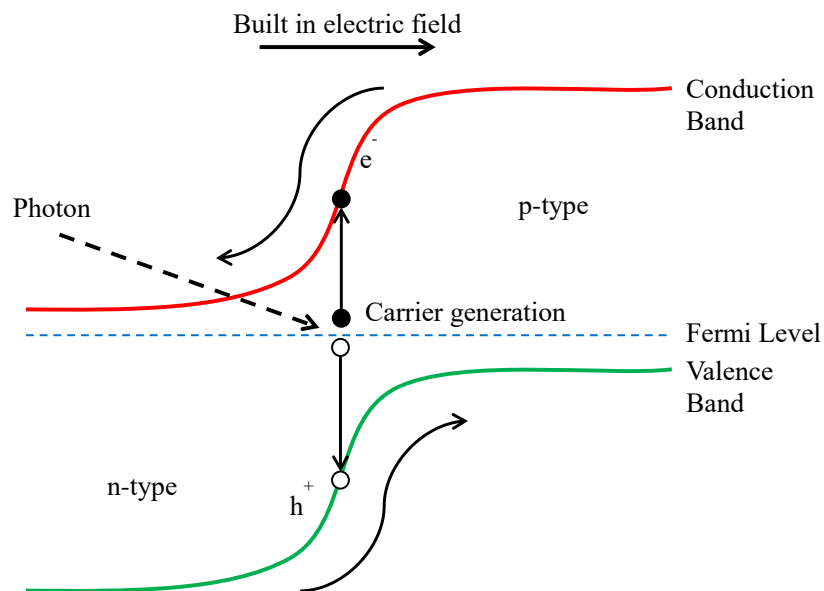

Figure 1.1 P/N junction band diagram.

3

A conventional solar cell based on mono-crystalline silicon has a theoretical limit to its maximum efficiency of approximately 29%, which is based on three factors: blackbody radiation, electron hole recombination and spectral losses due to the nature and size of the silicon band gap.[3] Spectral losses are the largest contributor to the loss. The band gap of a semiconductor will absorb incident electromagnetic radiation which has a frequency corresponding to the energy difference between the valence and conduction band of the semiconductor. Any photon of lower frequency lacks the necessary energy to promote an electron between the bands. There are additional thermodynamic and quantum mechanical considerations such as radiative recombination and blackbody radiation which lower the theoretical efficiency of the charge separation even further. While laboratory based semiconductor junctions based on silicon can be fabricated to approach this limit, the cost of a commercial version makes such a device untenable for manufacture on a large scale.

One of the primary manufacturing costs in producing a device of this nature is the process of refining and purifying the raw silicon. The manufacturing cost raises the unit price for conventional solar cells and therefore the price per Watt. Using multi-crystalline, polycrystalline or amorphous silicon lowers the cost, thanks to cheaper fabrication techniques, but this also lowers the efficiency of the end product.

Silicon is not the only semiconductor material to be explored. Various combinations of group 12-16 elements have been used to create p-n junctions with varying benefits and drawbacks - e.g. gallium arsenide and cadmium telluride.[4]

Multijunction cells, also known as stacked or tandem cells, are a convenient workaround for the inefficiency of a single p-n junction. Via the sandwiching of multiple different semiconductor materials, each with different absorption ranges, it is possible to boost the overall efficiency per unit cell (to approx. 40%).[5] The layering of multiple junctions with complementary absorption ranges allows for the more efficient capture of incident light in the visible spectrum. If the junctions are thin enough, it is possible to layer multiple junctions vertically into a single cell (Figure 1.2). When light passes into the cell, the highest energy photons are captured in the first junction with lower energy light passing into subsequent layers. The total efficiency of the cell can be said to be directly proportional to the number of junctions. However, as the size of

the cell increases the intensity of light reaching the lower junctions decreases and so the cell efficiency drops. In addition; as the number of junctions increases so, too, does the cost of manufacturing, due to the multiple components required and the need to carefully tune the band gap of such materials.
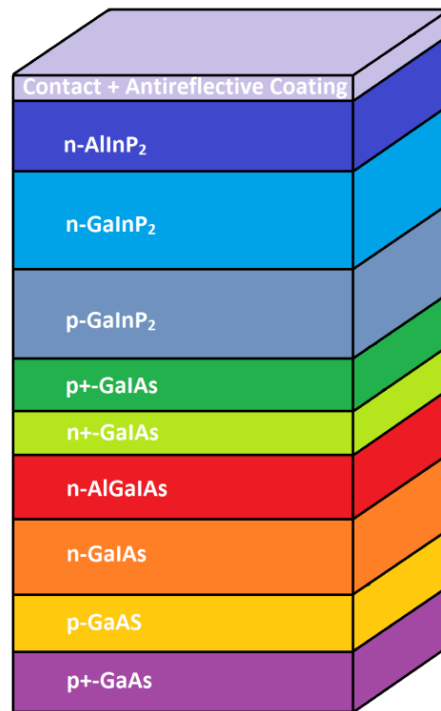

Figure 1.2 Multi-junction solar cell diagram.

The opposite balance between efficiency and cost is found in the dye-sensitised solar cell. In a dye-sensitised solar cell, the homogenous p-n junction is replaced by a heterogeneous photovoltaic assembly.[6] The fundamentals of the system are still the same in that the cell relies on the promotion of an electron and a subsequent external circuit to provide a faster method of charge recombination. In a Dye-Sensitised Solar Cell (DSSC) a photoactive dye is bound onto the surface of a semiconductor substrate (Figure 1.3) which is in contact with a redox active electrolyte such as an iodide/iodine solution (Figure 1.4).[7] In this system, an electron is promoted from its ground state to an excited state (either singlet or triplet state) within the photoactive dye, rather than from the valence band to the conduction band of a p-type semiconductor. The excited electron which moves away from the interface is effectively "injected" into the semiconductor substrate. This is due to the charge gradient caused by the increase in

electron density in the conduction band at the interface between the dye and the semiconductor.
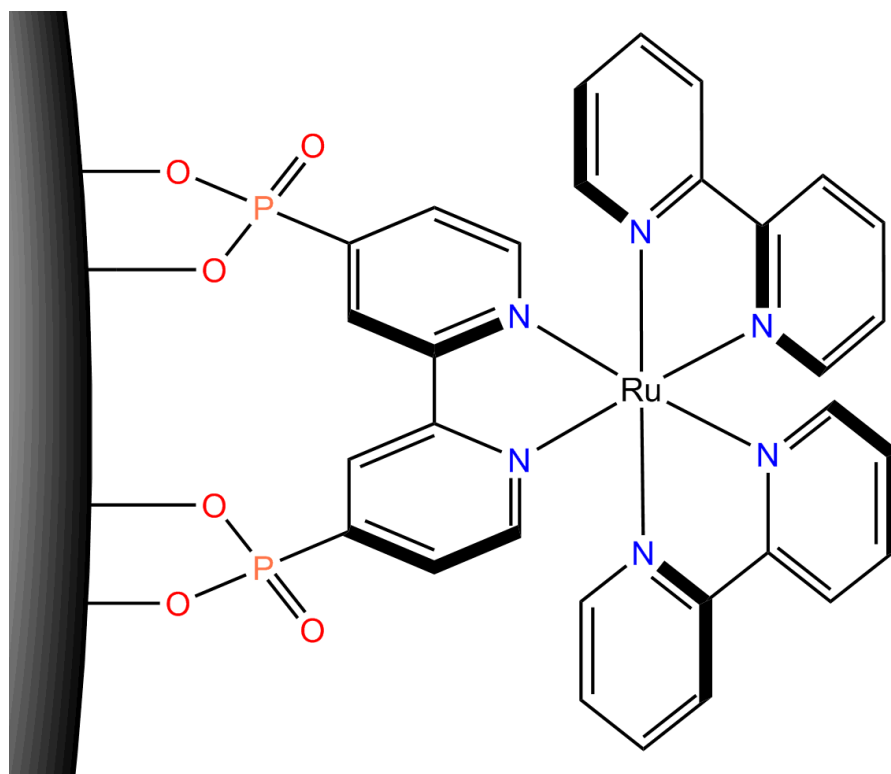

Figure 1.3 Schematic of TiO_2 sensitised by ruthenium pyridyl dye.

The semiconductor substrate is mounted on a metal anode, linked to an external circuit which allows the electrons to flow to the corresponding cathode, which is separated from the semiconductor and dye by the electrolyte. Electrons flow from the cathode into the electrolyte which in turn reduces the oxidised form of the photoactive dye ready for photoexcitation.

The drawback for this type of system is that in order to harvest visible light, the dye requires direct contact with the semiconductor and is therefore limited in its maximum surface coverage to a monolayer.[8] On a smooth semiconductor surface this monolayer limits the absorbance to less than 1% of monochromatic light. The solution to this problem is to increase the surface roughness of the semiconductor in order to increase the available area for dye deposition and therefore the absorbance of the photoactive cathode. If amorphous, or nanocrystalline TiO_2 is used as the substrate then increased dye surface coverage is possible although at the cost of a lower electronic conductivity when compared with monocrystalline anatase TiO_2.[9] The use of nanocrystalline TiO_2

allows for the same level of coverage but with the more uniform crystalline structure that allows for the higher conductivity.

Combining high surface area substrates with photoactive dyes allows for the development of semiconductor-based electrodes with the capability to harvest a greater range of visible light. The photoactive dyes currently being studied are predominantly based on ruthenium poly pyridyl systems due to the accessible long lived excited states and strong charge transfer bands. The use of nanocrystalline TiO_2 and ruthenium polypyridyl based dyes form the basis of the development of the Grätzel Cell.[6]
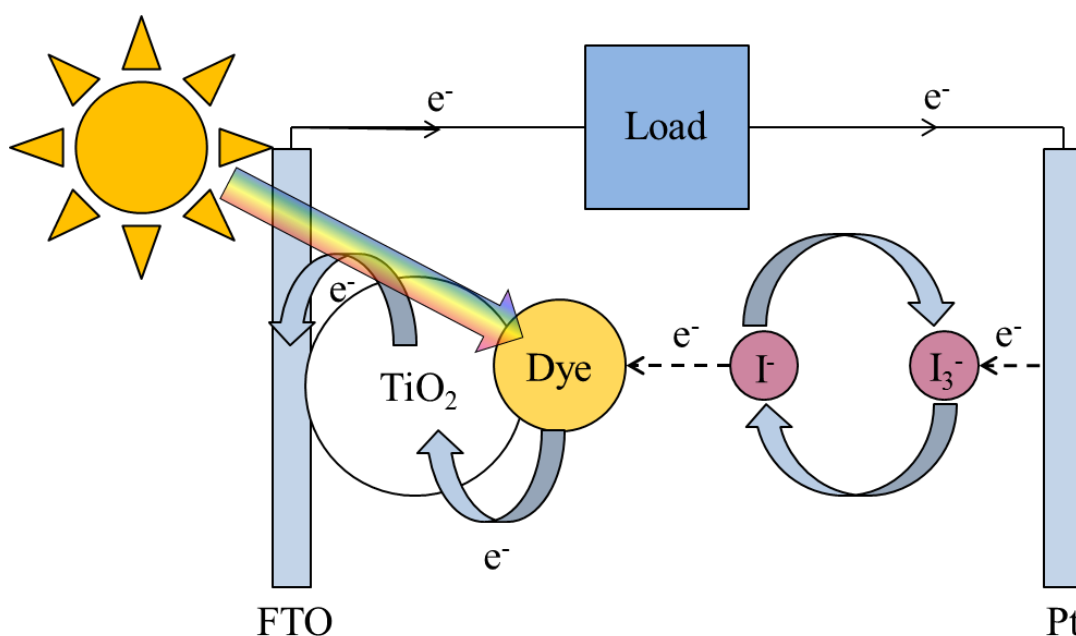
Figure 1.4 Diagram of a dye sensitised solar cell.

The development of the Grätzel Cell has been the main focus of research in the area of DSSCs for the past twenty years although it remains at its core a system for generating electrical energy rather than chemical energy. For practical usage it requires alternative energy storage systems such as batteries, redox flow batteries, etc, as the hours of domestic peak demand do not match the hours of most intense daylight. The generation of energy-rich fuels as opposed to direct electricity generation is much more appealing in terms of both long and short term storage.

Fuels are excellent energy storage mediums as energy degradation in this format is much slower than in electrical-, electrochemical- or mechanical-based systems. Additionally, the use of fuels only requires storage of one of the reaction components, as the energy release can be achieved during combustion with atmospheric oxygen.

In terms of the sheer production scale of energy-rich fuels, nature far exceeds even the most industrialised of energy capture systems constructed to date. The fuels that it generates are both energy-rich and relatively easy to handle. The drawback is that they actually come from living matter, from which the fuel must be extracted.

Copying nature

When working to create a system to generate solar fuels from sunlight, it is useful to look to pre-existing systems such as those found in nature. The primary method of solar energy capture found in nature is that of the photosynthetic system found in flora and cyanobacteria.

Photosynthesis is broken down into two systems; photosystem II and photosystem I (the reason for photosystem II being described first will be made apparent). These systems represent the respective oxidative and reductive reactions required to store solar energy via the spitting of water.[10]
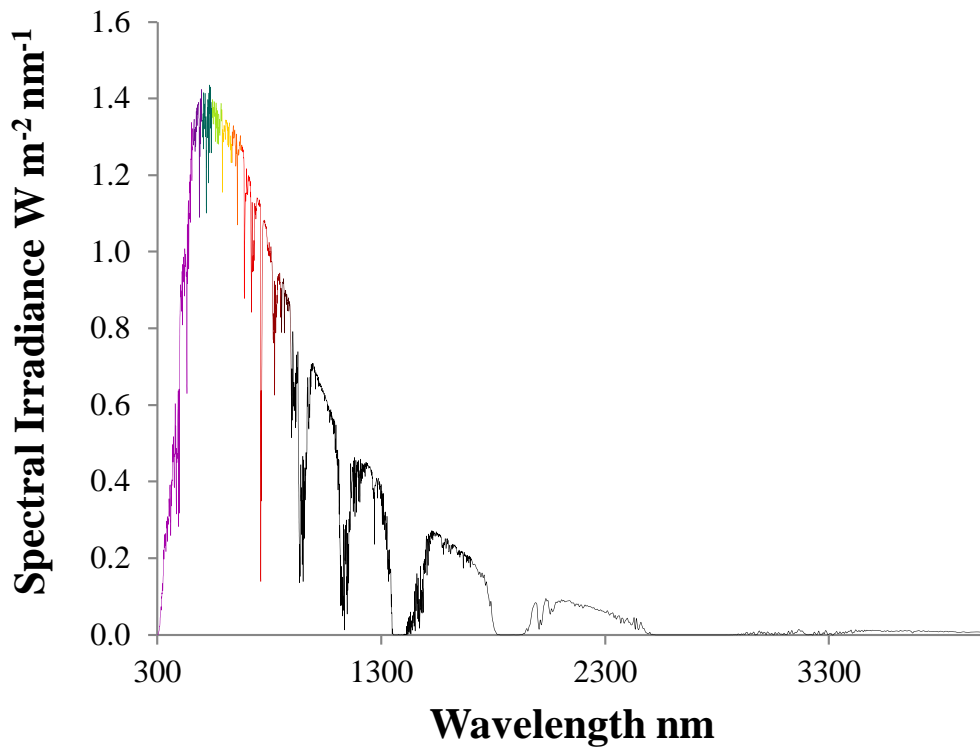
Figure 1.5 ASTMG173-modified solar spectrum. Visible region corresponding to highest intensity incident to earth's surface.

Complete photosynthesis utilises two sets of photoactive pigments. These pigments are named P680 and P700 (where the P stands for pigment and the number for the lambda max for each pigment). These absorption profiles correspond to the lower energy region of the visible spectrum but are still within the high intensity region of solar radiation impacting the earth's surface (Figure 1.5).[11] Although these pigment sets are where the initial energy conversion takes place, it is not where energy is first absorbed by the organism. Several families of organic and inorganic photoactive species act to absorb incident solar radiation and transfer it to the reaction centres. The structure of the reaction centres allows for the effective photoexcitation and charge separation required for the oxidation and reduction mechanisms required to photolyse water into molecular oxygen and to create a proton sink for the reduction of carbon dioxide into carbohydrates. The absorption profiles of the reaction centres, however, show that only certain energy ranges within the visible spectrum are effectively absorbed. The reaction centres p680 and p700 utilise energy in the lowest energy part of visible spectrum and exhibit strong absorption bands in that range. Such narrow absorption bands would limit the efficiency of the photosynthetic mechanism to

unsustainable levels were it not for the attenuation of other ranges of light within the visible spectrum by antenna molecules.[12] The most common antenna molecules are chlorophyll a (Figure 1.6) and chlorophyll b both of which absorb strongly in the high energy and low energy part of the spectrum but absorb relatively weakly in the medium energy range. The absorption ranges are expanded by the inclusion of a variety of accessory antenna chromophores such as carotenoids or protein-bound phycoblins.
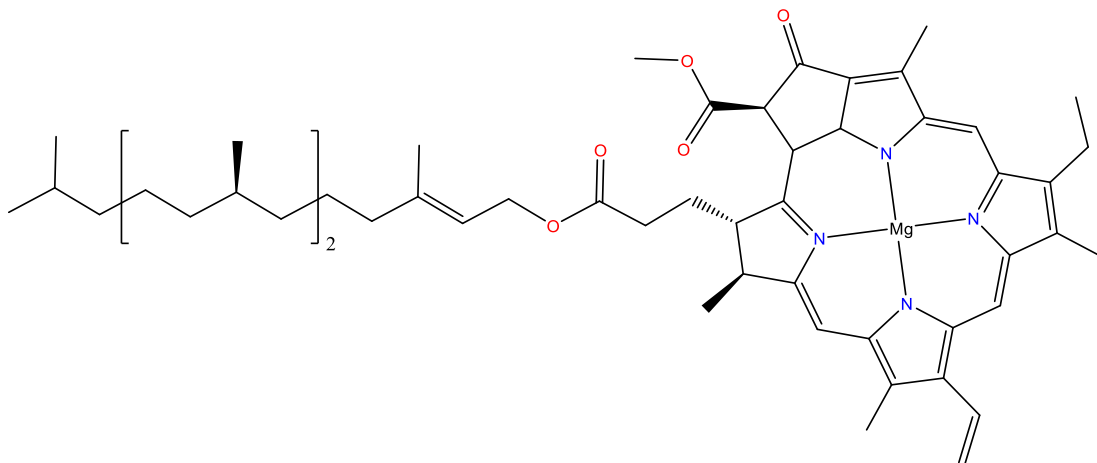

Figure 1.6 Structure of chlorophyll a.

The precise antenna chromophores and their concentrations within the chloroplasts are dependent on the organism and the lighting conditions - e.g. chlorophyll a has a higher concentration than chlorophyll b in land-based photosynthetic organisms while the reverse is true for the aquatic counterparts. Antenna chromophores absorb light forming singlet excited species that transfer energy to the reaction centres of the photosystems via a series of fluorescence resonance energy transfers (FRET). The energy transfer is not, however, adiabatic as energy is lost through vibrational relaxation of the various excited states. This serves to redshift the emission spectra of the chromophores to afford a better overlap with the absorption band of the active site.
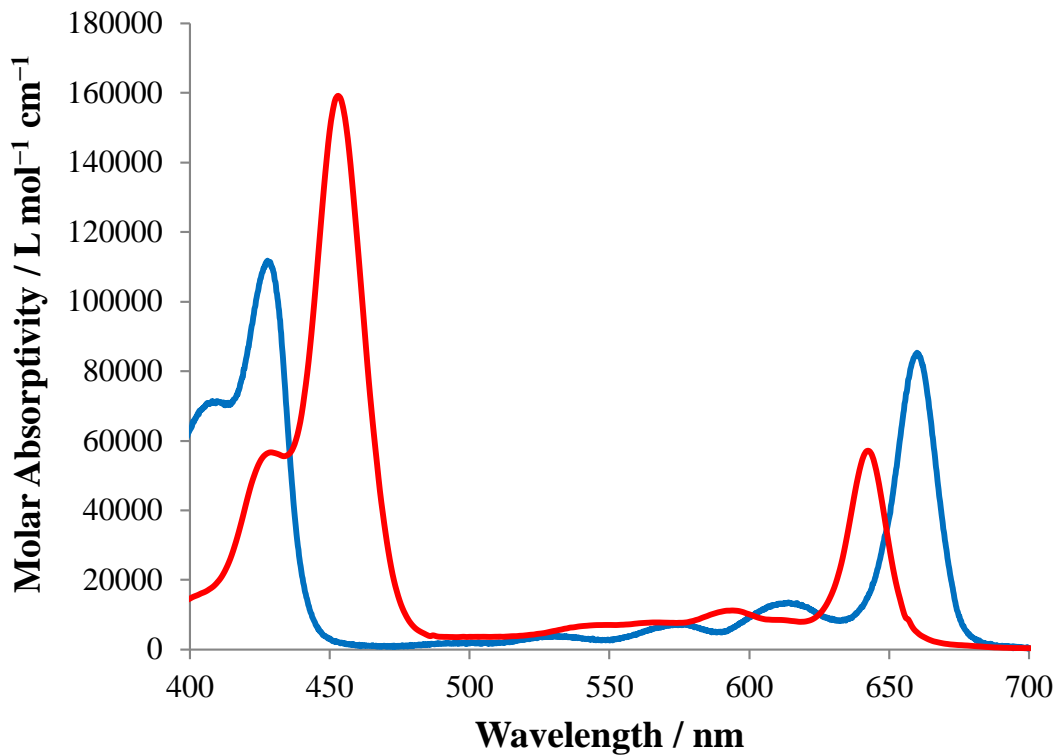
Figure 1.7 Absorption bands of common light harvesting species. Chlorophyll a (blue), chlorophyll b (red)

The use of these red shifting chromophores also serves to concentrate light as the number of chromophore molecules are far in excess of the number of reaction centres. The presence of different chromophores will vary between species, as shown in Table 1.[13] It must be stated, however, that they have not all evolved to exploit the same wavelengths. For example, purple bacteria absorb in the mid energy region of the visible spectrum (~550 nm) rather than the typical high and low energy as seen in green plants (Figure 1.7).

Table 1.1 Light harvesting species in different photosynthetic life forms.[13]

	Eukaryotes				Prokaryotes		
	Higher Plants	Green Algae	Diatoms, brown algae	Red algae	Cyanobacteria	Purple bacteria	Green bacteria
Chlorophylls							
Chlorophyll *a*	+	+	+	+	+		
Chlorophyll *b*	+	+					
Chlorophyll *c*			+				
Bacteriochlorophyll *a*						+	+
Bacteriochlorophyll *b*						+	
Chlorobium chlorophyll							+
Cartenoids	+	+	+	+	+	+	+
Phycobilins				+	+		

Photosystem II (P680)

P680 consists of a specialised dimer of chlorophyll *a* molecules. The particular properties of this dimer - i.e. the ability to undergo effective photoactivated charge separation and then to oxidise and reduce its surroundings - are attributed to the two binding proteins (D^1 and D^2) attached to it via a histidine group (Figure 1.8).[14] The proteins act to regulate the electron transport mechanism via the selective binding of the species involved in that mechanism.
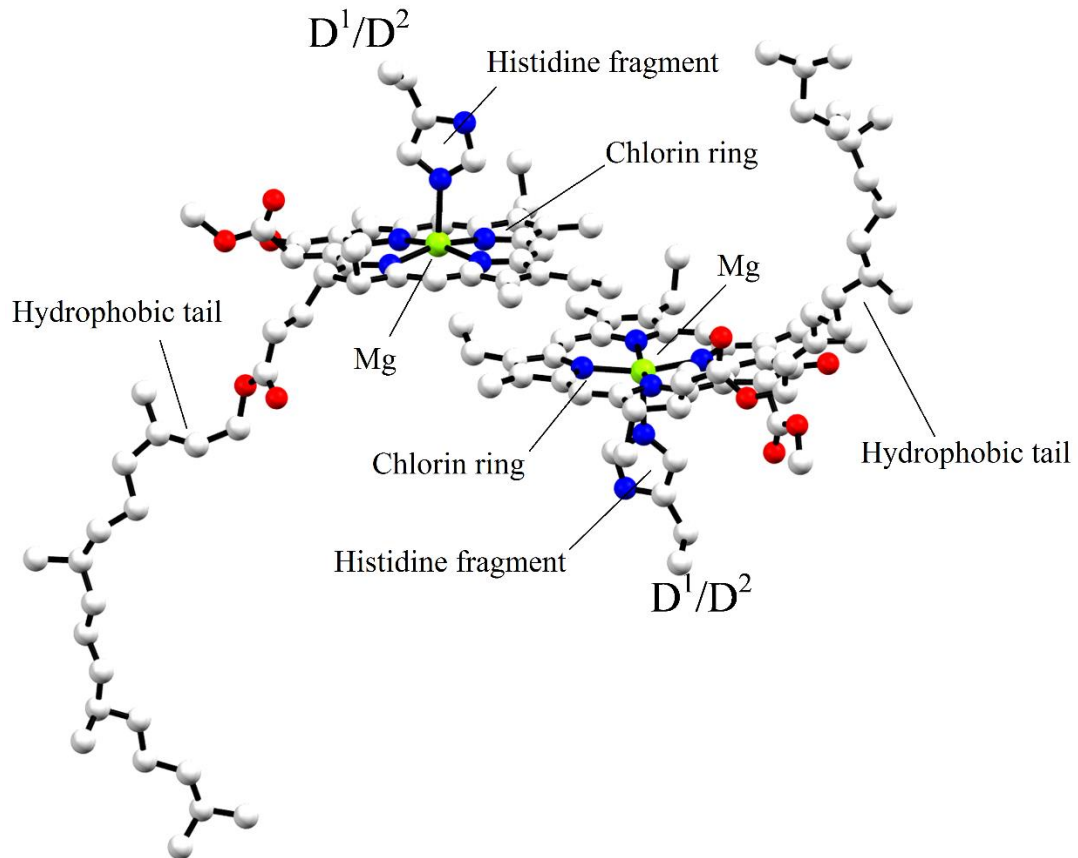

Figure 1.8 X-ray structure of P680 Dimer.[15] Protons ommitted for clarity.

The promoted electron in the photoexcited P680* is now strongly reducing and reduces plastoquinone to plastoquinol (Scheme 1.1) using pheophytin (chlorophyll *a* without the magnesium centre) in the electron transport mechanism. The reduction of plastoquinone by P680* also forms the oxidised species P680[+] which is important in the water oxidation step. The aqueous medium surrounding the photosynthetic structures within individual chloroplasts (stroma) provides the protons for the reduction. There then follows a complex series of biochemical reactions to shuttle the

electron to the start of the photosystem I reaction centre. The reduction also serves to sequester protons from the stroma. This creates a proton concentration gradient which is necessary for the phosphorylation of ADP to ATP.[10]
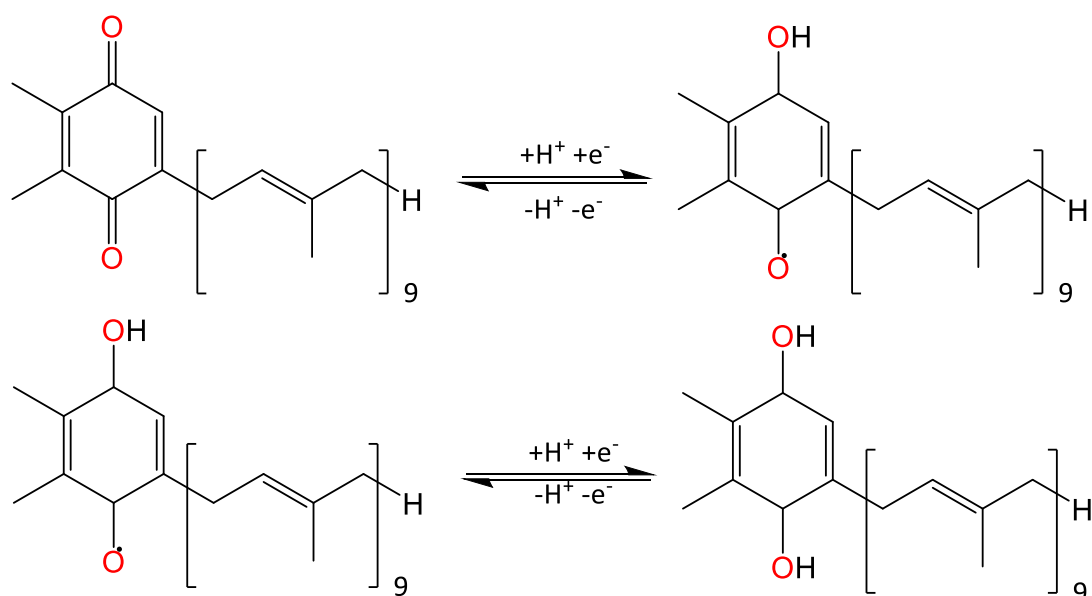
Scheme 1.1 Reduction of plastoquinone to plastoquinol.

The reduction of P680$^+$ back to P680 is achieved via the oxidation of water to molecular oxygen and protons. In doing so the reaction replaces those protons sequestered from the stroma in the reduction of plastoquinone to plastoquinol. P680$^+$, being the strongest biological oxidising agent known, has a redox potential of 1.26V, which is able to oxidise water; however, it does not have the structure required to perform that oxidation. In order to oxidise water to molecular oxygen, the reaction centre of photosystem II contains a calcium-manganese-oxo cluster usually termed the oxygen evolving complex (OEC) and is shown in Figure 1.9.[16] The OEC is structurally supported by a series of protein structures which stabilise and bind the OEC in close proximity to the P680 dimer. The amino acid tyrosine acts as electron transfer agent between the oxidised P680 group and the OEC via the redox activity of its phenol group.
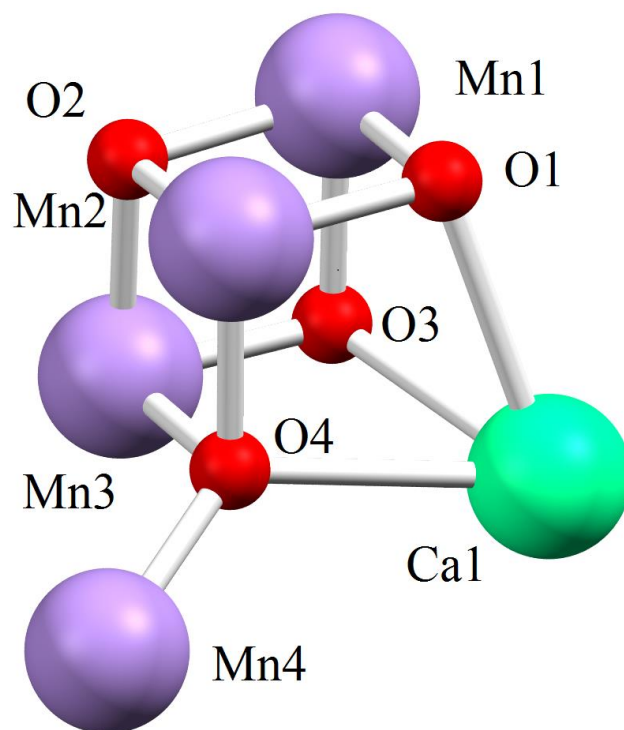
Figure 1.9 Structure of the core of the oxygen evolving complex. Coordinating groups omitted for clarity.

The exact structure of the OEC is a matter of contention as the structure varies between different states as it performs water oxidation. The formula is most often written as $Mn_4Ca_1O_xCl_{1-2}(HCO_3)_y$ with the most common number of oxygen atoms in the cluster being four. What can be agreed upon is that the cluster has multiple water molecules coordinated to it, divided between the manganese and calcium atoms, of which two act as a substrate for dioxygen formation.[16]

The nature of the charge on this structure (Figure 1.9) is also debatable, as the multiple manganese atoms will exist in different oxidation states depending on their environment. The multiple possible oxidation states of manganese are the key to the functionality of the OEC. The cluster acts like a charge sink, oxidising two water molecules to create dioxygen before undergoing four sequential oxidations by tyrosine to return it to its initial state (Figure 1.10).[17] It should be noted that the oxidative process that occurs at the OEC evolves molecular oxygen directly and not unbound peroxide or hydroxide radicals - although these could exist as short lived species coordinated to the cluster.
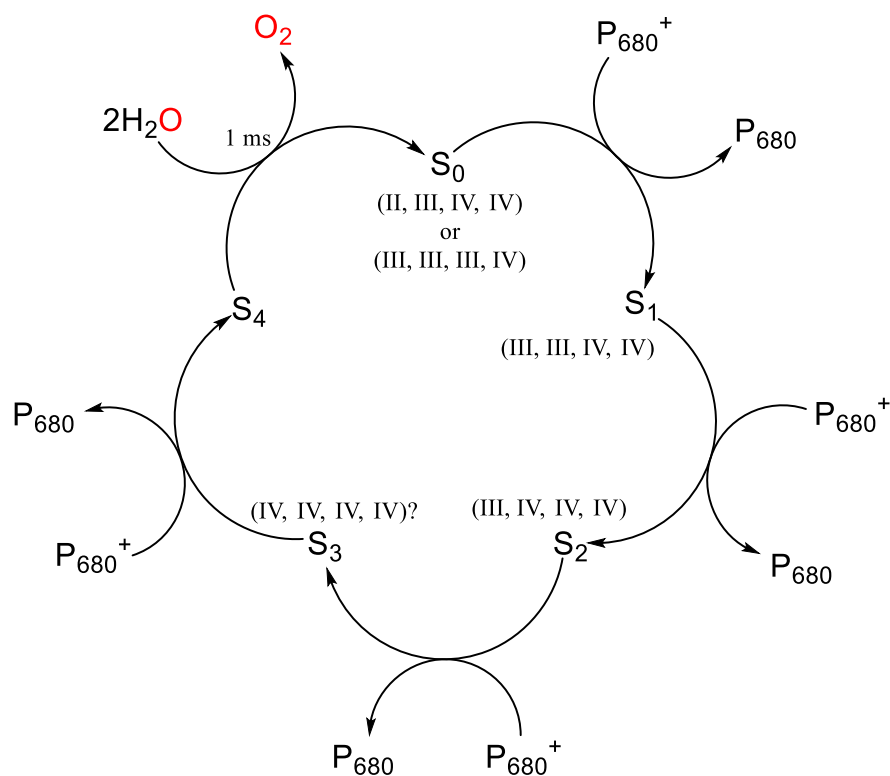
Figure 1.10 Kok cycle for the catalytic oxidation of water by the OEC.[18]

The structure of the reaction centre is maintained by the D1 and D2 proteins surrounding the P680 dimer; OEC and several other cofactors such as tyrosine and pheophytin. The proteins act to provide a substrate for the cofactors involved in the electron transport mechanisms to bind to. Additionally, they provide a structural framework which allows for the regeneration of the photosystem if one or more of the compounds within the photosystem is damaged or degraded.

Here it is important to note that the delicate light absorbing structures are separate from the oxygen evolution site. This separation limits the contact the organic/inorganic dyes have with the highly oxidative active site. If this separation did not exist, then it is as likely that the dyes would be oxidised rather than water, which would lead to the decomposition of the light-absorbing components of the system. This is an important lesson to remember when creating a synthetic photosystem.

Photosystem I (P700)

The reaction centre for photosystem I is similar to photosystem II in that it is composed of chlorophyll dimers that absorb energy from light absorbing dyes via a FRET mechanism. The light energy promotes an electron which then triggers a series of reductive reactions until $NADP^+$ is reduced to NADPH (Figure 1.11). As in photosystem II, the end reaction of photosystem I is metal-catalysed, this time by the iron- and sulphur-containing ferredoxin-$NADP^+$ reductase enzyme.[19]
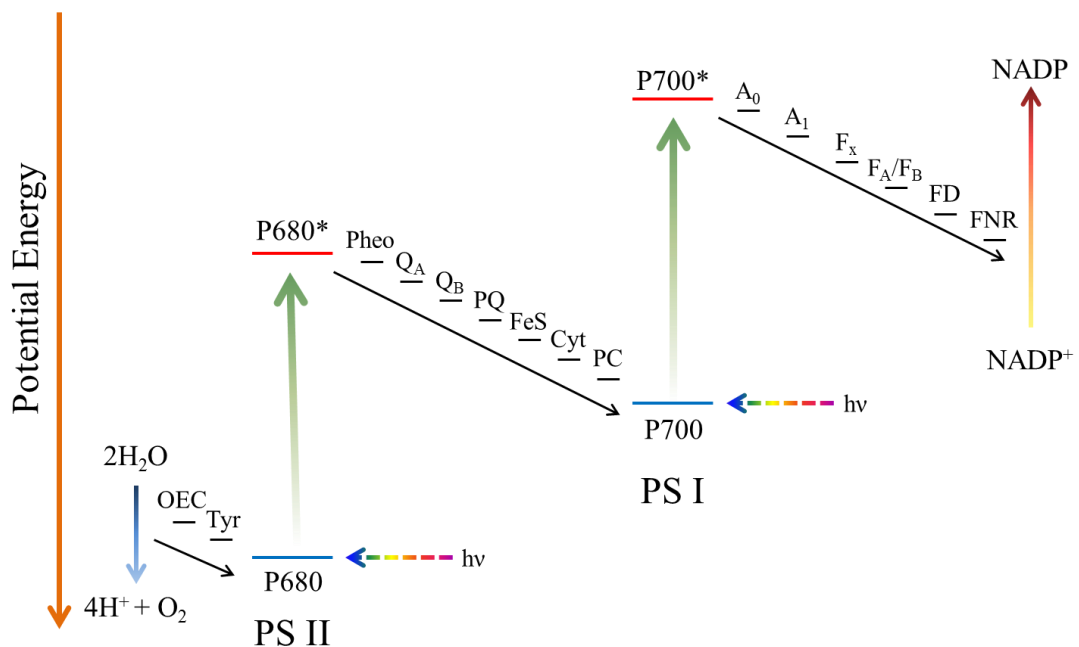

Figure 1.11 Photosynthetic pathway for green plants. OEC (Oxygen evolving centre), Tyr (Tyrosine), Pheo (Pheophytin), Q_A (Primary plastoquinone electron acceptor), Q_B (Secondary plastoquinone electron acceptor), PQ (Plastoquinone), FeS (Rieske protein), Cyt (Cytochrome f), PC (Plastocyanin), A_0 (Primary electron acceptor of PS I), A_1 (Phylloquinone), F_x F_A F_B (Iron-sulfur clusters), FD (Ferredoxin), FNR (Ferredoxin-$NADP^+$ reductase), NADP (Nicotinamide adenine dinucleotide phosphate).

One of the most important flaws in the photosynthetic system is that the mechanism that allows for energy conversion is also damaged by it, a process known as photoinhibition. Photosystem II is particularly vulnerable to damage, with the level of damage suffered increasing with the energy of the light absorbed. This provides an additional explanation to the attenuation of higher energy light to lower energy light rather than direct conversion of the higher energy light to chemical energy.

While the damage to the reaction centre is continuous under illumination so is the repair of the reaction centre. The mechanism for the regeneration of the reaction centre has been well established as the degradation of the D1 protein followed by de novo biosynthesis and insertion of a new D1 protein. While several mechanisms for the photoinhibition of the P680 reaction centre have been proposed, such as direct photolysis of the OEC or protein degradation caused by the formation of singlet oxygen species, the fact that these degradation pathways occur under the operating conditions of the mechanism confirms that we must consider that multiple degradation pathways are occurring simultaneously but to different degrees.[20]

While the chromophores present in the chloroplasts will primarily generate excited singlet states at higher light intensities the concentration of singlet states can give rise to excited triplet states which raises a problem for biologically housed system. The excited triplet state of the chromaphore is significantly longer lived compared to its singlet excited state due to it requiring a spin transition before the chromaphore can return to its ground state. As the long lived triplet excited state is much more reactive it can generate singlet oxygen. Singlet oxygen is molecular oxygen where the spins of the two highest energy electrons are paired. Due to the degeneracy of the highest energy occupied orbitals the electrons are in violation of the selection rules and are therefore unstable (Figure 1.12). The instability of singlet oxygen makes it an extremely aggressive oxidant.[21]
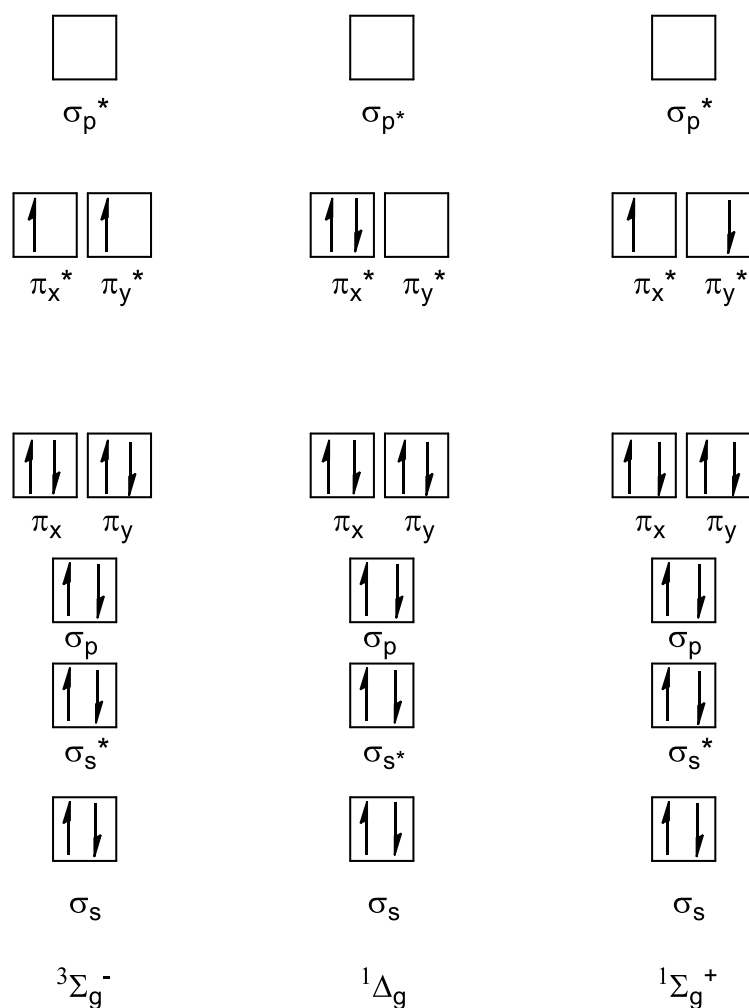
Figure 1.12 Spin states of triplet oxygen (left), metastable singlet oxygen (centre) and secondary singlet excited state (right).

The formation of such a powerful oxidant in an uncontrolled manner within such a complex reaction chain would inevitably lead to damage of the photosynthetic apparatus.[22] While the formation of such reactive species by the antenna molecules would be damaging to the antenna molecules themselves it is even more damaging when singlet oxygen is generated within the active centre of PSII. The charge recombination of $P680^+$ and the monoprotonated plastoquinone anion can lead to the generation of the highly oxidising singlet oxygen which degrades the surrounding photosynthetic architectures.
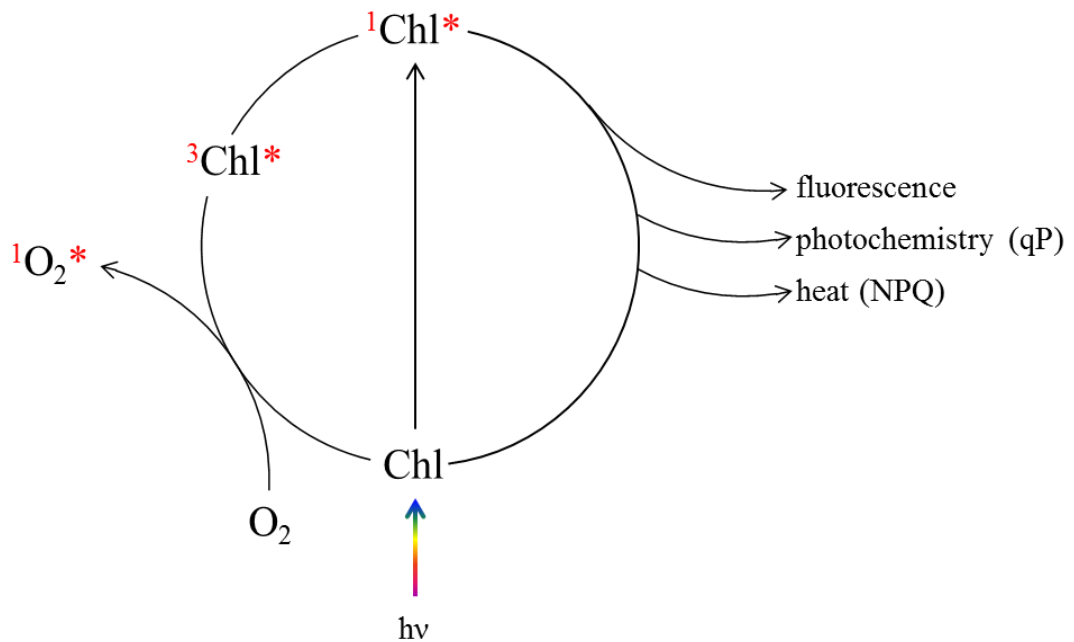
$^1Chl*$

$^3Chl*$

$^1O_2*$

O_2

Chl

hν

→ fluorescence
→ photochemistry (qP)
→ heat (NPQ)

Figure 1.13 Possible decay pathways of photoexcited chlorophyll, including singlet oxygen formation.[23]

The use of non-photochemical quenching (NPQ) regulates the concentration of singlet excited states by the thermal decay of the singlet excited state (Figure 1.13).[24] It does not, however, limit direct damage to the OEC. The OEC can directly absorb visible or UV light; however, it is not able to utilise any of this energy as it immediately deactivates the complex by the splitting of a Mn-O bond and releasing a Mn ion from the structure. Deactivation of the manganese cluster does not, however, stop light absorption but inhibits electron transfer to the P680 reaction centre. As the usual mechanism for the reduction of P680$^+$ is no longer viable, the lifetime of the cation increases - which promotes recombination and singlet oxygen generation. Alternatively, the P680$^+$ cation as the most powerful biological oxidising agent can begin to damage the surrounding molecules and protein structures.[25]

There are other available mechanisms for the photoinhibition of PSII such as the reduction of the plastoquinone electron transport chain connecting PSII to PSI.[26] This will occur under high intensity illumination and will have a similar effect to the deactivation of the OEC. When the electron transport chain is limited, the lifetime of the photoexcited P680 active site increases as it is not being quenched. This increase in lifetime of the singlet excited state leads to triplet state formation via intersystem crossing, which in turn will generate singlet oxygen.

The mechanism for photoinhibition is troubling from an applied chemistry perspective as the regeneration of such a complex photochemical system in situ is regarded as a practical impossibility at the current level of manufacturing technology. Self-regenerating systems are not unknown to chemistry but are relatively simple and will usually follow an entropic or endothermic gradient. The number of constituent parts of the photosynthetic assembly makes a direct synthetic version unattainable at our current level of understanding although a simplified version may be possible. Any research into this area would, however, have an extremely high cost and low reward compared with alternate research paths. Additionally, any products derived from regenerative systems would have such high costs as to make any savings gained from fuel production pale in comparison to the enormous capital cost of such a system. The disparity in the capital costs and the financial savings removes any economic drive for the implementation of synthetic photosynthetic systems on the scale required to drive down the manufacturing costs and compete with alternate solar energy technologies.

The four key aspects of natural photosynthesis are the separation of oxidative and reductive systems; the separation of the light absorbing chromophores; the photoactive sensitisers and the oxidatively stable catalytic centres; the four-electron water-oxidation reaction and the regenerative photosynthetic assembly.

While both the oxidation and reductive mechanisms have been examined extensively it is a vast step from understanding the nature of a biological mechanism to being able to create a system inspired by those mechanisms that would be able to convert quantities of energy similar to what can be converted by the simplest of plants and photosynthetic bacteria. This discrepancy is in part due to the nature of the plant's energy storage system. Electromagnetic energy is converted to chemical energy and then stored in the reduced form of certain cofactors ($NADP^+$, NAD^+) and eventually used to synthesise complex carbohydrates. This system is specifically evolved to store energy in the organism and does not lend itself to extracting energy for other purposes. The only method available is to destroy the organism and process it into a fuel source such as bioethanol/ biodiesel. This method is viable under certain conditions although the output vs. processing costs makes it uneconomical under all but the most industrialised conditions. The viability of small scale solar fuel generation is dependent

on the ability to extract chemical energy from a photosynthetic system in a greatly simplified form. While research has been carried out in the area of direct hydrocarbon synthesis from the reduction of atmospheric CO_2, by far the most examined solar fuel is molecular hydrogen.

Photosystem I is more complex than photosystem II and is also the more difficult to replicate as it requires the continual reduction of complex organic species. Compare this with photosystem II which simply oxidises water to molecular oxygen. Extracting molecular oxygen from photosystem II is only desired in order to prevent the saturation of photoactive apparatus with a reactive species. Extracting energy-rich materials from photosystem I is a much more pressing concern as it is by this route that energy storage is attained in the form of fuel. The apparatus of photosystem I does not generate small molecular fuels - rather it regenerates the carrier molecules ADP and $NADP^+$ back into ATP and NADPH, which are used in the Calvin cycle for carbon fixation and carbohydrate synthesis. To replicate such a system in a synthetic manner would be to mimic and incorporate an additional complex biological mechanism into an already synthetically challenging process.

Replacing the extended pathway of photosystem II with a shorter hydrogen evolution path offers a much simpler system which generates an easily extracted fuel. It is at this stage that it is important to examine if the mimicking of a biological process is necessarily the most efficient and effective way to generate fuels from solar energy. The two-photosystem approach may be sustainable for biological systems but a single excitation may be feasible for a synthetic approach, i.e. a single photoactive species which provides the necessary charge separation for both oxidation and reduction reactions. The two excitation approaches, while allowing for a greater absorption of radiation, does not necessarily make it the more synthetically appealing, as it adds a secondary rate-limiting step compared with a single step for the single excitation path. Additionally, as development of the oxidation and reduction steps in the photochemical splitting of water are often examined separately it can be argued that development of a single excitation pathway will be the more easily developed to a higher standard.

Of the two steps, the reduction of protons is the easier of the systems to examine and has enjoyed relative success, as the reaction does not have the same thermodynamic barrier as does the oxidation of water directly, being only a two-electron process rather than a four-electron process. The oxidation of water, additionally, has the problem that the oxidative environment it generates can irreversibly oxidise the catalyst itself. The oxidative pathway is, however, the more important of the two, as it generates the protons and electrons required for the reductive step, and can therefore be regarded as rate-limiting. Without an efficient water oxidation step, any hydrogen evolution catalysts will be unable to generate hydrogen in any useful quantities without the addition of additional protons, and by applying a bias voltage. While data gained in this way may be useful, over-reliance on that data would bias any conclusions in favour of systems whose performance is derived from electrode dynamics rather than from their photochemical properties.

Molecular Catalysis

The simplest systems for water oxidation from a structural perspective are homogeneous as they do not suffer from problems of surface diffusion limiting reactions and deactivation of the active surface compared to heterogeneous and to a lesser degree microheterogenous reaction systems. Ideally a molecular water oxidation catalyst (WOC) would contain both a high absorptivity chromaphore and suitable oxidation site in a single molecule; however, the use of a separate photosensitiser, such as $Ru(bipy)_3^{2+}$ is generally accepted as being necessary due to the difficulty in generating a single reactant system. The range of molecular catalysts generally falls into two categories: mononuclear and multinuclear.

As the water oxidation reaction is a four-electron process, it requires that molecular species used as catalysts for this reaction are able to form high-valent metal-oxo species at low redox potentials. These species are most commonly generated in situ via the oxidation of aqua-substituted metal centres and from part of a catalytic cycle which regenerates the species if a suitable oxidant is available. The key issue in all proposed mechanisms is the formation of the O-O bond of which the most common pathway involves the nucleophilic attack of a solvent water molecule on the high valent species $Ru^V{=}O$, referred to as water nucleophilic attack (WNA). The alternate mechanism is based on having a high enough concentration of metal-oxo species where two metal oxo units interact to form a dimer (I2M) (Figure 1.14).[27]
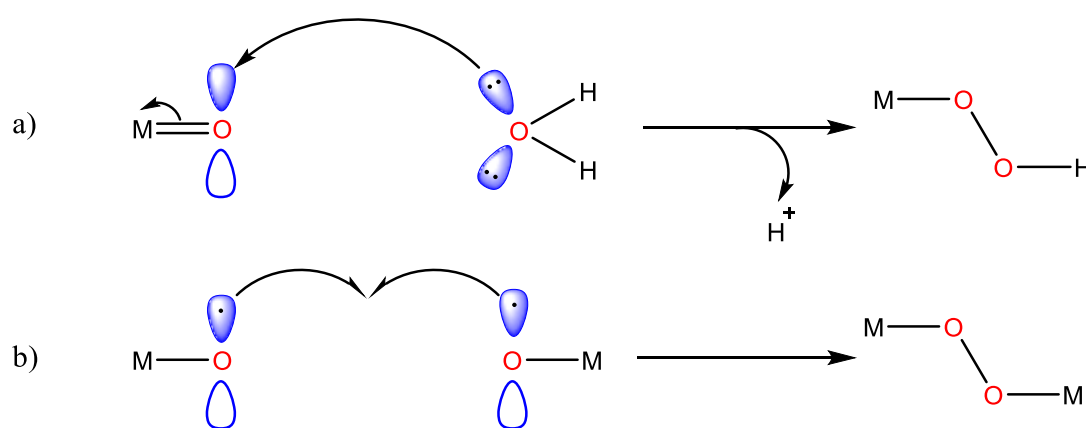

Figure 1.14 a) WNA mechanism b) I2M mechanism

In the WNA mechanism the high-valent metal-oxo is attacked by solvent water, forming the required O-O bond while cleaving the metal-oxo π-bond to form the metal hydroperoxide species (M-OOH). Cleavage of the metal-oxo π-bond results in the two-electron reduction of the metal centre (usually from Ru^{V} to Ru^{III}). Proton- coupled electron transfer (PCET) cycles the reaction centre to the ruthenium peroxo species, at which point the peroxide can be oxidised by the Ru^{IV} centre before being displaced as O_2 by an aqua species to regenerate the aqua precursor. Alternatively, in low pH environments the peroxo species can undergo another oxidation step to form Ru^{V}, followed by the oxidation of the peroxide to O_2 and displacement via an aqua. As the oxidation state of the ruthenium is higher in this second path, the coordinated aqua is immediately oxidised to the hydroxide with release of a proton. Oxidation steps and PCET cycle the two pathways back to the Ru^{V}=O species, ready to begin the cycle again (Figure 1.15).[28] While this mechanism is most readily applied to mononuclear catalysts, the same basic cycle is present in dinuclear catalysts, as discussed below.
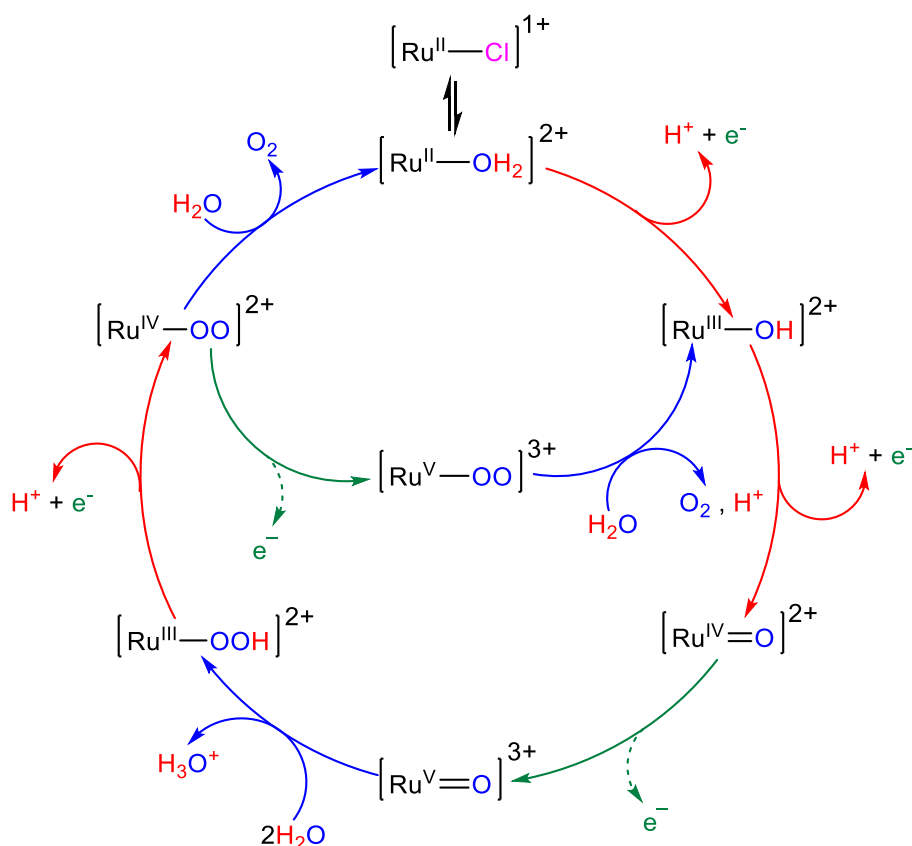

Figure 1.15 WNA catalytic cycle for mononuclear water oxidation catalysts. Red arrows: Proton coupled electron transfer. Blue arrows: Aqua addition. Green arrows: Oxidation.

Mononuclear catalysts

Mononuclear ruthenium water oxidation catalysts (WOC) can be broken down into two groups: those whose coordinating ligands are charge-neutral and those which contain anionic groups. The first well-characterised example of the former was published in 2005. It consisted of a large polypyridyl ligand (2,6-di(1,8-naphthyridin-2-yl)4-(tert-butyl)pyridine) meridionally coordinated to a Ru^{II} centre in a tridentate moiety. The axial positions of the complex are taken up by two 4-methylpyridine ligands leaving the coordination site opposite the central pyridyl group on the first ligand free for water coordination. The uncoordinated naphthyridine sites stabilise the aqua complex by hydrogen bonding to the aqua group's protons (Figure 1.16).[29] This complex, and its sister complexes using either 4-(dimethylamino)pyridine or 4-(trifluoromethyl)pyridine, differ from later mononuclear catalysts in that the mechanism it employs appears to progress through PCET alone rather than a mix of PCET and one-electron oxidations. This causes the catalytic intermediate to be the $Ru^{IV}=O^{2+}$ complex rather than $Ru^{V}=O^{3+}$.
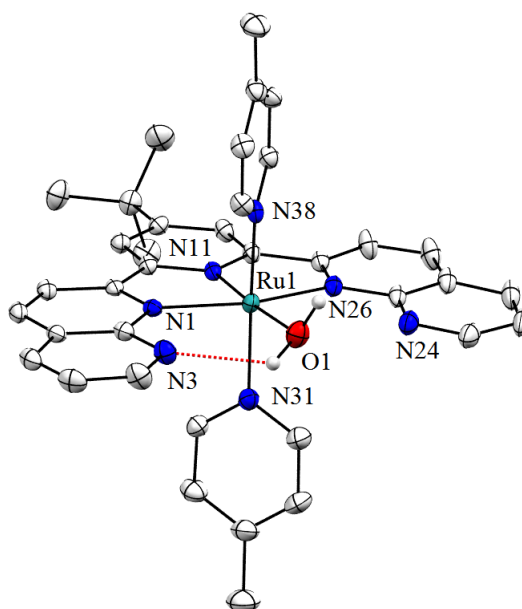

Figure 1.16 X-ray structure of trans-[Ru(2,6-di(1,8-naphthyridin-2-yl)4-(tert-butyl)pyridine)(4-Me-py)$_2$(OH$_2$)]$^{2+}$ 2[PF$_6$]$^-$. Non-aqua protons and counter anions omitted for clarity. Ellipsoids shown at 50% probability.

This group of water oxidation catalysts was followed soon after by a better studied series based on a ruthenium centre surrounded by a terpyridyl and a bipyridyl ligand (Figure 1.17).
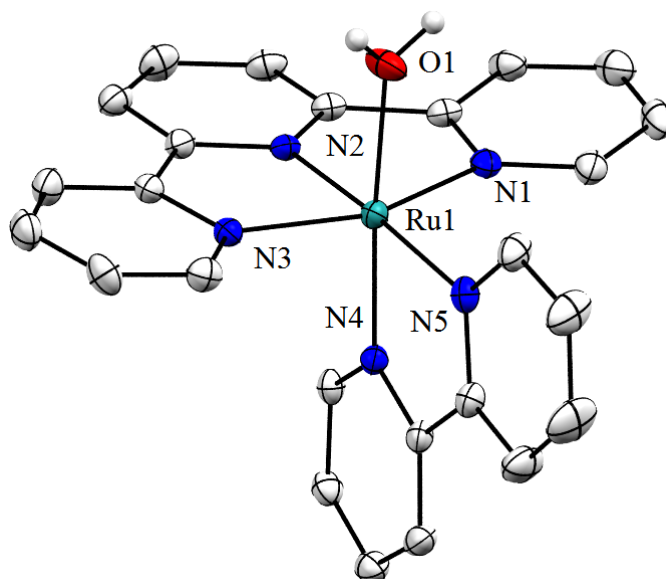
Figure 1.17 X-ray structure of [Ru(bipy)(terpy)(H₂O)]²⁺. 2[ClO₄]⁻. Non-aqua protons and counter anions omitted for clarity. Ellipsoids shown at 50% probability.

Initially synthesised with a chloride occupying the remaining site, it was found that the chloride must be exchanged with solvent aqua species before water oxidation can occur (Figure 1.18). The rate of exchange is proportional to the electron-withdrawing effect of the coordination site trans to the chloride.[30-31] This has been observed in similar species bearing halides, with O_2 production having an induction period indicating that these species do indeed act as pre-catalysts rather than catalysts in their own right.
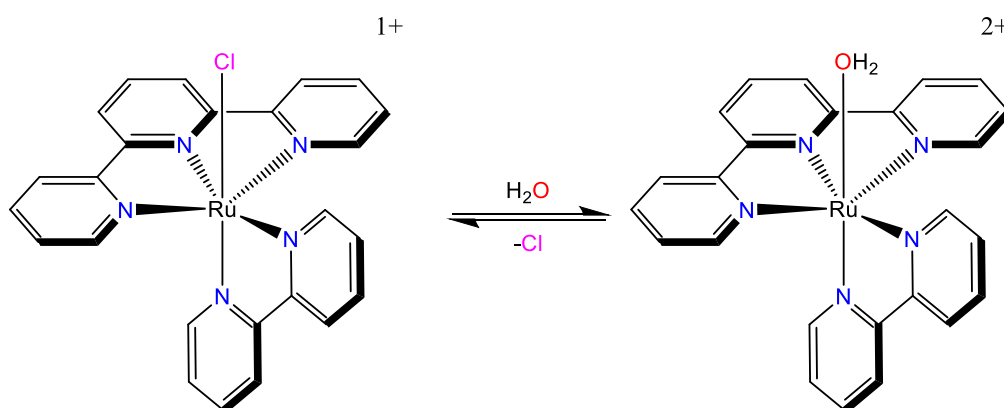

Figure 1.18 Equilibrium of an example catalytic and precatalytic species in solution.

In these modified systems the observed catalytic rate was found to inversely correlate with the electron-withdrawing properties of the bipyridyl. Similar modifications of the terpyridyl ligand had the opposite effect, increasing the catalytic activity rather than

decreasing it, however the effect was not of the same order as that observed in the modified bipyridyl species. Electrochemical experiments show clearly that substituents on both bipyridyl and terpyridyl have a marked effect on the electronic couples required for the catalytic cycle, with electron donating groups lowering the three primary redox couples of the catalyst and electron withdrawing groups raising them.[32] Analysis revealed that the site located trans to the aqua is weakened at higher oxidation states, leading to an increase of the length of the Ru-N bond. Comparing the activity of catalysts with the active site either cis or trans to the tridentate ligand demonstrated that the species with the catalytic site in the trans position tended to exhibit the higher activity. It has also been noted that the activity of a selected catalyst is not always easily correlated to the shifts in the primary and secondary redox couples compared to other catalysts. Other systems have sought to improve on the activity of initial systems by increasing the electron donating properties of the ligand site trans to the aqua group. Exchange of the pyridine group for a group exhibiting increased σ-donor character, e.g. N-heterocyclic carbenes, was found to have a marked effect on the activity with the increase in activity being ascribed to increased O-O coupling from the $Ru^{V}=O^{3+}$.[33]

The addition of pendant electron donating groups upon the bipyridyl ligand is known to increase the activity of the catalyst but the position is also important as shown in the two complexes derived from 4,4'-dimethoxy-2,2'-bipyridine and 6,6'-dimethoxy-2,2'-bipyridine having a turnover number of 98 and 215 respectively.[34-35] The increased turnover number is attributed to the hydrogen bonding between the methoxy adjacent to the reaction centre and the incoming water molecule. The effect of hydrogen bonding is not always a positive one, as seen when the methoxy group is replaced with a hydroxy or fluoride.[35-36] The hydrogen bonding in this instance is thought to hinder PCET mechanisms and leads to a decreased turn over number (TON) and turn over frequency (TOF) in the fluoride substituted species and no activity at all in the hydroxy. In these two examples it is thought that the hydrogen bonding interferes with the PCET mechanism by stabilising the $[Ru^{III}\text{-}OOH]^{2+}$ species. It must however be stated that in the case of hydroxyl further investigation is required to precisely determine the lack of activity shown. Similarly the two photoisomers of [Ru(2,2';6',2''-terpyridine)(2-(2-pyridyl)-1,8-naphthyridine)(OH$_2$)]$^{2+}$ show markedly differing

activity due to the effect of hydrogen bonding similar to that seen in the (2,6-di(1,8-naphthyridin-2-yl)4-(tert-butyl)pyridine) species with the hydrogen bonding isomer having the lower activity.[37-38]

One limiting factor in the use of neutral ligand containing systems is the requirement of a strong chemical oxidant e.g. Ce^{IV}. An additional photosensitiser is required in order to make these systems practicable. The most commonly used is the ever popular $Ru(bpy)_3^{2+}$. However, the oxidative potential of the photoexcited $Ru(bpy)_3^{2+*}$ is not great enough to engender catalytic turnover of the majority of molecular systems. Lowering of the oxidation potential of the catalyst via the inclusion of σ-donating groups is an effective option as has been mentioned above in the Ce^{IV} driven reactions. There is however an inbuilt limit to how much electron density can be donated to the metal centre without charge transfer occurring. If the neutral ligand becomes too electron poor it opens up decomposition pathways, which reduces the overall TON for the catalyst.

In order to circumvent this limit several research groups have now begun to include coordinating anionic moieties into their ligands. These act to stabilise the higher oxidation state metal centres and lower the potential required to attain them. The first of these mononuclear species produced specifically for this purpose contained a modified version of bipyridine with two carboxylate groups coordinated to the ruthenium centre and two axial 4-methylpyridines. $Ru(bda)(pic)_2$ ($H_2bda=$ 2,2′-bipyridine-6,6′-dicarboxylic acid) is charge neutral and exhibited reduction potentials of 0.86V (II/III) and 1.11V (III/IV) at pH 1 and a catalytic water oxidation peak at 1.5V.[39-40] As water oxidation occurs at a higher potential than the oxidative potential of the photoexcited $Ru(bpy)_3^{2+*}$ it is unsuitable for photochemical water oxidation at low pH. However, it was found that under neutral conditions the II/III couple is lowered to 0.72V with oxygen evolution occurring at 0.98V, below the potential from the excited $Ru(bpy)_3^{2+*}$ (1.26 V). Further investigation confirmed that the catalyst and similarly derived systems can act in tandem with photosensitisers to oxidise water but with significant pH dependence. Under operating conditions this pH dependence becomes a limiting factor, with protons inhibiting the catalytic cycle, as the cycle itself works to generate more protons. Isolation of one of the higher valent species revealed

a dimer containing two 7-coordinated ruthenium centres bridged by an anionic [HOHOH]⁻ group. Comparison of this catalyst with that of the structurally related 1,10-phenanthroline-2,9-dicarboxylic acid derived species showed that the reaction pathways for similar catalysts can diverge significantly.[41] The bipy-derived catalyst favours the I2M mechanism, while the phenanthroline species displays the WNA pathway favoured in the neutral ligand catalysts mentioned above. In the case of the I2M-favouring catalysts it was found that the choice of axial ligands had a strong influence on the performance of said catalysts. Of these species it was the catalysts with axial ligands which promoted dimerization, and this in turn engendered the highest activities. An example being that the substitution of the 4-methylpyridine by isoquinoline resulted in more than a sevenfold increase in TOF and more than a four-fold increase in TON. Due to the increased favourability of the I2M mechanism, the catalytic activity of these species can be enhanced via the inclusion of flexible linkages to the axial ligands. The now dinuclear species is able to cause I2M coupling regardless of molar concentration. The removal of the requirement of two catalytic species to encounter one another means that the there is no time lost for the transport of high oxidation state ruthenium species and therefore results in a higher TOF though not necessarily TON. Dinuclear WOCs will be discussed in the next section.

A simpler, anionic species based on the picolinic acid motif has been studied in the form of 2,6-pyridinedicarboxylic acid which coordinates in a similar planar manner as the terpyridyl based system (Figure 1.19).[42-43] It was found that the two anionic groups lowered the potential required for water oxidation. However, the activity of these species displayed significant dependence on the ligand occupying the site opposite the pyridine ring. This is similar to that found in the terpyridyl based system but a greater difference between the activities of the bipyridine and picoline containing complexes. As with the terpyridyl species, altering the donor capabilities of the tridentate ligand can have profound effects on the activity of the catalysts containing monodentate axial ligands.
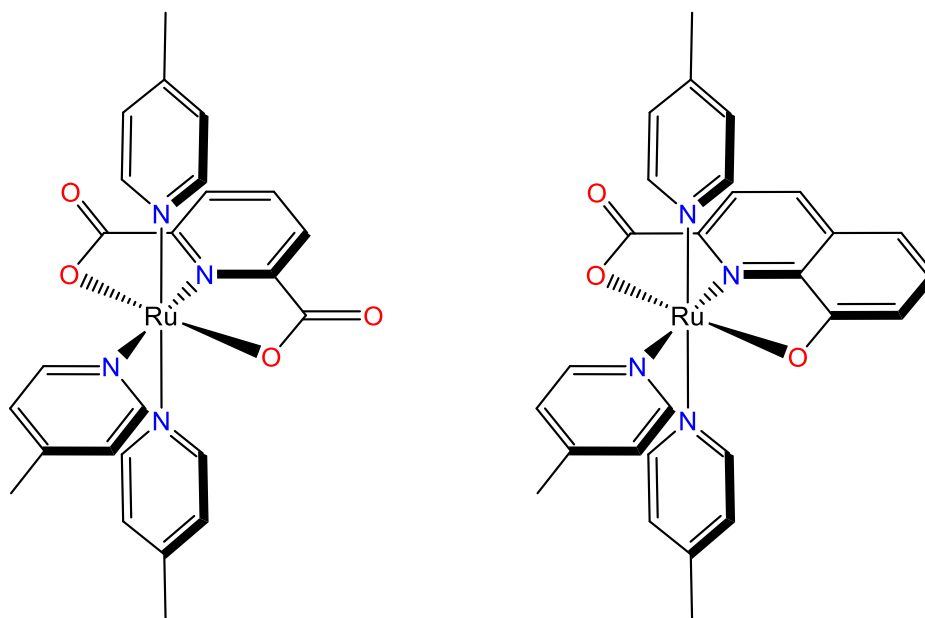
Figure 1.19 Left: Structure of $Ru^{II}(pdc)(pic)_3$, Right: Structure of $Ru^{II}(hqc)(pic)_3$

Replacing one of the carboxylate groups with a stronger π-donor, such as in 8-hydroxyquinoline-2-carboxylic acid (Figure 1.19), further increases the activity of derived catalysts.[44] The increase in activity is ascribed to the enhanced lability of the equatorially coordinated neutral ligand (picoline) and therefore the increased rate of ligand/aqua exchange. The higher rate of exchange is also found in the rate limiting O_2 release step with the Ru-O bond being destabilised by the increased electron donation from the quinoline group.

Non-pyridine based catalysts have also been explored with the use of substituted benzimidazole species (Figure 1.20).[45] The retention of a coordinated nitrogen contained within an aromatic system is required to accommodate the shifts in oxidation state of the metal centre. The coordinating nitrogen of the benzimidazole group also has the ability to become charge carrying if the second nitrogen of the imidazole ring is unprotonated, enabling the ligand to act in both a trianionic and dianionic manner without protonation occurring on coordinated donor atoms.
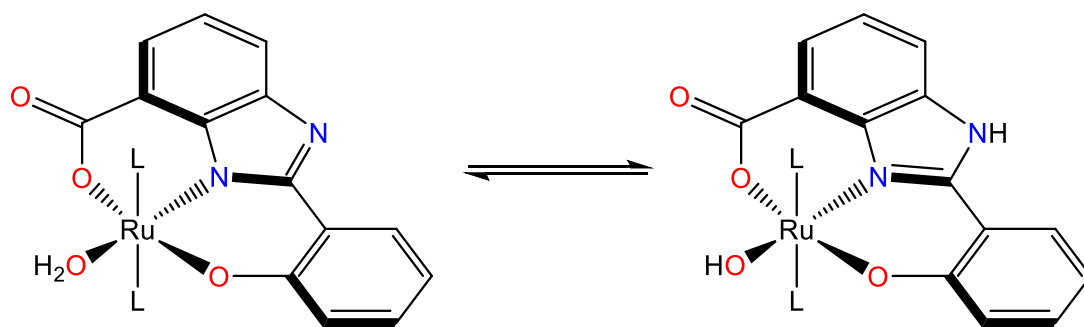
Figure 1.20 Tautomerisation in Ru^{III}(hpbc)(H_2O)(L)$_2$

The most common of the anionic groups employed in WOC are based on oxygen, due to the ease in ligand synthesis and that the pKa of the groups allow for easy complex formation. However, softer donors such as sulphur or nitrogen might provide a more favourable coordination to the ruthenium centre. Consideration must be made to the suitability of the donor atoms to the operating environment of the catalyst. Softer donors such as sulphur and phosphorus have significantly lower electronegativities than oxygen, making them more diffuse donors and allows for better coordination to the lower oxidation states of the ruthenium centre. The lower electronegativities have a penalty however, in that it leaves the sulphur and particularly the phosphorus susceptible to irreversible oxidation and decomposition under the required operating conditions of the catalyst. A trade-off between the hard nature of oxygen and the soft of sulphur/phosphorus is found in particular types of nitrogen donor.

Nitrogen has an electronegativity value approximately halfway between that of oxygen and sulphur, making it effective for coordination to both the high and low oxidation states of ruthenium. This has a contributing factor as to why the overwhelming majority of ruthenium complexes used in water oxidation, and indeed most types of ruthenium based catalysis, includes nitrogen donors. An anionic nitrogen-metal bond is more difficult to achieve, as anionic nitrogens are susceptible to protonation. Stabilisation of the nitrogen can be achieved through inclusion in a conjugated or aromatic moiety such as in the anionic isomer of the benzimidazole derived complex (Figure 1.20).

The other type of stable anionic nitrogen is that of an acid amide where the nitrogen exists in a resonance form with the oxygen (Figure 1.21).
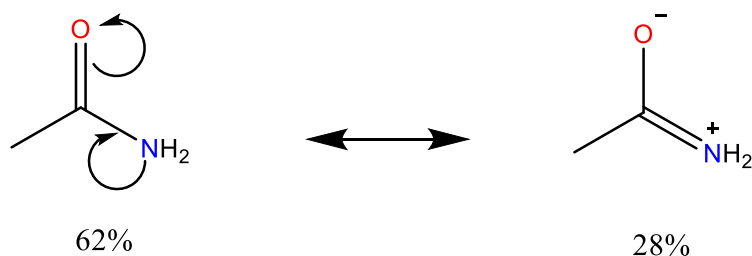
62%   28%

Figure 1.21 Resonance of acetamide. The remaining 10% was attributed to hyperconjugation resonance forms.[46]

The electron withdrawing effect of the oxygen lowers the pKa of the nitrogen allowing for it to deprotonate and coordinate to metals anionically as well as through its lone pair (Figure 1.22).
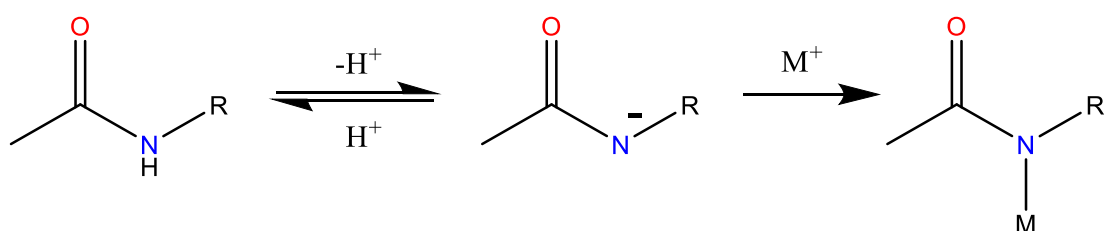

Figure 1.22 Deprotonation and metal coordination of acid amide.

Amides such as this have the added benefit of being good π-donors as well as good σ-donors due to the out of plane lone pair on the nitrogen being stabilised by the adjacent C=O π-orbital. Inclusion of this moiety into water oxidation catalysts have been attempted with the use of the non-innocent ligand H$_2$bpb (1,2-bis(pyridine-2-carboxamido)benzene) (Figure 1.23).[47] This tetradentate ligand coordinates to metal centres around the meridional plane with the nitrogen having a trigonal planar geometry rather than pyramidal. The lone pair on the nitrogen is further stabilised by extended conjugation across the entire ligand. This delocalisation mirrors that found in the porphyrin structure of the biological photocentres.
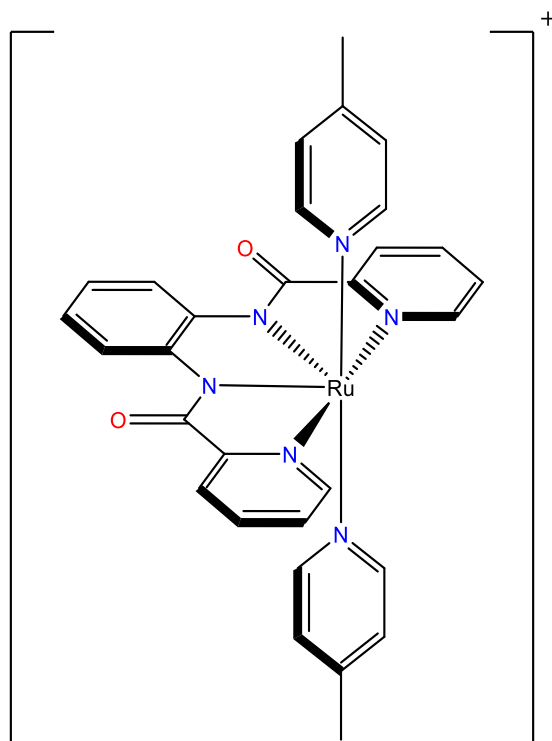
Figure 1.23 Structure of [Ru(bpb)(pic)$_2$]$^+$.

The picoline-containing ruthenium catalyst derived from this ligand exhibited good catalytic activity but was deactivated by poisoning via CO to become a CO, H$_2$O containing species. Poisoning by CO is common in a large number of precious metal catalysts due to the CO stabilising the lower oxidation state(s) of the metal centre. Nevertheless, the catalyst displayed unusual activity in that it appeared to catalyse water oxidation at a lower oxidation state.

Dinuclear catalysts

While the mononuclear catalysts seek to increase activity by increasing the electron density on the ruthenium centre in order to accomplish the four-electron water oxidation reaction an alternate approach is to use two ruthenium centres to "share the load".
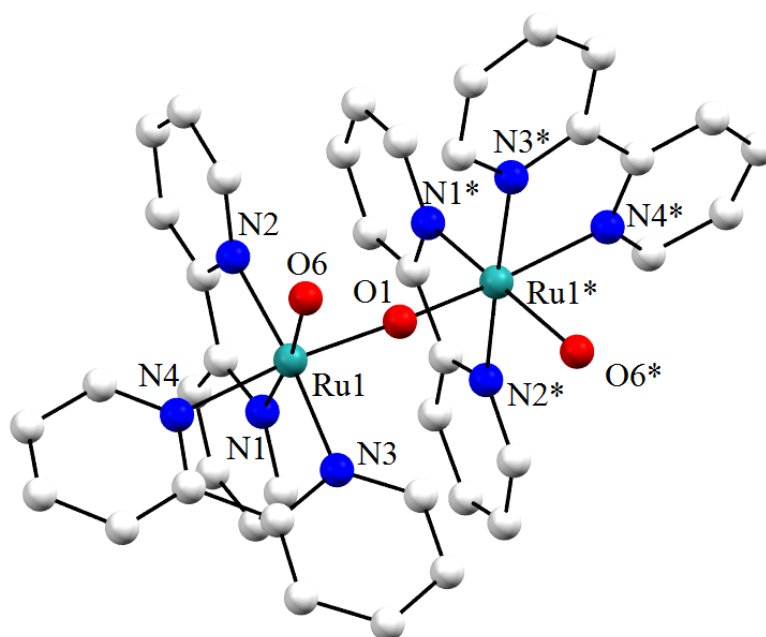
Figure 1.24 X-ray structure of the blue dimer. *cis,cis*-[(bpy)$_2$(H$_2$O)Ru(μ-O)Ru(H$_2$O)-(bpy)$_2$]$^{4+}$ 2[ClO$_4$]$^-$. Counter anions and protons omitted for clarity.[48]

The most well-known example of a dinuclear water oxidation catalyst is *cis,cis*-[(bpy)$_2$(H$_2$O)Ru(μ-O)Ru(H$_2$O)-(bpy)$_2$]$^{4+}$, colloquially known as the blue dimer (Figure 1.24). Discovered in 1985 by Meyer et al, the dimer contains two Ru^{III}-OH$_2$ cores bridged by an anionic O^{2-} with two 2,2'-bipyridine ligands coordinated to each metal centre.[48] The μ-oxo bridge facilitates strong electronic coupling between the two ruthenium centres which stabilises the complex in the higher oxidation state steps of the catalytic cycle. The mechanism is similar to that of single-site water oxidation in that it follows the WNA pathway through to the metal-hydroperoxide before finally liberating O$_2$ (Figure 1.25). It has also been postulated by Hurst and Cape that the bipyridine ligands are involved in the oxidation process, as they are capable of temporarily accommodating electron density from the attacking water.[49] Subsequent investigations by multiple groups have shown that this is an improbable mechanism for the catalytic cycle as it is likely to lead to decomposition of the catalyst itself.

Crystal structures of the blue dimer show that the two aqua groups are orientated out of plane with each other, meaning that unlike the dinuclear system mentioned above they cannot couple in a concerted I2M mechanism. That is not to say that the two water molecules only interact with the metal centres. On the contrary while the oxygen atoms may not couple to each other they are capable of hydrogen bonding to each other through bound protons and likely shuttle those protons between each other at various stages of the catalyst cycle.
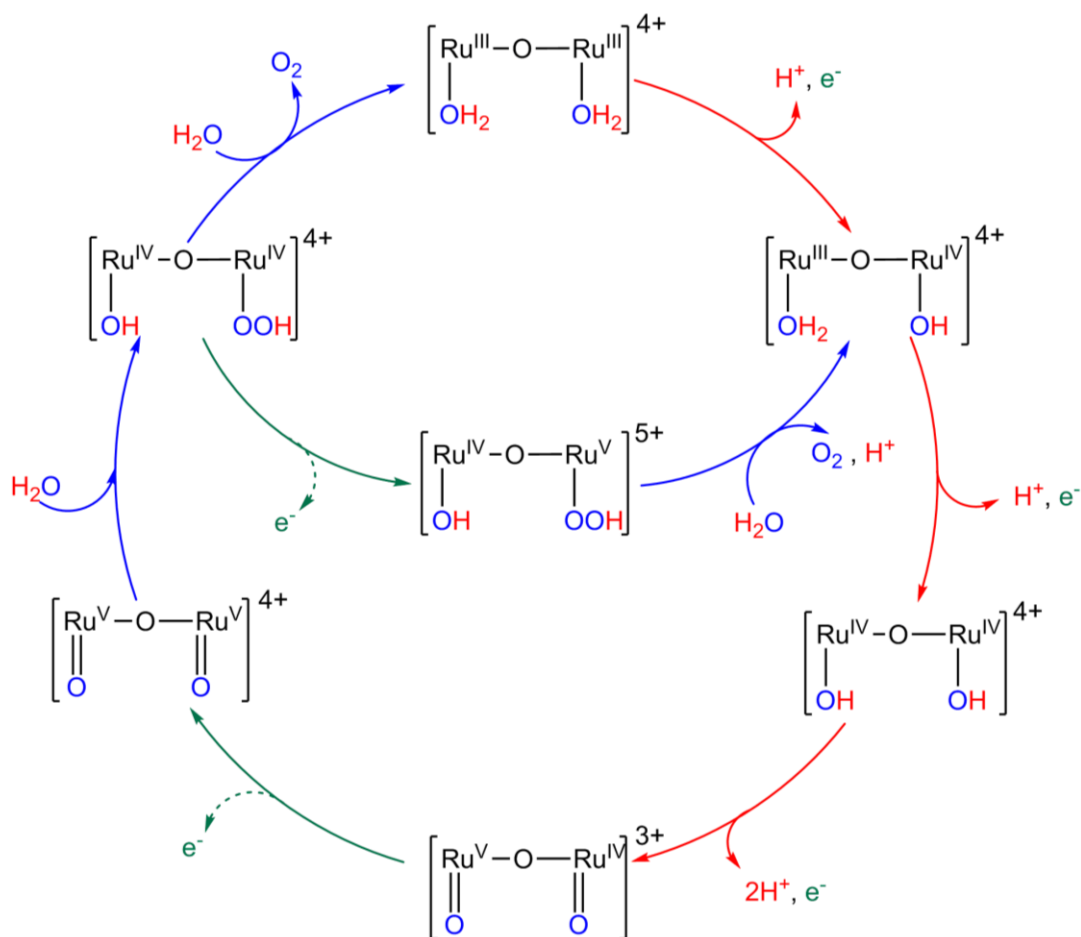
Figure 1.25 Catalytic cycle for dinuclear water oxidation catalysts. Red arrows: Proton coupled electron transfer. Blue arrows: Aqua addition. Green arrows: Oxidation.

The great advantage of the blue dimer is also its greatest weakness. The μ-oxo bridge, while allowing for strong electronic coupling between the ruthenium centres, is also susceptible to cleavage, resulting in non-active mononuclear products. The goal of many groups in this area has therefore been to synthesise ligands which allow for similarly strong coupling but without the susceptibility to cleavage. The primary route this research has taken is to replace the μ-oxo bridge with chelating aromatic ligands.

The aromaticity of the coordinating rings allows for the strong coupling required but is better able to accommodate the shifting electron density between the two ruthenium centres. By far the most common bridging group is the monoanionic pyrazolide. The two-coordinate, five-membered ring bridges the two ruthenium centres but only supplies a single negative charge unlike the oxy group's double negative charge. The replacement of the oxo group with the pyrazolide changes the geometry of the ruthenium centres as the bridged species must adopt a "bent" rather than linear configuration. This works to the favour of the catalysts as the bent motif orientates the coordinated aqua groups to facilitate both the hydrogen shuttling mentioned above but also to allow direct oxo coupling between the coordinated oxygens. Incorporation of the pyrazolide bridging group into a more ridged donor system allows for directional control of the oxygen containing groups via variation of the ancillary ligands. One of the most studied in the past decade is the 3,5-bis(2-pyridyl)pyrazole (Hbpp) tetradentate ligand first synthesised by Llobet et al in 2004 (Figure 1.26).[50]
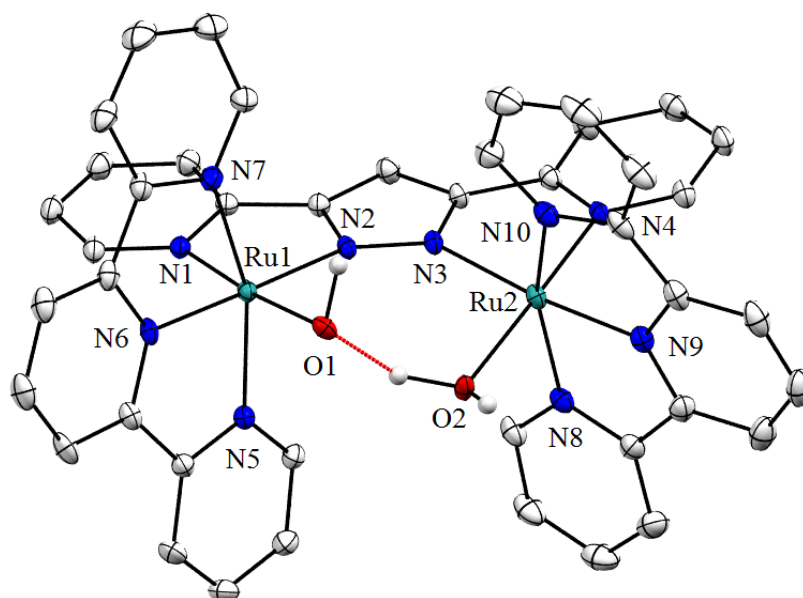
Figure 1.26 X-ray structure of $[Ru_2(OH_2)(OH^-)(bpp)(tpy)_2]^{2+}$ $4[PF_6]^-$. Counter anions and non-oxygen bound protons omitted for clarity. Ellipsoids shown at 50% probability.[50]

Modification of the tetra-coordinate Hbpp backbone to include additional conjugated donor sites can have a marked impact on the activity in that it changes the geometry of the remaining meridional coordination sites.[51] While this change can be small in structural terms, the effect on the mechanism is significant. This is clearly

demonstrated by the different mechanisms favoured by the catalysts formed by the replacement of the pyridyl group in Hbpp with a bipyridyl group. The newly formed hexadentate ligand saturates the meridonal coordination plane resulting in a smaller distance between the ruthenium centres. While it might be assumed that this would lead to an increase in the favourability of the I2M mechanism it is actually the reverse which occurs. The shift in mechanism demonstrates that the path to improving the activity of these catalysts is not a case of simply putting two ruthenium bound oxo species closer together.

While the pyrazolide bridged catalysts rely on electronic coupling through a short monoanionic five membered ring other catalysts have been generated which utilise neutral frameworks and separate non-innocent ligands such as dioxolenes (Figure 1.27).
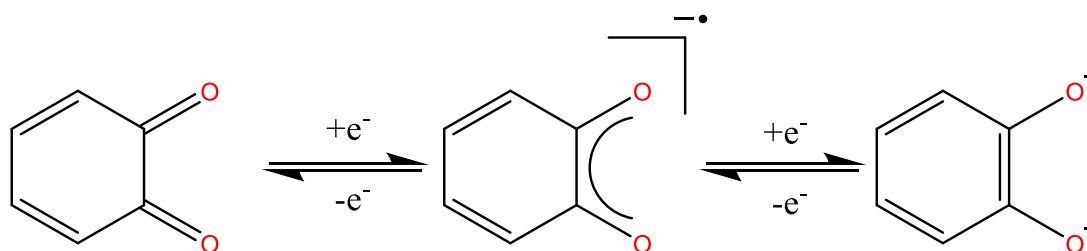
Figure 1.27 Reduction and oxidation of basic dioxolenes. Left: o-quinone Centre: o-semiquinone Right: Catecholate.

These act as redox active species electronically coupled to the ruthenium centres. As non-innocent ligands the dioxolenes are able to accommodate the different levels of electron density caused by shifting oxidation states of the ruthenium while also aiding in proton shuttling from the various catalytic intermediates.[52-54] The removal of direct electronic coupling between the two ruthenium centres means that these catalysts are much closer in design to the linked monomers mentioned above. The difference between these species, however, is that with these catalysts the linkage between the two ruthenium centres is extremely rigid. This rigidity forces the ruthenium-bound oxo species to orientate into a position where O-O coupling can take place.

As with the mononuclear catalysts there remains a problem with these classes of water oxidation catalysts. That being the case, the potential required to drive the catalytic cycle is higher than that generated by common photosensitisers. As with mononuclear

catalysts, the primary efforts in this area are to increase the electron donating capability of the coordinated ligands to lower the catalyst's redox potential. Both neutral and anionic ligands have been used to synthesise catalysts with promising results.

Even as the dinuclear systems result in a lessening of the electrochemical strain on a single ruthenium centre, increasing the number of reaction centres lessens the strain even further. The key point about this avenue of development is that in order for it to work there needs to be strong electronic coupling between the ruthenium centres. Organic linkages are capable of electronically coupling metal centres to form metal organic frameworks (MOFs) but that work has yet to receive a significant amount of focus.[55] An alternate approach is to re-examine the blue dimer with its oxide coupling. Metal centres linked via multiple anionic groups would engender the necessary coupling without the risk of reductive cleavage found in the molecular system. At this point we are moving into the field of heterogeneous catalysis and must begin to address the different rules for that area.

In a heterogeneous system multiple metal centres are able to undergo single electron oxidation in relation to each catalytic site. This is due to multiple electronically coupled centres in the bulk material, which do not interact with the solution environment. This sits in opposition to a homogeneous system where there are only one or two metal centres which must undergo multiple electron oxidation steps at the catalytic site. This causes a bottleneck in terms of the catalytic activity as the homogeneous system must return to its initial state before beginning the next cycle. A greater percentage of the metal centres in a heterogeneous system are contained in the bulk material than on the surface as catalytic sites. In this environment they are unable to coordinate to aqua groups or other solution phase materials. However, they are able to cycle oxidation states to accommodate the shifting potentials required by the water oxidation reaction. If the number of redox active metal centres in the bulk substrate is much greater than the number of catalytic sites, then the catalytic turnover can be regarded as no longer limited by the redox cycling of a few metal centres rather than by the bulk potential and the surface activity alone.

Development of heterogeneous water oxidation is becoming increasingly popular, as a functional heterogeneous water oxidation/reduction cell is simpler to scale up than a

corresponding homogeneous cell. This significantly reduces the development and production costs required for wide spread use. Heterogeneous systems also have the advantage of having thinner cells due to the higher concentration of redox-active metal centres in the solid phase as opposed to the dilute aqueous phase but at the cost of the active sites no longer being dispersed throughout the solution, leading to surface diffusion becoming a serious consideration.

Heterogeneous Catalysis

As previously stated heterogeneous water oxidation catalysts have several benefits compared to homogeneous counterparts. However, the chemistry of these heterogeneous systems can differ radically from the chemistry of the homogenous systems.

Heterogeneous substrates are more complex than homogeneous systems in terms of their architecture and the interaction that architecture has with a solution. However, when compared to homogeneous catalysts, the system is not limited by the redox cycling of a single species. Heterogeneous substrates are able to act as a single electrode so that the potential required for the oxidation of water is shared throughout the substrate. This means that the activity of the substrate can be altered by the modification of surface active species independently from the bulk material.

The majority of heterogeneous catalysis is performed using metal particles deposited onto inert substrates such as silicon dioxide. The substrates act to inhibit aggregation of the catalytically active metal particles and allow for easier handling and separation. The difficulty in this method of catalysis for water oxidation is that the metal particles can be oxidised into either passivation layers or into water soluble species leading to a sharp drop in the activity. Additionally, the substrates used do not tend to be able to transfer charge between metal particles meaning that reactions tend to be concerted, with no net electron transfer taking place. Semiconductor catalysis can alleviate the electron transfer problem by allowing electrons to move when in an excited state.

Semiconductor substrates

The nature of semiconductor heterogeneous catalysis has different considerations to homogeneous catalysis. In a heterogeneous system the number of linked atoms is greater by orders of magnitude with frequent repeating atomic environments. This causes degeneracy in almost identical molecular orbitals to the point that those orbitals are frequently simplified into molecular bands. As multiple filled and unfilled bands exist across the substrate they are grouped together according to their occupancy to form the "valence" and "conduction" bands respectively. Like their homogeneous counterparts, the HOMO and LUMO levels, the localisation of the orbitals that make up the bands are found on different atoms or groups of atoms. The non-uniformity of

the band structure across the substrate means that symmetry considerations must be included in analysis of heterogeneous photocatalysis. This is usually viewed as plot of energy vs. symmetry as is shown in Figure 1.28. For pure or alloyed metals, the two sets of bands "blend" together i.e. have energy levels which vary sufficiently that they overlap at different symmetries. In semiconductors there is no overlap resulting in a "band gap" which inhibits but does not stop electron transfer between energy levels. Thus semiconductors can conduct electricity if electrons in the valence band can be promoted into the conduction band. If the band gap grows too large then promotion becomes too difficult and the semiconductor becomes an insulator as in the case of diamond and silicon dioxide.
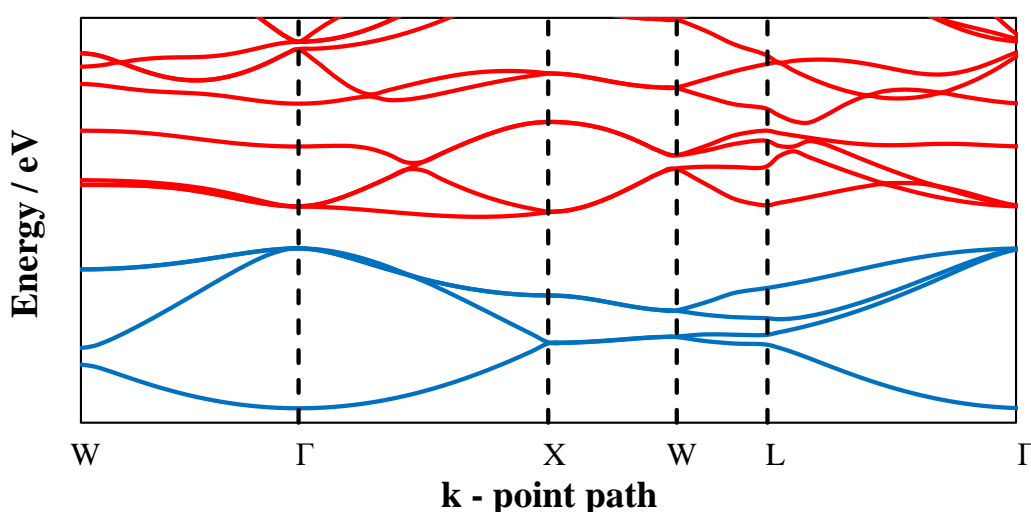
Figure 1.28 Band structure of diamond. Valence band (blue), conduction band (red). The horizontal axis represents the wavevector (k) within the Brillouin zone of a repeating crystal structure with W, Γ, X, L being high symmetry points.

As electronic transitions between different bands can require movement of an electron from one location within the semiconductor to another there is an inherent change in the symmetry. This affects how probable that transition is and how likely that excited state will decompose. If there is a good match between the symmetry of the highest energy part of a valence band and the lowest energy part of the conduction band then the band gap is characterised as being "direct". If there is difference between the symmetry of the bands then the band gap is "indirect".

Semiconductors have a second advantage over the metal/insulator pairing in that the band gap allows them to be light harvesting themselves, opening up the possibility for

direct photoelectrochemical water oxidation by the formation of oxidising electron-hole pairs.

Non-oxide semiconductor materials such as silicon, gallium arsenide, cadmium sulphide are able to separate electron hole pairs by doping. However, like many of the metal particles they have the drawback of being unstable in the oxidative environments required in the anodic half-reaction of water splitting. The use of metal oxide semiconductors, such as titanium dioxide, strontium titanate, zinc oxide, tungsten trioxide and α iron (III) oxide reduces this instability but raises the other issue of widening the band gap.

Table 1.2 Commonly used semiconductors and their band structures.

Semiconductor	Band gap		Band Structure
	eV	nm	
CdS	2.42	512	Direct
GaAs	1.43	867	Direct
Si	1.1	1127	Indirect
α-Fe$_2$O$_3$	2.2	564	Disputed
TiO$_2$ - anatase	3.25	381	Indirect
TiO$_2$ - rutile	3.0	413	Direct
SrTiO$_3$	3.2	387	Indirect
ZnO	3.3	376	Direct
WO$_3$	2.5	496	Indirect

The correct balance between low bandgap and a high stability semiconductor supports is of particular importance as any cost-effective photoelectrochemical device must possess both of these characteristics in order to have a practicable operating lifetime. The band gaps for most of the metal oxide semiconductors are found within the UV range of the electromagnetic spectrum (λ<400 nm) and as such are poor light absorbers for the majority of sunlight (Table 1.2, Figure 1.29).
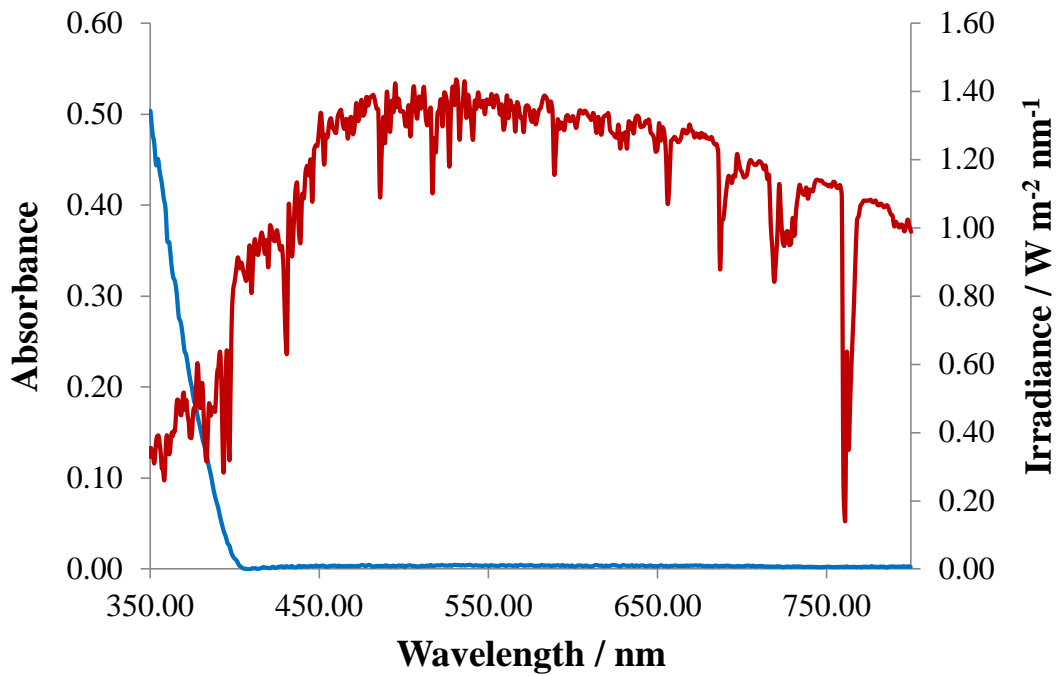
Figure 1.29 Plot of titanium dioxide P25 absorbance (blue) compared with average solar irradiance at sea level (red)

Titanium dioxide is the most widely studied of these metal oxide semiconductors, having four polymorphs - the two most commonly studied polymorphs being rutile and anatase, with rutile being the more abundant of the two in nature. Both polymorphs consist of Ti^{4+} surrounded by six oxygen atoms in a tetragonal unit cell (Figure 1.30).
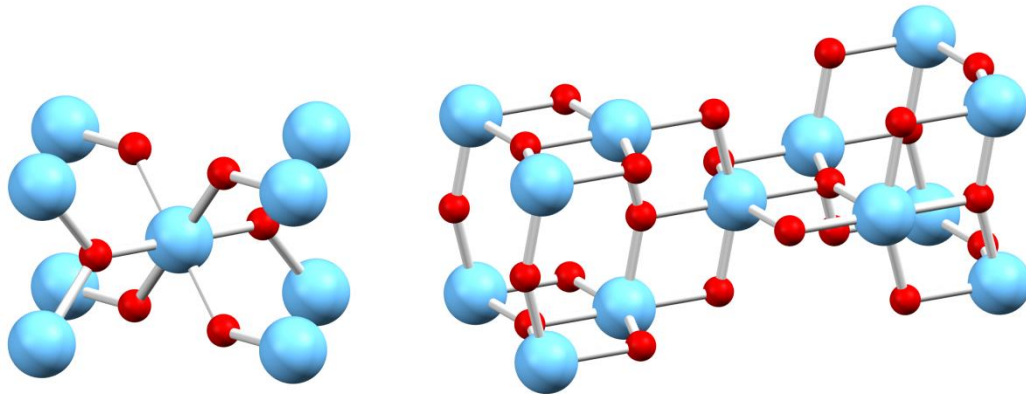
Figure 1.30 X-ray structures of rutile (left) and anatase (right).[56-57] Titanium atoms are identified as blue and oxygen as red.

Its rutile form was first used to photocatalytically split water in a tandem cell by Fujishima and Honda in 1972.[58] The basic design of this cell has remained fairly unchanged since that time, although the materials used for the electrodes have undergone much development. In the case of the original cell a single crystal of rutile TiO_2 was connected to a platinum black electrode via an external circuit. Submersion in an acidic aqueous medium and irradiation directly evolved molecular oxygen from the rutile electrode while hydrogen was evolved at the platinum black electrode via the reduction of aqueous protons by the current generated from the rutile photoanode (Figure 1.31).
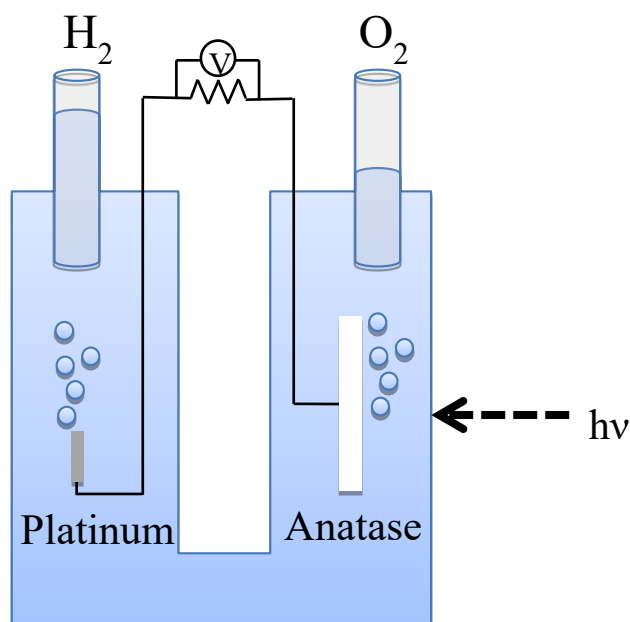
Figure 1.31 Schematic of original Fujishima/Honda cell.

While the rutile form of titanium dioxide was initially studied, in the following decades interest has grown in the anatase form. This may initially seem counterproductive as anatase has a larger band gap than rutile (3.2 eV versus 3.0 eV) and will therefore absorb less light. However, the reason for this shift in interest can be found by examining the band structure of anatase and rutile. Rutile contains a direct band gap and an indirect band gap of similar energy difference, which means that the momentum function for an electron in the homo level equates to the momentum of an electron in the lumo level. The crystal momentum is the momentum of an electron within a crystal lattice, (also known as the k-vector). For an electron to move between levels requires

only the absorption or emission of electromagnetic radiation, as the k-vectors for an electron in both the highest energy ground state and the lowest energy excited state are in close proximity.

Anatase, however, has an indirect band gap smaller in energy than its direct band gap (Figure 1.32), a characteristic that it shares with silicon.[59-60] In an indirect band gap semiconductor, electrons in the highest energy ground state and the lowest energy excited state differ in their crystal momentum; this adds a second component to any electron transfer between the bands. In order for an electron to transition between these states it needs to gain or lose momentum, in contrast to an electronic transition where a photon is unable to perform the required transfer, as it is unable to carry momentum. The required transfer is accomplished through the involvement of a phonon. A phonon is a quasiparticle which while not actually existing is a convenient descriptor of the elastic movement of atoms within the crystal lattice. The momentum of the phonon is equal to the momentum difference of the electron in the different states. As this secondary requirement for the transition of an excited state to a ground state decreases the probability of that transition occurring, the excited state is described as being "longer lived". While this feature also makes promotion less favourable in anatase than in rutile, when promotion does occur the greater lifetime of the formed electron hole pair leads to a higher probability of oxidation or reduction occurring.
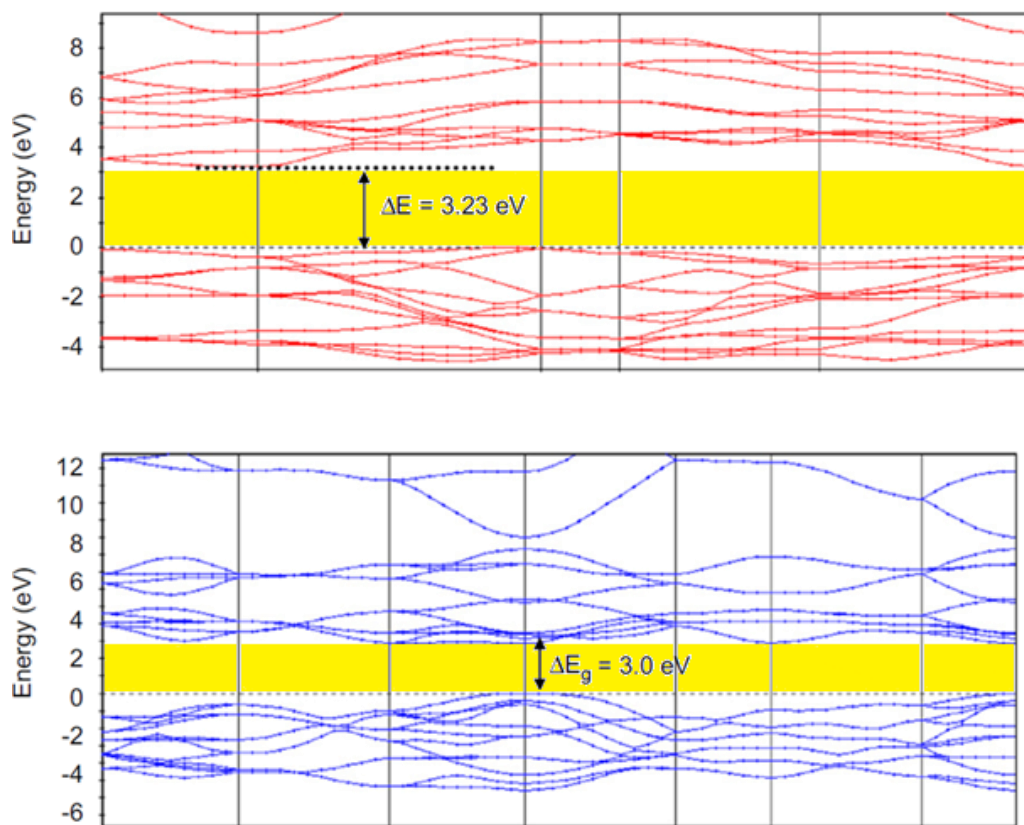
Figure 1.32 Band gap diagrams of anatase (top) and rutile (bottom). Vertical lines represent regions of particular symmetry

In addition to a smaller indirect band gap, anatase has a marginally greater hydrophilicity than rutile. Hydrophilicity, or superhydrophilicity as it occurs in titanium dioxide, is caused by the photoactivated disassociation of oxygen atoms from the surface of the bulk, leaving vacant sites for the coordination of water molecules or hydroxyl ions.[60] Since the reactions proposed for the photo-oxidation of water on a titanium dioxide substrate (Equations 1.1-1.13 below) require the coordination and eventual disassociation of oxygen containing species, the superhydrophilicity of anatase makes for a more appealing photoactive substrate.

Due to the intermediate steps in water splitting involving multiple different radical and anionic species the reaction pathways are pH dependant with different steps being favoured depending on concentration of protons in the medium. The reactions on a TiO_2 photoanode in a neutral medium are shown below (Equations 1.1-1.9).[61]

$$TiO_2 + h\nu \rightarrow e^-(TiO_2) + h^+(TiO_2) \qquad \text{Equation 1.1}$$

$$h^+(TiO_2) + H_2O \rightarrow OH + H^+_{(aq)} \qquad \text{Equation 1.2}$$

$$OH + OH \rightarrow H_2O_2 \qquad \left(k = 6 \times 10^9 M^{-1}S^{-1}\right) \qquad \text{Equation 1.3}$$

$$OH + H_2O_2 \rightarrow HO_2^{\cdot} + H_2O \qquad \left(k = 1.3 \times 10^{10} M^{-1}S^{-1}\right) \qquad \text{Equation 1.4}$$

$$HO_2^{\cdot} \rightarrow O_2^{\cdot -}{}_{(aq)} + H^+_{(aq)} \qquad (pK = 4.8) \qquad \text{Equation 1.5}$$

$$O_2^{\cdot -}{}_{(aq)} + h^+(TiO_2) \rightarrow TiO_2 + O_2 \uparrow \qquad \text{Equation 1.6}$$

$$O_2^{\cdot -}{}_{(aq)} + O_2^{\cdot -}{}_{(aq)} \rightarrow O_2^{2-} + O_2 \uparrow \qquad (pH \leq 6) \qquad \text{Equation 1.7}$$

$$HO_2^{\cdot} + O_2^{\cdot -}{}_{(aq)} \rightarrow HO_2^- + O_2 \uparrow \qquad \text{Equation 1.8}$$

$$HO_2^{\cdot} + HO_2^{\cdot} \rightarrow H_2O_2 + O_2 \uparrow \qquad (pH \leq 3) \qquad \text{Equation 1.9}$$
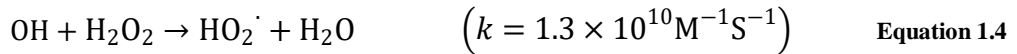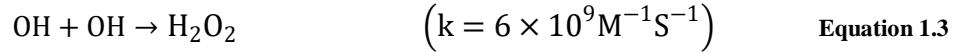
In alkali medium hydroxyl anions compete with aqua groups to combine with the electron-hole present on the TiO_2 surface. The reactions on a TiO_2 photoanode in an alkaline medium are shown below (equations 1.10-1.13).

$$h^+(TiO_2) + OH^- \rightarrow TiO_2 + OH \qquad \text{Equation 1.10}$$

$$OH \rightarrow O^{\cdot -}_{(aq)} + H^+_{(aq)} \qquad (pK = 11.9) \qquad \text{Equation 1.11}$$

$$h^+(TiO_2) + O^{\cdot -}_{(aq)} \rightarrow TiO_2 + O^{\cdot}_{(ads)} \qquad \text{Equation 1.12}$$

$$O^{\cdot}_{(ads)} + O^{\cdot}_{(ads)} \rightarrow O_2 \uparrow \qquad \text{Equation 1.13}$$
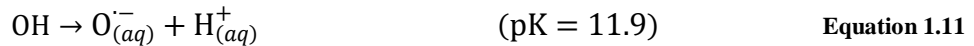
While the absorbance of pure titanium dioxide is limited in the visible region it can be extended by the addition of dopants such as Al^{3+} and Cr^{3+}. The performance of doped substrate is dependent on the crystal phase of the titanium dioxide, and considerations of the stability of substrate have to be made as the dopants can be susceptible to oxidation - and this therefore can alter the internal structure of the substrate upon illumination.[1] Surface modification of the substrate can also alter the optical properties of the semiconductor by the formation of unusual cluster architectures which differ from the bulk structure and provide additional bands to the absorbance profile. Testing and computational analysis of materials generated in this manner is required to understand how these units interact with the bulk semiconductor structure. In that respect these clusters are treated much more like deposited molecular catalysts rather than altered surface topology. The stability of these structures is variable over time as thermodynamics favours them adopting the structure of the underlying material. If the activation barrier for rearrangement of these clusters is lower than that found in the catalytic cycle, then the clusters will become simply another layer of semiconductor and any positive effects lost.

Other metal oxides have been studied with various advantages and disadvantages, the majority of these being non-precious transition metals and 4p/5p main group metals (Figure 1.33).[62]
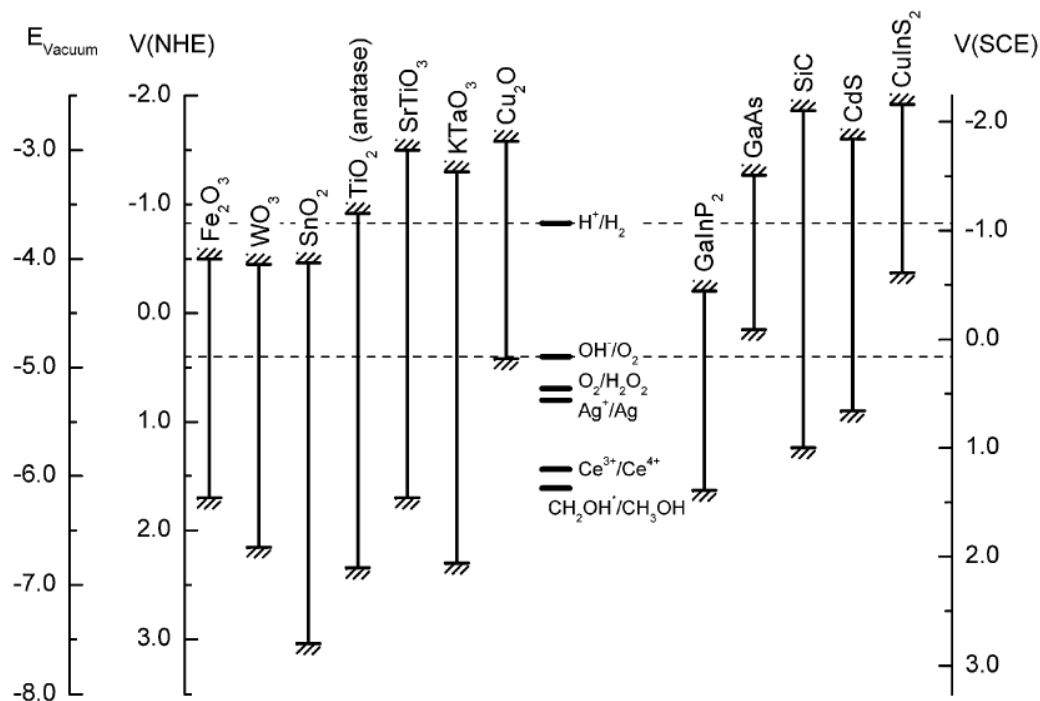
Figure 1.33 Energy band positions for various semiconductors at pH 14. When no experimental data were available for this pH, the band positions were extrapolated using -59 mV per pH unit. It should be noted that values reported in the literature show significant scatter, up to a few tenths of a volt. Most values shown here are for polycrystalline films, obtained using capacitance (Mott–Schottky) measurements and corrected for the difference between the flatband potential and the conduction band.[62]

Iron oxide substrates (Figure 1.34) might be suitable for modification into catalytic material and this is of particular interest as its low band gap (2.0-2.2 eV) would allow for the absorbance of UV and visible light up to 564nm. Iron oxide does, however, suffer from poor charge mobility and a lower quantum efficiency at lower wavelengths. Development in this area is mostly focused on the generation of high absorbance nanostructures and thin films to boost efficiencies, although most focus on turnover at high wavelength rather than cycling within the bulk of the visible region. Additionally the conduction band edge for iron oxide is below that of the reversible hydrogen potential and would require an additional bias to reduce protons at the cathode.
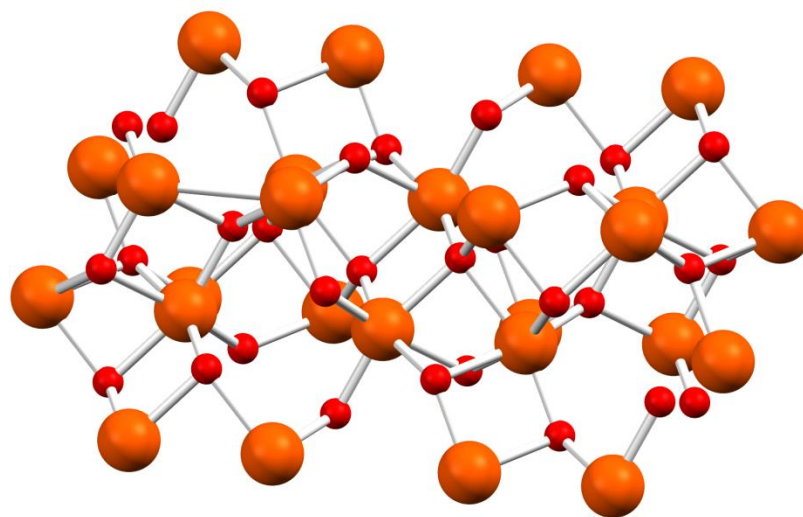
Figure 1.34 X-ray structure of α-Fe$_2$O$_3$. Iron atoms are identified as orange and oxygen as red.[63]

Other examples of metal oxide substrates include strontium titanate (SrTiO$_3$) (Figure 1.35) which is very similar in properties to TiO$_2$ in that they both have indirect band gaps lower than their direct band gaps. Strontium titanate has a perovskite structure with a high relative permeability meaning that while it can become highly polarised it does not conduct charge particularly well. Catalysts derived from this material tend to be doped and/or include a metal co catalysts such as platinum. Doping with rhodium and antimony has been shown to increase the activity of derived photoactive substrates.
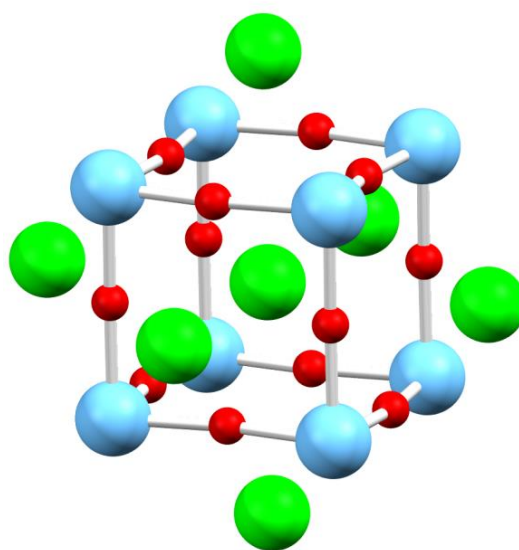
Figure 1.35 X-ray structure of SrTiO$_3$. Strontium atoms as identified as green, titanium as blue and oxygen as red.[64]

Zinc oxide (ZnO) (Figure 1.36) is a well-known photocatalyst for a variety of reactions, particularly decompositions; however, it is both a direct band gap semiconductor and is susceptible to photocorrosion to zinc hydroxide in aqueous media.[65] Initial results suggest that tungsten oxide (WO_3) initially indicates that it would make a perfect substrate as it has an indirect band gap, corresponding to the visible spectrum (496nm) and is stable across a wide pH range. However, its band potential is below that of the hydrogen evolution reaction and, similar to iron oxide, would require an additional potential to form a catalytic cell.
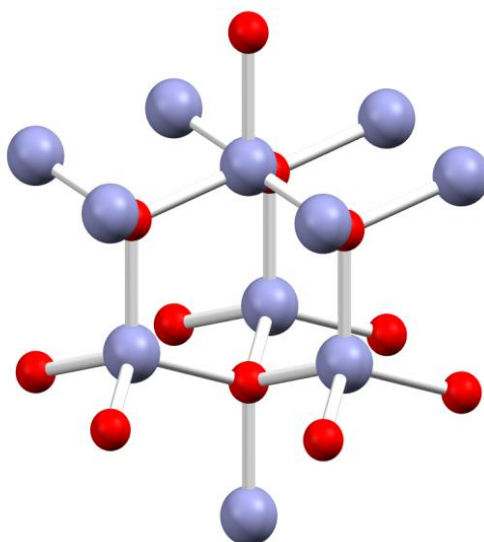
Figure 1.36 X-ray structure of ZnO. Zinc atoms are identified as purple and oxygen as red.[66]

One method of improving the performance of these substrates, rather than doping the substrate or applying an external bias, is to modify the surface of the material with clusters of synthetic oxygen evolving complexes. Unlike the clusters mentioned above these would be of a different material to the bulk semiconductor but share connectivity through oxides. These clusters while not increasing the absorption of light will stabilise the underlying semiconductor by providing preferential oxidation sites not susceptible to the same oxidative damage. The creation of specific oxygen evolution sites separate from the light absorbing material is similar in nature to the OEC present in photosystem II. These clusters would have to perform better as catalysts than the bulk substrate and be more stable under oxidising conditions than the metal particles already mentioned. In order for these sites to act as effective oxidation sites they need to be either extremely thin or possess a measure of electrical conductivity. Most metal

oxides do not conduct particularly well and first row transition metal oxides clusters such as the manganese oxo cluster of photosystem II are unstable. This is due to them being susceptible to degradation under either UV or visible light, or to the same dissolution and pacification as their metal precursors. As such more robust oxygen evolving catalysts are required.

Of the earlier transition metals titanium dioxide is the only metal oxide to display promising catalytic activity; however, its primary strength is as a photoactive substrate rather than an oxygen evolving catalyst itself. Group 5 and 6 metals have the ability to form multinuclear oxide based molecular architectures known as polyoxometalates (POMs). However, the difficulty of molecular design of these species and the varying stability of many of these compounds in different environments has limited this area.

Since these metal oxide clusters would have to be more redox-stable than the substrate, the later 3d and 4d transition metals are an attractive option. The more diffuse electron shells and d-orbital overlap with the substrate allow certain oxides to transfer electrons from the oxidative cluster into the bulk substrate without deterioration of the formed cluster.
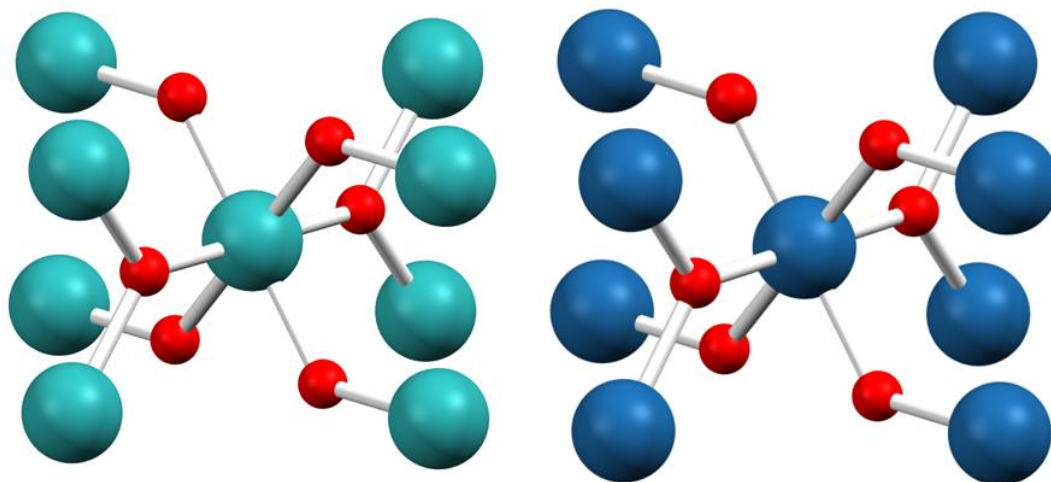
Figure 1.37 X-ray structure of RuO_2 (left) and IrO_2 (right).[67-68] Ruthenium are identified as green, iridium as blue and oxygen as red.

Partially hydrated ruthenium dioxide (Figure 1.37) is commonly examined for this purpose due to its excellent catalytic activity at a low overpotential. The structure of ruthenium dioxide is the same as that of the rutile polymorph of titanium dioxide,

sharing the same +4 oxidation state but with the higher oxidation states of the ruthenium being accessible.[69-70]

Unfortunately, ruthenium dioxide is susceptible to photooxidative degradation, forming either the perruthenate anion (Ru^{VII}) or the ruthenium tetroxide molecule (Ru^{VIII}). Both of these species would diffuse into the water layer and both of which are extremely toxic in this case the ruthenium has been a victim of its own success, forming the high oxidation state required to oxidise water but being too stable at that oxidation state to trigger O-O bond formation. Examining the highest oxidation states across the periodic table we see that the group eight elements sit at the second highest achievable oxidation states for the entire d-block (Figure 1.38). Only group nine elements have a higher recorded oxidation state and only under extreme conditions. Closer examination reveals that those group nine elements may make better catalysts. In particular iridium, which possesses the highest known oxidation state, is already used in several molecular water oxidation catalysts. Comparing the oxides of iridium to those of ruthenium reveals something interesting. The Ir^{IX} compound that holds the current record is the cationic form of the tetroxide (IrO_4^+) formed in the gas phase from laser ablation of a metallic target.[71] The neutral form of the tetroxide is the same as in group eight but unlike the tetroxides for ruthenium and osmium it is only stable under solid argon at 6 K and decomposes into the peroxide (η^1O_2)IrO_2 at higher temperatures. For water oxidation catalysts this is ideal, as in the unlikely event that the tetroxide forms it will immediately form the peroxide as part of the catalytic cycle. The lower oxidation state IrO_3 is achievable at high temperatures (973 K) but not under the conditions for heterogeneous water oxidation. Any IrO_3 formed as a side product in the catalytic cycle will decompose rapidly without alkali stabilisation, so that any production would be unfavoured in the proton-rich diffusion zone surrounding the iridium active sites.
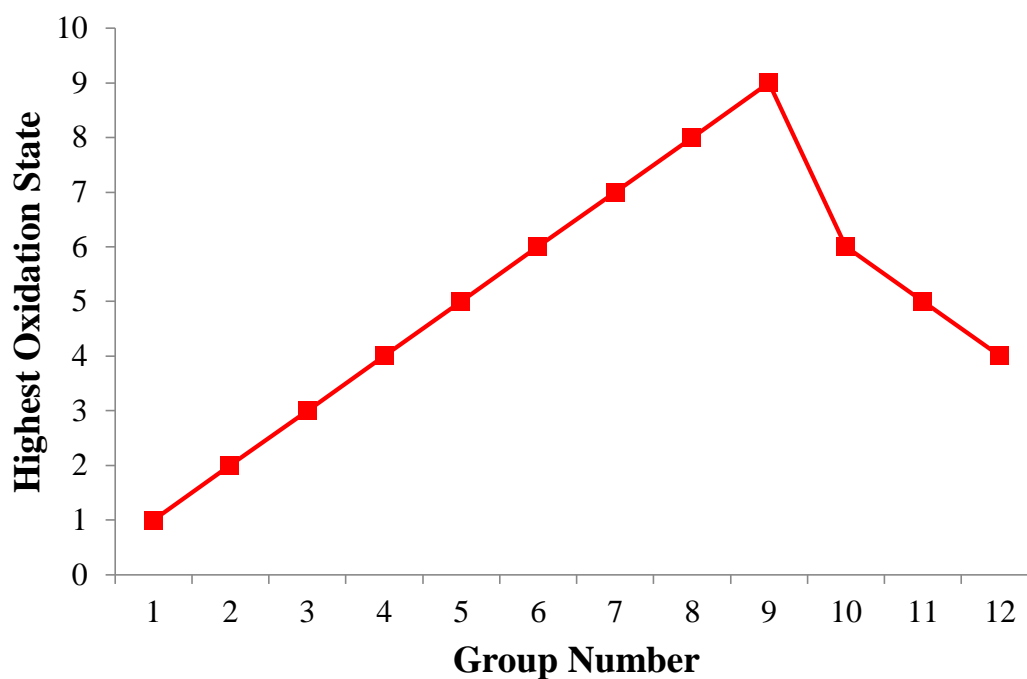
Figure 1.38 Highest recorded oxidation state of transition metal groups.

The reason that rhodium is not considered for this type of catalysis is that although it has similar chemical properties to iridium its oxide lacks the required electrical conductivity. Both iridium dioxide and ruthenium dioxide possess regions of metallic conductivity at the potential required for water oxidation. The conductive nature of the oxides allows for easy electron transfer into the substrate not possible in rhodium dioxide (as shown in Figure 1.39).[72]
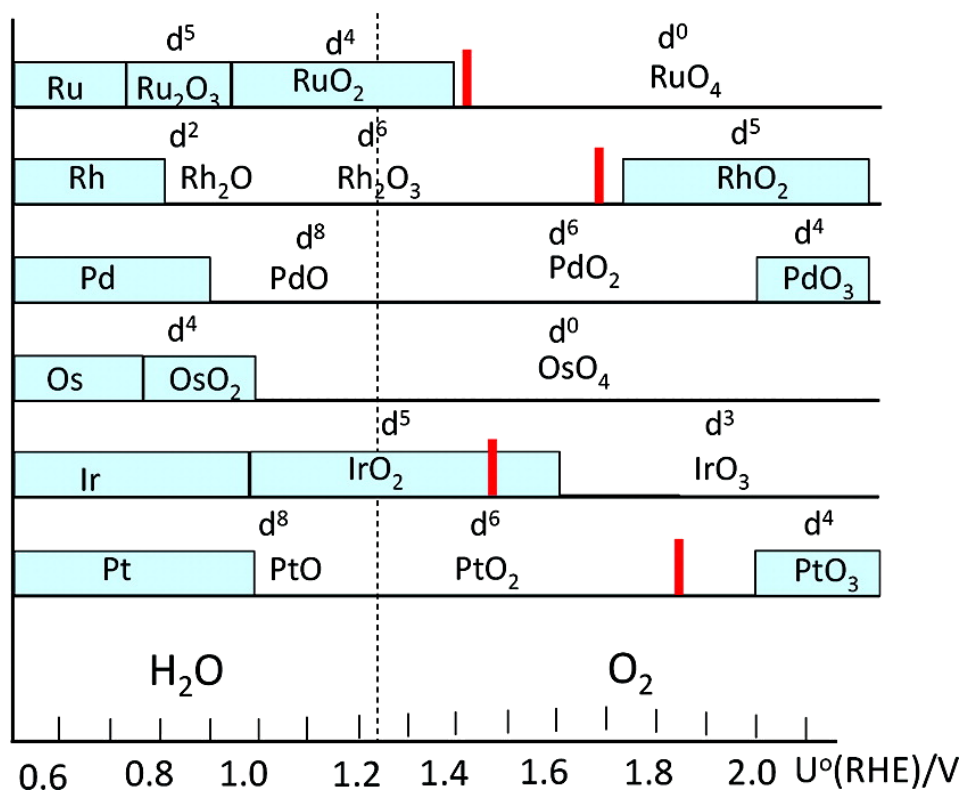
Figure 1.39 Stability diagram of typical platinum group metal and metal oxides (Ru, Rh, Pd, Os, Ir, Pt) according to Pourbaix. Light blue areas: Regions with metallic conductivity. Filled red bars: potential at which O_2 evolution of 1 mA cm^{-2} in 1 M H_2SO_4 on the corresponding metal electrode takes place. The thin dashed line at 1.23 eV indicates the reversible potential for OER under standard conditions.[73]

There is a penalty for the choice of iridium dioxide over ruthenium dioxide. The catalytic activity of iridium dioxide is marginally lower than that of ruthenium dioxide (Figure 1.40) due to the requirement for a higher overpotential compared with ruthenium dioxide. The difference in activity can be addressed by photodeposition of iridium precursors onto a titanium dioxide substrate followed by autoclaving. This results in a modified catalytic substrate with activity equal to if not greater than its ruthenium oxide counterpart, demonstrating that a synthetic method is able to overcome the difference in activity.

While catalysts such as iridium dioxide can aid in the oxygen evolution reaction itself, they do not as a rule increase the photoactivity of the substrate in the visible region.[74] In photosystem II the P680, the dimer absorbs light and uses the energy in that light to move an electron against a potential energy gradient.
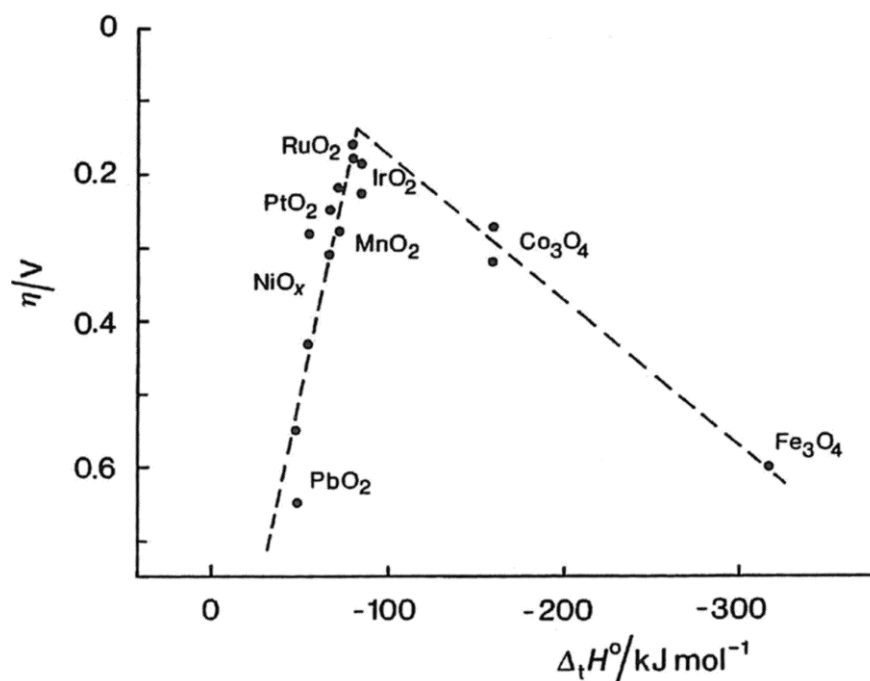
Figure 1.40 Activity (expressed as overpotential η at 0.1 mA/cm^2) for O$_2$ evolution (OER) on various electrodes as a function of adsorption enthalpy of oxygen on transition metals from lower to higher oxides.

The location the electron has just left now has the redox potential required for the oxidation of water but cannot itself oxidise two full molecule of water itself. Instead the potential is passed on to a species that can. The OEC oxidises water after a series of consecutive rather than concurrent one-electron oxidation reactions by P680. In the IrO$_2$/TiO$_2$ system the titanium dioxide is acting as the light harvester similar to P680. As shown above, its effective range is limited to the UV range but with modification it may be able to extend that adsorption into the visible region. The idea of using coordination complexes to inject photoexcited electrons into the conduction band of titanium dioxide is not new and has been mentioned in the form of DSSCs. In the water oxidation reaction however the aqueous solution lacks the same redox couple required to reduce the oxidised dye back to its ground state. In fact, any charge transfer is likely to lead to decomposition of the dye at the substrate/solution boundary. This necessitates the inclusion of co-catalysts such as iridium dioxide or surface-bound molecular catalysts which can be oxidised by the photoexcited dye, even as the dye inject electrons into the conduction band of the substrate.

Photosensitiser dyes

Some of the limitations in the spectral ranges of catalytic semiconductor substrates can be overcome via the use of visible light absorbing photoactive dyes. As in the Grätzel cell (Figure 1.4) the inclusion of a photosensitiser into the cell architecture allows the active surface to engender charge separation at lower energy wavelengths than would otherwise be possible. Careful selection of these photosensitisers allows for the photoexcited electron to be injected into the conduction band of the semiconductor substrate. For the system to be catalytic the photosensitiser has to then be reduced in situ. Ideally the reduction would be accomplished by the molecular oxidation of water. The nature of the surface environment makes such a possibility extremely difficult as the unstable charged photosensitiser is more likely to be degraded during the charge cycling and itself become irreversibly oxidised. The combination of photosensitising dyes with heterogenic water oxidation catalysts such as iridium dioxide allows for enhanced photoactivity of the substrate without the same level of degradation to the photoactive dye.

The key features of the families of photosensitising dyes commonly used in the modification of the semiconductor substrates are absorbances within the visible region of the spectrum, high molar absorptivities, photostability, and charged anchoring groups for the injection of electrons into the conduction band of the semiconductor substrate.
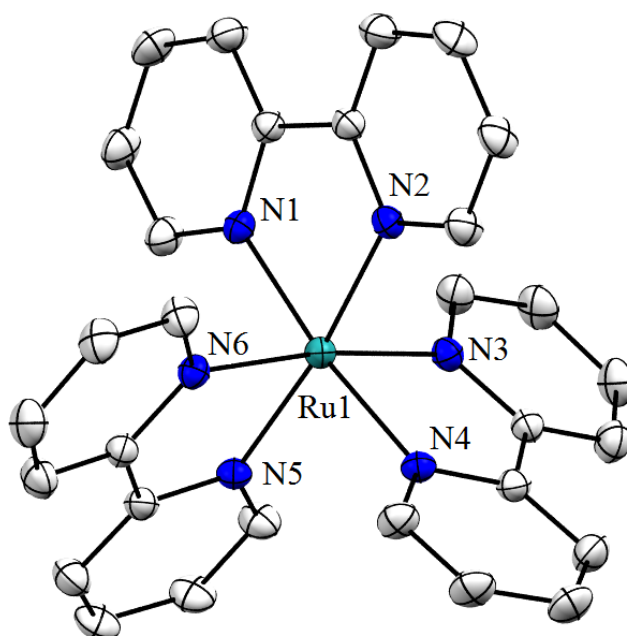
Figure 1.41 X-ray structure of $[Ru(bipy)_3]^{2+}2[PF_6]^-$. Counter anions and protons omitted for clarity. Ellipsoids shown at 50% probability.

There exists a variety of different dye types such as those based on porphyrin-derived systems which seek to mimic the light harvesting abilities of biological generated dyes.[75] The advantage of porphyrin derived systems is that they often have extremely high absorbances in the near infrared and lower energy visible region.[76]

Purely organic based sensitisers do exist and are formed from the use of large π-conjugated chains or rings, which bridge a donor and an acceptor group. The acceptor group is the injection site of electrons into the semiconductor substrate and therefore has a good electronic overlap with that substrate. An example of this is found in the most commonly used acceptor – i.e. cyanoacrylic acid with its LUMO overlapping the bulk surface energy of TiO_2. Organic molecules receive less attention in the field of water oxidation compared with metal centred species due to the possible degradation of the organic species due to radical formation upon redox cycling.

Ruthenium pyridyl-based systems are by far the most widely and intensively studied of the photosensitisers used for heterogeneous water oxidation. This is due to their favourable redox potentials and high molar absorptivity across a broad range. The most famous $Ru(bipy)_3^{2+}$ (Figure 1.41) was first identified as a photosensitiser in 1971.[77]

Unlike in molecular water oxidation, where only one or two metal atoms are available to redox cycle as part of the catalytic mechanism, heterogeneous systems are able to utilise a large number of metal centres. As mentioned above, the molecular orbitals in semiconductors are spread across the entire substrate. This blends together the various orbitals into bands. Compared to molecular catalysis the dye only has to inject electrons into the lowest energy band, as this sets up the required charge differential for water oxidation, meaning that heterogeneous water oxidation can occur with dyes that would be unsuitable for molecular water oxidation.

$Ru(bipy)_3{}^{2+}$ despite not having a particularly broad spectral range ($\lambda_{max} \approx 450nm$) is one of the most common photosensitisers for a variety of applications and is used in many of the photooxidation systems mentioned above. The reason for this choice is the long lived triplet state of the molecule.
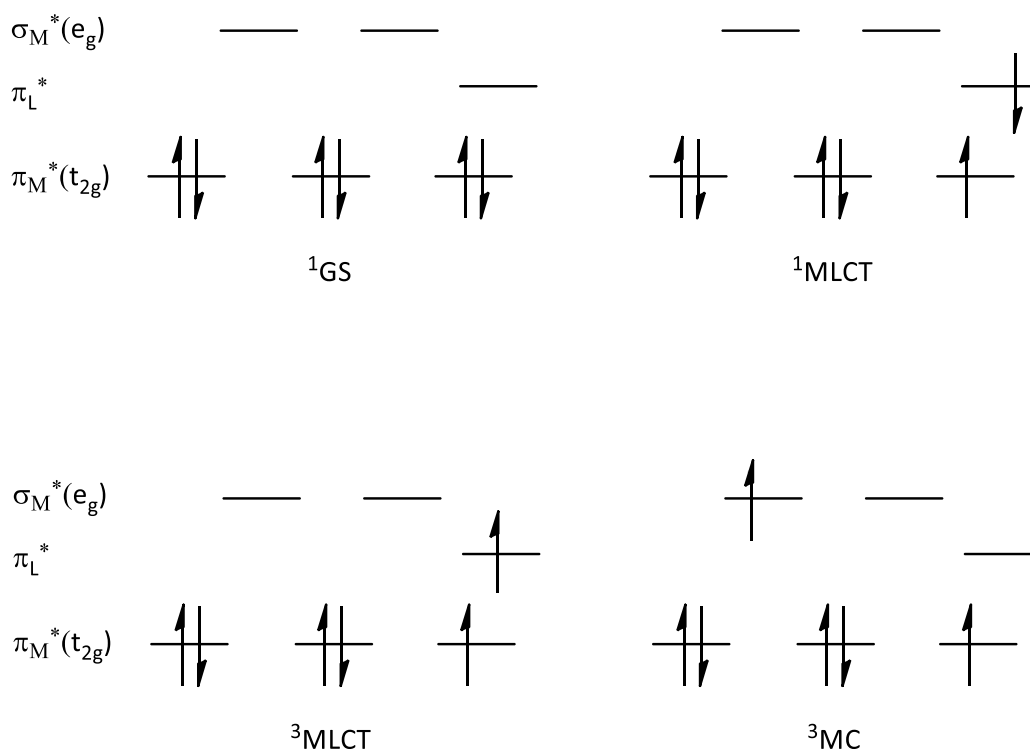
Figure 1.42 Orbital splitting diagram of ground state and primary excited states in ruthenium pyridyl based dyes.

The triplet form is believed to be a metal ligand charge transfer excited state. Upon photoexcitation the electron moves from molecular orbitals centred on the metal atom to low energy π^* orbitals located on the bipyridine ligands (Figure 1.42). The movement of electric charge is termed metal ligand charge transfer (MLCT) (Figure

1.43). MLCT can be described as an analogue of the excited state in semiconductors as it involves the photoexcited movement of electrical charge from a low energy ground state to a high energy excited state. As in semiconductors, this increases the oxidative potential of the now vacant ground state. The advantage of dyes compared with semiconductor charge separation is that the absorbances required to generate the excited states are much more tuneable due to the larger range of metal oxidation states and available ligand systems. $Ru(bipy)_3^{2+}$ has the added advantage of its triplet state (^{3}MLCT) being a longer lived excited state compared with its singlet state excitation, as it requires a spin transition to undergo radiative recombination, making the excited state of $Ru(bipy)_3^{2+}$ similar to the indirect band gap of anatase.
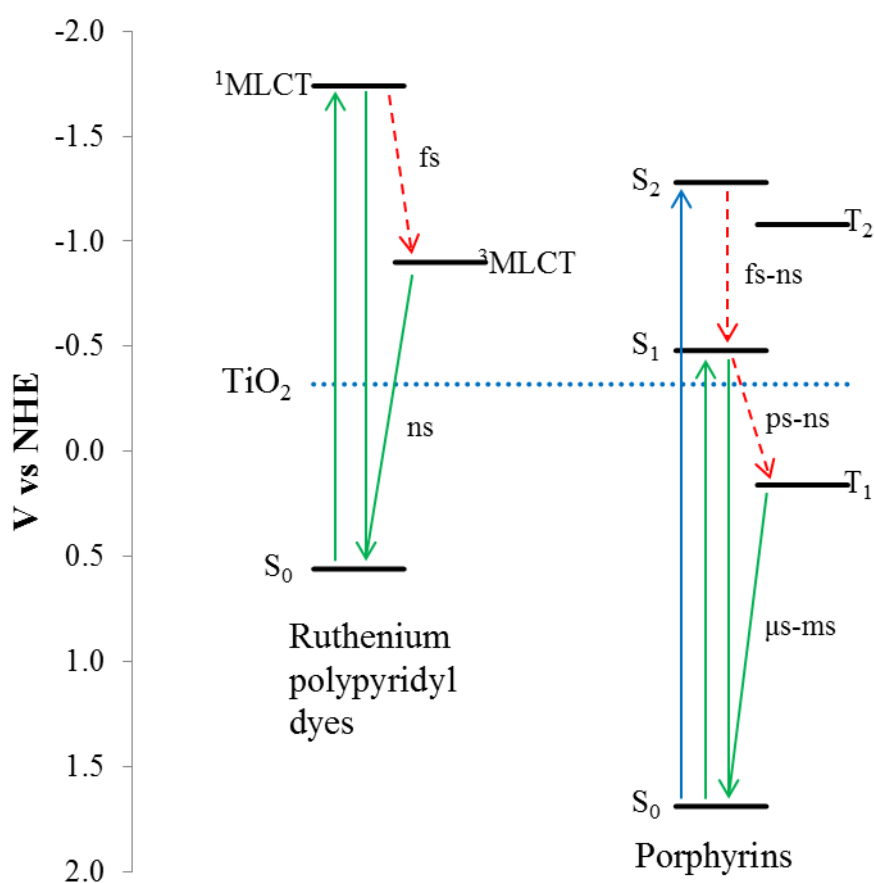
Figure 1.43 Energy level diagram showing the approximate reduction potentials of the excited states of two common classes of sensitisers and the conduction band edge of TiO_2 and the timescales of recombination processes

The probability of electron transfer between photosensitisers such as $Ru(bipy)_3^{2+}$ can be further increased via the incorporation of anchoring groups into the conjugation system of the ligand.[78-80] The anchoring groups act to both bind the photoactive dyes to the semiconductor substrate but also to allow direct charge transfer of the photoexcited electrons into the substrate. At the interface of the dye and semiconductor the conduction band of the semiconductor "bends" as the anchoring groups alter the surface of the semiconductor by coordination to the Ti^{4+} atoms (Figure 1.45).[81] In order for the dye to effectively contribute to the activity of the water oxidation reaction the rate of electron injection must exceed the rate of recombination of electron hole pairs in the substrate and of fluorescence/phosphorescence in the dye.
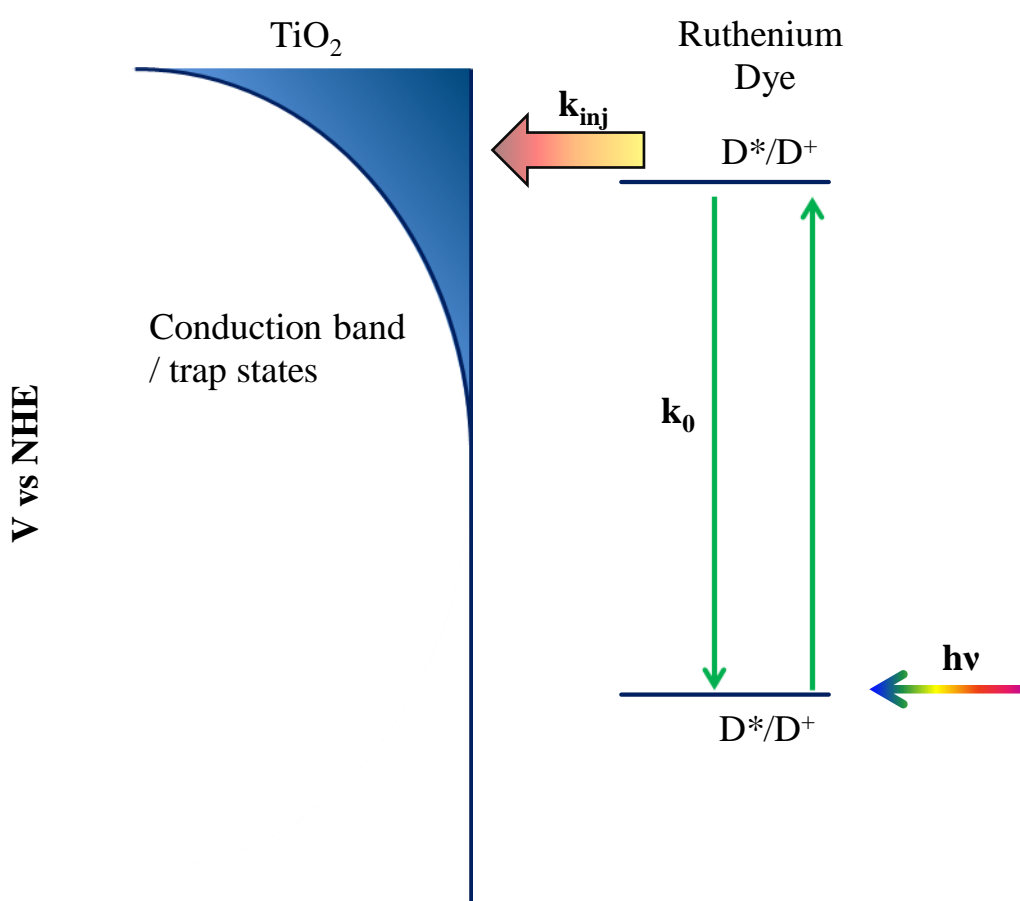
Figure 1.44 Energetic representation of electron injection from dye into semiconductor substrate if $k_{inj} > k_0$.

Dyes are commonly anchored to semiconductor catalytic support materials via charged oxygen containing groups with acidic protons groups (Figure 1.45). These groups allow for electron transfer directly into a catalytic substrate due to stronger interaction between the occupied dye orbitals and the conduction band of the semiconductor. The diverse anchoring groups have different effects on the activity of the dye and the substrate as a whole - e.g. phosphonate groups bind more strongly than carboxylate groups (80 times greater); however, carboxylate groups have electron injection rates double that of phosphonate. The number of anchoring groups on a dye molecule also affects the activity, with too many groups causing aggregation of the dye. The attachment of the anchoring group onto the dye is also important as the inclusion of a CH_2 or longer spacer between the anchoring group and the delocalised π system of the chromaphore leads to a decrease in the rate of electron transfer.[82] While the type of substituent anchoring group has been examined, very little work has been done upon the substitution pattern itself.
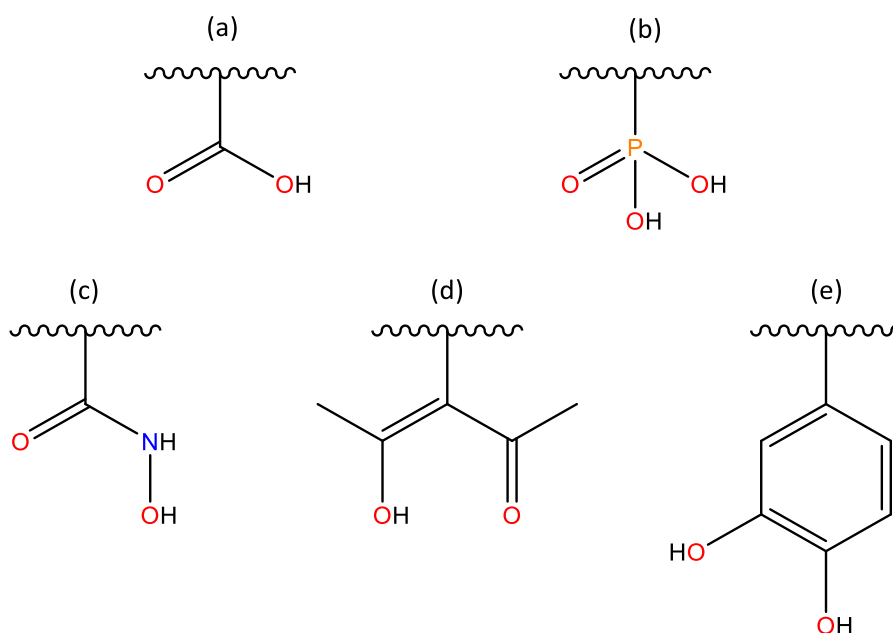
Figure 1.45 Anchoring groups for binding molecular species to titanium dioxide: (a) carboxylic acid, (b) phosphonic acid, (c) hydroxamic acid, (d) 3-substituted-2,4-pentanedione (acetylacetonate), and (e) catechol.

Given that the substituent can have a dramatic effect on the redox potential of complex and electron delocalisation, it is prudent to examine how these properties differ between substitution patterns.

While large polypyridyl ligand systems with extended conjugation systems dominate the field of ruthenium based dyes, the overlooked picolinic acids may provide some insight into the effect of the substitution pattern of these anchoring groups onto the catalytic activity of the dye-modified substrate.[83] By varying the position of a second carboxylate group around the pyridine ring it is possible to directly observe how the inductive effect of these groups can alter the activity of the catalyst as well as its spectral and electronic properties.

Citations

1. Grimes, C.; Varghese, O.; Ranjan, S., *Light, Water, Hydrogen*. 1 ed.; Springer US: **2008**.
2. Miller, E. L., Solar Hydrogen Production by Photoelectrochemical Water Splitting: The Promise and Challenge. In *On Solar Hydrogen & Nanotechnology*, John Wiley & Sons, Ltd: **2010**; pp 1-35.
3. Shockley, W.; Queisser, H. J., Detailed Balance Limit of Efficiency of p-n Junction Solar Cells. *J. Appl. Phys.* **1961**, *32* (3), 510-519.
4. Dharmadasa, I. M., Latest developments in CdTe, CuInGaSe$_2$ and GaAs/AlGaAs thin film PV solar cells. *Curr. Appl. Phys.* **2009**, *9* (2, Supplement), e2-e6.
5. Guo, F.; Li, N.; Fecher, F. W.; Gasparini, N.; Quiroz, C. O. R.; Bronnbauer, C.; Hou, Y.; Radmilovic, V. V.; Radmilovic, V. R.; Spiecker, E.; Forberich, K.; Brabec, C. J., A generic concept to overcome bandgap limitations for designing highly efficient multi-junction photovoltaic cells. *Nat. Commun.* **2015**, *6*.
6. O'Regan, B.; Grätzel, M., A low-cost, high-efficiency solar cell based on dye-sensitized colloidal TiO$_2$ films. *Nature* **1991**, *353*, 737-740.
7. Boschloo, G.; Hagfeldt, A., Characteristics of the Iodide/Triiodide Redox Mediator in Dye-Sensitized Solar Cells. *Acc. Chem. Res.* **2009**, *42* (11), 1819-1826.
8. Nazeeruddin, M. K.; Kay, A.; Rodicio, I.; Humphry-Baker, R.; Mueller, E.; Liska, P.; Vlachopoulos, N.; Graetzel, M., Conversion of light to electricity by cis-X$_2$bis(2,2'-bipyridyl-4,4'-dicarboxylate)ruthenium(II) charge-transfer sensitizers (X = Cl$^-$, Br$^-$, I$^-$, CN$^-$, and SCN$^-$) on nanocrystalline titanium dioxide electrodes. *J. Am. Chem. Soc.* **1993**, *115* (4), 6382-6390.
9. Swierk, J. R.; Mallouk, T. E., Design and development of photoanodes for water-splitting dye-sensitized photoelectrochemical cells. *Chem. Soc. Rev.* **2013**, *42*, 2357-2387.
10. Eckenhoff, W. T.; Eisenberg, R., Molecular systems for light driven hydrogen production. *Dalton Trans.* **2012**, *41*, 13004-13021.
11. Hall, D. O., Photobiological energy conversion. *FEBS Lett.* **1976**, *64* (1), 6-16.
12. Mellis, A., Photosystem-II damage and repair cycle in chloroplasts: What modulates the rate of photodamage in vivo? *Trends Plant Sci.* **1999**, *4* (99), 130-135.
13. Green, B.; Parson, W. W., *Light-Harvesting Antennas in Photosynthesis*. Springer Netherlands: 2003; Vol. 13.
14. Saito, K.; Shen, J. R.; Ishikita, H., Cationic state distribution over the chlorophyll d-containing P D1/PD2 pair in photosystem II. *Biochim. Biophys. Acta, Bioenerg.* **2012**, *1817* (8), 1191-1195.
15. Guskov, A.; Kern, J.; Gabdulkhakov, A.; Broser, M.; Zouni, A.; Saenger, W., Cyanobacterial photosystem II at 2.9-A resolution and the role of quinones, lipids, channels and chloride. *Nat. Struct. Mol. Biol.* **2009**, *16* (3), 334-342.
16. Galstyan, A.; Robertazzi, A.; Knapp, E. W., Oxygen-evolving Mn cluster in photosystem II: The protonation pattern and oxidation state in the high-resolution crystal structure. *J. Am. Chem. Soc.* **2012**, *134*, 7442-7449.

17. Cady, C. W.; Crabtree, R. H.; Brudvig, G. W., Functional models for the oxygen-evolving complex of photosystem II. *Coord. Chem. Rev.* **2008,** *252,* 444-455.

18. Kok, B.; Forbush, B.; McGloin, M., Cooperation of charges in photosynthetic O_2 evolution. A linear four step mechanism. *Photochem. Photobiol.* **1970,** *11* (6), 457-475.

19. Fromme, P.; Mathis, P., Unraveling the Photosystem I Reaction Center: A History, or the Sum of Many Efforts. *Photosynth. Res.* **2004,** *80* (1), 109-124.

20. Wu, H.; Roy, S.; Alami, M.; Green, B. R.; Campbell, D. a., Photosystem II Photoinactivation, Repair, and Protection in Marine Centric Diatoms. *Plant Physiol.* **2012,** *160* (September), 464-476.

21. Foote, C. S.; Wexler, S.; Ando, W.; Higgins, R., Chemistry of singlet oxygen. IV. Oxygenations with hypochlorite-hydrogen peroxide. *J. Am. Chem. Soc.* **1968,** *90* (4), 975-981.

22. Kanofsky, J. R., Singlet oxygen production by biological systems. *Chem. Biol. Interact.* **1989,** *70* (1), 1-28.

23. Štroch, M.; Špunda, V.; Kurasová, I., Non-Radiative Dissipation of Absorbed Excitation Energy Within Photosynthetic Apparatus of Higher Plants. *Photosynthetica* **2004,** *42* (3), 323-337.

24. Lambrev, P. H.; Miloslavina, Y.; Jahns, P.; Holzwarth, A. R., On the relationship between non-photochemical quenching and photoprotection of Photosystem II. *Biochim. Biophys. Acta, Bioenerg.* **2012,** *1817* (5), 760-769.

25. Ohnishi, N.; Allakhverdiev, S. I.; Takahashi, S.; Higashi, S.; Watanabe, M.; Nishiyama, Y.; Murata, N., Two-Step Mechanism of Photodamage to Photosystem II: Step 1 Occurs at the Oxygen-Evolving Complex and Step 2 Occurs at the Photochemical Reaction Center. *Biochemistry* **2005,** *44* (23), 8494-8499.

26. Rochaix, J.-D., Regulation of photosynthetic electron transport. *Biochim. Biophys. Acta, Bioenerg.* **2011,** *1807* (3), 375-383.

27. Romain, S.; Vigara, L.; Llobet, A., Oxygen-oxygen bond formation pathways promoted by ruthenium complexes. *Acc. Chem. Res.* **2009,** *42* (12), 1944-1953.

28. Concepcion, J. J.; Tsai, M. K.; Muckerman, J. T.; Meyer, T. J., Mechanism of water oxidation by single-site ruthenium complex catalysts. *J. Am. Chem. Soc.* **2010,** *132* (14), 1545-1557.

29. Tseng, H.-w.; Zong, R.; Muckerman, J. T.; Thummel, R., Mononuclear Ruthenium (II) Complexes That Catalyze Water Oxidation. *Inorg. Chem.* **2008,** *47* (24), 11763-11773.

30. Tseng, H.-W.; Zong, R.; Muckerman, J. T.; Thummel, R., Mononuclear Ruthenium(II) Complexes That Catalyze Water Oxidation. *Inorg. Chem.* **2008,** *47* (24), 11763-11773.

31. Wasylenko, D. J.; Ganesamoorthy, C.; Henderson, M. A.; Koivisto, B. D.; Osthoff, H. D.; Berlinguette, C. P., Electronic Modification of the $[Ru^{II}(tpy)(bpy)(OH_2)]^{2+}$ Scaffold: Effects on Catalytic Water Oxidation. *J. Am. Chem. Soc.* **2010,** *132* (45), 16094-16106.

32. Wasylenko, D. J.; Ganesamoorthy, C.; Koivisto, B. D.; Henderson, M. A.; Berlinguette, C. P., Insight into Water Oxidation by Mononuclear Polypyridyl Ru Catalysts. *Inorg. Chem.* **2010,** *49* (5), 2202-2209.

33. Concepcion, J. J.; Jurss, J. W.; Norris, M. R.; Chen, Z.; Templeton, J. L.; Meyer, T. J., Catalytic Water Oxidation by Single-Site Ruthenium Catalysts. *Inorg. Chem.* **2010,** *49* (4), 1277-1279.

34. Wasylenko, D. J.; Ganesamoorthy, C.; Koivisto, B. D.; Henderson, M. A.; Berlinguette, C. P., Insight into Water Oxidation by Mononuclear Polypyridyl Ru Catalysts. *Inorg. Chem.* **2010,** *49* (5), 2202-2209.

35. Marelius, D. C.; Bhagan, S.; Charboneau, D. J.; Schroeder, K. M.; Kamdar, J. M.; McGettigan, A. R.; Freeman, B. J.; Moore, C. E.; Rheingold, A. L.; Cooksy, A. L.; Smith, D. K.; Paul, J. J.; Papish, E. T.; Grotjahn, D. B., How Do Proximal Hydroxy or Methoxy Groups on the Bidentate Ligand Affect [(2,2′;6′,2″-Terpyridine)Ru(N,N)X] Water-Oxidation Catalysts? Synthesis, Characterization, and Reactivity at Acidic and Near-Neutral pH. *Eur. J. Inorg. Chem.* **2014,** *2014* (4), 676-689.

36. Maji, S.; López, I.; Bozoglian, F.; Benet-Buchholz, J.; Llobet, A., Mononuclear Ruthenium–Water Oxidation Catalysts: Discerning between Electronic and Hydrogen-Bonding Effects. *Inorg. Chem.* **2013,** *52* (7), 3591-3593.

37. Boyer, J. L.; Polyansky, D. E.; Szalda, D. J.; Zong, R.; Thummel, R. P.; Fujita, E., Effects of a Proximal Base on Water Oxidation and Proton Reduction Catalyzed by Geometric Isomers of [Ru(tpy)(pynap)(OH$_2$)]$^{2+}$. *Angew. Chem. Int. Ed.* **2011,** *50* (52), 12600-12604.

38. Hirahara, M.; Ertem, M. Z.; Komi, M.; Yamazaki, H.; Cramer, C. J.; Yagi, M., Mechanisms of Photoisomerization and Water-Oxidation Catalysis of Mononuclear Ruthenium(II) Monoaquo Complexes. *Inorg. Chem.* **2013,** *52* (11), 6354-6364.

39. Duan, L.; Fischer, A.; Xu, Y.; Sun, L., Isolated Seven-Coordinate Ru(IV) Dimer Complex with [HOHOH]− Bridging Ligand as an Intermediate for Catalytic Water Oxidation. *J. Am. Chem. Soc.* **2009,** *131* (30), 10397-10399.

40. Duan, L.; Xu, Y.; Zhang, P.; Wang, M.; Sun, L., Visible Light-Driven Water Oxidation by a Molecular Ruthenium Catalyst in Homogeneous System. *Inorg. Chem.* **2010,** *49* (1), 209-215.

41. Suzuki, M., Ligand Effects on Dioxygen Activation by Copper and Nickel Complexes: Reactivity and Intermediates. *Acc. Chem. Res.* **2007,** *40* (7), 609-617.

42. Duan, L.; Xu, Y.; Gorlov, M.; Tong, L.; Andersson, S.; Sun, L., Chemical and Photochemical Water Oxidation Catalyzed by Mononuclear Ruthenium Complexes with a Negatively Charged Tridentate Ligand. *Chem. Eur. J.* **2010,** *16* (15), 4659-4668.

43. An, J.; Duan, L.; Sun, L., Ru complexes containing pyridine dicarboxylate ligands: electronic effects on their catalytic activity toward water oxidation. *Faraday Discuss.* **2012,** *155* (0), 267-275.

44. Tong, L.; Wang, Y.; Duan, L.; Xu, Y.; Cheng, X.; Fischer, A.; Ahlquist, M. S. G.; Sun, L., Water Oxidation Catalysis: Influence of Anionic Ligands upon the Redox Properties and Catalytic Performance of Mononuclear Ruthenium Complexes. *Inorg. Chem.* **2012,** *51* (6), 3388-3398.

45. Kärkäs, M. D.; Åkermark, T.; Johnston, E. V.; Karim, S. R.; Laine, T. M.; Lee, B.-L.; Åkermark, T.; Privalov, T.; Åkermark, B., Water Oxidation by Single-Site Ruthenium Complexes: Using Ligands as Redox and Proton Transfer Mediators. *Angew. Chem. Int. Ed* **2012,** *51* (46), 11589-11593.

46. Kemnitz, C. R.; Loewen, M. J., "Amide Resonance" Correlates with a Breadth of C−N Rotation Barriers. *J. Am. Chem. Soc.* **2007,** *129* (9), 2521-2528.

47. Kärkäs, M. D.; Åkermark, T.; Chen, H.; Sun, J.; Åkermark, B., A tailor-made molecular ruthenium catalyst for the oxidation of water and its deactivation through poisoning by carbon monoxide. *Angew. Chem. Int. Ed* **2013,** *52*, 4189-4193.

48. Gilbert, J. a.; Eggleston, D. S.; Murphy, W. R.; Geselowitz, D. a.; Gersten, S. W.; Hodgson, D. J.; Meyer, T. J., Structure and redox properties of the water-oxidation catalyst $[(bpy)_2(OH_2)RuORu(OH_2)(bpy)_2]^{4+}$ *J. Am. Chem. Soc.* **1985,** *107*, 3855-3864.

49. Hurst, J. K.; Cape, J. L.; Clark, A. E.; Das, S.; Qin, C., Mechanisms of water oxidation catalyzed by ruthenium diimine complexes. *Inorg. Chem.* **2008,** *47*, 1753-1764.

50. Sens, C.; Romero, I.; Rodríguez, M.; Llobet, A.; Parella, T.; Benet-Buchholz, J., A New Ru Complex Capable of Catalytically Oxidizing Water to Molecular Dioxygen. *J. Am. Chem. Soc.* **2004,** *126* (25), 7798-7799.

51. Neudeck, S.; Maji, S.; López, I.; Meyer, S.; Meyer, F.; Llobet, A., New Powerful and Oxidatively Rugged Dinuclear Ru Water Oxidation Catalyst: Control of Mechanistic Pathways by Tailored Ligand Design. *J. Am. Chem. Soc.* **2014,** *136* (1), 24-27.

52. Wada, T.; Tsuge, K.; Tanaka, K., Syntheses and Redox Properties of Bis(hydroxoruthenium) Complexes with Quinone and Bipyridine Ligands. Water-Oxidation Catalysis. *Inorg. Chem.* **2001,** *40* (2), 329-337.

53. Muckerman, J. T.; Polyansky, D. E.; Wada, T.; Tanaka, K.; Fujita, E., Water Oxidation by a Ruthenium Complex with Noninnocent Quinone Ligands: Possible Formation of an O−O Bond at a Low Oxidation State of the Metal. *Inorg. Chem.* **2008,** *47* (6), 1787-1802.

54. Kobayashi, K.; Ohtsu, H.; Wada, T.; Kato, T.; Tanaka, K., Characterization of a Stable Ruthenium Complex with an Oxyl Radical. *J. Am. Chem. Soc.* **2003,** *125* (22), 6729-6739.

55. Horiuchi, Y.; Toyao, T.; Miyahara, K.; Zakary, L.; Van, D. D.; Kamata, Y.; Kim, T.-H.; Lee, S. W.; Matsuoka, M., Visible-light-driven photocatalytic water oxidation catalysed by iron-based metal-organic frameworks. *Chem. Commun.* **2016**, 52 (29), 5190-5193.

56. Baur, W. H.; Khan, A. A., Rutile-type compounds. IV. SiO2, GeO2 and a comparison with other rutile-type structures. *Acta Cryst. B* **1971**, 27, 2133-2139.

57. Horn, M.; Schwebdtfeger, C.F.; Meagher, E.P., Refinement of the structure of anatase at several temperatures. *Zeitschrift Für Krist. Mater.* **1972**, 136, 273–281.

58. Fujishima, A.; Honda, K., Electrochemical Photolysis of Water at a Semiconductor Electrode. *Nature* **1972,** *238* (5358), 37-38.

59. Kim, W.; Tachikawa, T.; Moon, G.-h.; Majima, T.; Choi, W., Molecular-Level Understanding of the Photocatalytic Activity Difference between Anatase and Rutile Nanoparticles. *Angew. Chem. Int. Ed.* **2014,** *53* (51), 14036-14041.

60. Sumita, M.; Hu, C.; Tateyama, Y., Interface water on TiO_2 anatase (101) and (001) surfaces: First-principles study with TiO_2 slabs dipped in bulk water. *J. Phys. Chem. C* **2010,** *114* (101), 18529-18537.

61. Waterhouse, G. I. N.; Idriss, H., Photocatalytic Reactions on Model Single Crystal TiO_2 Surfaces. In *On Solar Hydrogen & Nanotechnology*, John Wiley & Sons, Ltd: 2010; pp 77-89.

62. Ganesh, I.; Gupta, A. K.; Kumar, P. P.; Sekhar, P. S. C.; Radha, K.; Padmanabham, G.; Sundararajan, G., Preparation and Characterization of Ni-Doped TiO_2 Materials for Photocurrent and Photocatalytic Applications. *Scientific World J.* **2012**, *2012*, 127326.

63. Blake, R. L.; Hessevic. R.E.; Zoltai, T.; Finger, L. W., Refinement of hematite structure. *Am. Mineral* **1966** 51 (1-2), 123-129.

64. Nelmes, R. J.; Meyer, G. M.; Hutton, J., Thermal motion in $SrTiO_3$ at room temperature: Anharmonic or disordered? *Ferroelectrics* **1978** 21, 461-462.

65. Spathis, P.; Poulios, I., The corrosion and photocorrosion of zinc and zinc oxide coatings. *Corros. Sci.* **1995,** *37* (5), 673-680.

66. Abrahams, S. C.; Bernstein, J. L., Remeasurement of the structure of hexagonal ZnO. *Acta Cryst. B* **1969** 25, 1233-1236.

67. Boman, C. E., Refinement of the crystal structure of ruthenium dioxide. *Acta Chem. Scand.* **1970** 24 (1), 116-122.

68. Bolzan, A. A.; Fong, C.; Kennedy, B. J.; Howard, C. J., Structural studies of rutile-type metal dioxides. *Acta Cryst. B* **1997** 53, 373-380.

69. Baglio, V.; Di Blasi, a.; Denaro, T.; Antonucci, V.; Arico, A. S.; Ornelas, R.; Matteucci, F.; Alonso, G.; Morales, L.; Orozco, G.; Arriaga, L. G., Synthesis, characterization and evaluation of IrO_2-RuO_2 electrocatalytic powders for oxygen evolution reaction. *J. New Mater. Electrochem. Syst.* **2008,** *11*, 105-108.

70. Näslund, L. Å.; Sánchez-Sánchez, C. M.; Ingason, Á. S.; Bäckström, J.; Herrero, E.; Rosen, J.; Holmin, S., The role of TiO_2 doping on RuO_2-coated electrodes for the water oxidation reaction. *J. Phys. Chem. C* **2013,** *117*, 6126-6135.

71. Wang, G.; Zhou, M.; Goettel, J. T.; Schrobilgen, G. J.; Su, J.; Li, J.; Schloder, T.; Riedel, S., Identification of an iridium-containing compound with a formal oxidation state of IX. *Nature* **2014,** *514* (7523), 475-477.

72. Over, H., Surface chemistry of ruthenium dioxide in heterogeneous catalysis and electrocatalysis: From fundamental to applied research. *Chem. Rev.* **2012,** *112* (6), 3356-3426.

73. Fabbri, E.; Habereder, A.; Waltar, K.; Kotz, R.; Schmidt, T. J., Developments and perspectives of oxide-based catalysts for the oxygen evolution reaction. *Catal. Sci. Tech.* **2014,** *4* (11), 3800-3821.

74. Meekins, B. H.; Kamat, P. V., Role of water oxidation catalyst IrO_2 in shuttling photogenerated holes across TiO_2 interface. *J. Phys. Chem. Lett.* **2011,** *2*, 2304-2310.

75. Wasielewski, M. R., Photoinduced electron transfer in supramolecular systems for artificial photosynthesis. *Chem. Rev.* **1992,** *92* (3), 435-461.

76. Young, K. J.; Martini, L. A.; Milot, R. L.; Snoeberger Iii, R. C.; Batista, V. S.; Schmuttenmaer, C. A.; Crabtree, R. H.; Brudvig, G. W., Light-driven water oxidation for solar fuels. *Coord. Chem. Rev.* **2012,** *256* (21–22), 2503-2520.

77. Adamson, A. W.; Demas, J. N., New photosensitizer. Tris(2,2'-bipyridine)ruthenium(II) chloride. *J. Am. Chem. Soc.* **1971,** *93* (7), 1800-1801.

78. Péchy, P.; Rotzinger, F. P.; Nazeeruddin, M. K.; Kohle, O.; Zakeeruddin, S. M.; Humphry-Baker, R.; Grätzel, M., Preparation of phosphonated polypyridyl ligands to anchor transition-metal complexes on oxide surfaces: application for the conversion of light to electricity with nanocrystalline TiO_2 films. *J. Chem. Soc., Chem. Commun.* **1995,** *369* (1), 65-66.

79. Bae, E.; Choi, W.; Park, J.; Shin, H. S.; Kim, S. B.; Lee, J. S., Effects of surface anchoring groups (Carboxylate vs Phosphonate) in ruthenium-complex-sensitized TiO_2 on visible light reactivity in aqueous suspensions. *J. Phys. Chem. B* **2004,** *108* (37), 14093-14101.

80. Nilsing, M.; Persson, P.; Ojamäe, L., Anchor group influence on molecule-metal oxide interfaces: Periodic hybrid DFT study of pyridine bound to TiO_2 via carboxylic and phosphonic acid. *Chem. Phys. Lett.* **2005,** *415*, 375-380.

81. Pastore, M.; De Angelis, F., Computational modelling of TiO_2 surfaces sensitized by organic dyes with different anchoring groups: adsorption modes, electronic structure and implication for electron injection/recombination. *Phys. Chem. Chem. Phys.* **2012,** *14*, 920-928.

82. Galoppini, E., Linkers for anchoring sensitizers to semiconductor nanoparticles. *Coord. Chem. Rev.* **2004,** *248* (13–14), 1283-1297.

83. Gabrielsson, E.; Tian, H.; Eriksson, S. K.; Gao, J.; Chen, H.; Li, F., Dipicolinic acid: a strong anchoring group with tunable redox and spectral behavior for stable dye-sensitized solar cells. *Chem. Commun.* **2015,** *51* (18), 3858-3861.

Chapter II

Ru^{III} and Ru^{IV} dipicolinic acid complexes for the examination of anchor substitution effects

Introduction

At standard temperature and pressure the enthalpy change ($\Delta H°$) to convert one mole of water into one mole of hydrogen and half a mole of oxygen is 285.83 kJmol⁻¹. This energy is composed of both electrical and thermal energy. The electrical component is derived from the Gibbs free energy of formation ($\Delta G°$) of one mole of water and states that the minimum theoretical energy required to split water is 237.13 kJmol⁻¹, corresponding to a voltage of 1.229 V. The remaining 48.7 kJmol⁻¹ of thermal energy is usually contributed via the internal resistance if the electrolysis cell. As the thermal load is derived from the electrical load on the cell, a higher voltage is required for the electrolysis reaction to occur (Figure 2.1).[1]
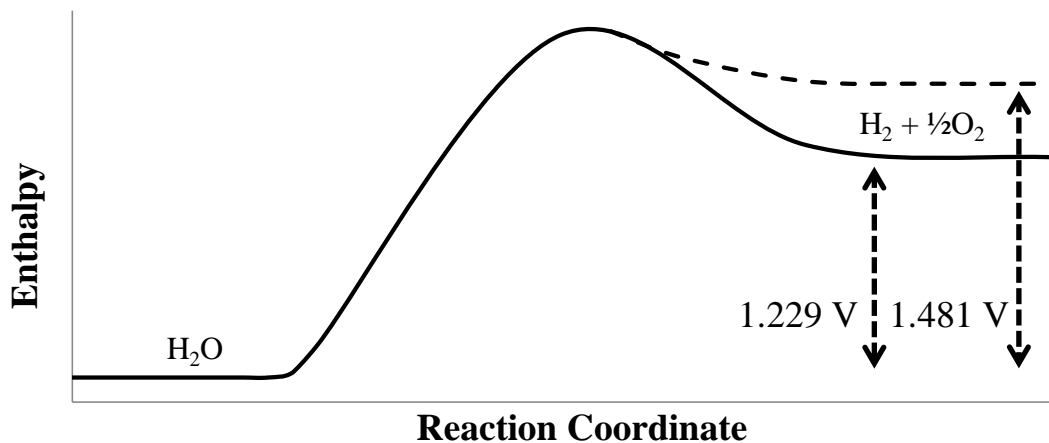
Figure 2.1 Simplified reaction coordinate diagram of the electrolysis of water.

So for isothermal (no heat exchanged with its environment) electrolysis cells the minimum voltage for continual electrolysis without additional thermal input is 285.83 kJmol⁻¹. This corresponds to 1.481 V (E_0) as shown in Equation 2.1 where z is the number of electrons required to produce one molecule of H_2 and F is Faraday's constant.

$$E_0 = \frac{\Delta H°}{zF} = \frac{285\ 830\ \text{J mol}^{-1}}{2 \times 96485\ \text{C mol}^{-1}} = 1.481\ \text{V} \qquad \text{Equation 2.1}$$

It should be noted that in commercial electrolysis the operating potential is closer to 2 V in order to maintain a higher efficiency.

In a heterogeneous water oxidation junction, the potential required to oxidise water is generated in electron hole pairs which form in the semiconductor. The electrical potential used to split water is the potential of the electron hole pair itself and is therefore dependant on the band gap of that semiconductor. The concentration of electron hole pairs is dependent on the concentration of incident photons (solar flux). As only photons above a certain wavelength can be promote an electron from the valence band to the conduction band different wavelengths will contribute to the total current density differently. Recent developments in solar cell technology now have current densities ranging up to 30mAcm^{-2} with ranges of 1.5-2 V.[2-4]

These are higher than those of the potentials of the molecular systems mentioned in Chapter 1. The difference is due to molecular catalysts separating out the oxidation into sequential steps and lowering the overall activation barrier compared to heterogeneous catalysis where multiple steps are taking place concurrently.

While semiconductors, whose band gap corresponds to this voltage are known, their instability at the solution interface means that higher band gap oxide semiconductors must be used. These oxides are able to create the necessary voltage but the larger band gap limits their absorption to the UV region of the spectrum. This is the same problem encountered in DSSC. DSSCs include a dye in the cell, to increase the light absorption range, and similar dyes can be used to improve the performance of heterogeneous water oxidation catalysts. As mentioned in the previous chapter the dye can "inject" a photoexcited electron into the conductance band of the semiconductor. If the potential of the now oxidised dye is positive enough it can oxidise the catalyst (e.g. IrO_2) which in turn can oxidise water to molecular oxygen (Figure 2.2). The first example of this type of assembly was reported in 2009 and consisted of a $Ru(bpy)_3^{2+}$ derived dye stabilising IrO_2 nanoparticles supported on a TiO_2 substrate.
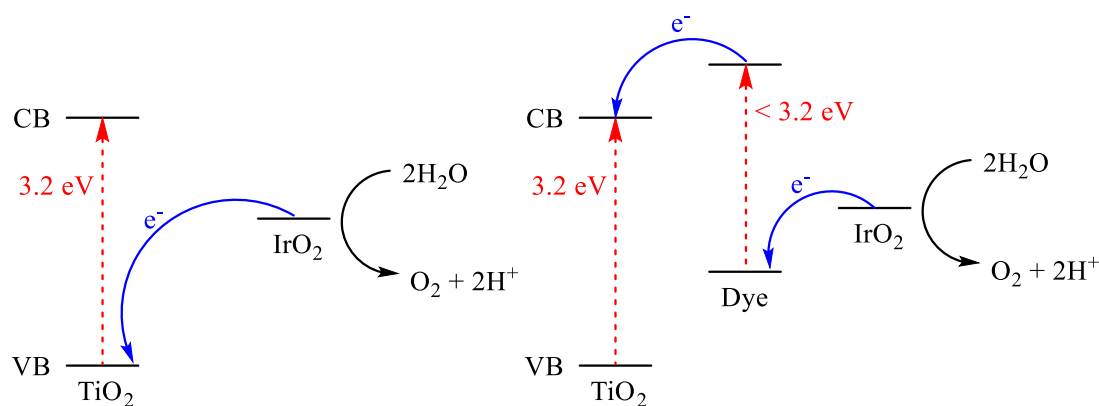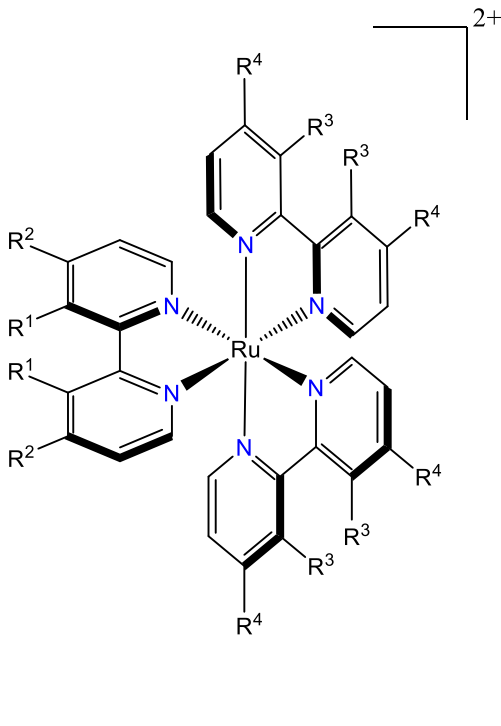
Figure 2.2 Electron transfer in a heterogeneous water oxidation catalyst.

Once the decision to include a dye has been made, the anatase phase of TiO_2 becomes more favoured over rutile as the potential of its conduction band is 200 mV more negative than that of rutile. Although this reduces the range of light that the substrate can absorb, the potential of the excited electrons becomes more favourable for the hydrogen evolution reaction. The difference is that in DSSCs a I_3^-/I^- couple is used with a potential of 0.53 V, significantly lower than the 1.229 V for the water oxidation reaction. In order for dye sensitised heterogeneous water oxidation to occur the dye must have a more positive oxidation potential than that of the water oxidation reaction (1.229 V). The inclusion of anchoring groups actually points towards the solution to this problem as they stabilise the higher oxidation states of bipyridine derived ruthenium dyes as shown in Table 2.1.[5]

Dyes of this type follow the simple rule: electron withdrawing groups raise the potential, electron donating groups lower the potential. In a simple DSSC the obvious solution would be to attach electron withdrawing groups to the ligand bound to the substrate, and electron donating groups to all other positions. In a heterogeneous water oxidation cell, however, the potential of the dye must lie above that of the water oxidation reaction, so the addition of an exorbitant number of electron donating groups would lower the potential too far.

Table 2.1 Substituent effect on redox couples of ruthenium bipyridine complexes vs. NHE.

Substitution	E (Ru^{III}/Ru^{II})
$R^1,R^2,R^3,R^4=H$	1.26 V
$R^1=CH_3$, $R^2,R^3,R^4=H$	1.22 V
$R^1, R^2, R^4=H$ $R^3=CH_3$	1.18 V
$R^1, R^3=CH_3$ $R^2, R^4=H$	1.15 V
$R^1, R^3=H$ $R^2, R^4=CH_3$	1.10 V
$R^1,R^3,R^4=H$ $R^2=t\text{-butyl}$	1.21 V
$R^1, R^2, R^3=H$ $R^4= t\text{-butyl}$	1.16 V
$R^2, R^4=H$ $R^2, R^4= t\text{-butyl}$	1.11 V
$R^1,R^3,R^4=H$ $R^2=CO_2Et$	1.40 V
$R^1, R^2, R^3=H$ $R^4= CO_2Et$	1.54 V

In Ru(bpy)$_3$ an excited electron is initially distributed across the three bipyridine ligands before localising on a single bipyridine. Electron withdrawing groups direct which bipyridine it eventually localises on. This holds true in systems with multiple substituted bipyridines. In these systems the most electronegative ligand can be chosen by the addition of electron donating rather than withdrawing groups to one or both of the other bipyridines. In choosing which of the coordinated bipyridines is the most electronegative, and by anchoring that ligand onto the substrate, it is possible to more effectively direct current generated from photoexcitation.

When using heterogeneous co-catalysts such as iridium oxide this raises a problem. As the anchoring groups tend to be electron withdrawing in nature, the difficulty is now how to attach the co-catalysts to the dye while keeping the substrate bound ligand being the most electron withdrawing. One way is to substitute two sites on the substrate bound ligand with electron withdrawing anchors, but only one site on the co-catalyst bound ligand, with the other site on that ligand having an electron donating group.

Mollouk *et al* used this system in 2009, employing two phosphonates on the substrate bound ligand and a single malonate on the iridium oxide bound ligand (Figure 2.3).[6] One of the key performance issues that was noted in this system was the slow electron transfer from the iridium oxide to the excited dye. This can be attributed to the presence of a sp^3 hybridised carbon between the aromatic ring and the iridium coordinated carboxylate groups. While the inclusion of non-aromatic or conjugated atoms in the electron transport chain would limit the electron withdrawing effects of the ligand on the ruthenium it would also inhibit electron transport itself.
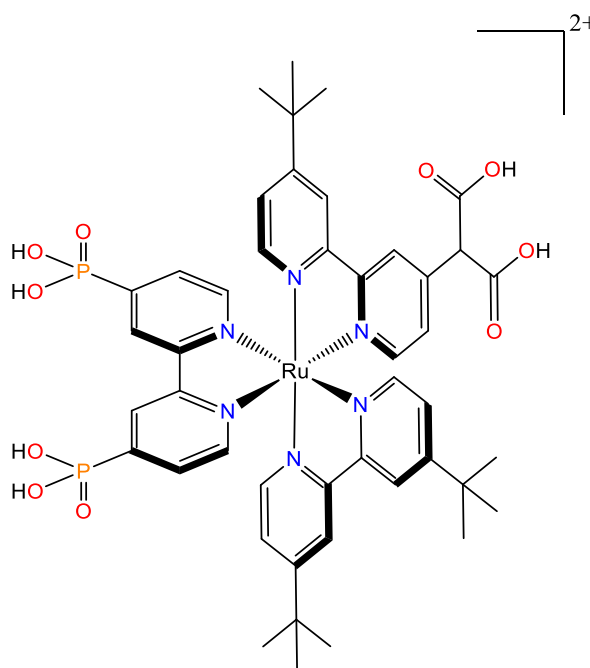
Figure 2.3 Ruthenium photosensitiser for heterogeneous water oxidation.

A higher oxidation potential is important to dye performance; nevertheless, it cannot be considered independently of the mechanism as a whole. The quantum yield of an electron excited from a dye ground state is heavily influenced by the interface conditions of the dye with the substrate. The conduction band edge potential for anatase is 0 V vs NHE at pH 0, and decreases by 55 mV for every pH unit.[7] At low pH the potential is proximate to 0 V so that there will be significant overlap between the dye's excited states and the conduction band of the anatase substrate. If the pH rises, the band edge potential of the anatase will become progressively more negative.[8] If the band edge becomes too negative, then the overlap between the dye's excited states and the conduction band orbitals decreases and therefore so does the injection rate of excited electrons into the substrate (Figure 2.4).
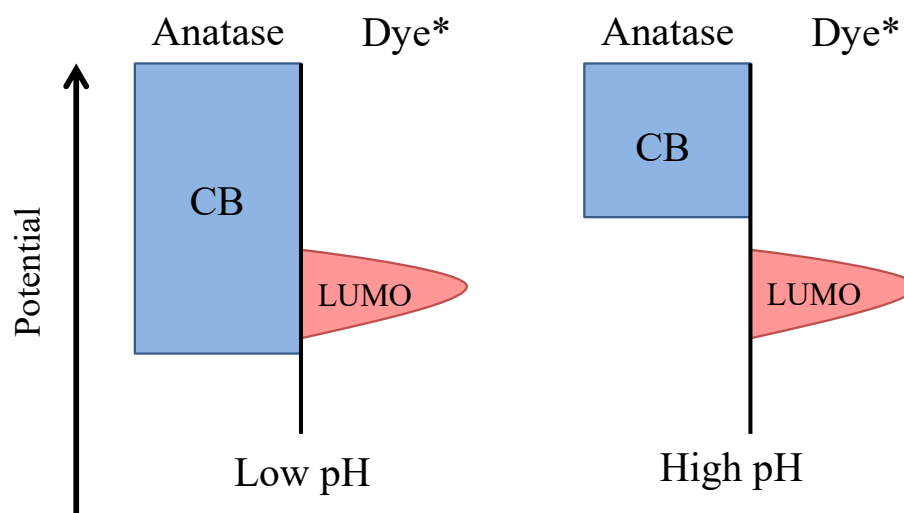
Figure 2.4 Overlap of conductance band of substrate and LUMO levels of dye at different pH.

As the operating conditions of the system will produce protons at the interface it will maintain its own low pH environment. This condition will remain as long as the rate of diffusion of protons away from the surface is lower than the rate of proton production. If it is assumed that the driving force of the reaction is found within the water oxidation side, then the likelihood that the pH will rise significantly is low. If, however the water oxidation step is coupled with a light absorbing reduction step or via the application of a bias, then the water oxidation step may become rate limiting. In this case the pH at the oxidation surface will rise, resulting in an increase of the conduction band edge and a further lowering of the rate of water oxidation.

The result of this situation is that dyes coupled to anatase substrates should be stable across a range of pH values and have good overlap between excited state orbitals and the conduction band. In practice it is enough for dyes to be stable under acidic operating conditions, as changes in the pH dependant heterogeneous water oxidation reactions will have a more significant impact on the performance of the system, at least in the short term.

In order to test the efficacy of a dye we need to create a uniform substrate and catalyst that can be used to make meaningful comparisons between the activities of different dyes. The problem in generating such a system from dye stabilised nanoparticles is that the ratio of dye to nanoparticle and the size of the nanoparticle will vary depending

on the dye, so no comparable systems can be easily created. Direct deposition of unstabilised iridium oxide nanoparticles onto TiO_2 surfaces followed by dye deposition will produce a series of catalyst dye assemblies required to examine dye performance. Direct deposition of IrO_2 nanoparticles has two additional effects. The useful effect is to increase the electron transfer from water oxidation catalyst to the substrate. This effect is counterpoised by increased rate of electron hole recombination between the substrate conduction band and the hole in the oxidised iridium oxide nanoparticle. Derived assemblies while not being the most efficient at the oxygen evolution reaction do however allow for a controlled series of experiments on the performance of different dyes for the sensitisation of the substrate to the oxygen evolution reaction. The dyes we wish to examine as stated in the previous chapter are derived from picolinic acid, which allows for examination of the substitution pattern in a manner that would be difficult in the more common bipyridine based ligands but similar enough in nature to indicate how the properties of such dyes might be influenced. The key difference is that the picolinic acids are charge carrying ligands and as such direct comparison with charge neutral ligand systems cannot be made. However, as such charge neutral ligands are prohibitively difficult to modify in a systematic manner this is an acceptable price to pay.

Aim

Picolinic acid binds to metals in a bidentate manner leaving four positions on the pyridine ring free for anchor attachment (Figure 2.5). The aim of this chapter is therefore to synthesise and characterise the ruthenium complexes of the four different isomers of carboxyl substituted picolinic acid. The structures of the complexes were elucidated via single crystal X-ray crystallography. Cyclic voltammetry and UV/vis spectroscopic analysis were used to ascertain redox potentials and catalytic testing of the complexes used to determine the effect of anchoring positon and determine the ability of the complexes to act as dye sensitisers.
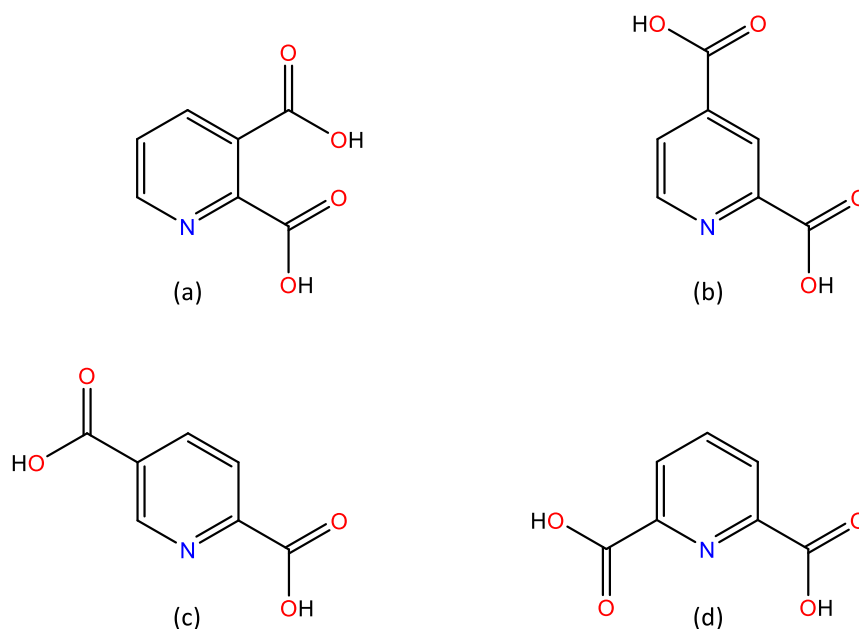
Figure 2.5 (a) 2,3 - dipicolinic acid (b) 2,4 - dipicolinic acid (c) 2,5 - dipicolinic acid (d) 2,6 - dipicolinic acid.

Results and Discussion
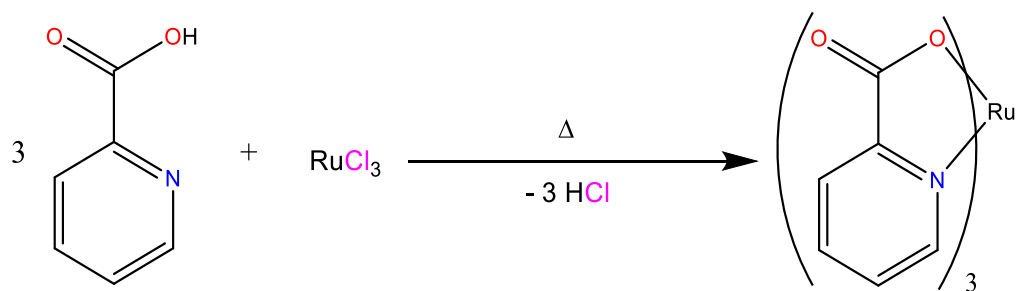
Scheme 2.1 Synthesis of ruthenium complexes derived from dipicolinic acid isomers.

The complexes were synthesised using hydrated ruthenium trichloride as the primary starting material (Scheme 2.1). In order to have a baseline for the non-catalytic properties of the dyes we first synthesised dyes using simple non-substituted picolinic acid by modification of the published procedure.[9] Ruthenium trichloride was refluxed with four equivalents of picolinic acid in ethanol. The resulting orange solution produced yellow/white crystals which when recrystallised from water yielded the ruthenium trispicolinate as a monohydrate (Figure 2.6). As reported, this species exits as two enantiomers due to its C_3 symmetry but as the coordinating groups are not the same it lacks the C_2 symmetry found in its bipyridine analogue.[10] The change in symmetry means that charge transfer from the metal to the ligand will not be equally shared across the two coordinated groups.

Table 2.2 Bond length comparison between tris ruthenium species.

Bond	Ru(pic)$_3$	Ru(bpy)$_3{}^{2+}$
Ru-N$_1$	2.057(2)	2.058(3)
Ru-N$_2$	2.063(2)	2.062(3)
Ru-N$_3$	2.060(2)	2.063(5)
Ru-N$_4$		2.065(3)
Ru-N$_5$		2.066(4)
Ru-N$_6$		2.067(4)
Ru-O$_1$	2.0015(18)	
Ru-O$_3$	2.0251(18)	-
Ru-O$_5$	2.0047(18)	

There is also an elongation of the ruthenium–oxygen bond of the picolinic acid trans to the two carboxylates (Ru-O bond length ~ 0.02 Å greater) so that there is an inequivalency in the coordination sphere (Table 2.2).
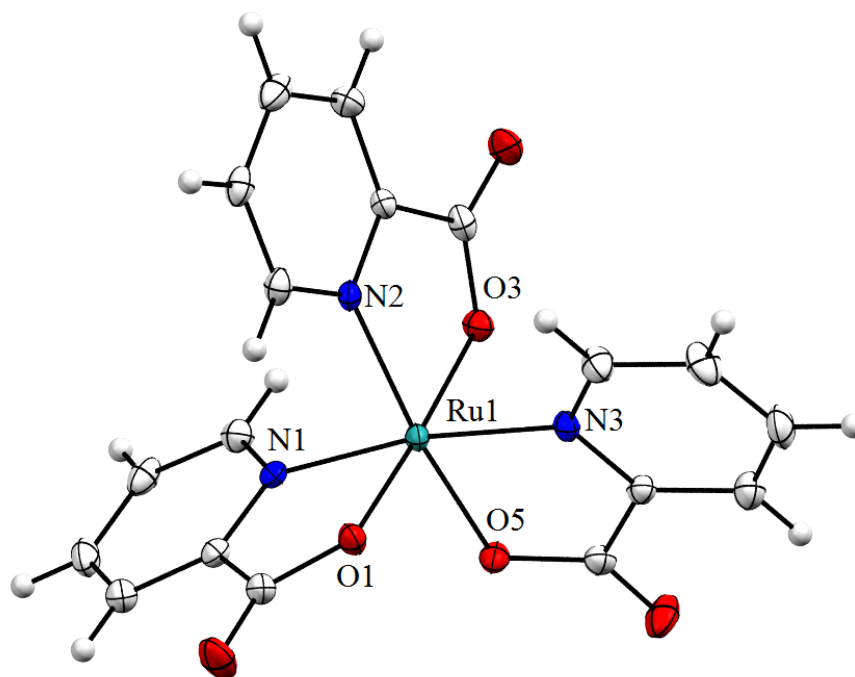
Figure 2.6 X-ray structure of tris(pyridine-2-carboxylate) ruthenium (III). Ellipsoids shown at 50% probability.

Table 2.3 Bite angle comparison between tris ruthenium species.

Bite Angle	Ru(pic)$_3$	Ru(bpy)$_3^{2+}$
N$_1$-Ru1-O$_1$	80.59(8)	78.4(1)
N$_2$-Ru1-O$_3$	79.21(8)	79.3(1)
N$_3$-Ru1-O$_5$	81.41(8)	79.1(1)

The bite angle of the picolinate complex did not vary significantly from that of the bipyridine species (~2°) (Table 2.3). The difference in bite angle was attributed to the ruthenium-oxygen bond being shorter than that of the ruthenium-nitrogen bond in both complexes.

Examination of the aqueous UV spectrum indicated that the complex would make a poor sensitiser as its visible absorbance range terminated at approximately 400 nm. While it may have been possible to analyse the effect of substitution patterns with this complex configuration, an alternate option would be to form the bis picolinate rather than the tris species and use the remaining two sites for ligands that would enhance the

complexes' absorption in the visible range. The simplest of these species would be the chloride species since it required only a minor modification of the initial preparative procedure. By only using two equivalents of picolinic acid it is possible to isolate the dichloride complex which possessed a bright orange colour both in solution and crystal form.
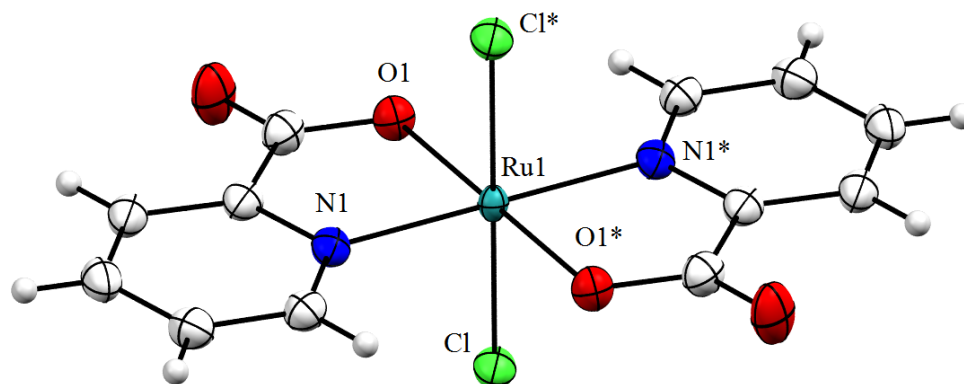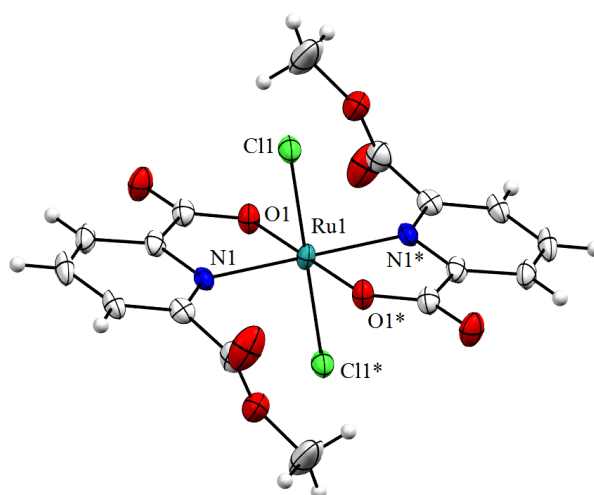

Figure 2.7 X-ray structure of dichlorobis(pyridine-2-carboxylate) ruthenium (IV). Ellipsoids shown at 50% probability. Symmetry operators to generate equivalent atoms: (*) -x, -y, -z .

Compared to the tris species, the picolinic ligands in the bis species take up an equatorial configuration with the chlorides occupying axial positions rather than being cis to one another (Figure 2.7). Electronically the two products are quite different as the additional anionic ligand in the bis picolinate promoted the oxidation of the ruthenium centre to the +4 oxidation state from the +3 state of the RuCl$_3$ starting material. The ruthenium-nitrogen bond is shorter in the bis species (~0.015Å) but with the ruthenium-oxygen bonds being longer (Table 2.4). The lengthening of the ruthenium oxygen bond is attributed to the increased electron donation from the chlorides.

Table 2.4 Nitrogen and oxygen bond lengths of unsubstituted ruthenium tris and bis picolinate complexes. [a]corresponds to second molecule in the unit cell.

Ru^{III}(pic)$_3$		Ru^{IV}(pic)$_2$Cl$_2$	
Ru-N$_1$	2.057(2)	Ru-N$_1$	2.044(2)
Ru-N$_2$	2.063(2)	Ru-N$_2$[a]	2.052(2)[a]
Ru-N$_3$	2.060(2)		
Ru-O$_1$	2.0015(18)	Ru-O$_1$	2.0237(18)
Ru-O$_3$	2.0251(18)	Ru-O$_3$[a]	2.0361(19)[a]
Ru-O$_5$	2.0047(18)		

Comparison of the UV spectra of the two products showed that the dichloride species had a stronger absorption profile in both the visible and UV range (Figure 2.8).
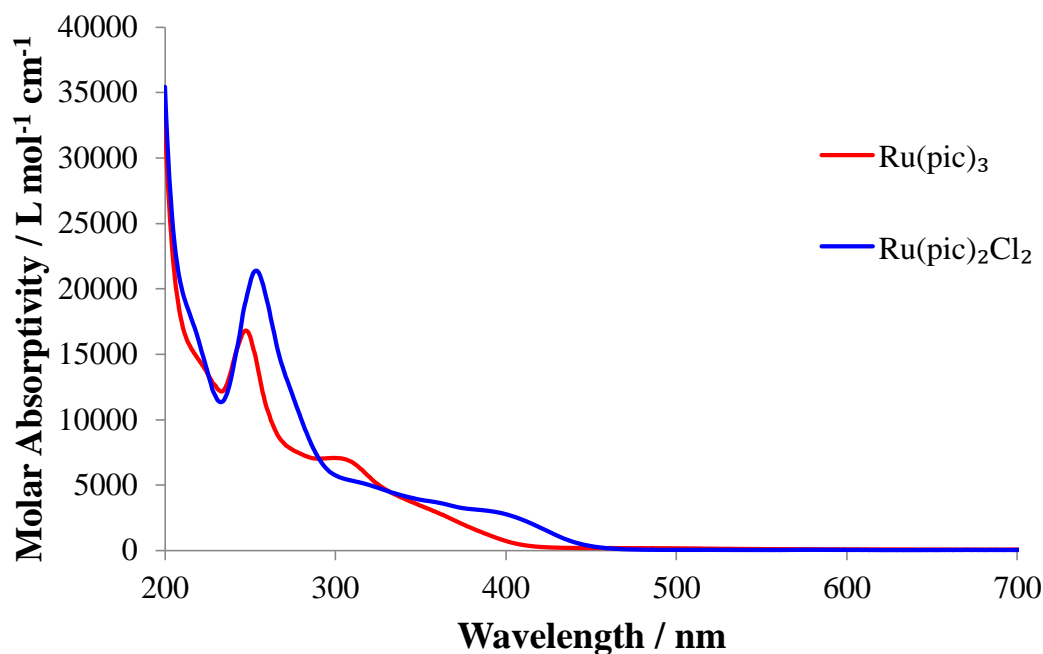
Figure 2.8 Absorbance spectrum of unsubstituted ruthenium tris and bis picolinate complexes.

The structure of the bis species has two additional advantages, the first being that there is less steric bulk around the 6 position on the pyridyl ring, allowing for increased accessibility to the complex of that dipicolinic isomer. The second advantage is that as the pyridyl rings now lie in plane with each other across the ruthenium centre allowing electronic effects to be more uniform due to delocalisation across both rings. Delocalisation of this type is observed in multiple species, such as dithiolenes, where ligands exhibiting π-delocalisation coordinate in a planar configuration across a metal centre.

Bis dipicolinates

The four complexes which would be tested were synthesised in the same manner as the bis picolinate. Two equivalents of the dipicolinic acid isomer were refluxed with one equivalent of ruthenium trichloride in ethanol (Scheme 2.2). As with the bis picolinic complex the solutions turned orange/red and yielded the Ru^{IV} complex of each of the dipicolinic acid isomers. The anchoring groups in all four complexes esterified in the reaction were most likely catalysed by hydrochloric acid generated by the complex formation. This is actually advantageous as it reduces the effect of the free protic anchor on the behaviour of the complex and more closely reflects the behaviour of the deposited dye.
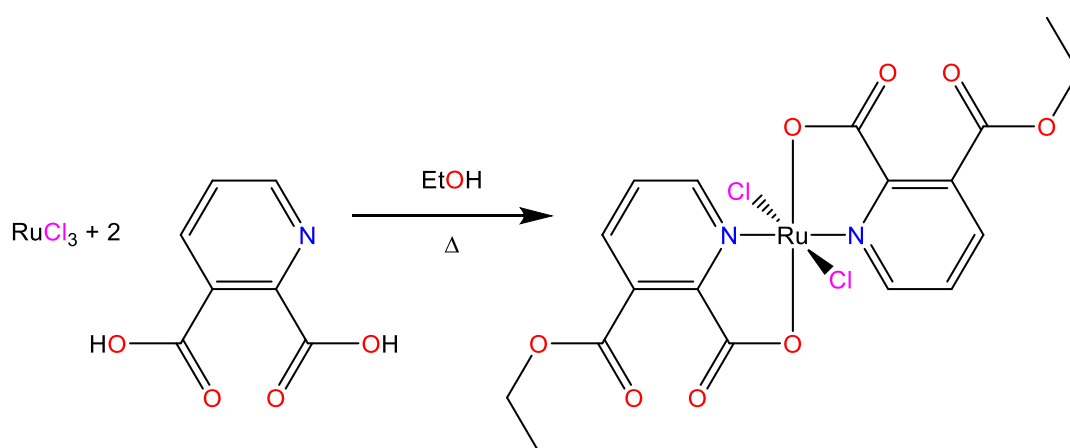
Scheme 2.2 Reaction scheme for the formation of the bis dipicolinic acid complex derived from ruthenium trichloride and 2,3 – dipicolinic acid in ethanol.

Characterisation of the complexes was carried out using single crystal X-ray crystallography, elemental microanalysis, FTIR and UV-Vis spectroscopy. The X-ray structures revealed that the complexes formed from the 2,3, 2,5 and 2,6 dipicolinic acid displayed chloride coordination to the ruthenium in a trans-axial geometry (see figs 2.9, 2.11 and 2.12). In contrast the complex derived from the 2,4 structural isomer displayed the chlorides in a cis coordination (Figure 2.10). As this is the solid state crystal structure it should be noted that solution phase structure may be different, as molecular rearrangements of ruthenium structures depending on solvent, temperature and exposure to light are not unknown e.g. $RuCl_2(dmso)_4$ and trans-[Ru(2,2′:6′,2″-terpyridine)(2-(2-pyridyl)-1,8-naphthyridine)OH$_2$]$^{2+}$.[11-12] In order to determine if any

of the isomeric complexes possess cis configurations and how stable they are compared to the trans configuration computational analysis is needed (*vide infra*).
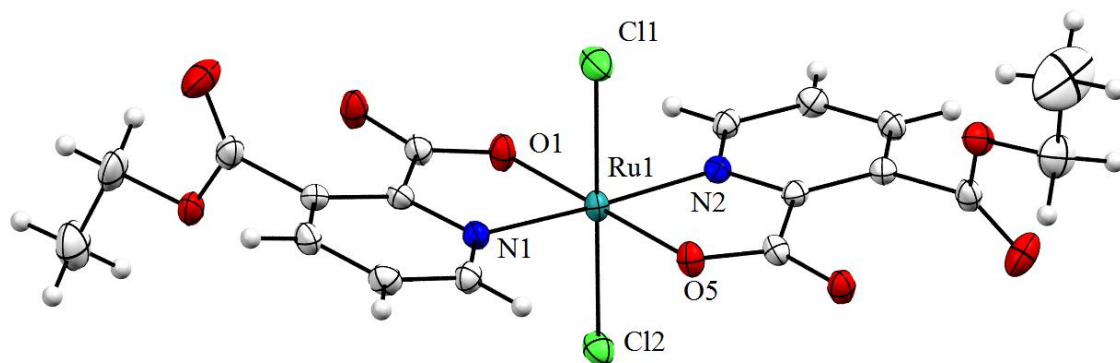
Figure 2.9 X-ray structure of dichlorobis(3-ethoxycarbonyl(pyridine-2-carboxylate)) ruthenium (IV). Ellipsoids shown at 50% probability.
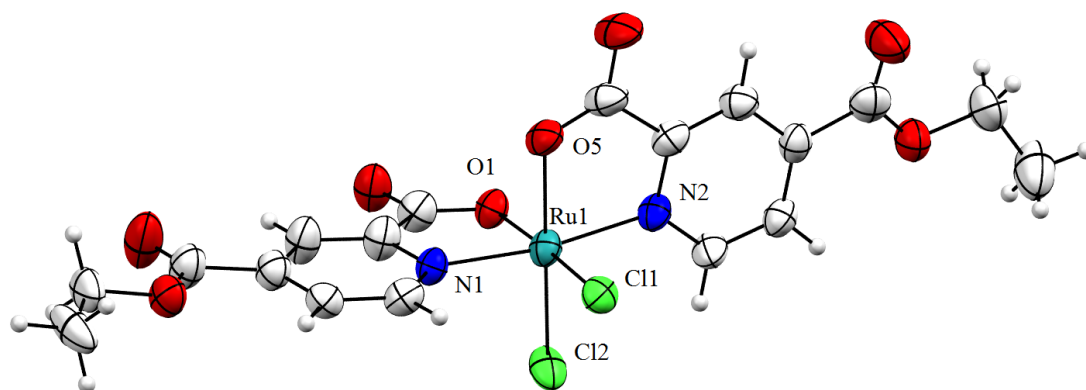
Figure 2.10 X-ray structure of dichlorobis(4-ethoxycarbonyl(pyridine-2-carboxylate)) ruthenium (IV). Ellipsoids shown at 50% probability.
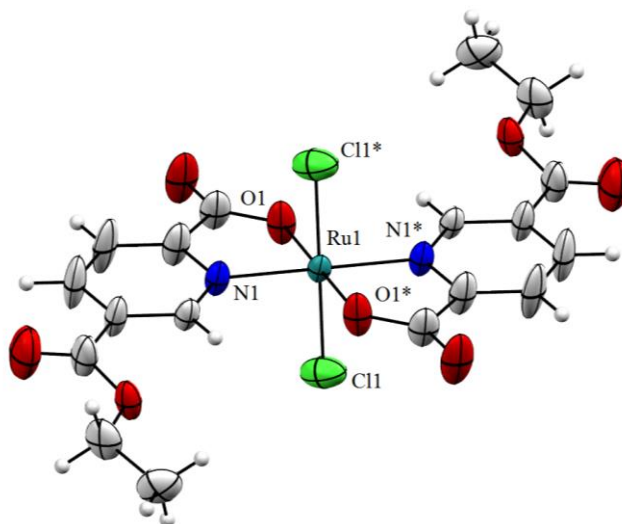
Figure 2.11 X-ray structure of dichlorobis(5-ethoxycarbonyl(pyridine-2-carboxylate)) ruthenium (IV). Ellipsoids shown at 50% probability. Symmetry operators to generate equivalent atoms: (*) -x-2, -y-1, -z-2 .
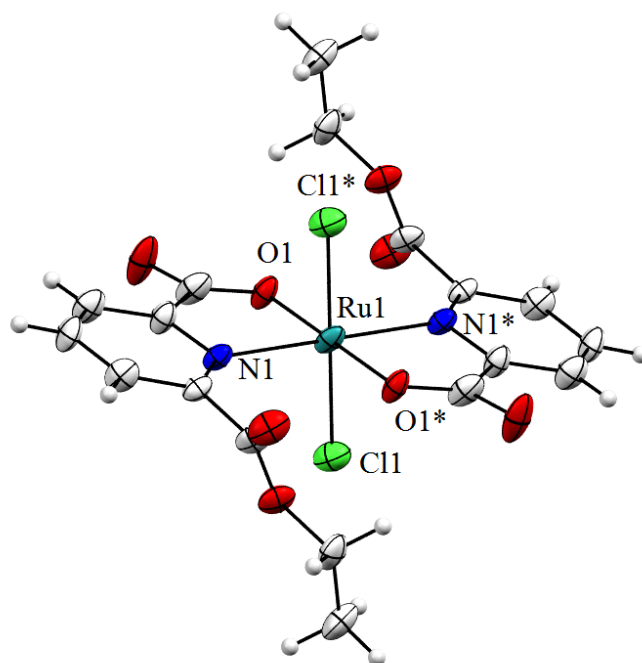
Figure 2.12 X-ray structure of dichlorobis(6-ethoxycarbonyl(pyridine-2-carboxylate)) ruthenium (IV). Ellipsoids shown at 50% probability. Symmetry operators to generate equivalent atoms: (*) **-x+2, -y, -z+2** .

The crystallisation of the 2,4 isomer in the cis configuration raises the question of the possible different configurations of the complexes and indeed it is likely that they exist as a mixture to some degree but for now that will be treated as structurally pure complexes based upon their crystal structure.

As with the bis picolinate, all the structures display the pyridine rings trans to each other due to the steric bulk of the ring. The acid groups also coordinate in a trans fashion except in the complex formed from the 2,4 isomer. The length of the ruthenium nitrogen bond varies between the four complexes (Table 2.5) and must be viewed in terms of both the steric bulk of the ester and its electron withdrawing effect.

Table 2.5 Nitrogen-ruthenium bond lengths of substituted bis picolinate complexes. [a]corresponds to second molecule in the unit cell.

Atoms	2,3	2,4	2,5	2,6
Ru-N_1	2.045(2)	2.053(4)	2.052(4)	2.081(5)
Ru-N_2	2.047(2)	2.063(4)		2.072(4)[a]
Ru-N_3	2.0499(18)[a]			
Ru-N_4	2.0469(17)[a]			

The greatest variance in bond length within the coordination sphere of the four complexes is the ruthenium-nitrogen length with a variance of 0.036 Å compared to 0.0179 Å for oxygen and 0.0294 Å for the chlorides. The ruthenium-nitrogen and ruthenium-oxygen bond lengths of the 2,4 and 2,6 isomers were marginally longer, which is attributed to increased trans directing character for the 2,4 isomer and due to the increased steric bulk of the carboxylate group impinging on the coordination sphere in the 2,6 complex. In order to determine if it is the ester or the carboxylate which is contributing to the steric bulk the complex was synthesised in methanol rather than ethanol and subsequently crystallised (Figure 2.13).

Figure 2.13 X-ray structure of dichlorobis(6-methoxycarbonyl(pyridine-2-carboxylate)) ruthenium (IV). Ellipsoids shown at 50% probability. Symmetry operators to generate equivalent atoms: (*) -x+1/2, -y+1/2, -z .

What was shown was that the reduction in the size of the bound ester had little effect on the coordination sphere, the largest observed difference in bond lengths was less than 0.7%, and that any steric bulk was mainly being contributed from the anchoring carboxyl group itself. Indeed, it is shown that the anchoring carboxyl rotates out of the plane of the pyridyl ring (85-125°) to minimise the steric bulk of the anchoring carboxyl on the coordination sphere of the ruthenium. This is also observed in the 2,3 complex but with the anchoring group twisting (75-100°) to reduce the steric bulk on the metal coordinated carboxylate (Figures 2.9 and 2.12). The result of this is that the 2,4 and 2,5 complexes are the only species to have their anchoring position remaining in the pyridyl plane and therefore to have electron delocalisation into the anchor. Of the four substituted complexes the 2,6 species is the only one whose anchoring carboxyl group is in a position which allows for it to interact with the ruthenium

coordination sphere. Other groups have synthesised complexes which display coordination with both carboxyl groups and can form either mononuclear or dinuclear species.[13] Previously reported species do not possess the esterified carboxyl group as the complexes discussed here. The unesterified carboxyl is attributed to the addition of a base in the preparatory methods described by those groups (Figure 2.14).
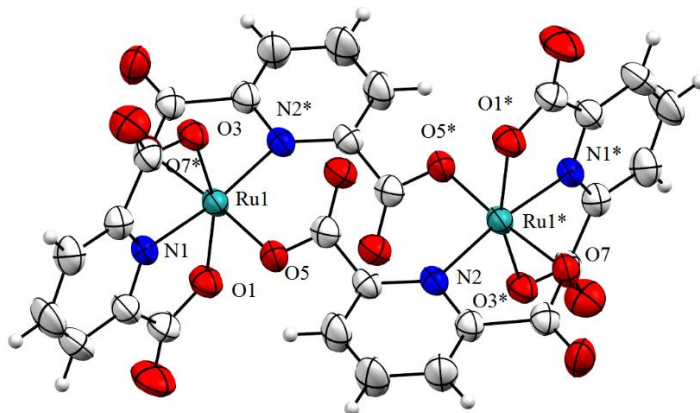
Figure 2.14 X-ray structure of dinuclear ruthenium dipicolinate complex $[(Ru^{III}(\kappa^3$-(pyridine-2,6-dicarboxylate)(μ_2-κ^1,κ^2-(pyridine-2,6-dicarboxylate)))_2]^{2-}$. Ellipsoids shown at 50% probability. $[Et3NH]^{2+}$ counter cations omitted for clarity. Symmetry operators to generate equivalent atoms: (*) -x, 1-y, -z .

The bite angle between the nitrogen and oxygen donors on the picolinic acid to the ruthenium centre is relatively unchanged between the systems formed from the different isomers (Table 2.7). Small increases in the angle were observed in the 2,4 system which was attributed to a decrease in steric repulsion on the donor oxygen when in the cis rather than in the trans coordination. This change is observed in the angle between the two coordinated oxygens and chlorides, with the angle between the oxygens being 4.27° smaller than the angle between the chlorides.

It can be seen that the substitution pattern of the anchoring group around an aromatic ring does alter the coordination of pyridine based ligands to ruthenium but in these complexes the variance is within 2%, possibly due to the dominating effect of the high positive charge on the metal centre. However, the substitution position does have an effect on the torsion of the anchor in relation to the pyridyl ring. While some of the changes can be explained by steric effects, it is concluded that the movement also alters the electronic properties of the delocalised orbitals within the ring and therefore its ability to donate to the ruthenium centre. The altering of the delocalised orbitals is of particular interest as it will alter the ligand's ability to transfer electron density from the metal centre to the substrate.

Table 2.6 Bond lengths of ruthenium picolinate complexes. [a]corresponds to second molecule in the unit cell.

Atoms	No anchor	2,3	2,4	2,5	2,6	2,6 Methyl
Ru-N_1	2.044(2)	2.045(2)	2.053(4)	2.052(4)	2.081(5)	2.079(5)
Ru-N_2	2.052(2)[a]	2.047(2)	2.063(4)		2.072(4)[a]	
Ru-N_3		2.0499(18)[a]				
Ru-N_4		2.0469(17)[a]				
Ru-O_1	2.0237(18)	2.041(2)	2.051(14)	2.033(4)	2.049(4)	2.043(4)
Ru-O_3	2.0361(19)[a]					
Ru-O_5		2.042(2)	2.041(4)		2.043(3)[a]	
Ru-O_9		2.0344(16)[a]				
Ru-O_{13}		2.0331(15)[a]				
Ru-Cl_1	2.3430(12)	2.3099(8)	2.3167(14)	2.305(2)	2.3196(15)	2.3344(17)
Ru-Cl_2	2.3449(10)[a]	2.3084(8)	2.3184(15)		2.3234(17)[a]	
Ru-Cl_3		2.3282(9)[a]				
Ru-Cl_4		2.3340(9)[a]				

Table 2.7 Bite angles of ruthenium picolinate complexes. [a]corresponds to second molecule in the unit cell.

Atoms	No anchor	2,3	2,4	2,5	2,6	2,6 Methyl
N_1-Ru-O_1	80.08(8)	79.77(9)	81.9(6)	79.76(17)	79.88(16)	79.28(19)
N_2-Ru-O_3	80.10(8)					
N_2-Ru-O_5		79.74(8)	80.64(16)		79.17(14)[a]	
N_3-Ru-O_9		79.64(7)[a]				
N_4-Ru-O_{13}		79.88(7)[a]				

Spectroscopy

UV/Vis spectroscopy of the complexes in solution show that they all broadly resemble that of the bis picolinate complex, as can be seen from the colour of the respective solutions (Figure 2.15).

Figure 2.15 1mM solutions of mononuclear ruthenium picolinic acid complexes Left to right: trispicolinate, bispicolinate, (2,3) , (2,4) , (2,5) , (2,6).

That being said, certain bands do vary depending on the anchoring position. The 2,5 has a markedly higher molar absorptivity of 23420 L mol^{-1} cm^{-1} in the UVC band. In contrast the 2,4 has a higher absorbance across the UVA band and into the visible region (Figure 2.16), which indicates it might be the superior substrate sensitiser for visible light. The 2,3 absorbs comparatively poorly in all regions. The spectrum for the 2,6 mirrors the 2,4 for wavelengths below 300 nm and mirrors the 2,3 for wavelengths above 300 nm. The spectrum indicates that to improve the catalytic performance of a water oxidation catalyst based on titanium dioxide that the 2,4 system would be most likely to improve the performance by extending light harvesting further into the visible region. In contrast, despite the stronger ruthenium picolinic acid coordination, the complex formed from the 2,5 isomer would only harvest in the higher energy UV range. Compared to other available dyes the absorbance profiles are relatively poor in both range and molar absorptivity. Compared to ruthenium tris bipyridine it has a significantly lower absoption in the UV range but as titanium dioxide is an excellent light harvester in UV range already (Figure 1.27) the benefit of modifying the substrate with an additional UV absorber is minimal.

In the visible range the absorption is restricted to the high energy region above 500 nm, as is the case for most ruthenium pyridyl complexes. There is sufficient absorbance in the region 400-500 nm to move forward with dye sensitisation of titanium oxide (*vide infra*) espescially since we are interested in the effect of the anchor rather than trying to create a high performance dye.
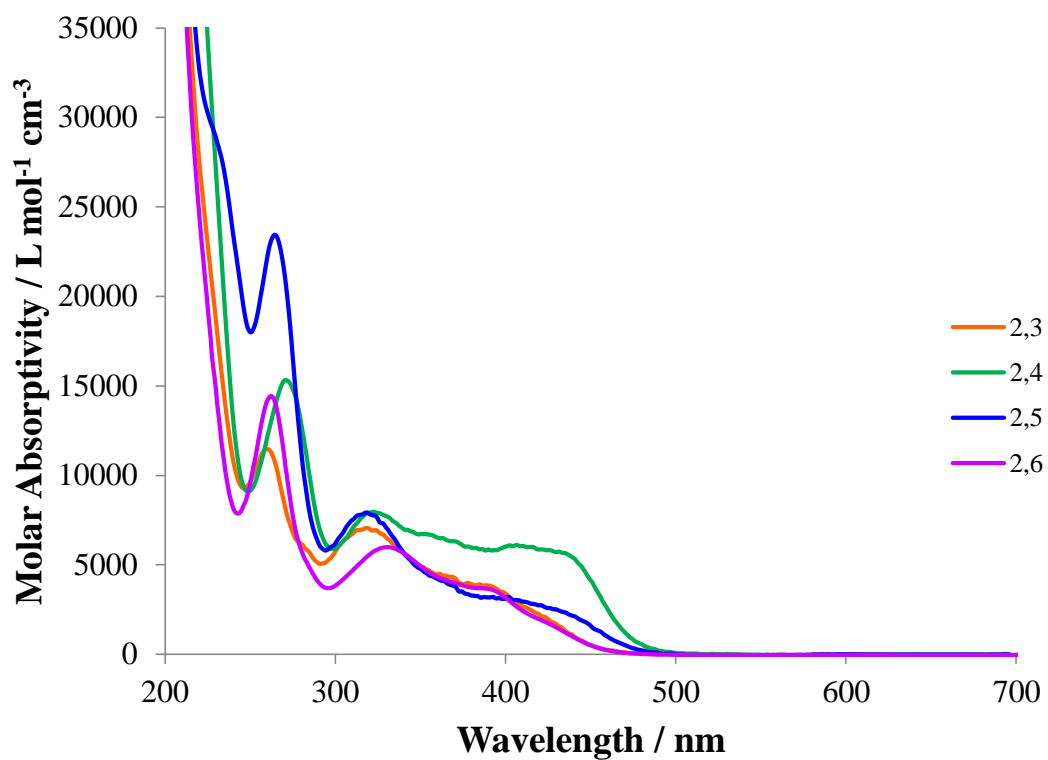
Figure 2.16 Aqueous UV/Vis absorption spectrum of ruthenium dipicolinic acid complexes.

Electrochemistry

Cyclic voltammetry was used to determine how the redox couples for the complexes behaved depending on the position of the anchoring group. The complexes were prepared at a concentration of 1 mM in a solution of 0.1 M tetrabutylammonium tetrafluoroborate (tBu_4NBF_4) in dry acetonitrile. The voltammograms were referenced using a ferrocene/ferrocenium standard before and after the measurements to account for any voltage drift - of which none was observed. The reference electrode was Ag/Ag^+ but for convenience all data has been converted to reference the normal hydrogen electrode (NHE).
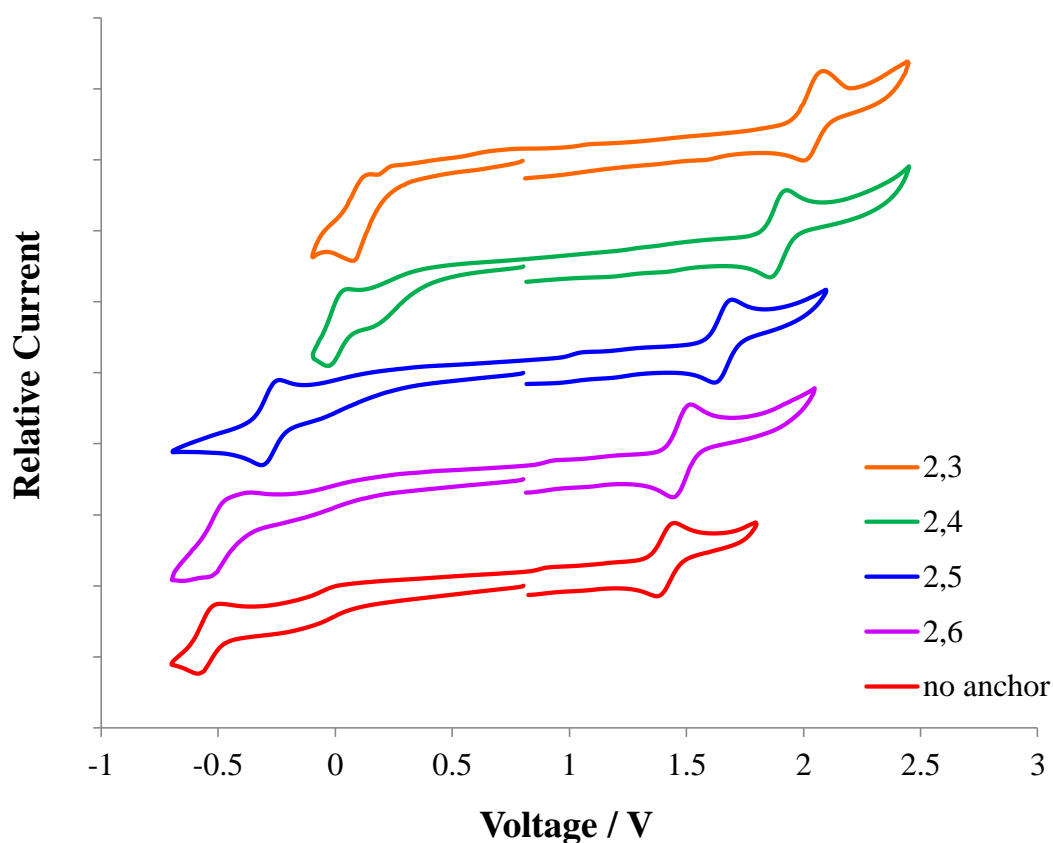
Figure 2.17 Cyclic voltammograms of ruthenium dichlorobispicolinate complexes in acetonitrile vs NHE.

Compared to the spectral data, the electrochemical data shows a much more marked trend as a function of anchor position (Figure 2.17). The four substituted complexes were compared using the bis picolinate as a control. As was expected the addition of an electron withdrawing anchor on the ring served to raise the potential of the primary couple, which in this case was the Ru^{III}/Ru^{IV} couple. The potential of the 2,6 substituted species was only 36 mV higher than that of the unsubstituted species but the potential rises as the anchoring position moves around the ring to its highest value

of 684 mV above the unsubstituted species (Table 2.8). This is an immediate validation of the concept that anchoring group position can have a profound effect on the behaviour of this class of complexes.

Table 2.8 Half wave potentials for III/IV couples in acetonitrile vs NHE.

Isomer	$E_{1/2}$ (mV)
No Anchor	1456
2,6	1492
2,5	1663
2,4	1979
2,3	2140

Comparing the potentials to that required for the oxidation of water show that all of the complexes have the potential to oxidise water, making them suitable for catalytic testing as part of a heterogeneous system (Figure 2.18).

$$H_2O \rightarrow \frac{1}{2}O_2 + 2H^+ + 2e^-$$
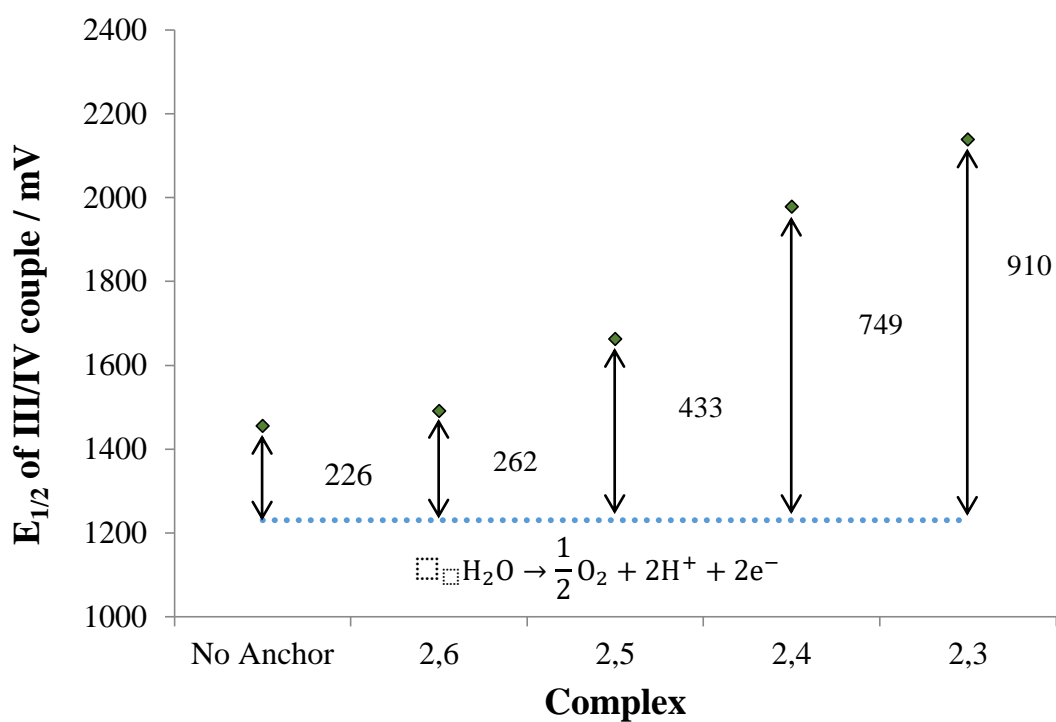
Figure 2.18 Comparison of half wave potentials for the III/IV couple of the ruthenium dichlorobispicolinate complexes and overpotential to the water oxidation reaction.

Closer examination of the potentials at different scan rates indicated that the redox couples were operating in both reductive and oxidative directions and that the oxidative and reductive mechanisms were proceeding using fast electron transfer rather than via any exchange or diffusion mechanism (Figure 2.19).
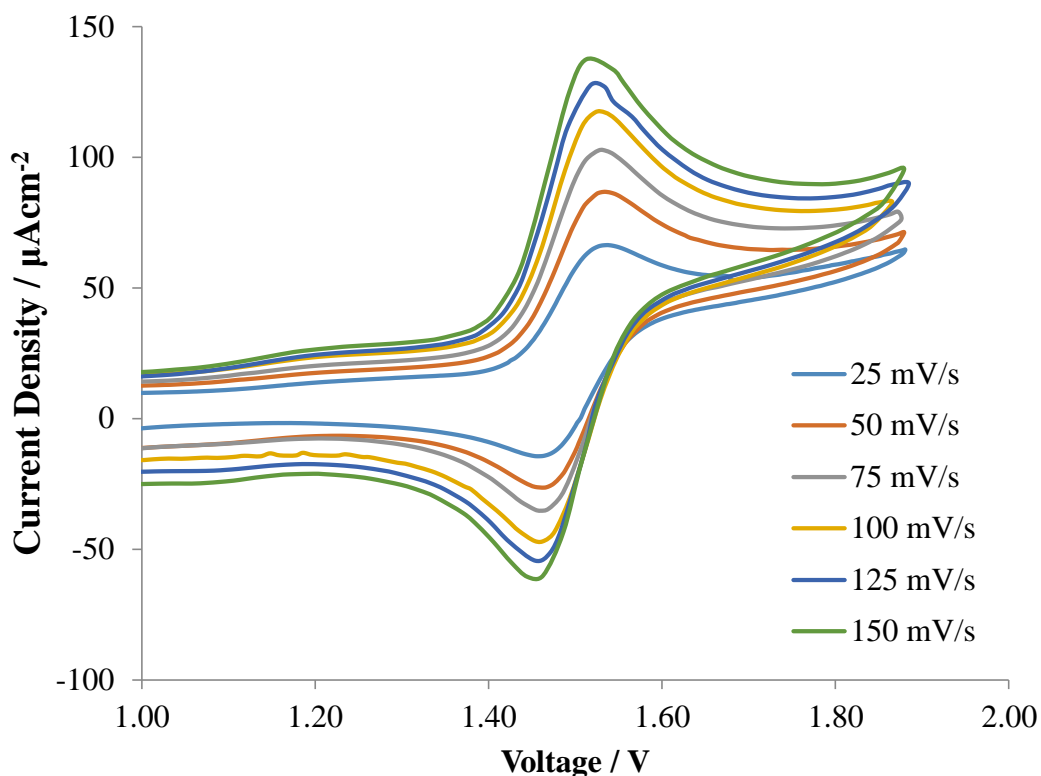
Figure 2.19 Cyclic voltammograms of III/IV couple of dichlorobis(6-methoxycarbonyl(pyridine-2-carboxylate)) ruthenium (IV) in acetonitrile vs NHE.

The less interesting redox couple is the II/III couple which appears outside the region which encompasses the reduction potential of water. However, as with the III/IV couple the potential varies with substitution pattern and follows the same trend as the III/IV couples (Table 2.9).

Isomer	$E_{1/2}$ (mV)
No Anchor	-538
2,6	-452
2,5	-273
2,4	16
2,3	131

While comparing the bis picolinate species it is prudent to examine the tris species. The data for the tris picolinate showed a similar II/III couple (169 mV) to that of the bis picolinate and the substituted complexes, but a significantly lower III/IV couple (755 mV) (Figure 2.20).
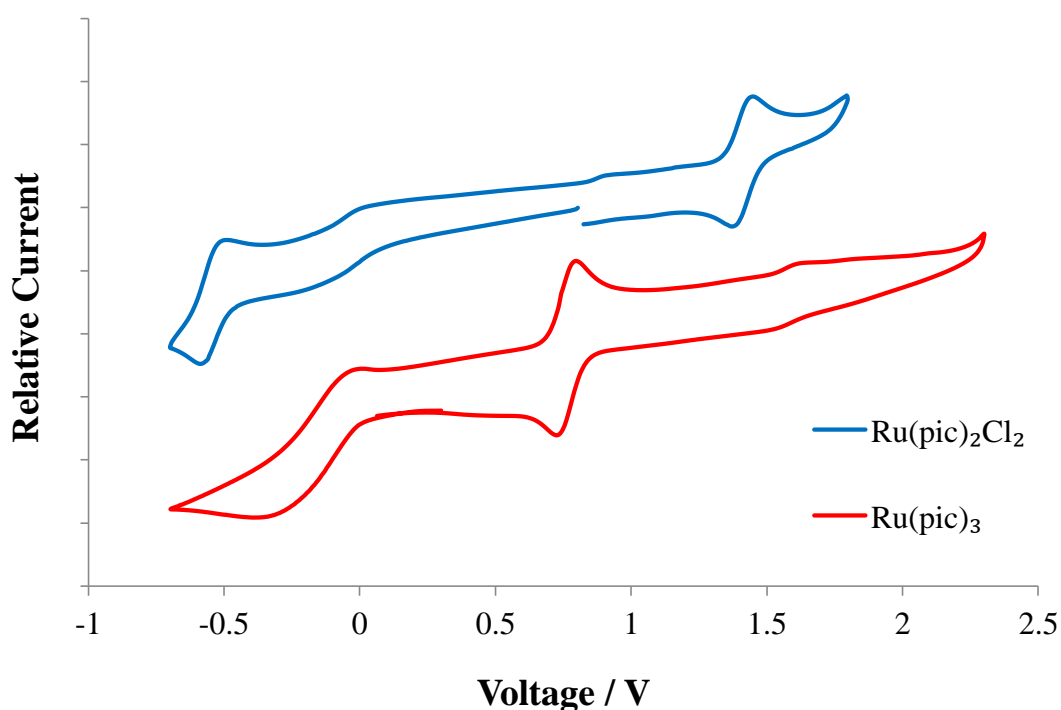
Figure 2.20 Cyclic voltammograms of unsubstituted ruthenium dichlorobispicolinate complexes in acetonitrile vs NHE.

The presence of the chlorides in the bis species does not appear to significantly influence the profile of the III/IV couple at different scan rates (Figure 2.21). However, the reduction in the voltage at which this couple appears in the tris picolinate makes this species unsuitable for water oxidation studies as its potential lies below that of the water oxidation reaction (1.23 V).
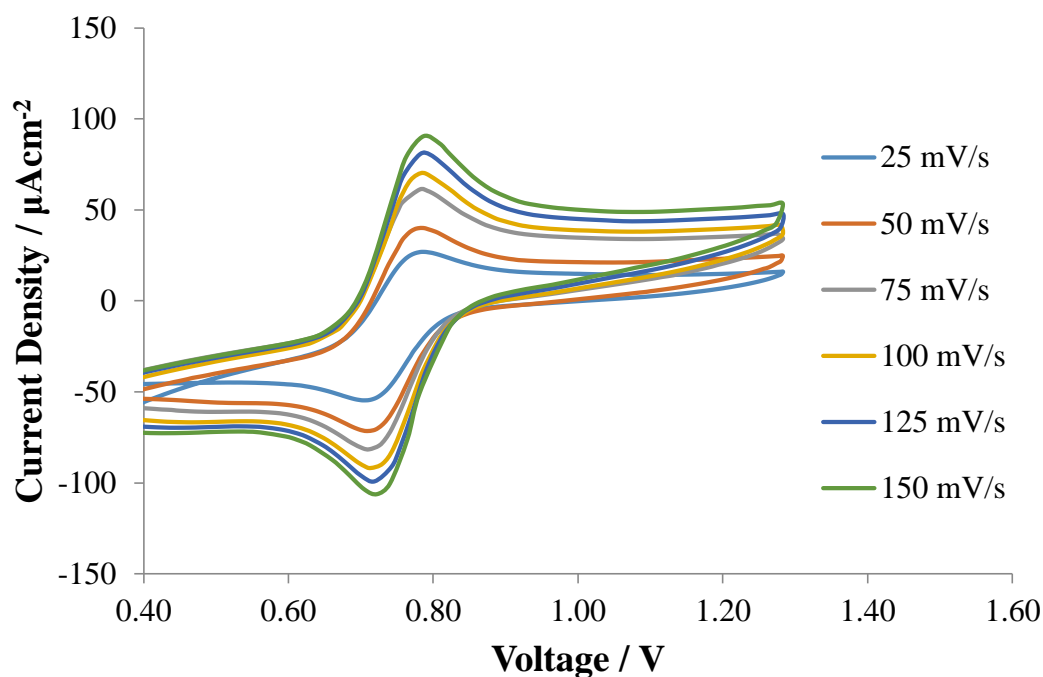
Figure 2.21 Cyclic voltammograms of III/IV couple of of tris(pyridine-2-carboxylate) ruthenium (III) in acetonitrile vs NHE.

Despite the bis complexes displaying a reversible potential for the III/IV couple in dry acetonitrile it was not possible to determine if these species behaved the same way in aqueous conditions as the voltage range required is greater than the solvent window for water - i.e. the solvent water would electrolyse before oxidising the complexes.

In order to determine if any structural changes occur in the complexes when under aqueous conditions they were recrystallised via the slow evaporation of aqueous solutions. What was found was that the complexes reduced from Ru^{IV} to Ru^{III}. Dissolution of these crystals back into aqueous solution gave the same UV-Vis spectrum as that of the Ru^{IV} crystals. This raises the question; what oxidation state are these complexes in aqueous solution?

Two of the complexes became anionic upon reduction, retaining their axial chlorides. In order to retain charge balance the compound scavenged counter cations from its surroundings. The 2,5 isomer crystallised using some trace 2,5 carboxyl picolinic acid diester to form a cationic pyridinium species (Figure 2.22).
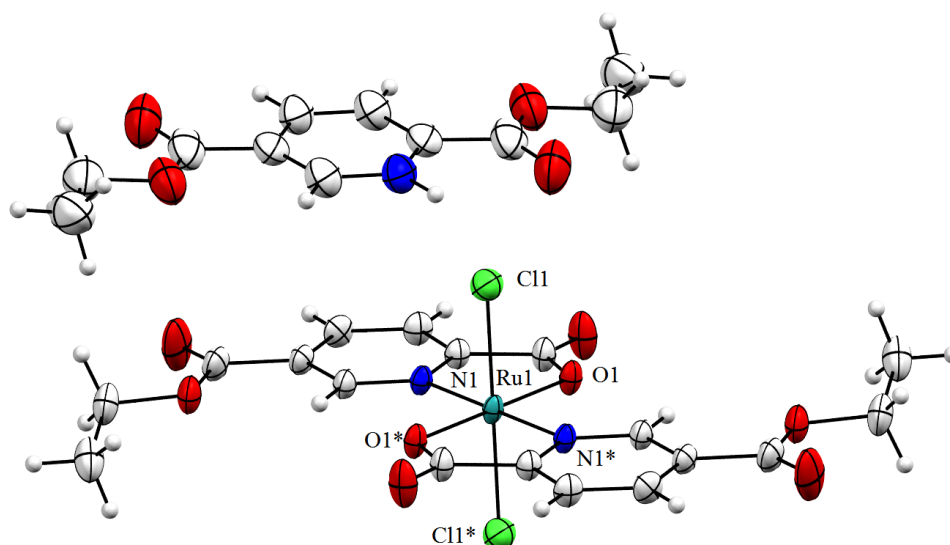
Figure 2.22 X-ray structure of dichlorobis(5-ethoxycarbonyl(pyridine-2-carboxylate)) ruthenium (III) anion and diethyl pyridinium-2,3-dicarboxylate cation. Ellipsoids shown at 50% probability. Symmetry operators to generate equivalent atoms: (*) -x+2, -y, -z+1 .

In the case of the 2,6 isomer, the complex oxidised metallic aluminium from the seal to the vessel to form the crystal (Figure 2.23). In this species the tricationic hexaaqua aluminium served to balance three anionic ruthenium complexes. This complex bears strong similarity to a non-esterified structure described in 1985, which consisted of the same anionic bis dipicolinic acid complex (although not esterified), balanced by a cationic ammonium species.[14]
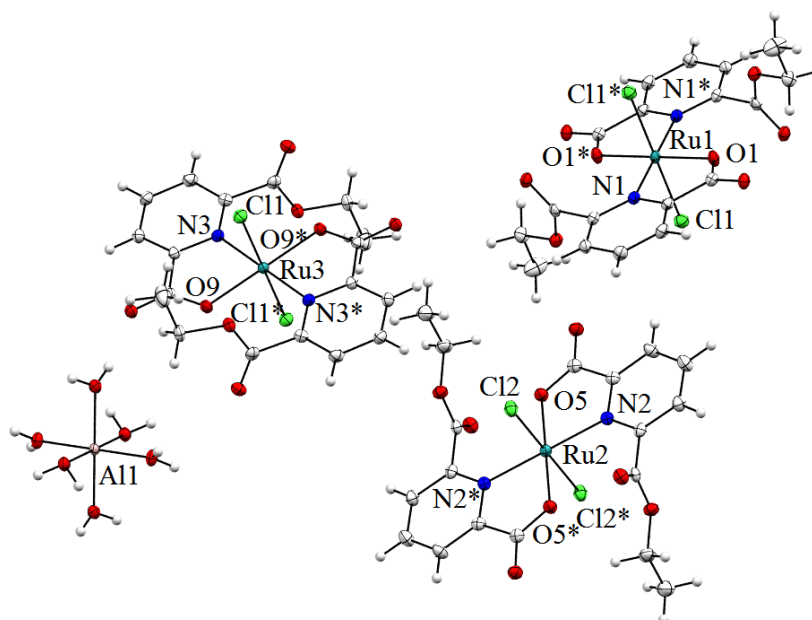
Figure 2.23 X-ray structure of dichlorobis(6-ethoxycarbonyl(pyridine-2-carboxylate)) ruthenium (III) anions and hexaaqua aluminium trication. Ellipsoids shown at 50% probability. Symmetry operators to generate equivalent atoms: (*) -x+2, -y, -z+2 .

If there was no counterion to be scavenged the complexes appeared to exchange a chloride with an aqua to maintain charge balance. The 2,5 isomer crystallised in this manner and displayed both chlorides on one of the complexes being replaced with two aqua groups (Figure 2.24). This is the only example out of the four complexes of both chlorides being exchanged. This molecule still contained ruthenium in a +3 oxidation state and as such the complex was a monocation. The new monocationic species served to balance the charge of the monoanionic complex.
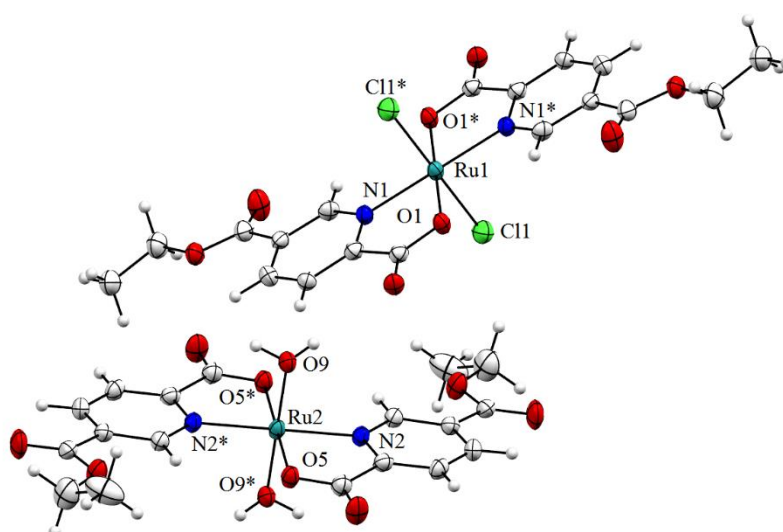
Figure 2.24 X-ray structure of dichlorobis(5-ethoxycarbonyl(pyridine-2-carboxylate)) ruthenium (III) anion and diaquabis(5-methoxycarbonyl(pyridine-2-carboxylate)) ruthenium (III) cation. Ellipsoids shown at 50% probability. Symmetry operators to generate equivalent atoms: (*) -x+2, -y, -z+2 .
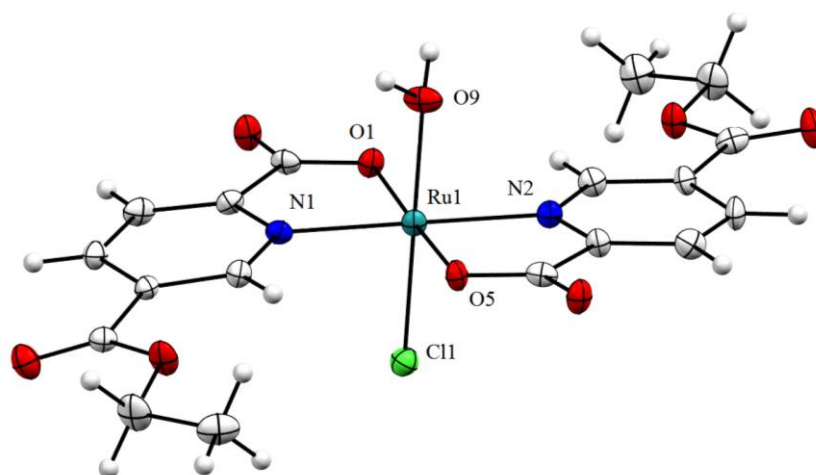
Figure 2.25 X-ray structure of chloraquabis(5-ethoxycarbonyl(pyridine-2-carboxylate)) ruthenium (III). Ellipsoids shown at 50% probability.

The last two examples of crystals of this type were of the 2,3 and the 2,5 isomers (Figures 2.25 and 2.26). In these two crystal structures only one of the chlorides on the ruthenium centre are replaced. These two complexes are charge neutral and resemble the mononuclear ruthenium water oxidation catalysts discussed in Chapter 1.
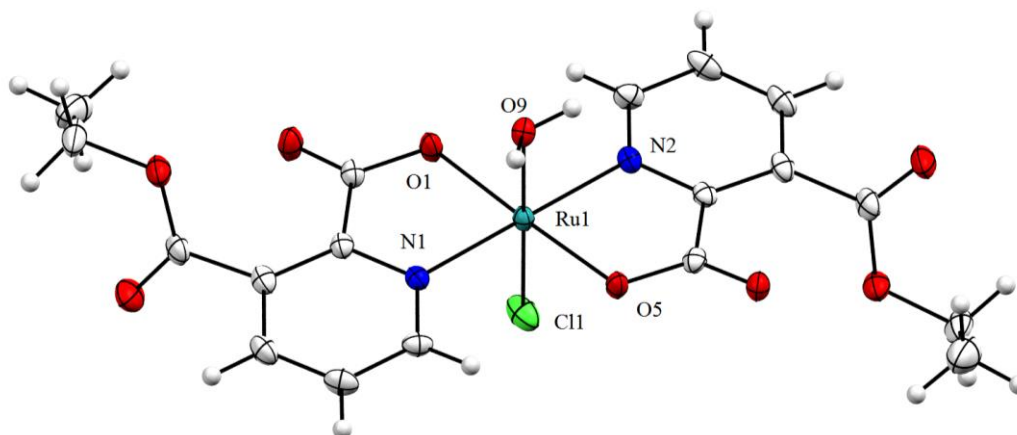
Figure 2.26 X-ray structure of dichlorobis(3-ethoxycarbonyl(pyridine-2-carboxylate)) ruthenium (III). Ellipsoids shown at 50% probability.

Comparison of the structures revealed that the ruthenium complexes in the +3 oxidation state exhibited a stronger coordination between the ruthenium centre and the picolinic acid in particular with the charge carrying acid group, as can be seen in Figure 2.27. This is in spite of the lower positive charge on the ruthenium centre.
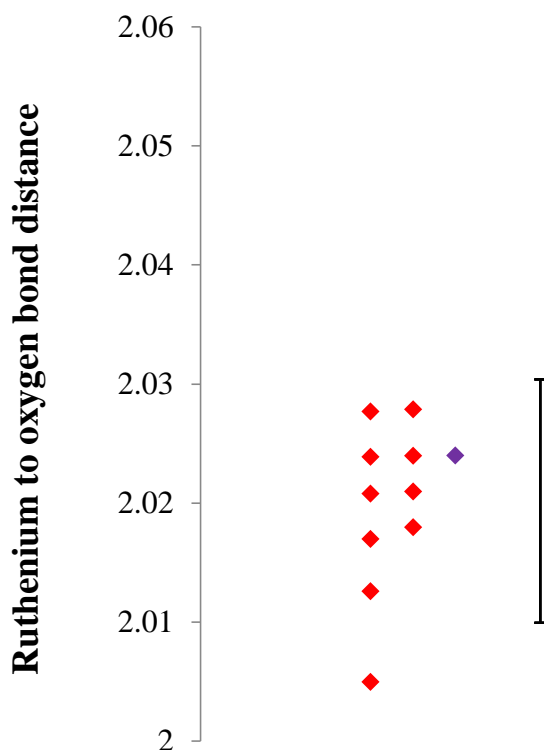
Figure 2.27 Comparison of ruthenium oxygen bond lengths between +3 (♦) and +4 (♦) oxidation states of substituted bispicolinate complexes. ♦ is previously reported structure from CDS. ▲ is the unsubstituted structure. Error bars are set to a standard deviation of 1.5 on substituted species only.

The X-ray structures indicate that under aqueous conditions in the presence of an available countercation the complexes will form anionic dichloride species but will otherwise exchange a chloride for an aqua group to either form a neutral species or two chlorides for two aqua groups, to form cations to the dichloride anion of its parent species (Scheme 2.3).

$$[Ru^{IV}(pic)_2Cl_2] \xrightleftharpoons[-e^-]{+e^-} [Ru^{III}(pic)_2Cl_2]^- \xrightarrow[-Cl^-]{+H_2O} [Ru^{III}(pic)_2(H_2O)Cl]$$
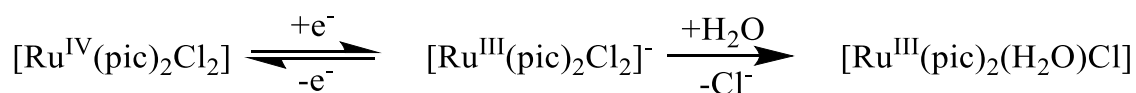
Scheme 2.3 Aqua exchange process.

In heterogeneous water oxidation the potential for an anchored ruthenium complex to coordinate water may be of benefit as a molecular water oxidation catalyst. If such a species were to function as a molecular water oxidation catalyst it would complicate any studies attempting to determine its performance as a sensitiser dye. Shifts in oxygen output may be attributed to enhanced, dye sensitised, heterogeneous water oxidation where the actual cause may be additional molecular water oxidation

combined with heterogeneous water oxidation. A possible solution to this complication can be found by approaching the problem via the probable testing conditions for the complexes. Based on the crystal data shown above, two considerations are taken. The complexes which exhibit the aqua exchange reaction do so to form a charge neutral species from an anionic species. The complexes which formed the stable anionic dichloride did so in the presence of a cationic species to balance the charge.

If the ionic strength of the test conditions is kept high and the pH low enough then the anionic species will be in the majority as the abundance of positively charged species will stabilise the anionic form. In addition, the substrate itself can act as a large counter ion consisting as it does of Ti^{IV} cations in an oxide lattice. As the complexes exhibited fast electron transfer between Ru^{III} and Ru^{IV} as demonstrated in their cyclic voltammograms, it is likely that such behaviour will be exhibited upon deposition onto the substrate meaning that the complex could inject electrons without a significant change in structure.

Catalytic testing

In order to ascertain the photocatalytic performance of the complexes we first needed a uniform catalytic substrate upon which to test. The complexes were tested after deposition onto a colloidal substrate. The substrate chosen was Aeroxide® P25, referred to as Degussa P25 in older literature. P25 consists of a composite blend of anatase and rutile (~3:1), which is popular as a photocatalytic substrate. The colloidal P25 was deposited with iridium oxide nanoparticles to act as a heterogeneous water oxidation catalyst. The nanoparticles were prepared via modification of a literature procedure before being deposited onto the surface of the P25 colloid.[15]
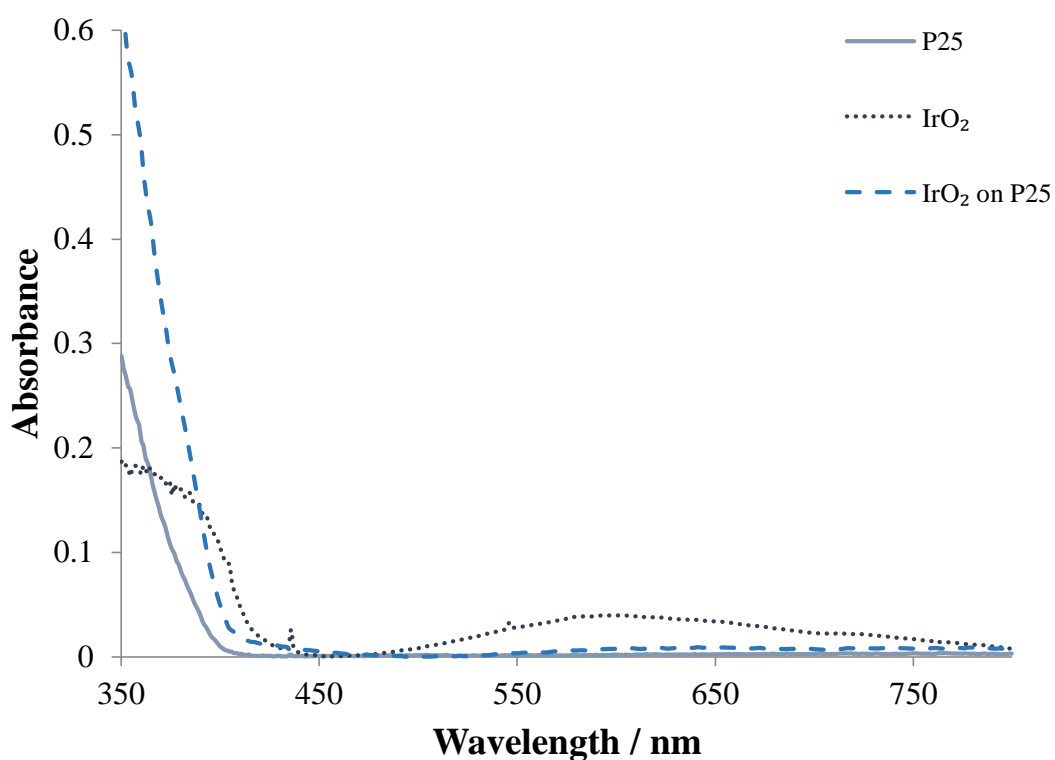
Figure 2.28 Solid UV/Vis reflectance spectrum of modified and unmodified substrates.

The nanoparticles exhibited a deep blue colour, as reported in literature, with the characteristic absorbance band at 580nm in the solid phase reflectance UV-Vis spectrum (Figures 2.28 and 2.29). The modified substrate displayed a blue/grey tint compared to the unmodified P25, as a result of the blue iridium oxide nanoparticles; but the band at 580nm was suppressed, indicating that colour was from deposited iridium oxide rather than intermixed free nanoparticles. The extinction coefficient in the UV region of the P25 substrate is increased upon deposition of the nanoparticles.

The substrate was not calcined to thermally decompose the iridium hydroxide as other heterogeneous catalysts would be, as it has been shown that for water oxidation catalysts a loss of hydration can reduce the activity of the catalyst via sintering.[16]
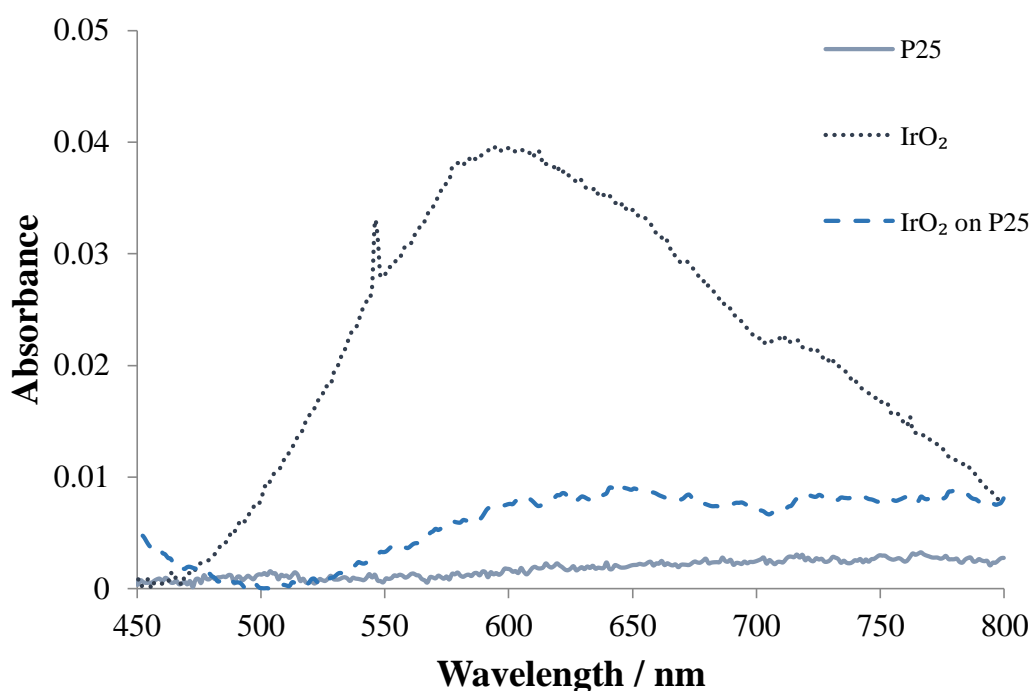
Figure 2.29 Solid UV/Vis reflectance spectrum of modified and unmodified substrates.

Catalytic testing was performed in a colloidal system, with a continuous phase of one molar perchloric acid, under irradiation by combination UV and visible light. Perchloric acid was used as it provided the acidic environment required to both stabilise the picolinic acid complexes and for the use of the cerium (IV) sacrificial oxidant, without the addition of coordinating anions. The test solution/suspension was injected with 0.1 M degassed cerium sulfate solution to act as sacrificial electron acceptor. This is required, as the test system is a colloid rather than a solid state electrode to which a stable circuit can form. A colloidal system is used as it allows for a uniform substrate which can be tested and then disposed of. As each dye must be deposited onto virgin substrate, grown electrodes are unsuitable since they vary in surface morphology and therefore cannot be considered a uniform testing environment. The sacrificial electron acceptor therefore acts to short circuit the reaction allowing for controlled test conditions and a much more stable testing environment.
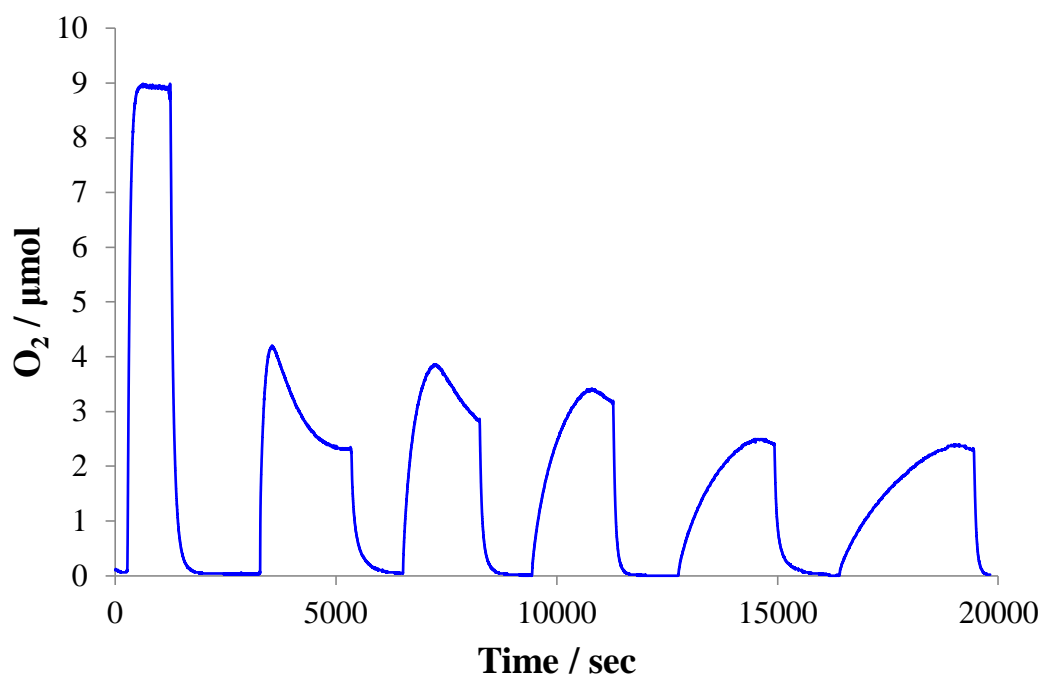
Figure 2.30 Catalytic oxygen evolution response plot, trace at far left is calibration response.

In order to compare the performance of the substituted ruthenium picolinate complexes three controls were used. The first was of a cerium sulfate injection without light or substrate to determine the background oxidation of the testing system under test conditions. The second was of the treated substrate without light but with cerium injection to determine the catalytic potential of the substrate; and the third was of the substrate with both cerium injection and light to determine the light harvesting ability of the substrate itself.

Multiple injections were performed for each test condition. Upon injection of the sacrificial electron acceptor $Ce^{IV}(SO_2)_2$ an immediate increase in the oxygen concentration within the solution was observed. The production of oxygen continued until a maximum after which the concentration of oxygen in the solution dropped, this has been attributed to the equilibration of the oxygen in the solution with the oxygen free headspace in the test chamber. After the colloid had been sparged and the headspace flushed with nitrogen, a second injection of the sacrificial electron acceptor produced a similar increase in the oxygen concentration to the first. The response time after the second injection is greater than that of the first injection and the maximum concentration of oxygen in the solution after the second injection was less than that of the first (Figure 2.30). Upon subsequent injections of the sacrificial electron acceptor

104

it was noted that there was a decrease in both the rate of oxygen production and the maximum oxygen produced (Figure 2.30). This was observed for all test conditions and is ascribed to the increasing concentration of cerium +3 species in solution.
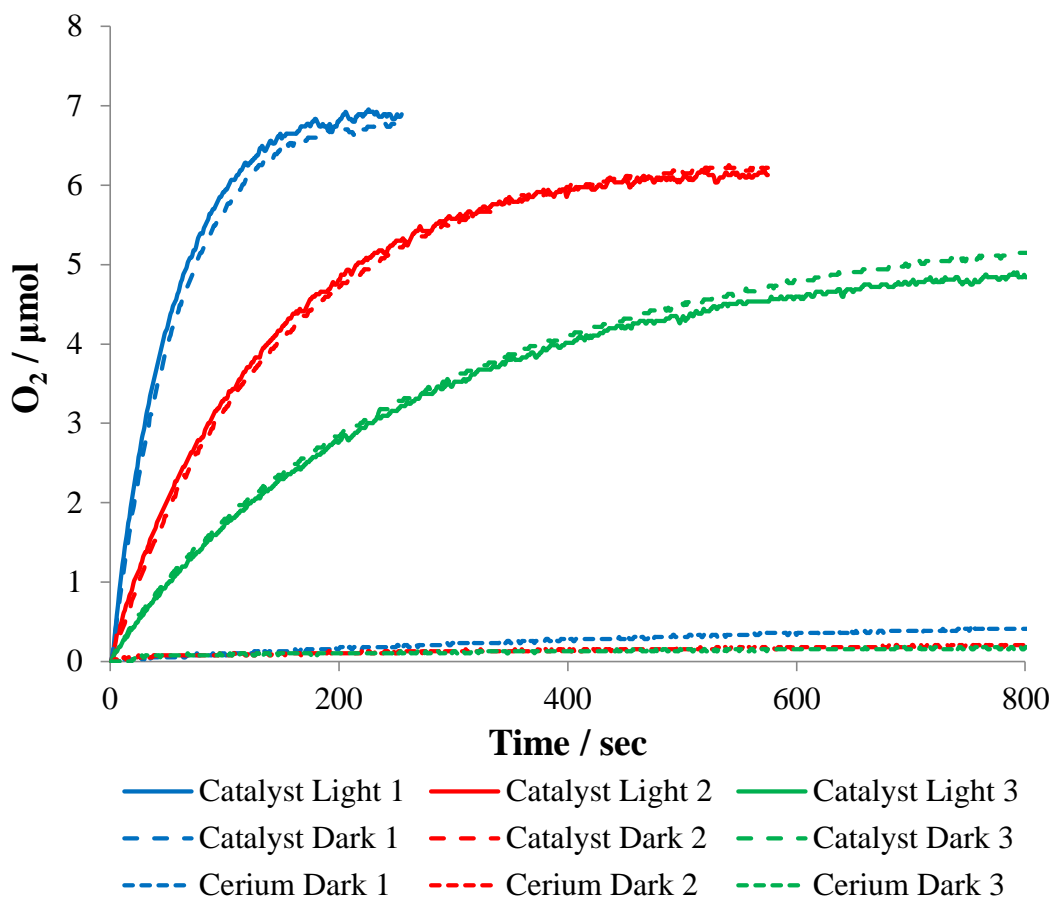
Figure 2.31 Catalytic oxygen evolution response plot for controls.

The cerium test proved to have little effect on oxygen evolution with a response time for the initial cerium injection of over 30 minutes. Comparatively the control using the catalytic substrate in the dark reached its maximum in less than a tenth of that time. The catalytic substrate also demonstrated a maximum amount of oxygen evolved being twelve times greater than that of cerium alone (Figure 2.31). The variance between the performance of the catalytic substrate in both light and dark conditions is attributed to photoexcitation. The effect is minimal in this system as the intensity of UV light is low compared to the intensity of visible light and as the substrate has minimal absorbance in the visible region.
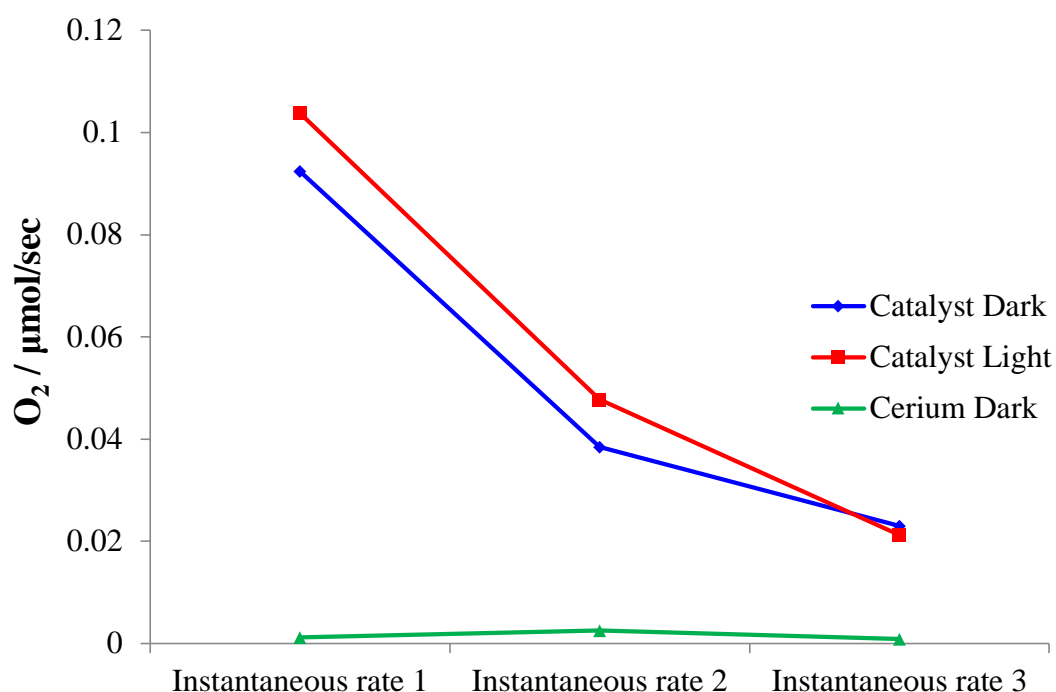
Figure 2.32 Comparison of the instantaneous rates of oxygen evolution over the first 25 seconds following each Ce[IV] injection for the control test conditions.

As the testing conditions measure the oxygen concentration in the solution it is the instantaneous rates which give the best indication of performance as it does not compete with gas diffusion/solubility. For the two catalytic substrate test conditions, the rate for the second injection was between fifty and sixty percent of the response rates observed for the first cerium injection (Figure 2.32 and Table 2.10).

Table 2.10 Instantaneous rate of oxygen evolution over the first 25 seconds following each Ce[IV] injection.

	Instantaneous rate 1 µmol/sec	Instantaneous rate 2 µmol/sec	Instantaneous rate 3 µmol/sec
Catalyst + Light	0.1038	0.0477	0.0212
Catalyst – Light	0.0924	0.0385	0.0230
Cerium – Light	0.0012	0.0026	0.0009

The four substituted picolinic acid complexes were deposited on the substrate by stirring a known quantity of substrate in an ethanolic solution of the individual substituted ruthenium complex at 40°C for 16 hours. Filtration of the modified substrates and subsequent washing with ethanol yielded the substrates free of the undeposited ruthenium complexes.

Reflectance spectra of the substrates after dye modification indicated that all the dyes had successfully adhered to the substrate with the bands of the ruthenium complexes being clearly visible and in good agreement with their solution absorbance ratios (Figure 2.33).
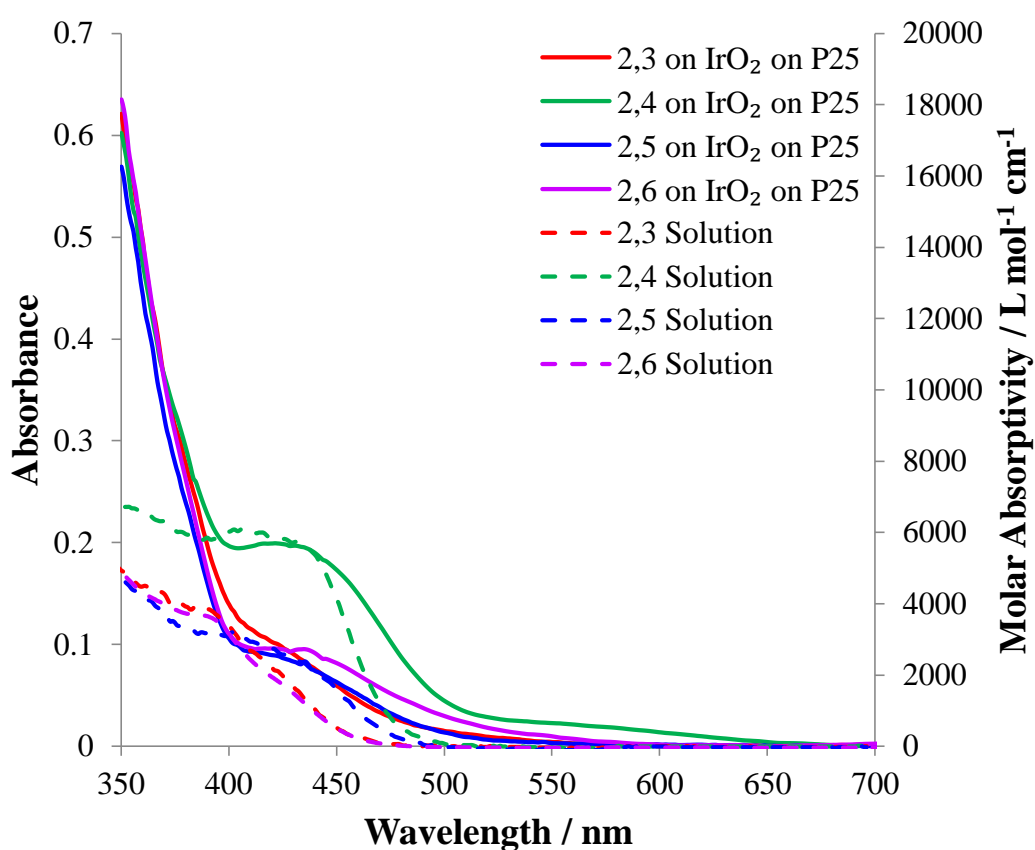
Figure 2.33 Solid reflectance and solution UV/Vis spectra of ruthenium dyes and dye modified catalytic substrates.

The performance of the dyes after the first injection varied according to their substitution pattern with all performing better than the untreated substrate. The catalytic substrate, modified with the ruthenium complex formed from the 2,4 isomer of dipicolinic acid, demonstrated the highest activity, as might be expected given the combination of its higher absorbance in the visible region and the greater potential of its primary redox couple. The second cerium injection displayed this comparatively higher activity for the 2,4 system but what was more intriguing was the reduction in variance between the other dye modified substrates and between those substrates and the unmodified substrate. The third cerium injection continued to follow this trend with the performance of the dyes being indistinguishable from that of the unmodified substrate, the exception being the 2,4 system which still displayed higher performance (Figure 2.34).

The proposed reason for this reduction in performance is that the dyes are being deactivated after electron injection is taking place. The reasons for this are that if the complexes were decomposing they would form ruthenium dioxide on the substrate, which would increase the activity above that of the unmodified substrate. Equally the complexes cannot be poisoning the substrate as the performance would drop below that of the unmodified substrate. This leaves two proposed routes to the performance reduction: the complexes are detaching from the surface which would be tied to how the electron injection is taking place; or the complexes are deactivating, possibly due to the aqua exchange process discussed above.
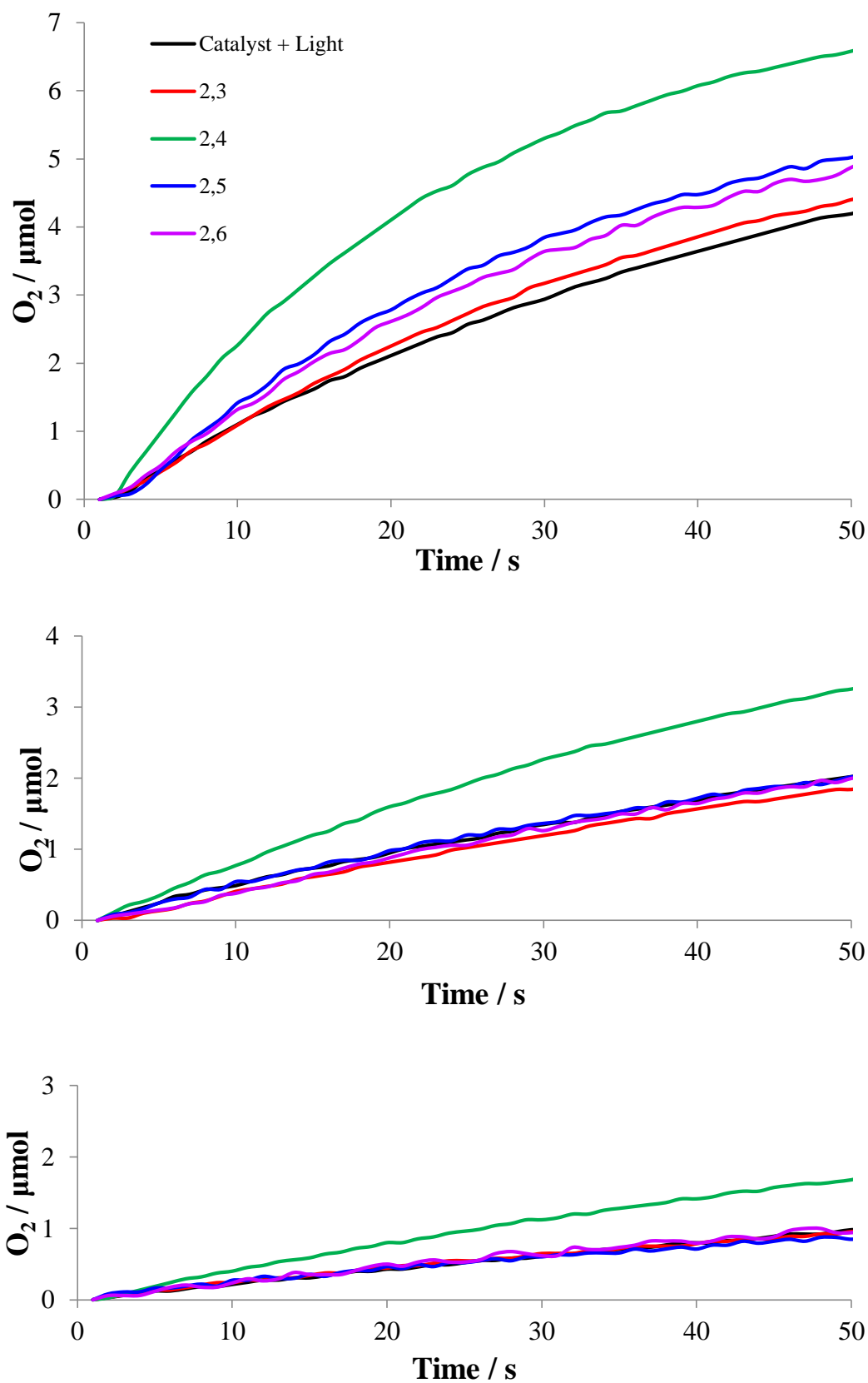
Figure 2.34 Catalytic oxygen evolution response plots for dye modified substrates. Top - first injection, Middle - second injection, Bottom - third injection.
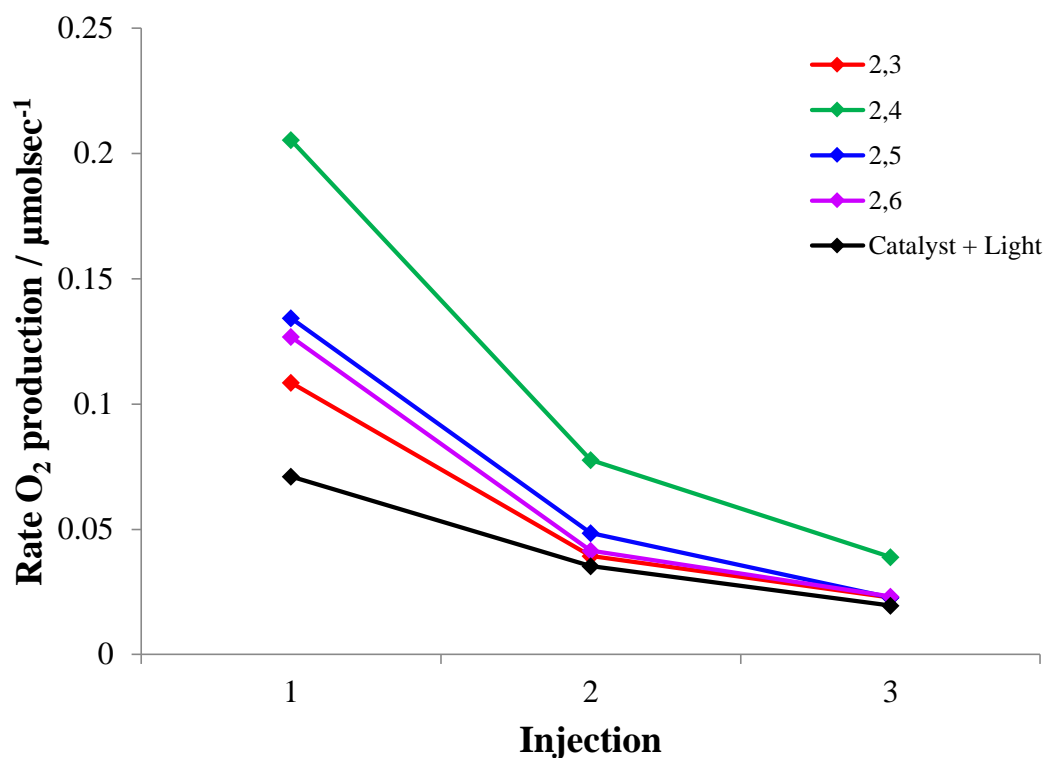
Figure 2.35 Comparison of the instantaneous rates of oxygen evolution over the first 25 seconds following each Ce^{IV} injection for the the ruthenium picolinic acid complex treated substrates.

Table 2.11 Instantaneous rate of oxygen evolution over the first 25 seconds following each Ce^{IV} injection from the ruthenium picolinic acid complex treated substrates.

	Instantaneous rate 1 µmol/sec	Instantaneous rate 2 µmol/sec	Instantaneous rate 3 µmol/sec
Catalyst + Light	0.1038	0.0477	0.0212
2,3	0.1085	0.0392	0.0229
2,4	0.2054	0.0777	0.0389
2,5	0.1344	0.0485	0.0229
2,6	0.1268	0.0415	0.0231

The difference in performance between the 2,4 system and that of the other complexes validates the original hypothesis that behaviour of ruthenium pyridyl sensitised heterogeneous water oxidation is influenced by the positioning of the anchoring group on the pyridyl ring. The position of the anchor has been shown to affect absorption, redox potential and catalytic performance.

Further investigation using computational methods will be required to correlate catalytic activity with factors such as the strength of the dye-substrate binding and the position of molecular orbitals as these play a vital role in the rate of electron injection from the dye into the catalytic substrate. The computational methods will also examine the aqua substituted complexes to determine if they could have a role in the deactivation of the complexes.

To conclude, the position of an anchoring group does affect the performance of a sensitisers dye for the heterogeneous water oxidation reaction. In particular, the potential of the dyes II/III and III/IV couples vary by 0.59 V and 0.65 V respectively (Figure 2.36).
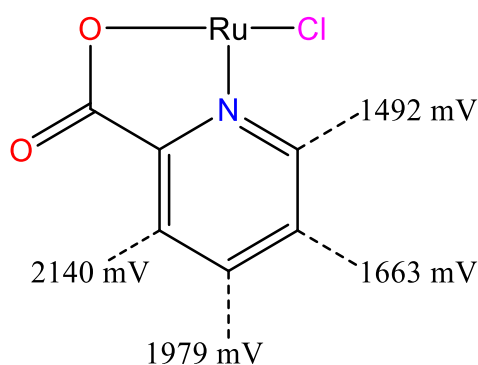
Figure 2.36 Variation in III/IV redox couple by substation of anchoring group.

The absorbance of the dyes also varied but to a lesser magnitude. The catalytic rate of the substrate sensitised with the 2,4 isomer had the highest performance but that the performance of the other isomers became uniform after the first catalytic injection cycle. The work here shows that it is possible to elicit improvements in the performance of sensitiser dyes by the manipulation of the anchoring position.

Experimental

All experiments were carried out using standard apparatus and commercially available chemicals. Solid reflectance spectra (between 380 – 800 nm) were recorded on a Photonics CCD array UV-Vis spectrophotometer. Solution absorbance spectra (200-600nm) were recorded on a unicam UV 300 spectrophotometer. Elemental microanalysis was carried out in house on a Perkin Elmer 2400 CHN Analyser. Crystals were coated in mineral oil and mounted on glass fibres or loops. X-Ray measurements were conducted using either an Oxford Diffraction Gemini CCD diffractometer at 123 K using graphite monochromated Mo-Kα radiation or an Oxford Diffraction Gemini CCD diffractometer at 123 K using graphite monochromated Mo-Kα or Cu-Kα radiation. Cyclic Voltammetry was carried out on a EG&G model 263a potentiostat operating Powersuite.

Synthesis of tris(pyridine-2-carboxylate) ruthenium (III):

Pyridine-2-carboxylic acid (494 mg, 4 mmol) and ruthenium trichloride trihydrate (0.5g, 2 mmol) were refluxed in ethanol (50ml) for 5 hours to produce a bright orange solution. The solution was cooled to room temperature and reduced in volume to approximately 2-3 ml via rotary evaporation. Crystals formed and were then filtered and recrystallised from water via evaporation. Yield 42% (393 mg). Anal. Found: C, 43.97; H, 2.83; N, 8.50 % Calcd. for $C_{18}H_{14}N_3O_7Ru_1.1(H_2O)$: C, 44.54; H, 2.91; N, 8.66 %.

Synthesis of dichlorobis(pyridine-2-carboxylate) ruthenium(IV):

Pyridine-2-carboxylic acid (493 mg, 4 mmol) and ruthenium trichloride trihydrate (0.5g, 2 mmol) were refluxed in ethanol (50ml) for 5 hours to produce a bright orange solution. The solution was cooled to room temperature and reduced in volume to approximately 2-3 ml via rotary evaporation. Crystals formed and were then filtered and recrystallised via diffusion in ethanol with diethyl ether. Yield 73% (605 mg). Anal. Found: C, 35.43; H, 1.93; N, 6.65 % Calcd. for $C_{12}H_8Cl_2N_2O_4Ru_1$. : C, 34.63; H, 1.94; N, 6.73 %.

Synthesis of dichlorobis(4-(ethoxycarbonyl)picolinic acid) ruthenium(IV):

Pyridine-2,3-dicarboxylic acid (668.5 mg, 4 mmol) and ruthenium trichloride trihydrate (0.5g, 2 mmol) were refluxed in ethanol (50ml) for 5 hours to produce a bright orange solution. The solution was cooled to room temperature and reduced in

volume to approximately 2-3 ml via rotary evaporation. Crystals formed and were then filtered and recrystallised via diffusion in ethanol with diethyl ether. Yield 64% (808 mg). FTIR [(ν/cm^{-1} (ATR)]: 1738 (-C=O), 1634 (-C=O), 1589 (C=C). Anal. Found: C, 34.45; H, 3.69; N, 4.24 % Calcd. for $C_{18}H_{22}Cl_2N_2O_{11}Ru.4(H_2O)$: C, 34.19; H, 3.83; N, 4.43 %.

Synthesis of dichlorobis(4-(ethoxycarbonyl)picolinic acid) ruthenium(IV):
Pyridine-2,4-dicarboxylic acid (668.5 mg, 4 mmol) and ruthenium trichloride trihydrate (0.5g, 2 mmol) were refluxed in ethanol (50ml) for 5 hours to produce a dark orange solution. The solution was cooled to room temperature and reduced in volume to approximately 2-3 ml via rotary evaporation. Crystals formed and were then filtered and recrystallised via diffusion in ethanol with diethyl ether. Yield 57% (638 mg). FTIR [(ν/cm^{-1} (ATR)]: 1727 (-C=O), 1615 (-C=O), 1563 (C=C). Anal. Found: C, 38.49; H, 2.93; N, 4.81 % Calcd. for $C_{18}H_{22}Cl_2N_2O_{11}Ru$: C, 38.58; H, 2.88; N, 5 %.

Synthesis of dichlorobis(5-(ethoxycarbonyl)picolinic acid) ruthenium(IV):
Pyridine-2,5-dicarboxylic acid (668.5 mg, 4 mmol) and ruthenium trichloride trihydrate (0.5g, 2 mmol) were refluxed in ethanol (50ml) for 5 hours to produce a dark orange solution. The solution was cooled to room temperature and reduced in volume to approximately 2-3 ml via rotary evaporation. Crystals formed and were then filtered and recrystallised via diffusion in ethanol with diethyl ether. Yield 61% (728 mg). FTIR [(ν/cm^{-1} (ATR)]: 1731 (-C=O), 1617 (-C=O), 1574 (C=C). Anal. Found: C, 36.45; H, 3.23; N, 4.6 % Calcd. for $C_{18}H_{22}Cl_2N_2O_{11}Ru.2(H_2O)$: C, 36.25; H, 3.38; N, 4.7 %.

Synthesis of dichlorobis(6-(ethoxycarbonyl)picolinic acid) ruthenium(IV):
Pyridine-2,6-dicarboxylic acid (668.5 mg, 4 mmol) and ruthenium trichloride trihydrate (0.5g, 2 mmol) were refluxed in ethanol (50ml) for 5 hours to produce a dark orange solution. The solution was cooled to room temperature and reduced in volume to approximately 2-3 ml via rotary evaporation. Crystals formed and were then filtered and recrystallised via diffusion in ethanol with diethyl ether. Yield 69% (772 mg). FTIR [(ν/cm^{-1} (ATR)]: 1729 (-C=O), 1622 (-C=O), 1593 (C=C). Anal. Found: C, 38.64; H, 3.04; N, 4.9 % Calcd. for $C_{18}H_{22}Cl_2N_2O_{11}Ru$: C, 38.58; H, 2.88; N, 5 %.

Cyclic voltammetry:

A 1mM solution of each complex was prepared in a 0.1 M solution of tetrabutylammonium tetrafluoroborate in acetonitrile (redistilled over calcium hydride). The electrodes were glass carbon, platinum wire and silver wire for the working, counter and reference respectively. The solutions were sparged with dry nitrogen before each voltage cycle and a nitrogen blanket kept on them constantly. To ensure there was no drift in testing conditions, voltammograms of a ferrocene/ferrocenium solution were recorded before and after the dyes.

Synthesis of catalytic substrate:

42 mg of potassium hexachloroiridate was dissolved in 50 ml of distilled water in a round bottomed flask. The solution was adjusted to pH 12 with 1M potassium hydroxide. The solution was heated to 90°C for 15 minutes during which time the colour changed from a dark brown to a pale blue as the IrO_2 nanoparticles formed. The now nanoparticle suspension was stored at -30°C for 10 minutes. The pH of the suspension was adjusted to 1 using 1M nitric acid. The suspension was stirred in an ice bath for 90 mins during which time the light blue colour became deeper and darker. The pH of the suspension was adjusted to 5 using potassium hydroxide before being diluted to 100ml in standard flask then being transferred to a 250 ml conical flask. 2 g of titanium dioxide (P25) was added and the mixture stirred overnight. The suspension was vacuum filtered and the filtrate washed with 300 ml distilled water. The powder was vacuum dried at room temperature for 3 hours. Yield 1846.6 mg (91.44%)

Modification of catalytic substrate:

200mg of the catalytic substrate was suspended in a 100ml of a 1mM ethanolic solution of the selected ruthenium complex. The suspension was stirred at 40° C for 16 hours. The solid was then vacuum filtered and washed with 200 ml of cold ethanol. The solid was then vacuum dried for 30 minutes.

Oxygen evolution testing of modified catalytic substrates:

30mg of dye modified catalytic substrate was suspended in 30 cm^3 of 1M perchloric acid and sonicated for 15 minutes. The suspension was introduced into the test chamber of a Clark-type oxygen electrode. The suspension was stirred at 550 rpm. Calibration of the suspension was achieved by purging with nitrogen then with compressed air to give a 0% and 100% saturation level. The chamber was purged with nitrogen again and sealed. The chamber was saturated with a blend of visible and UV light. Ce^{IV}(SO$_4$)$_2$ (0.1M, 300μl) was injected and the oxygen concentration in the solution monitored using data acquisition software. After the oxygen concentration reached a maximum, the chamber was unsealed and purged with nitrogen. The chamber was resealed and further injections were carried out.

Crystal Data

	Ru(pic)$_3$	Ru(pic)$_2$Cl$_2$	Ru(2,3)$_2$Cl$_2$	Ru(2,3)$_2$Cl$_2$ 2	Ru(2,4)$_2$Cl$_2$	Ru(2,5)$_2$Cl$_2$
Formula	C$_{18}$H$_{14}$N$_3$O$_7$Ru$_1$	C$_{16}$H$_{19}$Cl$_4$N$_3$O$_6$Ru$_1$	C$_{40}$H$_{44}$Cl$_4$N$_4$O$_{18}$Ru$_2$	C$_{22}$H$_{28}$Cl$_2$N$_2$O$_{10}$Ru$_1$	C$_{18}$H$_{16}$Cl$_2$N$_2$O$_8$Ru$_1$	C$_{20}$H$_{22}$Cl$_2$N$_2$O$_9$Ru$_1$
FW	485.35	450.37	1212.66	652.44	560.30	606.37
Crystal System	Monoclinic	Triclinic	Monoclinic	Orthorhombic	Monoclinic	Monoclinic
Space Group	C 2/c	P -1	P 2$_1$/c	P 2$_1$/ca	P 2$_1$/n	P -1
a/Å	30.3581(8)	8.737(5)	7.5019(5)	13.389(5)	15.4180(11)	14.093(6)
b/Å	8.4576(3)	11.302(5)	29.092(2)	14.192(5)	9.1381(5)	8.700(4)
c/Å	13.8558(4)	13.551(5)	12.6104(9)	14.428(5)	20.6486(14)	20.255(5)
α/°	90	70.672(5)	90	90	90	90
β/°	94.807(3)	89.673(5)	91.666(2)	90	104.792(7)	110.233(13)
γ/°	90	76.682(5)	90	90	90	90
Z	4	2	4	4	4	2
V/Å^3	3545.05(19)	1225.1(10)	2751.0(3)	2741.6(17)	2812.8(3)	2330.1(15)
Radiation type	MoK\a	MoK\a	MoK\a	MoK\a	MoK\a	MoK\a
Radiation wavelength / Å	0.71073	0.71073	0.71073	0.71073	0.71073	0.71073
μ_{calc}/mm^{-1}	0.498	1.300	0.782	0.821	0.784	0.473
No. reflections measured	11532	9341	17509	63603	32275	5430
No. unique reflections	4065	4829	6293	6598	6439	2863
No. parameters	270	327	349	347	290	222
R_w^a (1>2σ(l))	0.0320	0.0296	0.0367	0.0219	0.0703	0.0583
R_w^b (all reflections)	0.0641	0.0804	0.0922	0.0526	0.1641	0.1562
GOF	1.052	1.077	0.909	1.049	1.180	1.036

	Ru(2,6)$_2$Cl$_2$	Ru(2,6)$_2$Cl$_2$ Me	Ru(2,6)$_2$Cl$_2$ Me	Ru(2,3)$_2$Cl$_1$(H$_2$O)$_1$	Ru(2,5)$_2$Cl$_1$(H$_2$O)$_1$	[Ru^{III}(2,5)$_2$Cl$_2$]$^-$ [H(2,5)]$^+$
Formula	C$_{36}$H$_{32}$Cl$_4$N$_4$O$_{16}$Ru$_2$	C$_{18}$H$_{20}$Cl$_2$N$_2$O$_{10}$Ru$_1$	C$_{18}$H$_{20}$Cl$_2$N$_2$O$_{10}$Ru$_1$	C$_{18}$H$_{19}$Cl$_1$N$_2$O$_{10}$Ru$_1$	C$_{18}$H$_{17}$Cl$_1$N$_2$O$_9$Ru$_1$	C$_{29}$H$_{30}$Cl$_2$N$_3$O$_{12}$Ru$_1$
FW	1120.60	596.29	596.29	559.82	541.81	784.48
Crystal System	Triclinic	Monoclinic	Monoclinic	Triclinic	Monoclinic	Triclinic
Space Group	P -1	C 2$_1$/c	C 2$_1$/c	P -1	P 2$_1$/n	P 1
a/Å	9.0132(12)	13.007(5)	13.007(5)	9.9387(6)	11.023(5)	8.0257(7)
b/Å	10.8986(15)	8.870(5)	8.870(5)	10.0957(5)	13.234(5)	9.8844(9)
c/Å	11.3985(15)	18.514(5)	18.514(5)	11.5858(8)	14.620(5)	10.9436(7)
α/°	96.751(11)	90	90	81.491(5)	90	67.358(7)
β/°	90.989(11)	92.199(5)	92.199(5)	76.791(5)	108.185(5)	76.900(7)
γ/°	110.651(13)	90	90	72.694(5)	90	76.851(6)
Z	2	4	4	2	4	1
V/Å^3	1038.4(2)	2134.4(16)	2134.4(16)	1076.50(11)	2026.2(14)	770.83(11)
Radiation type	MoK\a	MoK\a	MoK\a	MoK\a	MoK\a	MoK\a
Radiation wavelength / Å	0.71073	0.71073	0.71073	0.71073	0.71073	0.71073
μ$_{calc}$/mm^{-1}	1.062	1.015	1.015	0.911	0.961	0.752
No. reflections measured	16017	6255	6255	9405	8750	10849
No. unique reflections	5232	1893	1893	4741	4363	3736
No. parameters	292	151	151	303	286	216
R$_w$^{a} (1>2σ(l))	0.0556	0.0527	0.0527	0.0351	0.0391	0.0410
R$_w$^{b} (all reflections)	0.1026	0.1274	0.1274	0.0686	0.0950	0.1103
GOF	0.828	1.355	1.355	1.055	1.075	1.074

	$[Ru^{III}(2,5)_2Cl_2]^-[Ru^{III}(2,5)_2(H_2O)_2]^+$	$3[Ru^{III}(2,6)_2Cl_2]^-[Al(H_2O)_6]^{3+}$
Formula	$C_{36}H_{44}Cl_2N_4O_{22}Ru_2$	$C_{54}H_{76}Cl_6N_6O_{39}Ru_3Al_1$
FW	1157.69	1975.92
Crystal System	Monoclinic	Triclinic
Space Group	P 2_1/c	P -1
a/Å	11.3674(4)	10.3368(7)
b/Å	13.5490(5)	14.4320(10)
c/Å	14.3613(6)	14.8346(10)
α/°	90	111.258(3)
β/°	98.009(4)	100.757(3)
γ/°	90	100.390(3)
Z	4	4
V/Å^3	2190.31(14)	1950.5(2)
Radiation type	MoK\a	MoK\a
Radiation wavelength / Å	0.71073	0.71073
μ_{calc}/mm^{-1}	0.901	0.998
No. reflections measured	10307	35576
No. unique reflections	4291	8943
No. parameters	325	558
R_w^a (1>2σ(l))	0.0294	0.0326
R_w^b (all reflections)	0.0653	0.0895
GOF	0.859	1.072

Citations

1. Bagotsky, V. S., Electrode Potentials. In *Fundamentals of Electrochemistry*, John Wiley & Sons, Inc.: **2005**; 19-31.
2. Bozhi, T.; Zheng, X.; Kempa, T. J.; Fang, Y.; Yu, N.; Yu, G.; Huang, J.; Lieber, C. M., Coaxial silicon nanowires as solar cells and nanoelectronic power sources. *Nature* **2007** *449* 885-889.
3. Zandi, O.; Hamann, T. W., Determination of photoelectrochemical water oxidation intermediates on haematite electrode surfaces using operando infrared spectroscopy. *Nat. Chem.* **2016** *8* 778-783.
4. Yan, B.; Yue, G.; Sivec, L.; Owens-Mawson, J.; Yand, J.; Guha, S., Correlation of texture of Ag/ZnO back reflector and photocurrent in hydrogenated nanocrystalline silicon solar cells. *Sol. Energ. Mat. Sol. Cells* **2012** *104* 13-17
5. Ka, M. D.; Verho, O.; Johnston, E. V.; Åkermark, B., Artificial Photosynthesis: Molecular Systems for Catalytic Water Oxidation. *Chem. Rev*. **2013,** *114* (24), 11863-12001.
6. Youngblood, W. J.; Lee, S.-H. A.; Kobayashi, Y.; Hernandez-Pagan, E. A.; Hoertz, P. G.; Moore, T. A.; Moore, A. L.; Gust, D.; Mallouk, T. E., Photoassisted Overall Water Splitting in a Visible Light-Absorbing Dye-Sensitized Photoelectrochemical Cell. *J. Am. Chem. Soc.* **2009,** *131*, 926-927.
7. Swierk, J. R.; Mallouk, T. E., Design and development of photoanodes for water-splitting dye-sensitized photoelectrochemical cells. *Chem. Soc. Rev.* **2013,** *42*, 2357-2387.
8. Lyon, L. A.; Hupp, J. T., Energetics of the Nanocrystalline Titanium Dioxide/Aqueous Solution Interface: Approximate Conduction Band Edge Variations between $H_0 = -10$ and $H_- = +26$. *J. Phys. Chem. B* **1999,** *103* (22), 4623-4628.
9. Bhattacharya, S., Synthesis, characterization and electron transfer properties of some picolinate complexes of ruthenium. *Polyhedron* **1995,** *14* (23), 3591-3597.
10. Katafias, A.; Impert, O.; Kita, P.; Fenska, J.; Koter, S.; Kaczmarek-Kędziera, A.; Różycki, H.; Bajek, A.; Uzarska, M.; van Eldik, R., Kinetics and Mechanism of the Reduction of mer -Tris-picolinatoruthenium(III) by L - Ascorbic Acid. *Eur. J. Inorg. Chem.* **2014,** *2014* (15), 2529-2535.
11. Brindell, M.; Stochel, G.; Bertolasi, V.; Boaretto, R.; Sostero, S., Photochemistry of trans- and cis-[RuCl$_2$(dmso)$_4$] in Aqueous and Nonaqueous Solutions. *Eur. J. Inorg. Chem.* **2007,** *2007* 16, 2353-2359.
12. Yamazaki, H.; Hakamata, T.; Komi, M.; Yagi, M., Stoichiometric Photoisomerization of Mononuclear Ruthenium(II) Monoaquo Complexes Controlling Redox Properties and Water Oxidation Catalysis. *J. Am. Chem. Soc.* **2011** *133* (23) 8846-8849.
13. Xie, Y.-F.; Zhu, H.; Shi, H.-T.; Jia, A.-Q.; Zhang, Q.-F., Ruthenium complexes containing pyridine-2,6-dicarboxylato ligands. *Inorg. Chim. Acta* **2015,** *428*, 147-153.
14. Ventur, D.; Wieghardt, K.; Weiss, J. Übergangsmetallkomplexe der Pyrazin-2,6-dicarbonsäure und der Pyridin-2,6-dicarbonsäure: Synthesen und Elektrochemie. Die Kristallstruktur von NH$_4$[RuCl$_2$(dipicH)$_2$] *Z. anorg. allg. Chem.* **1985** *524* (5) 40-50.

15.   Zhao, Y.; Hernandez-Pagan, E. A.; Vargas-Barbosa, N. M.; Dysart, J. L.; Mallouk, T. E., A high yield synthesis of ligand-free iridium oxide nanoparticles with high electrocatalytic activity. *J. Phys. Chem. Lett.* **2011,** *2*, 402-406.

16.   Shilpa, N.; Manna, J.; Rajput, P.; Rana R. K., Water Oxidation Catalyst via Heterogenization of Iridium Oxides on Silica: A Polyamine-Mediated Route To Achieve Activity and Stability. *ACS Catal.* **2016** 5699-5705.

Chapter III

DFT analysis of the electronic and optical properties of Ru^{III} and Ru^{IV} dipicolinic acid complexes for the examination of anchor substitution effects

Introduction

The computational examination of the electronic and optical properties of the complexes discussed in Chapter 2 is required in order to correlate those properties with the substitution pattern of the anchoring group. As was shown in Chapter 2, the complexes' crystal structures displayed ruthenium in both a +4 oxidation state as dichlorides and in +3 oxidation states as both dichlorides and chloroaqua complexes. The second objective is, therefore, to examine the multiple oxidation states and primary coordination environments of the dyes in order to determine the effect that those conditions have on the absorbance and the electron-injection capabilities of those complexes.

The primary method for examining these features is with quantum chemical calculations based on density functional theory (DFT). DFT has become the most common approach to answering these types of questions due to balance of accuracy and low computational cost, compared to purely wavefunction methods.

DFT displays a greater accuracy than the simpler Hartree-Fock (HF) methods due to its better description of electron correlation, which causes HF to significantly overestimate the energy of a system. The basis of DFT is the Hohenberg–Kohn theorems and the concept that the exact ground-state electronic energy of a system is determined by the electron density (ρ).[1] The energy is obtained from the electron density via a functional (a function of a function). The Hohenberg–Kohn theorems do not, however, provide the form that this functional will take. Early attempts to design DFT models performed poorly until Kohn and Sham postulated that the kinetic energy of the electron should be described separately. The new method split the energy functional into three parts, kinetic energy $T[\rho]$, electron-nuclei attraction $E_{ne}[\rho]$, and electron-electron repulsion $E_{ee}[\rho]$. The key part of Kohn-Sham theory (KS) is that the functionals can be split into components that can be solved exactly and a smaller correction term which cannot, (Equation 3.1).[2] KS theory utilises a hypothetical system of n non-interacting electrons in n orbitals, ϕ_i, moving in an external potential called the Kohn-Sham potential, v_s. As the electrons are non-interacting, the ground state wavefunction for this system can be described by a single Slater determinant.

The DFT functional can, therefore, be written as

$$E_{DFT}[\rho] = T_s[\rho] + E_{ne}[\rho] + J[\rho] + E_{xc}[\rho]$$

Equation 3.1

Where $E_{DFT}[\rho]$ is the energy of the system, $T_s[\rho]$ is kinetic energy of the hypothetical system composed of non-interacting electrons, $E_{ne}[\rho]$ is the attraction between nuclei and electrons, and $J[\rho]$ is the Coulombic repulsion between electrons. The fourth term $E_{xc}[\rho]$ is the exchange-correlation functional which as mentioned above is the "correction factor". This is the one piece of the total DFT functional which is not known, or rather it is the part of the total functional where all unknown pieces are combined. The non-explicit nature of the exchange-correlation functional is the reason that for practical purposes DFT is not the exact theory its name suggests - but rather an approximation. The exchange-correlation energy is frequently written as

$$E_{xc}[\rho] = E_x[\rho] + E_c[\rho]$$

Equation 3.2

The two terms can be handled separately but only the sum has any actual meaning. If spin-polarisation (when the densities of different spin states are not equal) is included, the equations become

$$E_x[\rho] = E_x^{\alpha}[\rho_{\alpha}] + E_x^{\beta}[\rho_{\beta}]$$

Equation 3.3

$$E_c[\rho] = E_c^{\alpha\alpha}[\rho_{\alpha}] + E_c^{\beta\beta}[\rho_{\beta\beta}] + E_c^{\alpha\beta}[\rho_{\alpha},\rho_{\beta}]$$

Equation 3.4

The total density is given by $\rho = \rho_{\alpha} + \rho_{\beta}$ and as the exchange energy only involves electrons of the same spin it does not include an $E_x^{\alpha\beta}$ term. The level of accuracy for DFT is based on the chosen exchange-correlation functional. The two terms, $E_x[\rho]$ and $E_c[\rho]$, how they are calculated and how they are scaled is what differentiates the different exchange-correlation functionals.[3]

At the simplest level of theory, the local density is treated as a uniform electron gas, where the density varies slowly - known as the local density approximation (LDA), which was modified into the local spin density approximation (LSDA) by the inclusion of spin-polarisation (see Equation 3.5 for exchange function). For closed shell systems LSDA equals LDA.

$$E_x^{LSDA}[\rho] = -2^{1/3}C_x \int \left(\rho_\alpha^{4/3} + \rho_\beta^{4/3}\right) d\mathbf{r}$$

<div align="right">**Equation 3.5**</div>

$$C_x = \frac{3}{4}\left(\frac{3}{\pi}\right)^{1/3}$$

<div align="right">**Equation 3.6**</div>

The most obvious improvement to the LDA method is to change the uniform electron gas to a non-uniform electron gas. The method that uses this approach is the generalised gradient approximation (GGA) which uses the first derivative of the density to correct some of the error in the LSDA exchange energy.

$$E_x^{B88}[\rho] = E_x^{LDA}[\rho] + \Delta E_x^{B88}[\rho]$$

<div align="right">**Equation 3.7**</div>

$$\Delta E_x^{B88}[\rho] = -\beta \int \rho^{4/3} \frac{x^2}{1 + \beta x \sinh^{-1} x} d^3\mathbf{r}$$

<div align="right">**Equation 3.8**</div>

$$x = \frac{|\nabla\rho|}{\rho^{4/3}}$$

<div align="right">**Equation 3.9**</div>

A. D. Becke proposed the above GGA functional (B88) (Equations 3.7-3.9) in 1988 where the constant β is determined by fitting the functional to known data for rare gas atoms.[4] A similar approach was used for the correlation functional by Lee, Yang and Parr (LYP) where the four parameters were determined by fitting to the helium atom. The B88 exchange and LYP correlation functionals are often combined into BLYP (Equation 3.10).[5]

$$E_{xc}^{BLYP}[\rho] = E_x^{B88}[\rho] + E_c^{LYP}[\rho]$$

<div align="right">**Equation 3.10**</div>

One of the key aspects of DFT is separating terms into exact and approximate parts and the exchange-correlation functional does not escape this treatment. The simplest form of the KS system is a system of non-interacting electrons. In this system there is only exchange energy and no correlation energy. The exchange energy can now be described by a single Slater determinant and the energy is exactly that described by the HF wave mechanics methods, but only for the KS system. Inclusion of this exact energy into the true exchange-correlation functional is in the form of hybrid functionals of which the most common is B3LYP (Equation 3.11).[6]

$$E_{xc}^{B3LYP}[\rho] = (1-a)E_x^{LSDA}[\rho] + aE_x^{exact}[\rho]$$
$$+ b\Delta E_x^{B88}[\rho] + (1-c)E_c^{LSDA}[\rho]$$
$$+ cE_c^{LYP}[\rho]$$

Equation 3.11

The three parameters (hence B3LYP) are determined by fitting to the G1 molecule set but differ depending on the form of the GGA exchange-correlation energies. The original values derived by Becke were 0.2, 0.72, and 0.81 for a, b and c respectively. These values derived from a slightly different hybrid which used the 1991 Perdew-Wang correlation gradient correction in place of LYP.[7]

As Kohn-Sham theory requires molecular orbitals, those orbitals must first be constructed. This is achieved using a set of functions (or atomic orbitals) which are combined to give the molecular orbital. This work uses Gaussian type orbitals (GTO) as it allows for a more efficient computation of molecular orbitals, at the cost of some accuracy compared to Slater type orbitals (STO), which mirror the analytical solution for the Schrödinger equation of the hydrogen atom. In practice, it requires three times as many GTOs to reach the same accuracy as a single STO but for larger systems the reduced computational cost makes GTOs more appropriate. Two primary basis sets were used, the first being the Los Alamos National Laboratory double zeta basis set, using the effect core potentials (ECP) of Wadt and Hay (LANL2DZ) for the ruthenium centre.[8-9] This basis set has twice the minimum number of basis functions needed to describe a neutral ruthenium atom and has been popular with calculations featuring ruthenium in both the ground and excited states. The use of ECPs further reduces the computational cost of calculations by treating the core electrons of an atom and the nucleus of an atom as a single function, and handling only the valence electrons explicitly. This is particularly effective when dealing with heavier elements where the effect the core electrons have on bonding is significantly lower than for lighter elements. The second basis set used was for the all other elements in the systems examined (C, N, O, Cl, H). The basis set used was the popular 6-31G split valence basis set which treats the core electrons separately from the valence electrons similar to ECPs but rather than reducing the core electrons/nucleus to a single term it treats the core electrons at a simpler level of theory.[10] In the case of 6-31G, the core orbitals are formed from the contraction of six of the full sets of basis functions, called primitive GTO (PGTO), into a single contracted GTO (CGTO). The lower valence

orbitals are formed from three PGTO into a single CGTO and the upper valence orbitals are a single PGTO. An additional diffuse function was added to better manage the anionic forms of the ruthenium complexes, and d-polarisation on the C, N, O and chlorine, and p-polarisation on the hydrogens. This basis set will be referred to from now on as 6-31+G (d, p). Solvent effects were estimated using the polarizable continuum model (PCM) in water.[11] In the PCM method the molecule is placed in cavity in a medium with a dielectric constant which responds be inducing polarisation in the molecule. The extent of the polarisation is dependent on the dielectric constant of the surrounding medium and therefore the solvent used, which in the case of this work is water, and has a dielectric constant of $\varepsilon=78.3553$.

Geometries were taken from crystal structures when available and optimised with no symmetry constraints; and vibrational mode analysis was used to confirm the ground state. The ethyl ester form of the anchoring group was not changed as it would better approximate the effect of binding onto the TiO_2 substrate than would the free acid.

Non-equilibrium time-dependent density functional theory (TD-DFT) calculations were used to calculate UV-absorption profiles and investigate the charge transfer properties of the complexes under irradiation. TD-DFT is an extension of DFT which includes a time-dependant variable and is regularly used to calculate non-ground state properties for various systems.[12]

All DFT calculations were performed using the Gaussian09 program.[13] GaussSum 3.017 was used to convolute the electronic spectrum from oscillation energies/magnitudes generated in the Gaussian09 output.[14]

Results and Discussion

As stated above, the ruthenium picolinic acid complexes discussed in Chapter 2 exhibited multiple properties which correlated to the substitution pattern of the anchoring group on the picolinic acids. In order to gain greater insight into the relationship between the anchoring group position and these properties, computational methods, such as those discussed above, must be employed.

As discovered in Chapter 2 the ruthenium complexes synthesised can exist in multiple oxidation states, being first synthesised as Ru^{IV} but reducing to Ru^{III} upon dissolution in water. Additionally, the ruthenium complexes in the +3 state could also display exchange of one or more chlorides for an aqua group. The second objective is, therefore, to examine the multiple oxidation states and primary coordination environments of the complexes in order to determine the effect that those conditions have on the absorbance and the electron-injection capabilities of those species.

Ru^{IV} dichlorides

The first complexes to be studied in this manner will be the Ru^{IV} dichloride complexes, as these were both the first to be crystallographically characterised and appear to be the parent compounds for the Ru^{III} complexes. All calculations were performed using the Gaussian09 program employing the B3LYP functional using the LANL2DZ basis set for Ru and the 6-31+G(d, p) for C N O H Cl atoms. Solvent effects were estimated using the polarizable continuum model (PCM) in water. Geometry optimisations were performed with no symmetry constraints and vibrational mode analysis used to confirm the ground state. Initial geometries were taken from the single-crystal XRD structures reported previously.

Structural variations

Of the two oxidation states of the ruthenium complexes, the Ru^{IV} form can exist in two different spin states. Ruthenium in a neutral +4 oxidation state has an even number of electrons, d4, which would normally indicate a diamagnetic species. However, attempts to measure an NMR spectrum revealed that the complexes were paramagnetic, i.e. having unpaired electrons. Since it is well known that higher spin multiplicities are less prevalent in the octahedral complexes derived from heavier elements, the initial conclusion was that the paramagnetism was due to the presence of doublet Ru^{III}. Further examination was still warranted as ruthenium has been shown

to exhibit both triplet and singlet states, depending on the ligand environment and oxidation state.
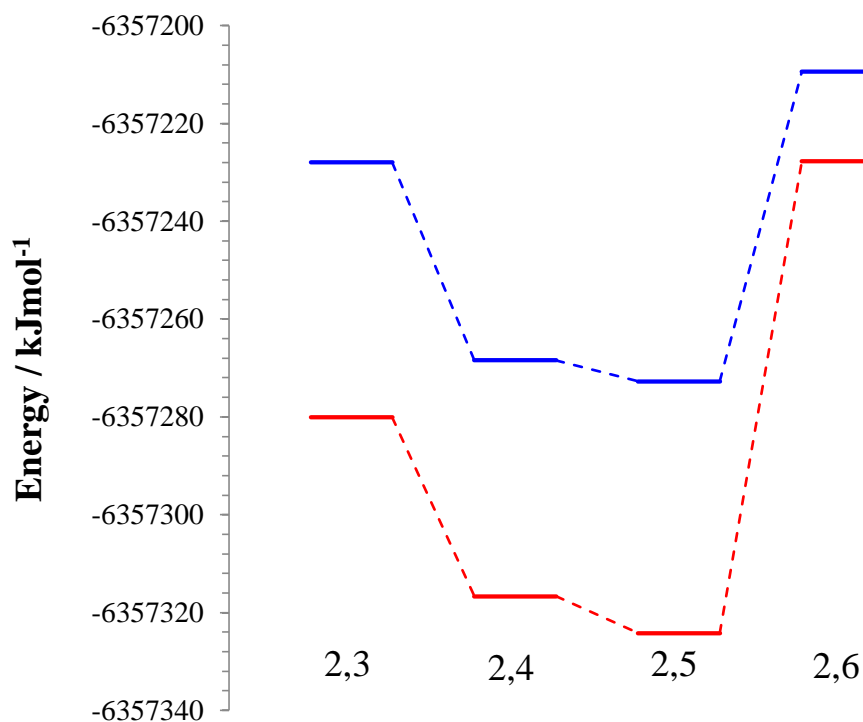
Figure 3.1 Comparison of singlet (red) and triplet (blue) total energies for Ru^{IV} complexes of substituted picolinic acid.

As shown in Figure 3.1 the energy of the singlet complexes was higher than those of the triplet complexes. The energy difference did not, however, remain constant between the isomers. While the 2,3 , 2,4 and 2,5 isomers were proximate in the energy difference between singlet and triplet states (~50 kJ/mol), the 2,6 spin states, by contrast, were markedly closer in energy, having only ~18 kJ/mol between its spin states (Table 3.1). The variance in the energy differences indicates that the electronic properties of the complexes may fluctuate significantly between isomeric forms.

Table 3.1 Singlet-triplet energy differences for the Ru^{IV} complexes of substituted picolinic acid

Complex	Singlet-triplet energy difference kJ/mol
2,3	52.118
2,4	48.294
2,5	51.483
2,6	18.324

Having established that for these four complexes it is the triplet state of Ru^{IV} which is the more stable of the spin states, the next consideration is the configurational isomerism of the complexes. As was shown in the previous chapter, the geometry of the complexes favoured the trans configuration of the chlorides - with the exception of the 2,4 complex, where a cis configuration was observed. This raised two questions, the first of which is: is the cis configuration of the 2,4 complex the thermodynamic product rather than the kinetic or did the complex rearrange to favour the crystal packing? The second question is: could similar cis configurations be found for the other isomers?
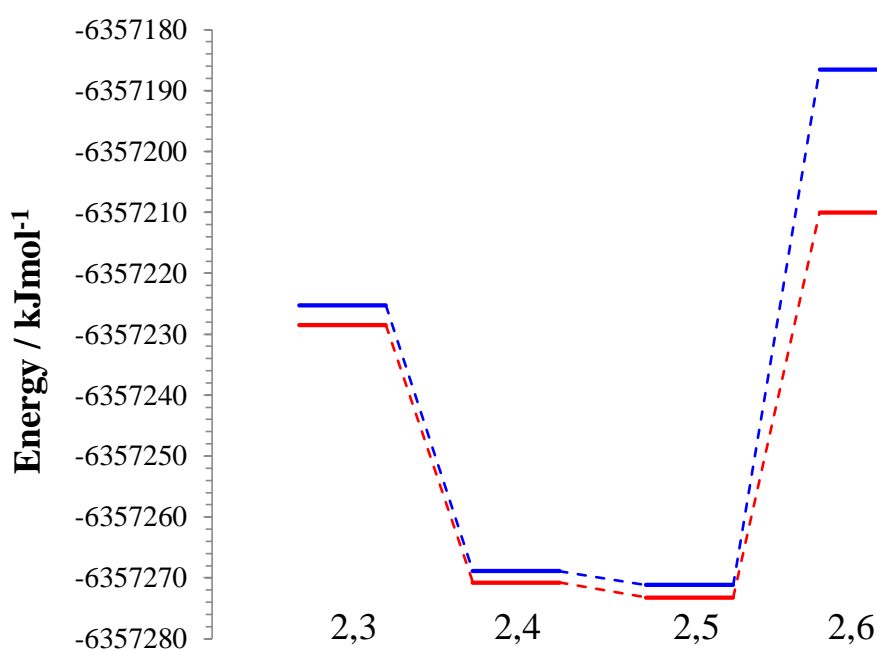
Figure 3.2 Comparison of cis (blue) and trans (red) total energies for Ru^{IV} complexes of substituted picolinic acid.

Comparison of both triplet and singlet state energies for the four isomers revealed that the most stable configurations are the trans isomers (Figure 3.2). However, similar to the energy differences between the spin states, the difference between cis and trans forms varies between structural isomers. For the 2,4 , 2,3 , 2,5 isomers, the energy difference is rather low (1.5-3.5 kJ/mol); however, the 2,6 isomer displays a

comparatively large difference in energy between configurations (23.5 kJ/mol). As the 2,6 isomer has the second anchoring group adjacent to the coordination sphere of the ruthenium, this will have an added influence on any groups in that coordination sphere, and vice versa. In this case, the larger chlorides repel the anchoring group, which, due to its limited ability to rotate out of position, will pass on that additional strain to the pyridine ring, distorting out of the plane of the N-Ru-N axis (Figure 3.3).
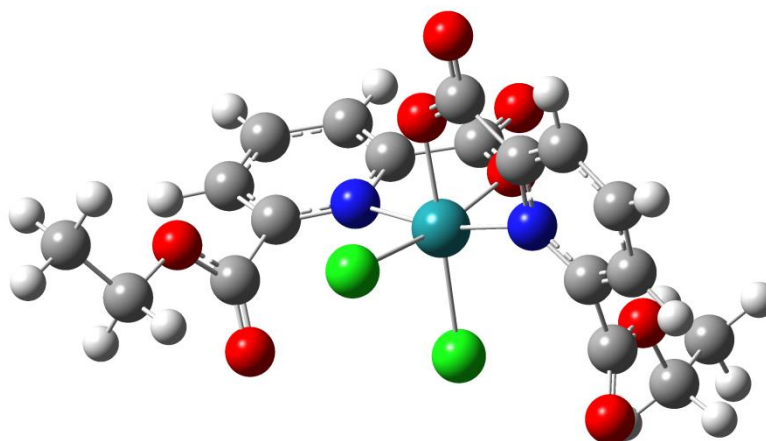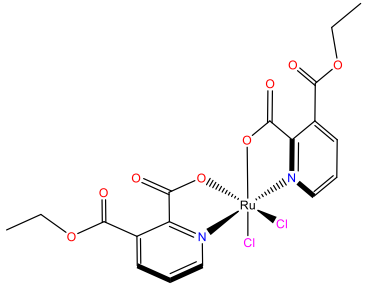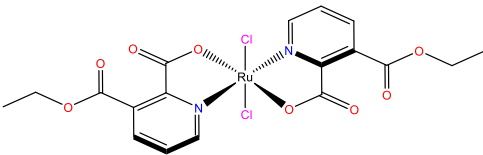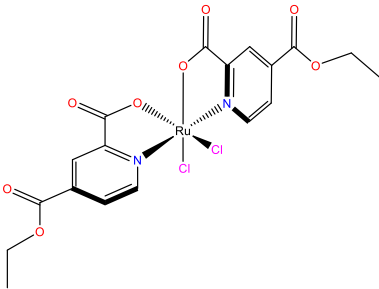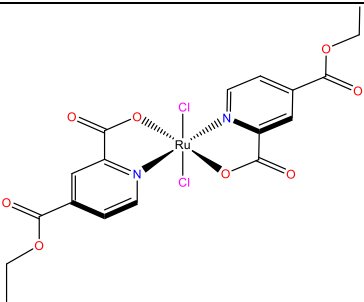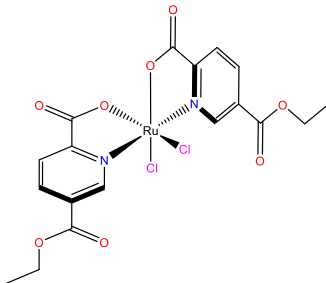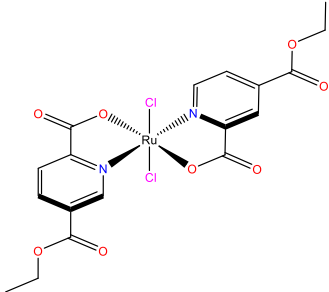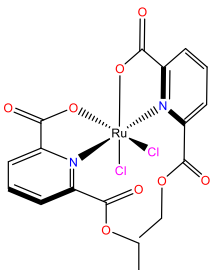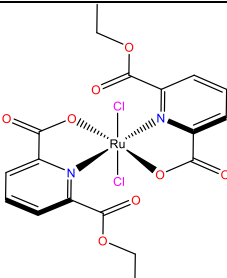
Figure 3.3 Cis configuration of dichlorobis(6-ethoxycarbonyl(pyridine-2-carboxylate)) ruthenium (IV).

Examining the explicit energy differences, it is found that they are of the same order as the Boltzmann distribution at room temperature (2.48 kJ/mol), raising the possibility of the cis isomers of the 2,3 , 2,4 and 2,5 existing at room temperature (Table 3.2). The energy requirement to convert one form to another, however, would be large, as it would require the cleavage of either one or both of the ruthenium chloride bonds and possibly one of the ruthenium oxygen bonds. It is more likely that the structure of the cis isomer of the 2,4 substituted picolinic acid complex shown in Chapter 2 was formed during the initial reaction and crystallised out. Given that it is the only evidence so far of a cis complex and that the trans is still lower in energy it can be said with confidence that even for the 2,4 and 2,5 isomers the vast majority of the species in a given sample of the complexes in a +4 oxidation state will exhibit the trans configuration.

Table 3.2 Cis and trans configurations of the ruthenium complexes formed from the isomers of ethylcarboxylate picolinic acid.

Cis	Trans	ΔE / kJmol^{-1}
		3.262
		1.889
		2.058
		23.499

Comparison of the calculated and crystal structures showed them to be in good agreement with the coordination sphere of the ruthenium centre being well reproduced for each structure (Figures 3.4-3.8). The atom positioning in the structures did, however, diverge further from the ruthenium centre. The reason for the discrepancy is that the movement of the anchoring position has less significant impact on the energy of the system than the atoms involved in the ruthenium coordination sphere. Since the crystal structures involve multiple packing considerations as well as intermolecular

interactions the minor energy differences involved in altering the conformations of the outer parts of the molecule can rapidly become subsumed by those solid state interactions.
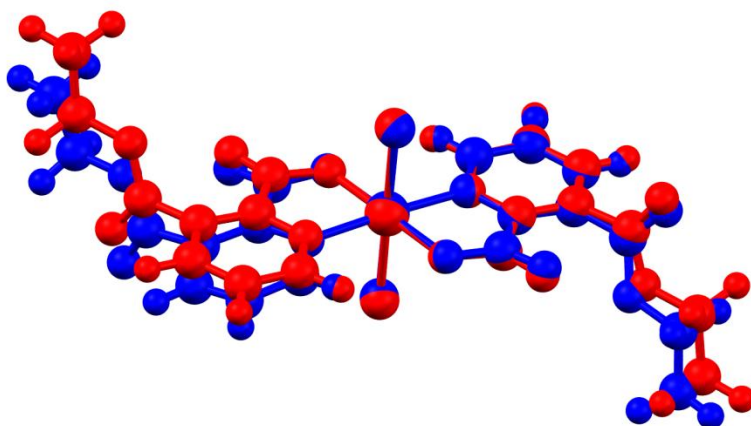
Figure 3.4 Overlap diagrams of X-ray (blue) and calculated (red) structures of the trans configuration of dichlorobis(3-ethoxycarbonyl(pyridine-2-carboxylate)) ruthenium (IV).
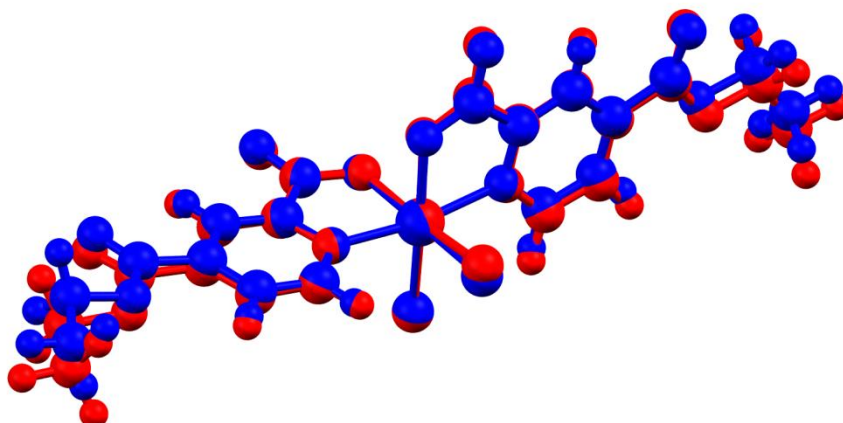
Figure 3.5 Overlap diagrams of X-ray (blue) and calculated (red) structures of the trans configuration of dichlorobis(4-ethoxycarbonyl(pyridine-2-carboxylate)) ruthenium (IV).
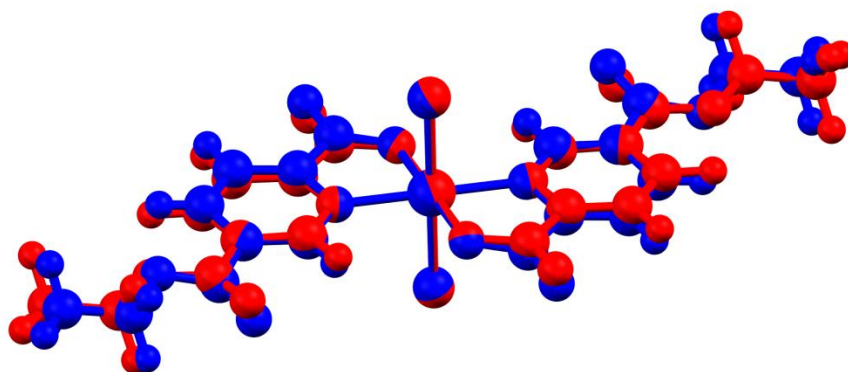
Figure 3.6 Overlap diagrams of X-ray (blue) and calculated (red) structures of the trans configuration of dichlorobis(5-ethoxycarbonyl(pyridine-2-carboxylate)) ruthenium (IV).
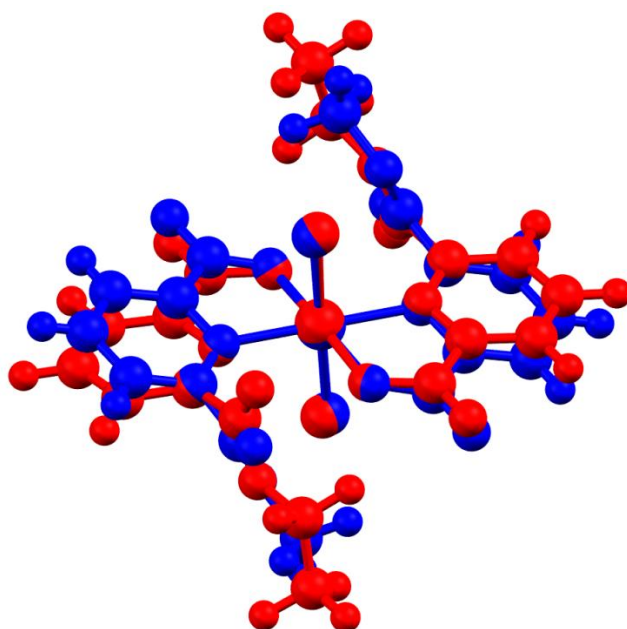
Figure 3.7 Overlap diagrams of X-ray (blue) and calculated (red) structures of the trans configuration of dichlorobis(6-ethoxycarbonyl(pyridine-2-carboxylate)) ruthenium (IV).

Table 3.3 Comparison of Ru-N distances between X-ray and calculated structures including variance between calculated and experimental values as a percentage of experimental value.

	2,3	**2,4**	**2,5**	**2,6**
X-ray	2.045(2) 2.047(2) 2.0499(18) 2.0469(17)	2.053(4) 2.063(4)	2.052(4)	2.081(5) 2.072(4)
Calculated	2.09174	2.08554 2.12111	2.09151	2.13864
Percentage Difference	+2.04 - +2.29	+1.09 – +3.32	+1.925	+2.77 – +3.22

Comparison of the optimised triplet structures and the crystal structures discussed in Chapter 2 showed the calculated structures overestimating the ruthenium-nitrogen distances by 0.025-0.068 Å (Table 3.3). This is in line with the results from the use of similar basis set and functional combinations.

Table 3.4 Comparison of Ru-O distances between X-ray and calculated structures including variance between calculated and experimental values as a percentage of experimental value.

	2,3	2,4	2,5	2,6
X-ray	2.041(2) 2.042(2) 2.0344(16) 2.0331(15)	2.051(14) 2.041(4)	2.033(4)	2.049(4) 2.043(3)
Calculated	2.03147	2.02343 1.98234	2.03299	1.95669
Percentage Difference	-0.08 - -0.52	-0.86 - -3.35	-0.0005	-4.23 - -4.51

Table 3.5 Comparison of Ru-Cl distances between X-ray and calculated structures including variance between calculated and experimental values as a percentage of experimental value.

	2,3	2,4	2,5	2,6
X-ray	2.3099(8) 2.3084(8) 2.3282(9) 2.3340(9)	2.3167(14) 2.3184(15)	2.305(2)	2.3196(15) 2.3234(17)
Calculated	2.33217	2.38845 2.31800	2.33170	2.40013
Percentage Difference	-0.08 - +1.03	-0.017 - +3.097	+1.16	+3.30 - +3.47

The charge carrying chlorides and oxygen atoms also showed variance (Tables 3.4 and 3.5). The oxygen-ruthenium distances were underestimated but to a lesser degree than the overestimation of the ruthenium-nitrogen distances. In the case of the 2,6 isomer the distances were significantly underestimated compared to the other isomers. The majority of the calculated ruthenium-chloride distances were overestimated but for the 2,3 and 2,4 isomers the calculated distances were fractionally lower than some of the reported crystal structures.

The anomalous ruthenium-oxygen distance for the calculated 2,6 complex was attributed to overestimation of the distance between the anchoring carboxyl and the opposing carboxyl. The increased distance twists the axis of the pyridyl ring away from the N-Ru-N axis and shortens the distance between the ruthenium and coordinated oxygen. The reason for the distance between the anchoring carboxyl and the opposing carboxyl being overestimated is that the B3LYP functional does not take into account dispersion corrections, leading to overestimated intramolecular contacts as shown in Figure 3.8.
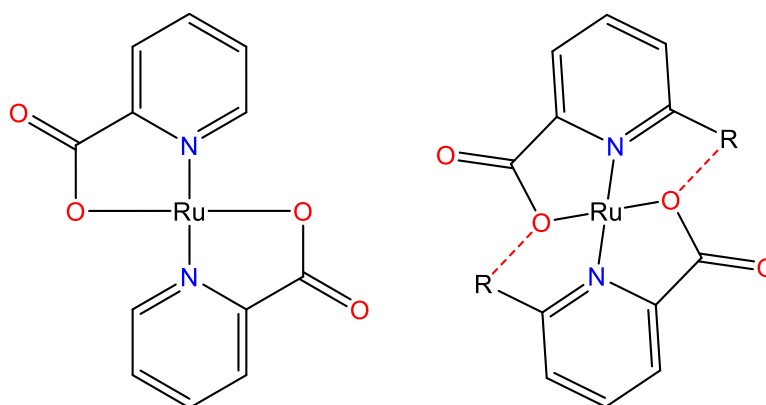
Figure 3.8 Distortion due to overestimated steric repulsion.

Table 3.6 Comparison of N-Ru-O angles between X-ray and calculated structures including variance between calculated and experimental values as a percentage of experimental value.

	2,3	2,4	2,5	2,6
X-ray	79.87(6) 79.64(6)	80.6(2) 80.7(4)	79.83(17)	79.88(16) 79.17(14)
Calculated	79.62	80.47 78.55	78.49	79.81
Percentage Difference	-0.025 - -0.625	-0.161 - -2.664	-1.679	-0.088 - -0.808

The distortion due to the overestimation of steric repulsion and the subsequently shorter ruthenium-oxygen bond did not significantly affect the bite angles of the picolinic acid (Table 3.6). The cis 2,4 complex, due to it less symmetrical nature, displays variation in its bond lengths within the structure itself. The chloride distances differ by 0.0706Å in the calculated structure but by only 0.0017 Å in the crystal structure. The longer ruthenium-chloride bond is reflected in the greater antibonding character of that chloride in the HOMO-2 orbital. The difference between the calculated and crystal structures is attributed to limitation of the calculation method rather than inaccuracy of the crystal structure. Variation between trans-cis bond lengths was seen in the other isomers: for the 2,3 and 2,5 isomers the difference was minor but was significant for the 2,6 - as was expected, given the additional steric repulsion of the anchoring group. However, as there is no crystal structure for the cis

configuration of the 2,6 isomer, the varied bond length cannot be isolated from the same inaccuracy found in the cis–2,4 calculations.

Comparison of the only trans configurations gives the clearest interpretation of the calculated structures, with the bond lengths within the coordination sphere being mostly uniform with the exception of the 2,6 isomer, as discussed above.

Table 3.7 Coordination sphere distances of calculated structures.

	Ru-N	**Ru-O**	**Ru-Cl**
2,3	2.0917	2.0314	2.3322
2,4	2.0923	2.0321	2.3313
2,5	2.0915	2.0330	2.3317
2,6	2.1386	1.9567	2.4002

Electronic properties

The next step in examining these complexes is to look to the individual molecular orbitals that compose the complexes, beginning with the ground state electronic structure.

The calculated orbital splitting corresponds to what would be expected for a transition metal in an octahedral field with the HOMO, HOMO-1 and HOMO-2 being composed of the $4d_{yz}$, $4d_{xz}$ and $4d_{xy}$ atomic orbitals respectively. These orbitals displayed $d\pi$ antibonding character (70-75% for HOMO) with significant contributions from the coordinated groups (Figure 3.9). The d_{yz} and d_{xz} containing HOMO and HOMO-1 levels match the symmetry of the chlorides p_y and p_x orbitals. This destabilizes the orbitals relative to the d_{xz} containing HOMO-2 that shares symmetry with the coordinated carboxyl groups, but with a lesser antibonding contribution from the carboxyl's oxygen p orbitals. In the 2,6 complex there is a reduced contribution from the chlorides in the HOMO level (~8% compared to ~14% for the other isomers) and an increase in the contribution from the coordinated carboxyl group, rising from approximately 10% for the other complexes to 16% for the 2,6 isomer.
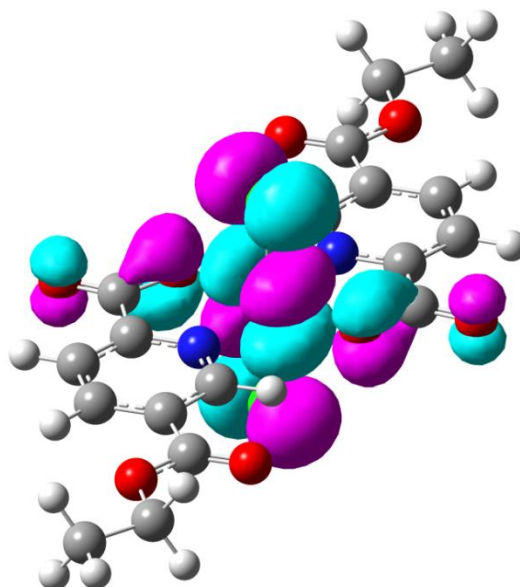
Figure 3.9 HOMO level of optimised structure of dichlorobis(5-ethoxycarbonyl(pyridine-2-carboxylate)) ruthenium (IV) showing electron density centred on the chlorides and ruthenium centre.

Of the three highest occupied orbitals the HOMO-1 has the highest contribution from the chlorides (~25%) as the chloride's p_x orbital lies out of plane with the coordinating carboxyl groups. The carboxyl groups, therefore, have a minimal contribution to the molecular orbital, which as a result is ~95% d_{xz}-p_x π^*. Examining the cis configuration of the 2,4 complex, and comparing it to the trans, shows significant difference in the HOMO and HOMO-1. The orbitals are similar in energy to those in the trans configuration, but show markedly different compositions. The contribution from the ruthenium is reduced to between 30 and 45% with a much greater contribution from the pyridyl ring. Indeed, the HOMO-1 level is now mostly ring based but interestingly enough it is not delocalised across both rings. It can be thought of that if the complex is in the cis configuration the ring based orbitals are raised in energy relative to the ruthenium based orbitals, which explains the greater contribution in the higher energy levels.

The HOMO-2 levels consist of the d_{xy} orbital antibonding to the pyridyl ring and coordinated carboxyl group. The metal centre of the 2,6 isomer has more metal centred character in this orbital, 35% compared to 11-14% for the other isomers.

137

The destabilised, singly occupied HOMO and HOMO-1 levels lie very close to each other in energy (0.23-0.24 eV*) but are isolated from the other molecular orbitals by comparatively large energy gaps (3.24-3.27 eV). Interestingly the two HOMO and HOMO-1 levels lie closer to the LUMO rather than the HOMO-2 (Figure 3.10). The closeness of the LUMO levels would indicate that the promotion of an electron from either the HOMO or HOMO-1 levels would be favourable, particularly in the 2,6 isomer where the LUMO level lies only 1.24 eV above the HOMO.
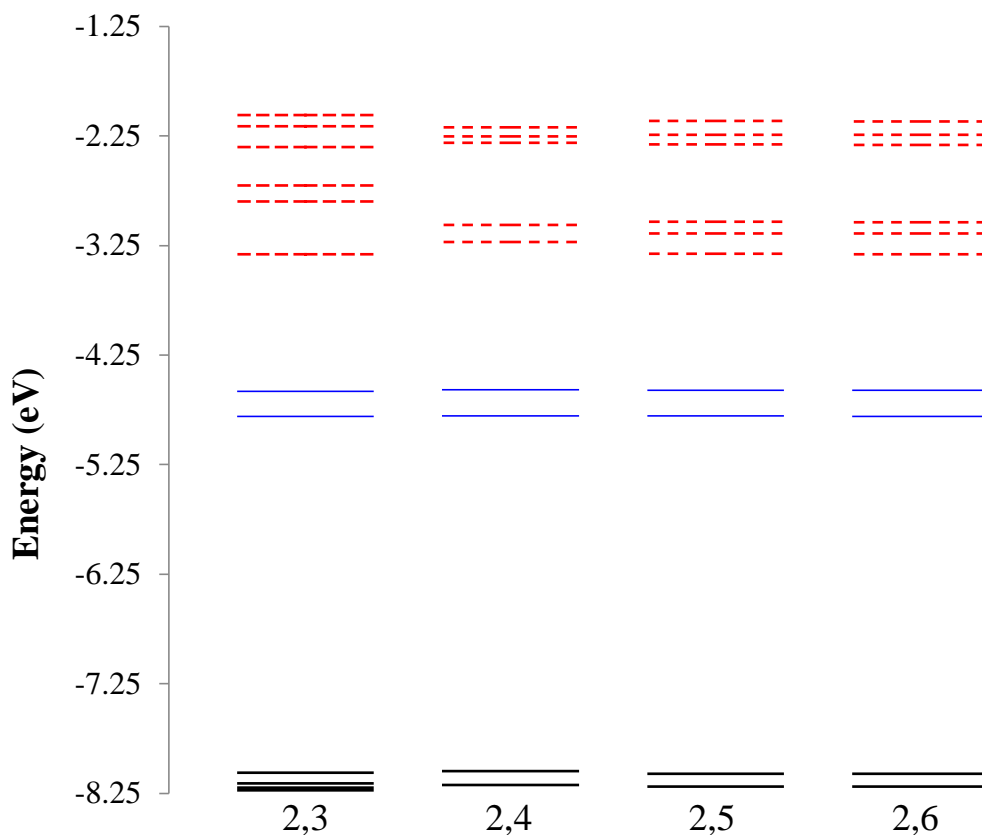
Figure 3.10 Calculated energy level diagrams for the frontier molecular orbitals for the four ruthenium IV complexes of substituted dipicolinic acid. HOMO and HOMO-1 (—), LUMOs (- - -)

The LUMO for all the complexes was the d_{z^2} orbital with significant contributions from all coordinated groups (Figure 3.11). Again the 2,6 complex is different from the others with higher contribution from the metal centre to the molecular orbital, and a reduced contribution from the coordinated carboxyl group.

*Energies for individual orbitals are referenced as eV rather than kJ to avoid confusion with the total energies of the complexes.

138
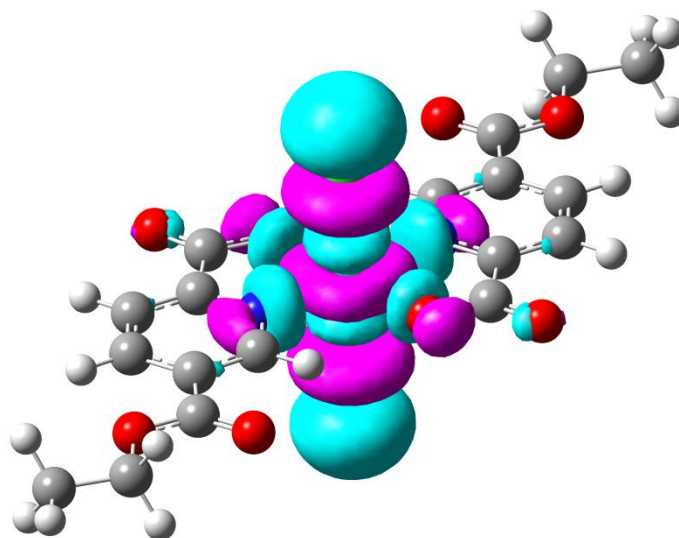
Figure 3.11 LUMO level of optimised structure of dichlorobis(5-ethoxycarbonyl(pyridine-2-carboxylate)) ruthenium (IV) showing electron density centred on the chlorides and ruthenium centre.

The majority of the next lowest energy virtual orbitals are π^* based on the pyridyl rings, but with several $d\sigma^*$ orbitals of different energy based around the metal d_{z^2} and $d_{x^2-y^2}$ orbitals. The LUMO+1 for the complexes are ring based π^*-orbitals but delocalised across both the ring and the coordinated carboxyl group (Figure 3.12). In the trans complexes of the 2,4 and 2,5 isomers this delocalisation includes the anchoring carboxyl group. The delocalisation into the anchor is an indication that the 2,4 and 2,5 complexes may prove to have a higher rate of electron injection into the substrate compared to the 2,3 and 2,6 isomers where such delocalisation is not found. Of note is the LUMO+3 which is the last of the five d-based frontier orbitals. Comprising the $d_{x^2-y^2}$, this orbital lies in the plane of the pyridyl ring and as such does not interact with the chlorides but rather with the ring and coordinating carboxyl group.
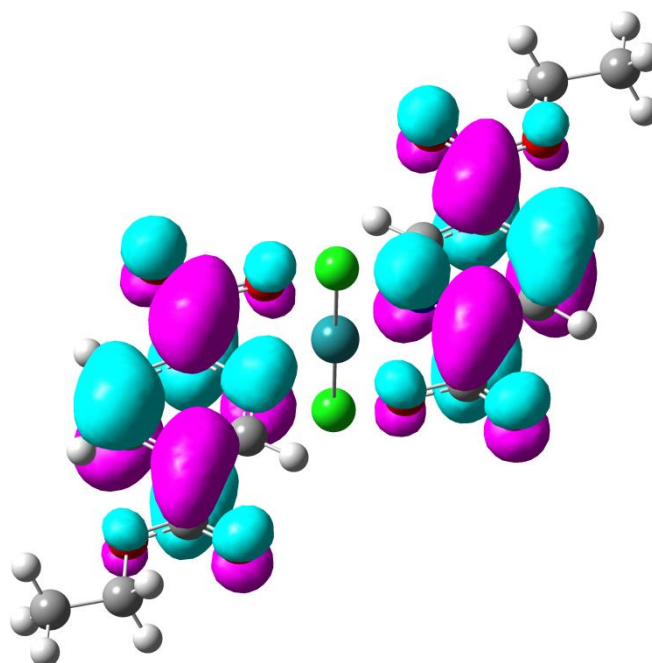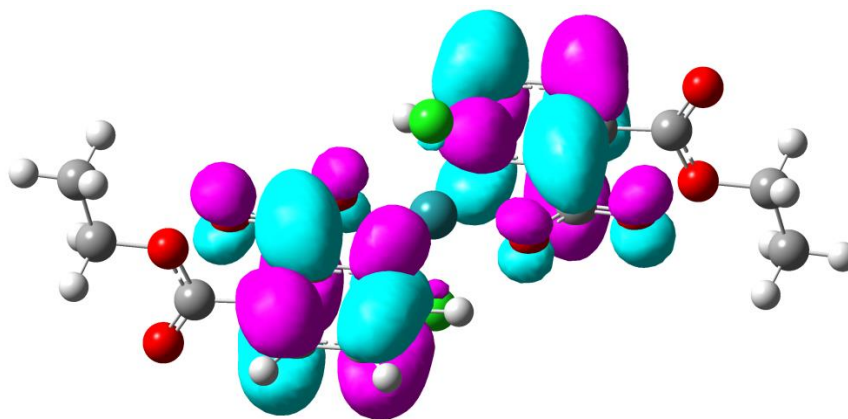
Figure 3.12 LUMO+1 level of optimised structure of dichlorobis(5-ethoxycarbonyl(pyridine-2-carboxylate)) ruthenium (IV) showing electron density centred on the pyridine rings and substituents.

The ruthenium bonding orbitals are found approximately 10-50 energy levels below the HOMO level. Due to the lower energy differences between the orbitals in this range the order they are found from the HOMO is less important. The orbitals primarily consist of p orbitals from the chloride and sp^2 orbitals from the pyridyl nitrogen and carboxyl oxygen donating to low lying p orbitals on the ruthenium centres. There are additional π interactions between the chlorides px/y and ruthenium centres $d_{xz/yz}$ (Figure 3.13). As expected, the anchoring group position has the most pronounced effect on the ring based orbitals with varying degrees of influence depending on orbital compositions. The coordinated and anchoring carboxyls displayed overlap with the delocalised π-orbitals of the ring but with different levels of overlap depending on the energy of the orbital.
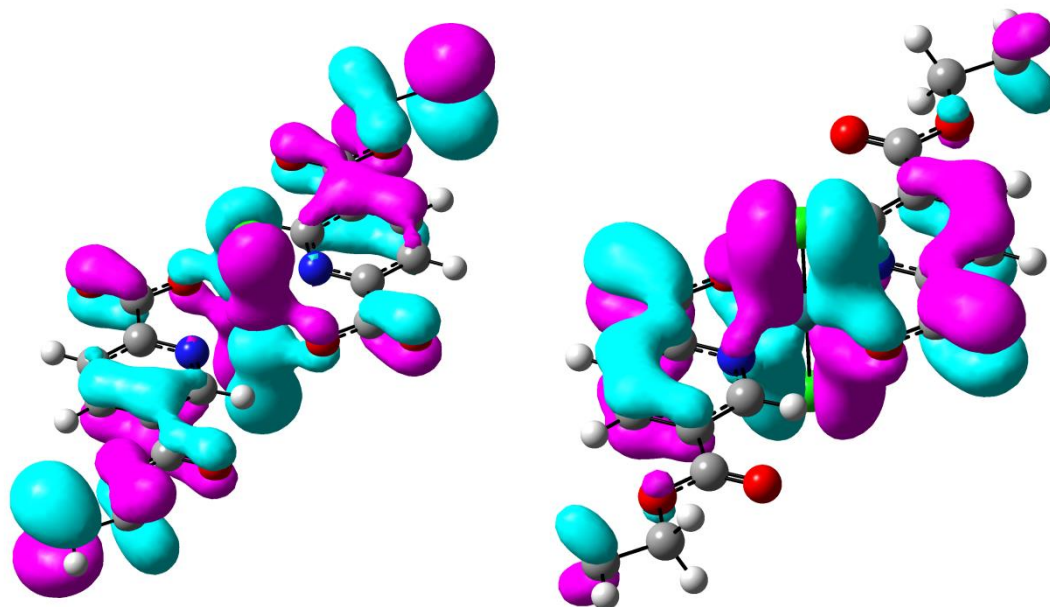
Figure 3.13 π-bonding orbitals of optimised structure of dichlorobis(5-ethoxycarbonyl(pyridine-2-carboxylate)) ruthenium (IV).

Due to the lack of work in the area of ruthenium (IV) dyes for water oxidation it is not possible to relate the calculated orbital data of this oxidation state to possible performance as a sensitiser dye. In order to broaden understanding of these species TDDFT was performed using the optimised ground state geometry, with PCM in water, for all four complexes; the simulated and experimental absorption profiles are plotted with oscillator strength values (*f*, vertical lines) in Figures 3.14-3.17.

The spectra for all four complexes exhibit three primary sets of bands at 450-550 nm, 380-420 nm, and 250-300 nm. The lack of strong d-d transitions in the complexes is in accordance with Laportes rule due to the centrosymmetric nature of the species. The first excited states of the complexes fell outside of the visible region with the calculated first excited state corresponding to wavelengths in the mid and far infrared region. These transitions correspond to the HOMO-LUMO transitions and as has been shown the HOMO-LUMO gap in the complexes is small compared to the HOMO-1 to HOMO-2 gap. However, these transitions display zero oscillation and are outwith the range of useful energy capture, so are of little consequence.
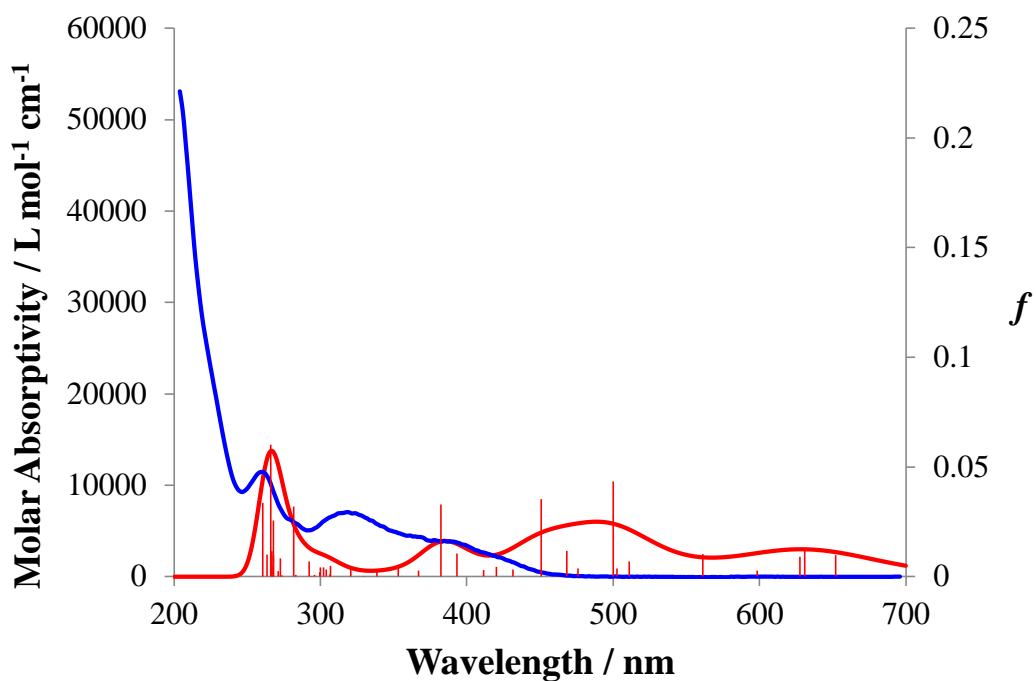
Figure 3.14 Comparison of experimental (blue) and calculated UV-Vis spectrum of dichlorobis(3-ethoxycarbonyl(pyridine-2-carboxylate)) ruthenium (IV) (red).
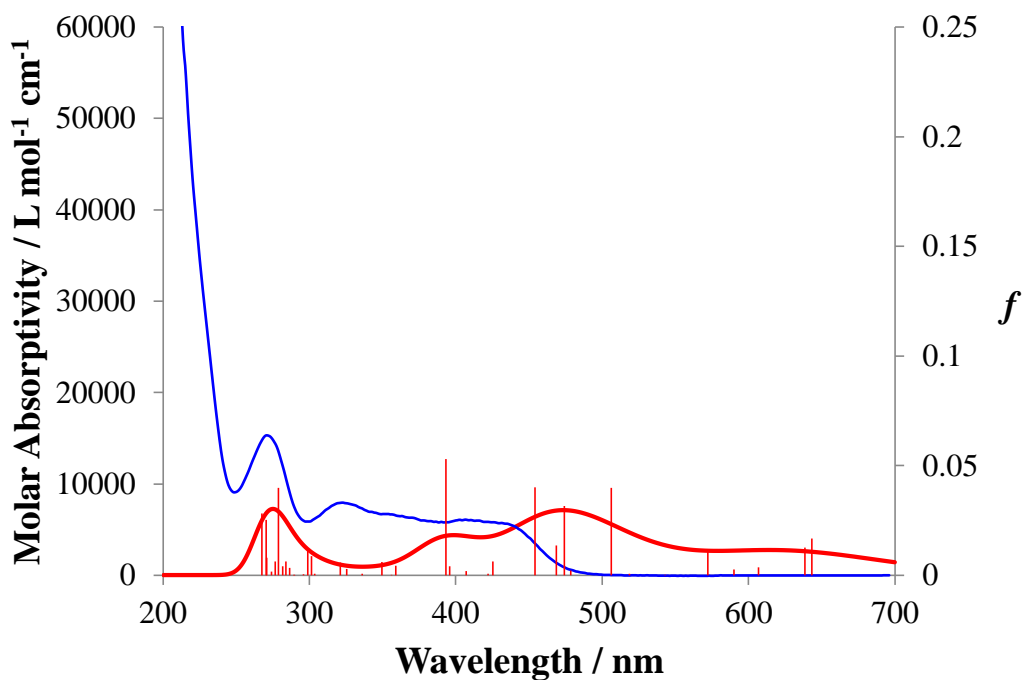
Figure 3.15 Comparison of experimental (blue) and calculated UV-Vis spectrum of dichlorobis(4-ethoxycarbonyl(pyridine-2-carboxylate)) ruthenium (IV) (red).
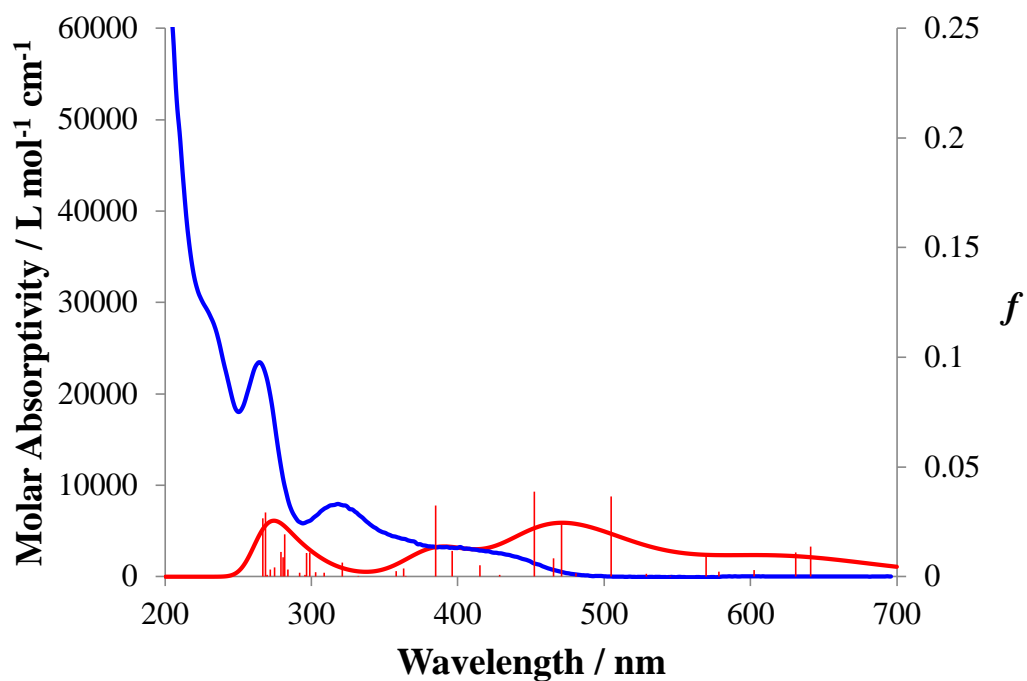
Figure 3.16 Comparison of experimental (blue) and calculated UV-Vis spectrum of dichlorobis(5-ethoxycarbonyl(pyridine-2-carboxylate)) ruthenium (IV) (red).
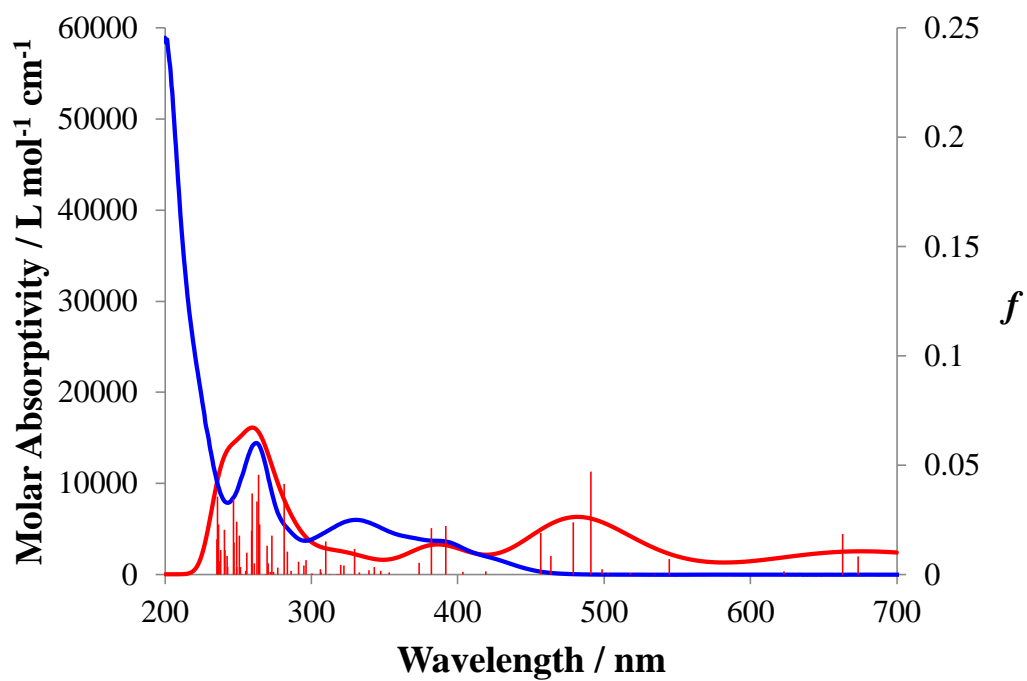
Figure 3.17 Comparison of experimental (blue) and calculated UV-Vis spectrum of dichlorobis(6-ethoxycarbonyl(pyridine-2-carboxylate)) ruthenium (IV) (red).

Lower energy transitions in the region 450-550 nm are calculated to be primarily composed of metal to ligand charge transfer (MLCT) from the orbitals covering the ruthenium and the coordinated carboxyl group. There are also transitions from non-bonding p-orbitals on the chlorides and the coordinated carboxyl group to π^*-orbitals on the ring, in particular the LUMO+1 level. This type of MLCT is commonplace in ruthenium photosensitisers, although as the majority of those complexes are singlet Ru^{II} , the process is better studied for that electron configuration. The bands at 380-420 nm are ligand to metal charge transfer (LMCT) from both the picolinic acid and chloride p/π^*-orbitals to the ruthenium d_{z^2} antibonding orbital. This transition would not be able to inject electrons into the TiO_2 substrate but it would, however, be likely to transfer electrons from any bound water oxidation catalysts to the ruthenium centre. The bands at 250-300 nm are a mix of LMCT, some minor MLCT transitions but with the largest transition being π-π^* between the ring/anchoring carboxyl up to the ring/coordinated carboxyl group.

In the 2,6 complex there are additional transitions observed due to the close proximity of the anchoring carboxyl group. The transition at 478 nm is a LMCT transition from p orbitals on both the anchoring carboxyl and the ethyl group to the ruthenium d_{z^2} LUMO level.

What can be seen from the comparison of the calculated and experimental spectra is that, while there are similarities in the spectra, the calculated spectra have additional transitions below that observed in the measured spectra. As these transitions are attributed to charge transfer, the mismatch of experimental and calculated spectra can be explained by the complexes not being in a +4 ground state when in solution. In order to prove this, however, calculations will need to be performed on both the anionic dichloride complexes and the neutral chloroaqua species.

Ru^{III} dichlorides

Since there are significant differences between the calculated spectra for the Ru^{IV} and the aqueous solution spectra we must examine the possibility that these complexes transform when under aqueous conditions. Since the recrystallisation from aqueous solutions yielded only complexes in a +3 oxidation state, it is likely that these are the active species in aqueous solution. As two distinct forms of the complexes were crystallised, namely the dichlorides and chloroaqua complexes, both will have to be explored.

The first of the complexes to be examined was the anionic dichloride species. As with Fe^{III} this d^5 configuration has two possible paramagnetic spin configurations (doublet or sextet); however, only the low spin configuration (doublet) is examined here, as field splitting for second and third row transition metals is significantly larger than the pairing energy for electrons in the ground state orbital configuration.
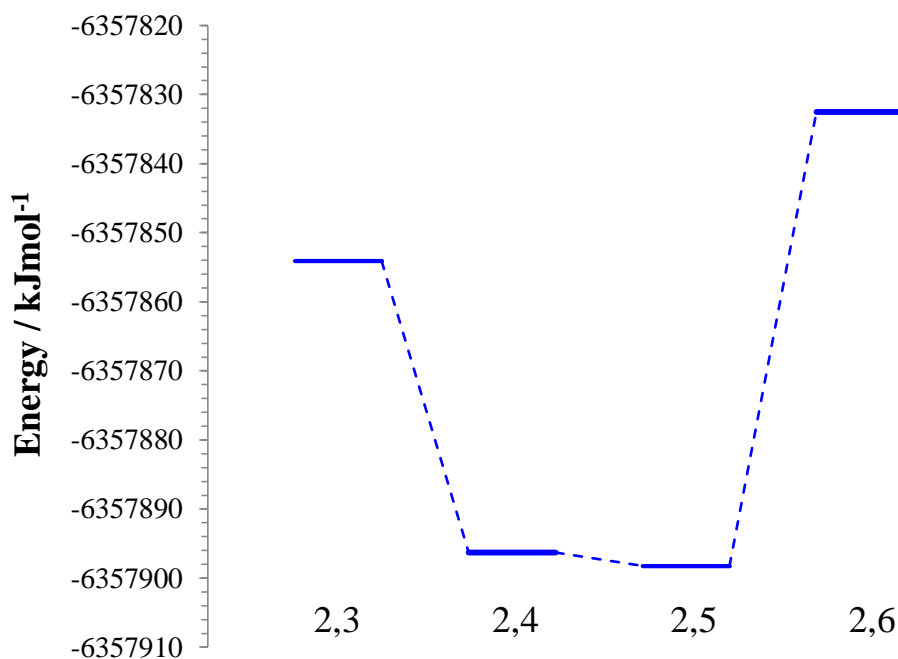
Figure 3.18 Comparison of total energies for Ru^{III} dichloride complexes of substituted picolinic acid.

As the observed Ru^{III} structures were not significantly different from the Ru^{IV} structures the energy differences between the calculated structures for the different isomers were in line with those for the Ru^{IV} structures, with the 2,3 and 2,6 being higher in energy than those of the 2,4 and 2,5 (Figure 3.18).

Comparison of the calculated structures of the 2,5 and 2,6 isomers with that of the X-ray structures showed that the calculated structures again overestimated the length of the ruthenium-nitrogen distance (0.039-0.054 Å) as shown in Table 3.8. Unlike the Ru^{IV} structures the Ru^{III} calculated structures overestimated the Ru-O and the Ru-Cl distances (Tables 3.9 and 3.10).

Table 3.8 Ru^{III} dichloride Ru-N bond lengths.

	2,5	2,6
X-ray	2.042(2) 2.041(2)	2.0829(19) 2.0778(19) 2.0726(18)
Calculated	2.0883	2.1269
Percentage Difference	+2.27 - +2.32	+2.11 - +2.62

Table 3.9 Ru^{III} dichloride Ru-O bond lengths.

	2,5	2,6
X-ray	2.024(2) 2.0279(18)	2.0239(15) 2.0277(16) 2.0208(15)
Calculated	2.0588	2.0468
Percentage Difference	+1.52 - +1.72	+0.94 - +1.29

Table 3.10 Ru^{III} dichloride Ru-Cl bond lengths.

	2,5	2,6
X-ray	2.3228(9) 2.3355(8)	2.3478(6) 2.3461(6) 2.3529(6)
Calculated	2.4269	2.4280
Percentage Difference	+3.91 - +4.48	+3.19 - +3.49

The length of the ruthenium-oxygen bonds being greater in the Ru^{III} contrasts with the crystal structures where the bonds are shorter than those of the Ru^{IV} species indicating that the computational model has greater accuracy for the Ru^{IV} complexes than for the Ru^{III}. However, such a discrepancy is not unexpected; as has already been stated, the

computational methods used have a tendency to overestimate bond lengths and the greatest discrepancy is within the range of such differences particularly with charge-carrying ligands. Such discrepancies between similar species of different oxidation states are as a result of the necessity of using the same basis sets and functionals. In order to compare the results of two separate calculations it is necessary to maintain continuity of calculational methodology. Even if an alternate model might provide better description with one species, it cannot be compared to that of the other if that other species is described using a different set of parameters. In the case of these $Ru^{III/IV}$ species, the Ru^{III} would in all probability benefit from the addition of diffuse functions into the basis set, to better accommodate their anionic nature, but such an addition would likely reduce the accuracy of the Ru^{IV} calculations.

Due to the only crystallised isomers of the Ru^{III} being the 2,5 and 2,6, analysis across the full range of isomers is not possible. However, the calculated structures of the Ru^{III} and Ru^{IV} can still be compared. As with the Ru^{IV} structures the Ru^{III} isomers are most stable with the chlorides in the trans configuration ($\sim$8 kJmol^{-1}). The Ru-N bond distances for the Ru^{III} structures were calculated to be 0.1-0.55% shorter than those of the corresponding Ru^{IV} complex.

Table 3.11 Calculated $Ru^{III/IV}$ trans dichloride Ru-N bond lengths.

	2,3	2,4	2,5	2,6
Ru^{IV}	2.0917	2.0923	2.0915	2.1386
Ru^{III}	2.0893	2.0858	2.0883	2.1269

The shortening of the Ru-N bond (Table 3.11) was attributed to a greater π-backbonding from the now electron-richer ruthenium into the pyridyl ring; but due to the already high oxidation state of the ruthenium, the effect is minimal.

Table 3.12 Calculated $Ru^{III/IV}$ trans dichloride Ru-O bond lengths.

	2,3	2,4	2,5	2,6
Ru^{IV}	2.0314	2.0321	2.0330	1.9567
Ru^{III}	2.0565	2.0562	2.0588	2.0468

Of greater interest is the increase in the bond distances of the Ru-O and Ru-Cl (Tables 3.12 and 3.13). In both cases, the bond distances increased but with the chloride having the greatest difference between oxidation states ($\sim$4.1% vs. $\sim$1.23% for Ru-O). In both

cases the 2,6 is once again the outlier, having the largest difference between oxidations states for the Ru-O distance and the lowest for the Ru-Cl distance. Given the charge carrying nature of these groups, the lower Ru-Cl difference can either be attributed to compensation for the large Ru-O difference or vice versa. What is clear to see is that the distance between the ruthenium centre and charge carrying coordinated atoms is greater in the Ru^{III} complex which is attributed to the decreased positive charge of the metal centre.

Table 3.13 Calculated Ru$^{III/IV}$ trans dichloride Ru-Cl bond lengths.

	2,3	2,4	2,5	2,6
Ru^{IV}	2.3322	2.3313	2.3317	2.4002
Ru^{III}	2.4274	2.4274	2.4269	2.4280

Table 3.14 Calculated Ru$^{III/IV}$ trans dichloride N-Ru-O angles.

	Ru^{IV}	Ru^{III}
2,3	79.62	78.90
2,4	79.75	79.11
2,5	79.81	79.10
2,6	78.49	79.11

Examination of the bite angles of the picolinic acid moieties (Table 3.14) showed that the Ru^{III} angles were slightly lower in the Ru^{IV} complexes but with the 2,6 isomer having a larger angle due to the longer ruthenium oxygen bond.

Electronic properties
In the same manner to the Ru^{IV} complexes, the electronic properties of the Ru^{III} dichlorides must be examined to determine how the molecular orbitals of the complexes are composed and how they relate to those of the Ru^{IV} complexes.

Compared to the triplet Ru^{IV} complexes, the Ru^{III} complexes exist in a doublet state with one rather than two single occupied orbitals (SOMO). The SOMO levels in the Ru^{III} complexes are raised in relation to its SOMO-1 level with the SOMO-1 being stabilised by electron pairing and now sits significantly closer in energy to the rest of the occupied orbitals (Figure 3.19). The energy difference between the SOMO and LUMO levels does not significantly increase between the oxidation states.
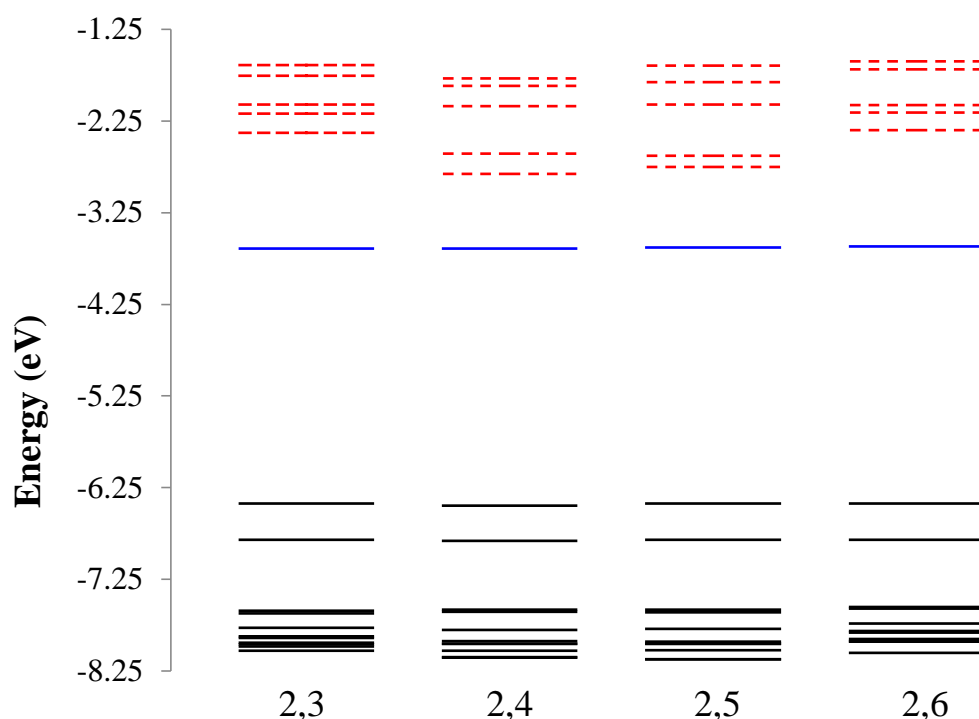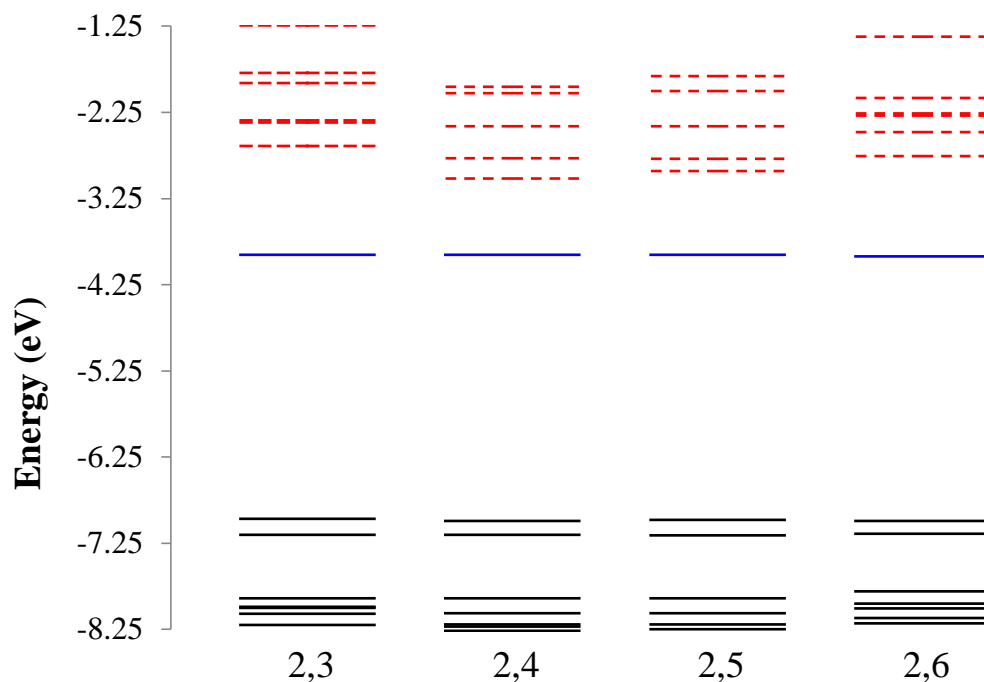
Figure 3.19 Calculated energy level diagrams for the frontier molecular orbitals for the four ruthenium III dichloride complexes of substituted dipicolinic acid. SOMO (−) and LUMOs (- - -).

As in the Ru^{IV} complexes, the largest energy difference is not the HOMO-LUMO gap; rather it is the SOMO-SOMO-1 with the SOMO-1 and SOMO-2 levels being comparatively raised in energy from the rest of the occupied orbitals. The SOMO-LUMO gap is not constant across the isomers, ranging from 0.815 eV for the 2,4 isomer to 1.271 eV for the 2,6. The SOMO level for all complexes displayed the same ruthenium centred $d\pi$ antibonding as was found in the Ru^{IV} structures; however, the ruthenium character was greater with correspondingly reduced contributions from the chlorides. As with the Ru^{IV} complexes the chlorides p_y orbitals match the symmetry of the ruthenium d_{yz}. The SOMO-1 has similar character to the HOMO-1 orbital in the Ru^{IV} complexes but with a shift of character from the ruthenium centre to the chlorides. The lengthening of the Ru-Cl bond is ascribed to the increased electron density in the now doubly occupied SOMO-1.
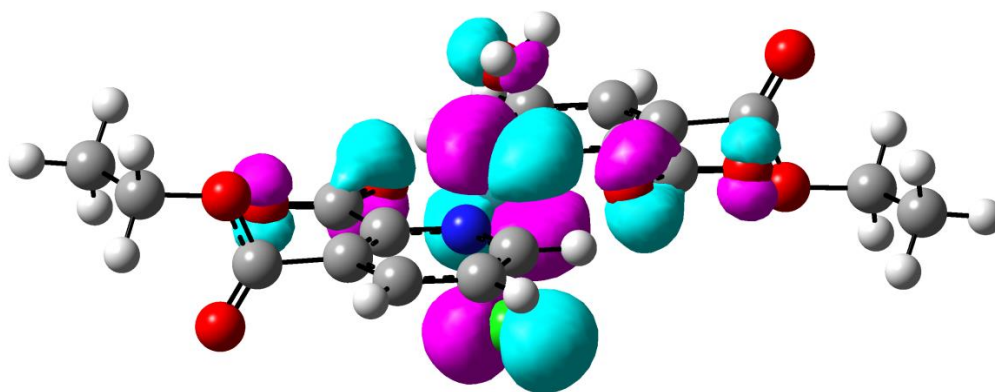
Figure 3.20 LUMO level of optimised structure of dichlorobis(3-ethoxycarbonyl(pyridine-2-carboxylate)) ruthenium (III) showing electron density centred on the pyridine rings and substituents.

The LUMO levels in the Ru^{III} structures differed from the Ru^{IV} as they were almost completely ring based π*-orbitals for the LUMO and LUMO+1, extending into the coordinated carboxyl group (Figure 3.20). The LUMO levels for the 2,4 and 2,5 isomers also include the anchoring carboxyl group as its p orbitals are aligned with those of the ring (Figure 3.21). The LUMO level from the Ru^{IV} structure is raised relative to these ring based orbitals to become the new LUMO+2. The orbital retained much of its original character across the four isomers with the 2,6 isomer still having approximately twice the metal centred character of the other isomers. The LUMO+3 and LUMO+4 were again ring based but with lower contributions from the coordinated carboxyls. The final d-based orbital, corresponding to the $d_{x^2-y^2}$, is the LUMO+5 and has similar metal-ring based character as the LUMO+3 orbital in the Ru^{IV} structures.
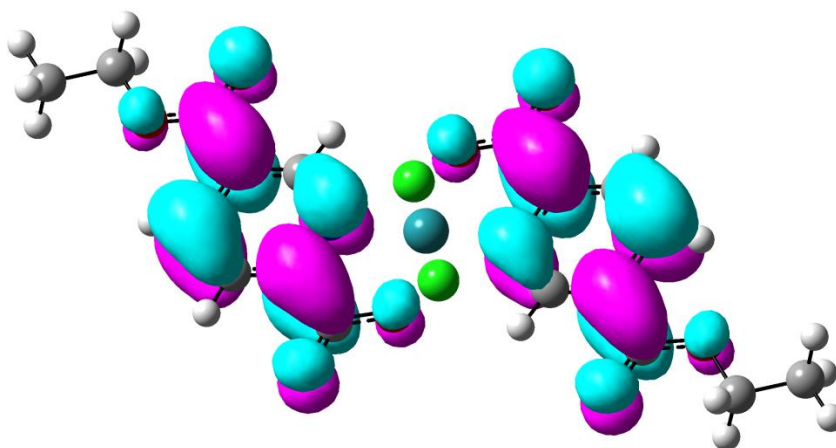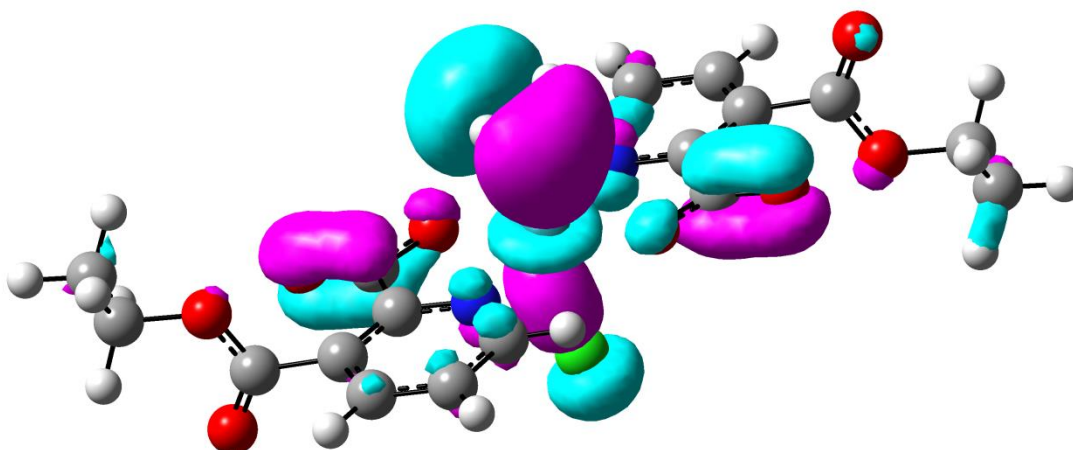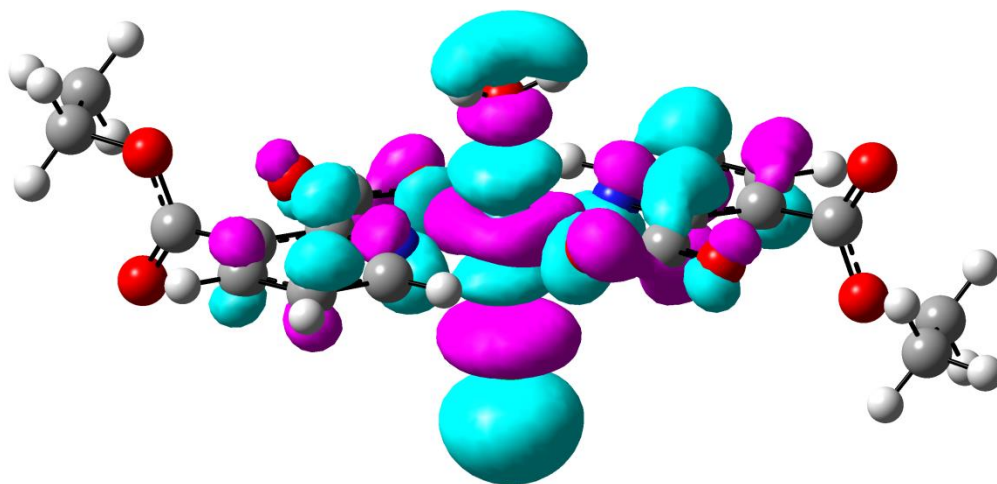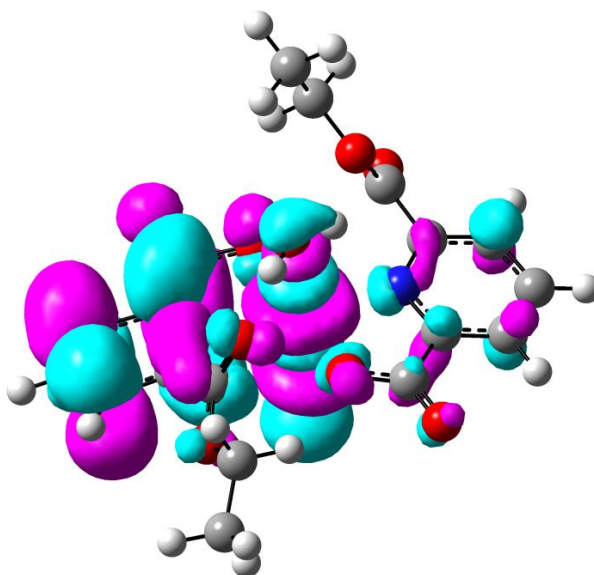

Figure 3.21 LUMO level of optimised structure of dichlorobis(5-ethoxycarbonyl(pyridine-2-carboxylate)) ruthenium (III) showing electron density centred on the pyridine rings and substituents.

Compared to the TDDFT UV-Vis spectra generated from the Ru^{IV} structures, the spectra for the Ru^{III} complexes displayed a better agreement with the experimental spectra from Chapter 2 (Figures 3.22-3.25). Of particular note is the loss of mid-to-low energy transitions corresponding to the region 450-700 nm. Significant transitions for the Ru^{III} complexes occur in the high energy visible to UV range. The loss of these transitions is not unexpected as the SOMO-1 level in the Ru^{III} complexes is significantly reduced in energy compared to its counterpart in the Ru^{IV} species. The reduction in energy means that transitions from this orbital to the delocalised π*-orbitals of the ring will require significantly more energy, putting those transitions into the UV range rather than the visible.

The bands from 360-460 are MLCT from the SOMO level to the LUMO and LUMO+1, shifting charge from the ruthenium centre to the pyridyl ring. The location of the primary transitions in this region appears to be dependent on the substitution pattern of the ring. The 2,4 and 2,5 complexes displayed red-shifting by 40-50 nm compared to the 2,3 and 2,6 isomers. The shift in these transitions is attributed to the extended nature of the π* LUMO and LUMO+1 levels into the anchoring groups of the 2,4 and 2,5 which is not available in the 2,3 and 2,6 due to contortion of the groups.

Transitions in the 300-400nm range include several strong LLCT transitions which include transitions from the anchoring group to the ring. These transitions appear to be static at ~320 nm but their intensity does decrease moving across the isomers from the 2,3 to the 2,6. The LMCT bands calculated for the Ru^{IV} structures are not present in these spectra due to the lack of two singly occupied orbitals and the increased energy of the highest occupied orbital. The first LMCT transition is not observed until below 275 nm. Those bands which are observed only include the d_{z^2} based LUMO+2 and not the $d_{x^2-y^2}$ as it lies too high in energy compared with the both ring and chloride based orbitals. The transitions in the region 275 nm and below are primarily composed of ligand-to-ligand transitions based on the rings, which exhibit higher intensities in the 2,4 and 2,5 isomers compared to those of the 2,3 and 2,6. As with the movement of the MLCT transitions, the intensities of these transitions is linked to the torsion of the anchoring group.

The significantly greater agreement between the experimental spectra and those of the calculated structures for the Ru^{III} complexes compared to those of the Ru^{IV} indicate that in aqueous solution the complexes exist in the reduced form. The transitions observed in the Ru^{III} calculated spectra while having a more limited absorbance in the visible region indicated that they would make superior dye sensitisers as the transitions in the visible region are MLCT, which puts them in the same category as ruthenium bipyridine based dyes. Of key interest is that these transitions shift depending on the torsion of the anchoring group which itself is dependent on the substitution pattern of that group.

The reduced nature of the complexes in an aqueous environment indicate the Ru^{IV} complexes may be acting as water oxidation agents as the only oxidisable substance available to the complexes is the water itself. It is doubtful that this is a catalytic process as there is no sacrificial oxidant present and no substrate to stabilise any photocatalytic cycle.
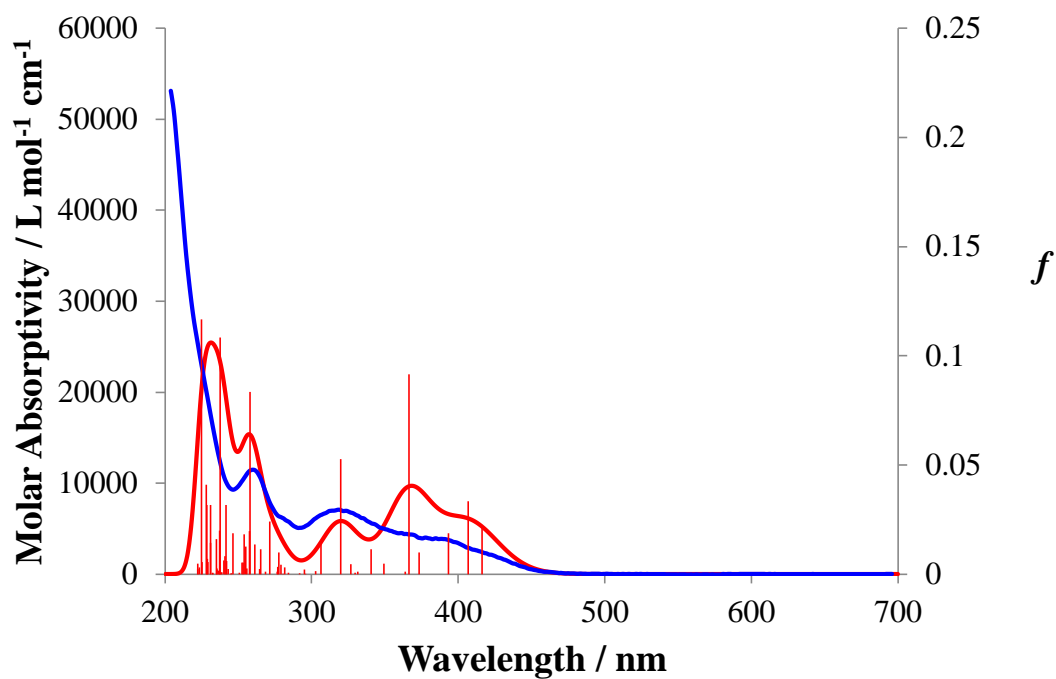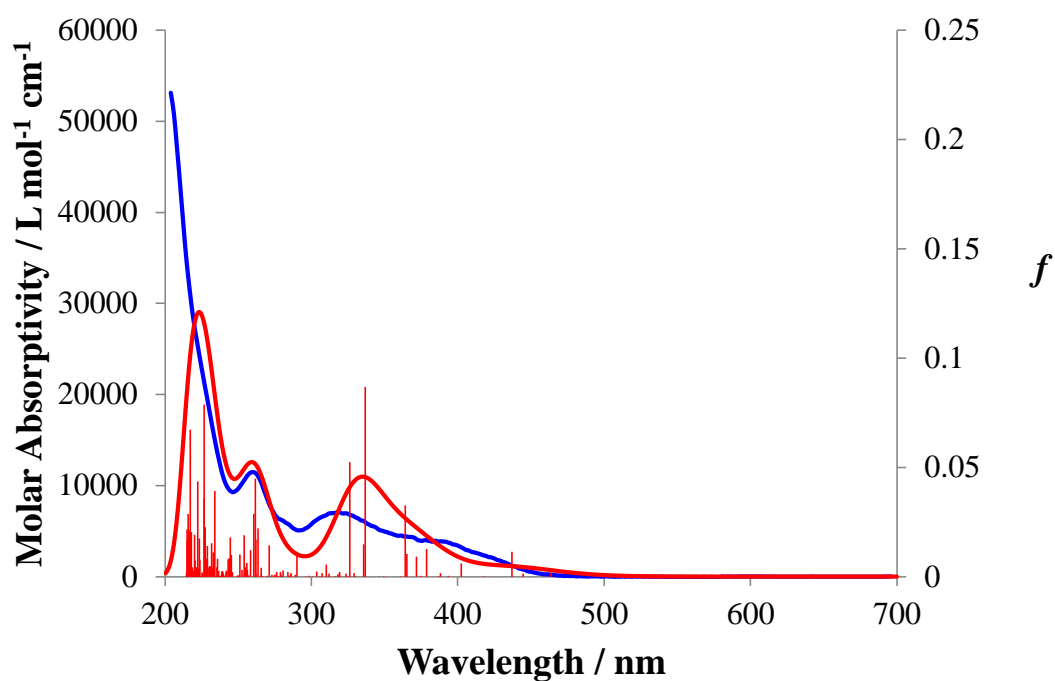
Figure 3.22 Comparison of experimental (blue) and calculated UV-Vis spectrum of dichlorobis(3-ethoxycarbonyl(pyridine-2-carboxylate)) ruthenium (III) (red) .
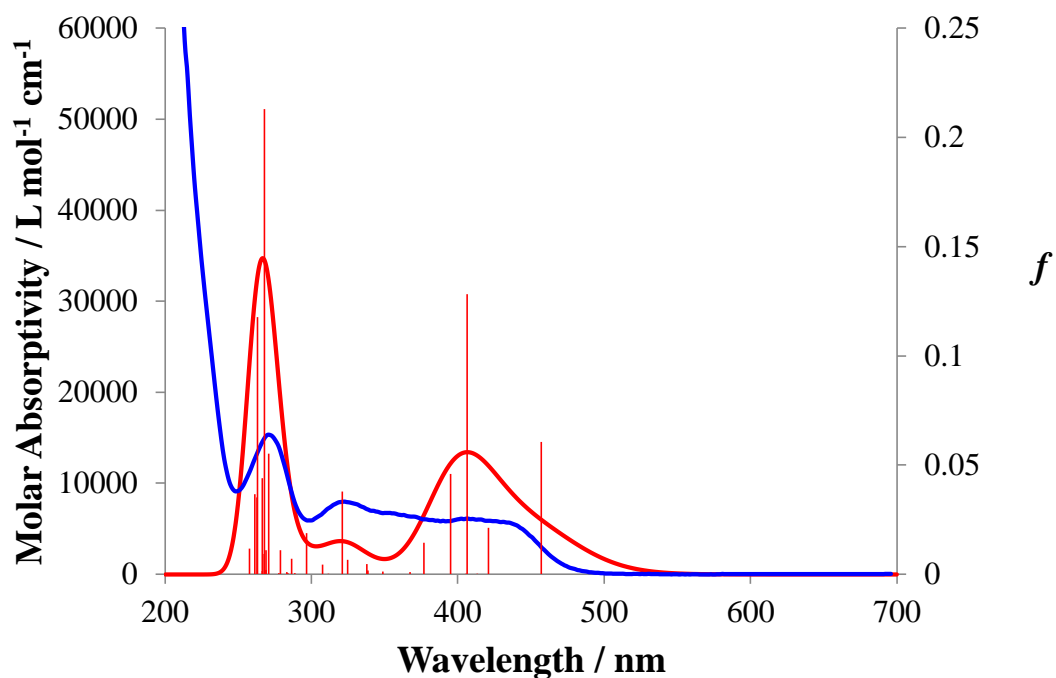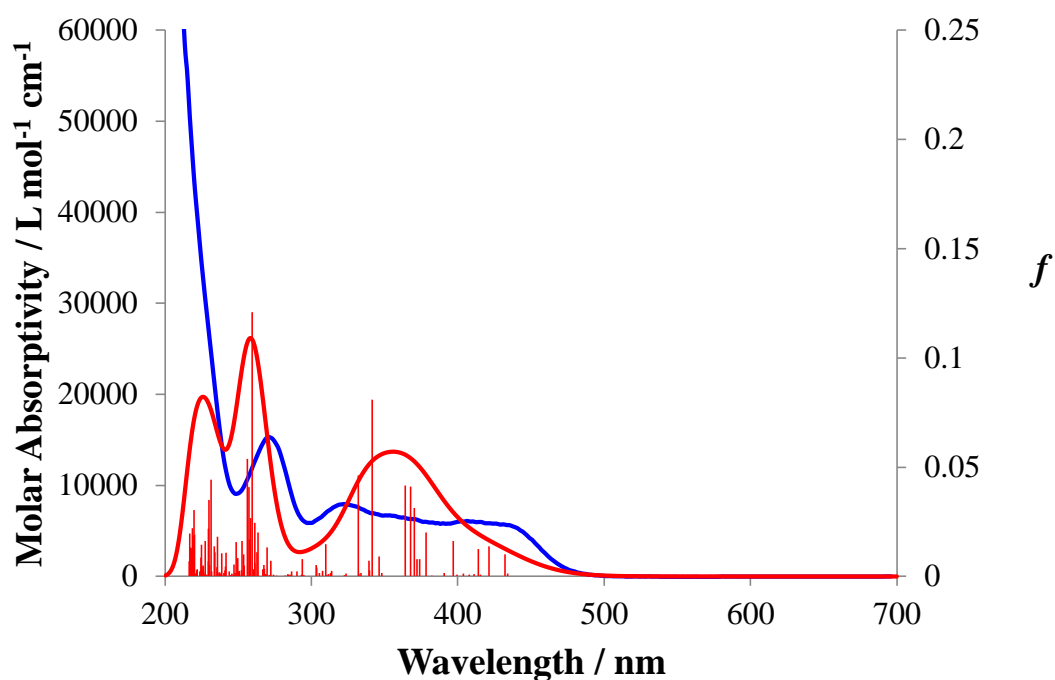

Figure 3.23 Comparison of experimental (blue) and calculated UV-Vis spectrum of dichlorobis(4-ethoxycarbonyl(pyridine-2-carboxylate)) ruthenium (III) (red).
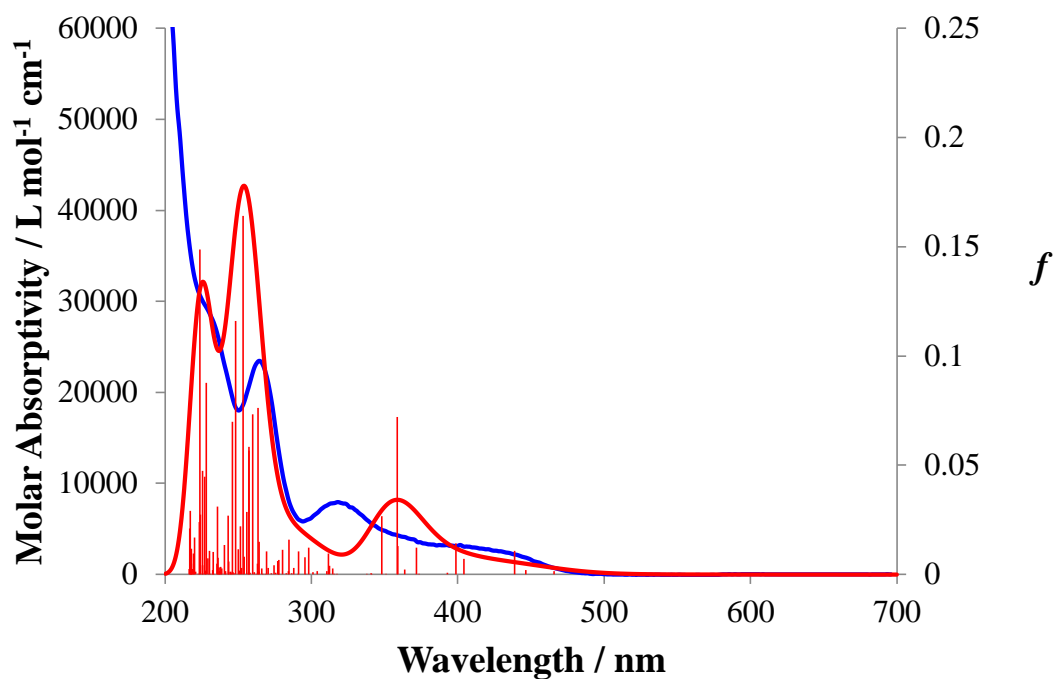
153
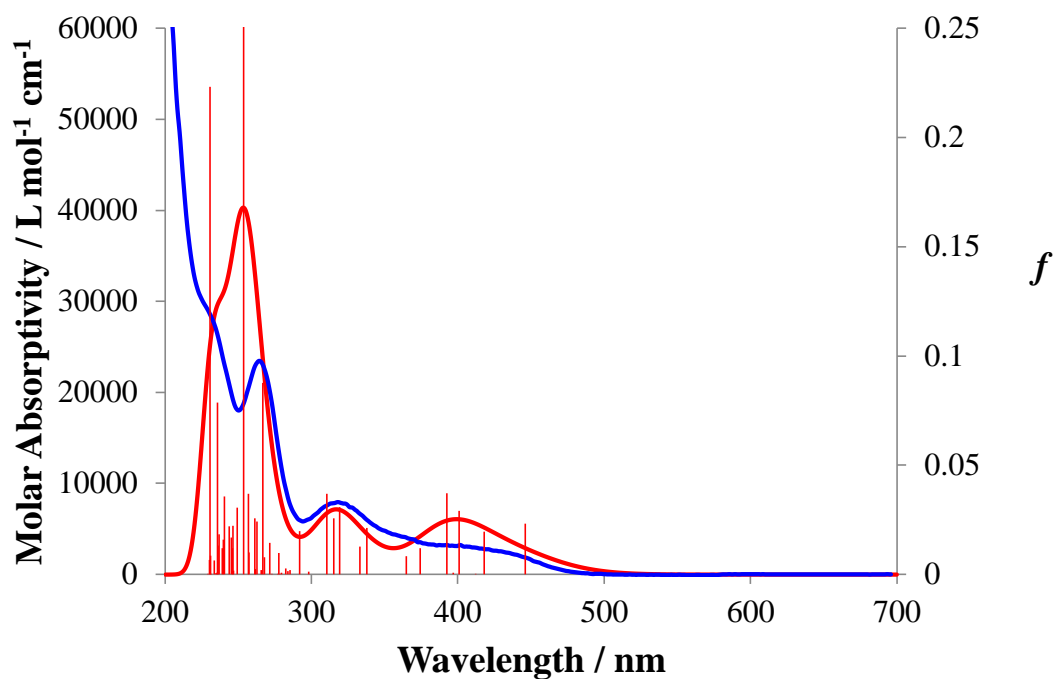
Figure 3.24 Comparison of experimental (blue) and calculated UV-Vis spectrum of dichlorobis(5-ethoxycarbonyl(pyridine-2-carboxylate)) ruthenium (III) (red).
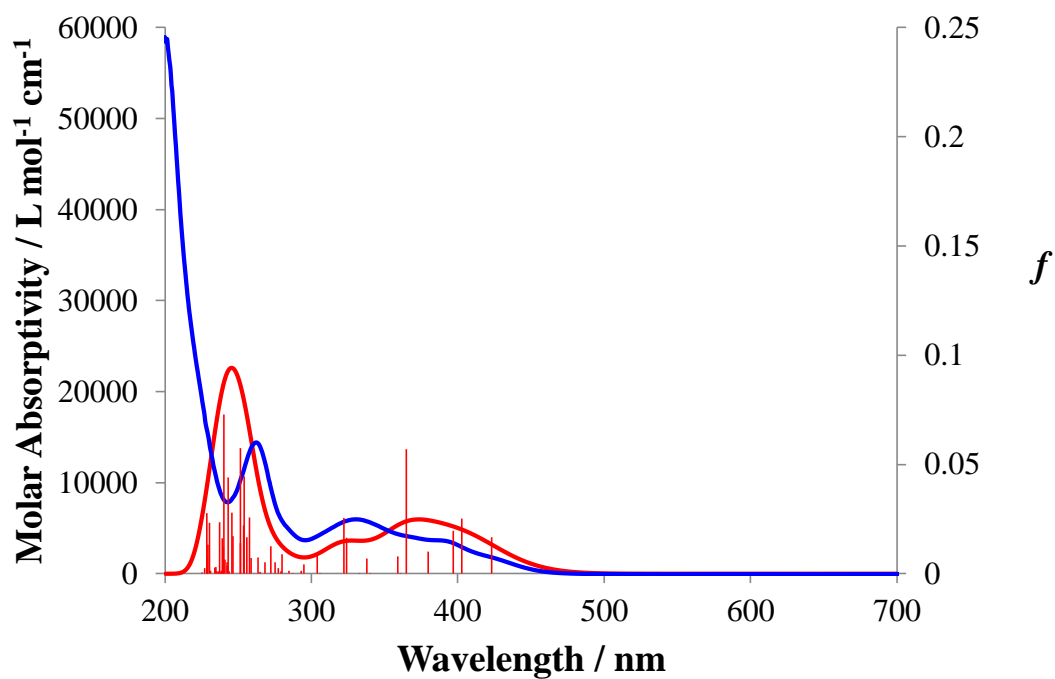
Figure 3.25 Comparison of experimental (blue) and calculated UV-Vis spectrum of dichlorobis(6-ethoxycarbonyl(pyridine-2-carboxylate)) ruthenium (III) (red).

The variation in reduction potentials between the isomers was not as easily explained. This is due to the calculation methods for Ru^{IV}/Ru^{III} couples being, as of yet, not as rigorously examined as those of Ru^{III}/Ru^{II}. The cause of the difference in the redox potentials is also more complex than the differences in the UV-vis spectra. The redox potential is dependent on multiple, difficult to differentiate, factors such as the effective nuclear charge of the ruthenium, frontier orbital compositions and solvent interactions, to name but a few. As all these aspects and more vary between the different isomers in a non-sequential manner it is not possible to attribute the variation in redox potential to a single characteristic.

Despite the spectra for the calculated Ru^{III} dichloride species showing good agreement with the experimental spectra, examination of the chloroaqua species is required. Due to the observed exchange of one of the chlorides for an aqua group it is necessary to determine if such an exchange is likely and what effect it would have across the range of isomers.

Ru^{III} chloraqua species

The substituted form that was investigated was the monosubstituted rather than the disubstituted as it was the only aqua species to be observed for more than one isomer. Differing from the dichloride these species were neutral rather than anionic but retaining the dichlorides doublet d^5 electron configuration. Examination of the energy differences between the isomers immediately shows that theses complexes differ from the dichlorides. In the chloraqua complexes it is the 2, 3 rather than the 2,6 which is the highest in energy (Figure 3.26).
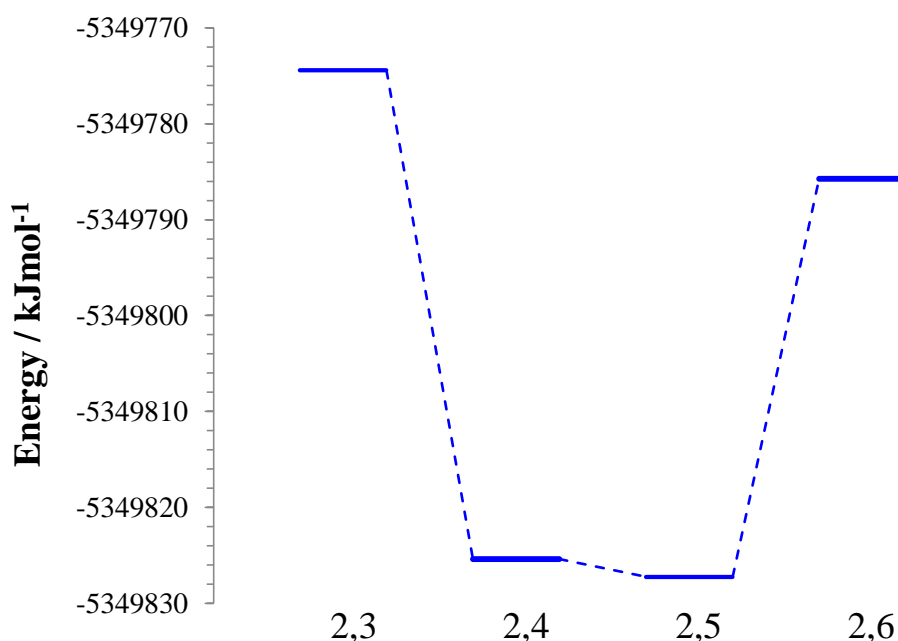
Figure 3.26 Comparison of total energies for Ru^{III} chloraqua complexes of substituted picolinic acid.

Examination of the optimised structures show that the 2,6 isomer has an intramolecular H-bond between the coordinated water and the carbonyl of one of the anchoring groups. The H-bonding distorts the geometry of the complex (Figure 3.27) but lowers the total energy to the point that it is now lower than that of the 2,3 complex. As the 2,6 complex is the only isomer in which the anchoring group impinges on the ruthenium coordination sphere, it is the only isomer in which this H-bonding is observed.
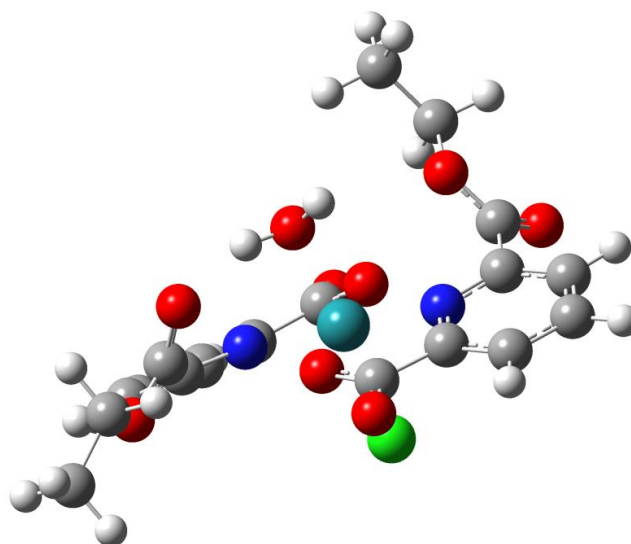
Figure 3.27 Trans configuration of chloroaquabis(6-ethoxycarbonyl(pyridine-2-carboxylate)) ruthenium (III) showing distortion due to hydrogen-bonded anchoring carboxylate and coordinated aqua group.

The variation in bond distances between the experimental and calculated structures of the chloroaqua complexes were comparable to the Ru^{III} dichloride complexes for nitrogen and oxygen (approx. 2.5% and 1.5% respectively) (Tables 3.15 and 3.16). The chlorides exhibited closer agreement between calculated and experimental structures for the chloroaqua species compared with the dichloride (Table 3.17). The difference in experimental and calculated ruthenium-oxygen distances for the coordinated aqua group is comparatively large (4-6%) when contrasted to that of the chloride (~2.5%) (Table 3.18).

Table 3.15 Ru^{III} dichloride Ru-N bond lengths.

	2,3	2,5
X-ray	2.046(2)	2.047(3)
	2.046(2)	2.041(3)
Calculated	2.09308	2.09178
	2.09524	2.09366
Percentage Difference	+2.3 - +2.4	+2.19 – +2.59

Table 3.16 Ru^{III} dichloride Ru-O bond lengths.

	2,3	2,5
X-ray	2.017(2)	2.018(3)
	2.005(2)	2.021(3)
Calculated	2.04304	2.04497
	2.03970	2.04145
Percentage Difference	+1.13- +1.77	+1.01 - +1.34

Table 3.17 Ru^{III} dichloride Ru-Cl bond lengths.

	2,5	2,6
X-ray	2.2968(7)	2.3070(13)
Calculated	2.36393	2.36261
Percentage Difference	+2.92	+2.41

Table 3.18 Ru^{III} dichloride Ru-H$_2$O bond lengths.

	2,5	2,6
X-ray	2.084(2)	2.060(3)
Calculated	2.16957	2.17336
Percentage Difference	+4.11	+5.50

Overlaying the calculated and X-ray structures showed that the torsion observed in the Ru^{IV} and Ru^{III} anchoring and ethyl groups remains (Figure 3.28). The orientation of the aqua group in both complexes is also rotated around the z-axis due to the H-bonding interactions with surrounding water molecules and ruthenium complexes in the crystal lattice not being present in the calculated structure. This change in orientation is the probable reason for the variance between the calculated and experimental ruthenium-oxygen bond distances.
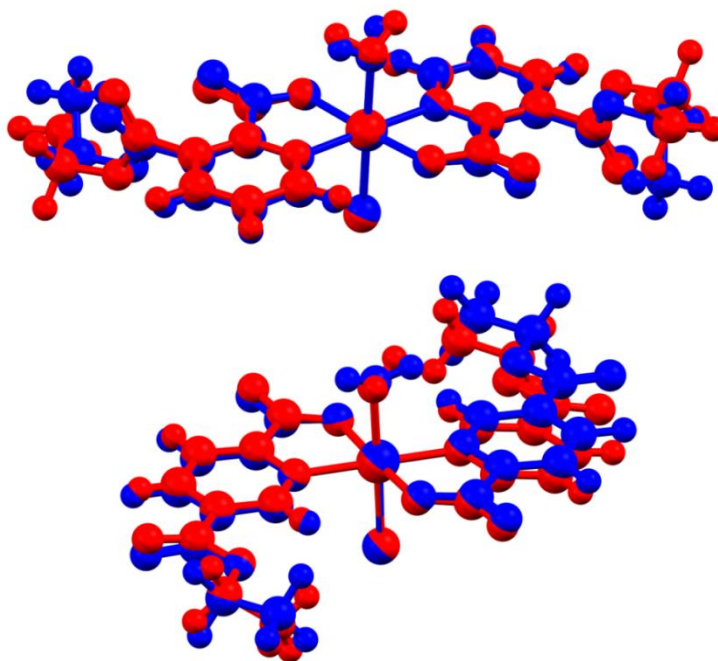
Figure 3.28 Overlap diagrams of X-ray (blue) and calculated (red) structures of the trans configuration of chloroaquabis(3-ethoxycarbonyl(pyridine-2-carboxylate)) ruthenium (III) and chloroaquabis(5-ethoxycarbonyl(pyridine-2-carboxylate)) ruthenium (III).

Table 3.19 Calculated Ru^{III} trans dichloride/chloroaqua Ru-N bond lengths.

	2,3	2,4	2,5	2,6
Dichloride	2.0893	2.0858	2.0883	2.1269
Chloroaqua	2.09308	2.09055	2.09178	2.12457
	2.09524	2.09018	2.09366	2.12517

Compared to the anionic dichloride species the chloroaqua complexes exhibited a slight lengthening of the ruthenium-nitrogen bond distance (Table 3.19). As the shortening of the Ru-N distance in the dichloride compared to the Ru^{IV} complexes was ascribed to increased π-backbonding from the electron rich ruthenium into the pyridyl ring, so must the lengthening of this distance in the chloroaqua complexes be attributed to a decrease in this effect.

Table 3.20 Calculated Ru^{III} trans dichloride/chloroaqua Ru-O bond lengths.

	2,3	2,4	2,5	2,6
Dichloride	2.0565	2.0562	2.0588	2.0468
Chloroaqua	2.04304	2.03909	2.04497	2.03968
	2.03970	2.04166	2.04145	2.03858

Conversely, both the ruthenium-oxygen (carboxylic) and ruthenium-chloride distances are shorter in the chloroaqua species (Tables 3.20 and 3.21) As with the ruthenium-nitrogen distance the effect is caused by the now decreased electron density on the ruthenium as a result of the complex being neutral rather than ionic and therefore having an increased positive charge on the ruthenium centre compared to the dichloride. The chloride has the contributing effect of no longer being trans influenced by its counterpart across the ruthenium, resulting in a shorter bond but also itself elongating the ruthenium-aqua bond, an effect which may be overestimated in the calculated structure but which is combined with the steric effects within the crystal lattice to make determination of the extent of that effect difficult.

Table 3.21 Calculated Ru^{III} trans dichloride/chloroaqua Ru-Cl bond lengths.

	2,3	2,4	2,5	2,6
Dichloride	2.4274	2.4274	2.4269	2.4280
Chloroaqua	2.36393	2.36299	2.36261	2.38938

Table 3.22 Calculated Ru^{III} trans chloroaqua Ru-H$_2$O bond lengths.

	2,3	2,4	2,5	2,6
Chloroaqua	2.16957	2.17530	2.17336	2.13918

Electronic properties

The chloroaqua complexes exhibit similar frontier orbital energies to those of the dichloride with the SOMO being closer in energy to the LUMO than the SOMO-1 and the SOMO-1 and SOMO-2 being close in energy and slightly raised in energy when compared to the remaining occupied orbitals (Figure 3.29).

Figure 3.29 Calculated energy level diagrams for the frontier molecular orbitals for the four ruthenium III chloroaqua complexes of substituted dipicolinic acid. SOMO (−) and LUMOs (- - -).

The SOMO-LUMO gap does not vary considerably from that of the Ru^{III} dichloride complexes ($\leq$ 0.09 eV) but the SOMO-SOMO-1 gap differed by 0.27-0.29 eV. The frontier orbital composition differs as expected with the aqua group contributing less electron density to the orbitals due to the oxygen bonding and antibonding orbitals being lower in energy. The SOMO-2 did not experience any significant change as it does not include contributions from the chloride or aqua group as the d orbital lies in the x-y plane.

Figure 3.30 SOMO level of optimised structure of chloroaquabis(3-ethoxycarbonyl(pyridine-2-carboxylate)) ruthenium (III) showing electron density centred on the ruthenium and coordinated chloride.

The bonding orbitals for the chloaqua species (Figure 3.31) are similar to those of the dichloride with the composition of the pyridyl ring and carboxyl bonding orbitals being predominantly unchanged. The chloride and aqua bonding orbitals experience more significant contribution from the aqua oxygen compared to that of the chloride.

Figure 3.31 H_2O σ-bonding orbital of optimised structure of chloroaquabis(3-ethoxycarbonyl(pyridine-2-carboxylate)) ruthenium (III) showing electron density centred on the coordinated aqua group.

The LUMO levels did not significantly vary with the first unoccupied orbitals remaining ring-based with the LUMO+2 and LUMO+5 being the metal-centred orbitals. The LUMO+5, like the SOMO-2, lies in the x-y plane so does not contain contributions from the chloride or aqua groups; but the LUMO+2, being d_{z^2} equates to being the antibonding counterpart of the bonding orbitals shown in Figure 3.32.

Figure 3.32 LUMO+2 level of optimised structure of chloroaquabis(3-ethoxycarbonyl(pyridine-2-carboxylate)) ruthenium (III) showing electron density centred on the ruthenium and coordinated chloride.

The 2,6 isomer is significantly different from the other three isomers as the distortion of the hydrogen bonded ligand from the plane of the other pyridyl ring reduces the equal distribution of electron density across the molecule (Figure 3.33). The SOMO, SOMO-1 and SOMO-2 levels are not significantly affected by this change but the LUMO, LUMO+2 and LUMO+3 are. These unoccupied orbitals display significantly more electron density on the ligand which hydrogen bonds to the aqua group, and in fact splits the d_{z^2} across the LUMO+2 and LUMO+3 levels.

Figure 3.33 LUMO+2 level of optimised structure of chloroaquabis(6-ethoxycarbonyl(pyridine-2-carboxylate)) ruthenium (III) showing electron density centred on the pyridine ring with the H-bonded carboxylate group, ruthenium and the coordinated chloride.

The TDDFT UV-Vis spectra, generated for the chloroaqua structures, displayed similar agreement with both the experimental spectra and those generated for the Ru^{III} dichloride calculated structures (Figures 3.34-3.37).

The two sets of calculated spectra display good agreement below 300 nm but in the region 300-500 nm the chloroaqua spectra are blue-shifted by between 25 and 50 nm, depending on the isomer. Examination of transitions with similar intensities in that range indicates that it is the movement of a few key transitions between frontier orbitals that cause this effect.

In the chloroaqua spectra the MLCT for the 2,4 and 2,5 isomers are still red shifted by 40-50 nm compared to those of the 2,3 isomer as was the case in the dichloride spectra. The LLCT transitions which were observed in the 300-400 nm range for the dichloride are either significantly suppressed or shifted in the chloroaqua spectra. While this would be expected for chloride to ring or ring to chloride transitions, as there is only one chloride remaining to promote to/from, the reduction in the transitions from anchoring group to ring is less expected.

The 2,6 isomer, being the most distinct of the isomers due to the intramolecular H-bond, has the greatest agreement between calculated and experimental spectra and also one of the most complex series of transitions. While the 2,6 isomer does contain the MLCT observed in the other isomers the intensity of such transitions is lower and is also of an unsymmetrical nature. Unlike the transitions in the other isomers the 2,6 MLCT are to a single ligand and not to both picolinic acids equally. The difference in the orbital compositions of the π^* LUMO levels between the H-bonded and unbonded picolinic acids mean that what were non charge transfer π^* transitions for the other isomers become LLCT between the two rings for the 2,6, and are observed as low as 388 nm.

Figure 3.34 Comparison of experimental (blue) and calculated UV-Vis spectrum of chloroaquabis(3-ethoxycarbonyl(pyridine-2-carboxylate)) ruthenium (III) (red).

Figure 3.35 Comparison of experimental (blue) and calculated UV-Vis spectrum of chloroaquabis(4-ethoxycarbonyl(pyridine-2-carboxylate)) ruthenium (III) (red).

Figure 3.36 Comparison of experimental (blue) and calculated UV-Vis spectrum of chloroaquabis(5-ethoxycarbonyl(pyridine-2-carboxylate)) ruthenium (III) (red).
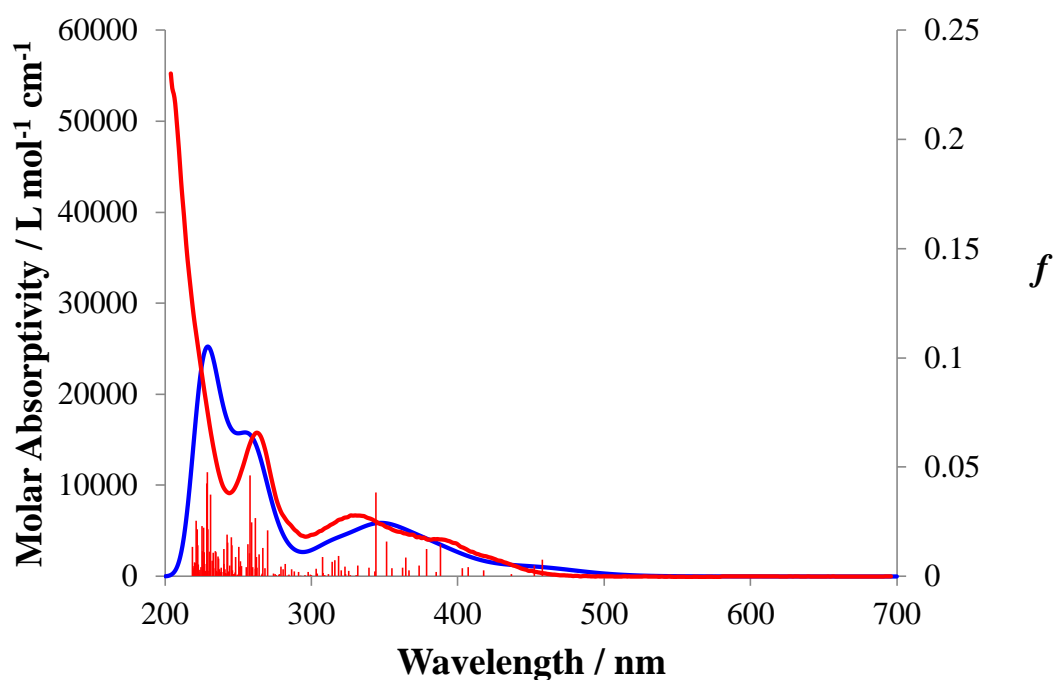
Figure 3.37 Comparison of experimental (blue) and calculated UV-Vis spectrum of chloroaquabis(6-ethoxycarbonyl(pyridine-2-carboxylate)) ruthenium (III) (red).

Conclusions

To conclude, the complexes in the +4 oxidation state exist in a triplet spin state and that the trans chloride form is more favoured than the cis form. It is now more probable that the ruthenium complexes exist in aqueous solution in the +3 oxidation state and not the +4 as initially believed. The first three occupied orbitals of the +3 complexes are metal based antibonding with the SOMO level sitting closer to the LUMO than the SOMO-1. The LUMO levels are predominantly $\pi*$ with remaining two metal antibonding orbitals sitting slightly higher in energy. The orbital compositions vary across the isomers with the 2,6 being the most divergent. The TDDFT spectra show that the movement of the anchoring group around the ring shifts the MLCT bands depending on whether or not the anchoring group lies in the plane of the ring. The chloroaqua complexes are very similar to those of the dichloride but with the MLCT bands in the TDDFT spectra being blue shifted. The 2,6 chloroaqua isomer has an intra-molecular H-bond which distorts the structure and the subsequent electronic and spectral properties. Connecting to the information gained in Chapter 2 it can now be stated that while the complexes are formed with ruthenium in a +4 oxidation state, they are reduced to +3 upon dissolution in an aqueous environment. As this reduction occurs in an aqueous environment it is assumed that this is the reducing agent with the complexes acting as water oxidation agents. As dichloride structures were obtained for the Ru^{III} oxidation state it might be assumed that the reduction occurs without requiring coordination of an aqua group to the ruthenium centre. This assumption doesn't however take into account the possibility that the Ru^{III} dichlorides are merely fractionally crystallised out of solution as are the chloroaqua complexes. Since computational analysis shows similar results for the UV spectra of dichloride and chloroaqua complexes, it is possible, if not likely, that they both exist in solution at the same time. In this scenario, the chloroaqua species act as poor mononuclear water oxidation catalysts and the Ru^{IV} dichlorides as a sacrificial oxidant (stronger than Ce^{IV}), forming the Ru^{III} dichloride species as a result. As to the performance as dye sensitisers, there does not appear to be an individual characteristic to which that variation can be attributed.

Citations

1. Hohenberg, P.; Kohn, W., Inhomogeneous Electron Gas. *Phys. Rev.* **1964,** *136* (3B), B864-B871.
2. Kohn, W.; Sham, L. J., Self-Consistent Equations Including Exchange and Correlation Effects. *Phys. Rev.* **1965,** *140* (4A), A1133-A1138.
3. Jensen, F., *Introduction to Computational Chemistry*. John Wiley & Sons: 2006.
4. Becke, A. D., Density-functional exchange-energy approximation with correct asymptotic behavior. *Phys. Rev. A* **1988,** *38* (6), 3098-3100.
5. Miehlich, B.; Savin, A.; Stoll, H.; Preuss, H., Results obtained with the correlation energy density functionals of becke and Lee, Yang and Parr. *Chem. Phys. Lett.* **1989,** *157* (3), 200-206.
6. Becke, A. D., Density-functional thermochemistry. III. The role of exact exchange. *J. Chem. Phys.* **1993,** *98* (7), 5648-5652.
7. Perdew, J. P.; Chevary, J. A.; Vosko, S. H.; Jackson, K. A.; Pederson, M. R.; Singh, D. J.; Fiolhais, C., Atoms, molecules, solids, and surfaces: Applications of the generalized gradient approximation for exchange and correlation. *Phys. Rev. B* **1992,** *46* (11), 6671-6687.
8. Martin, J. M. L.; Sundermann, A., Correlation consistent valence basis sets for use with the Stuttgart–Dresden–Bonn relativistic effective core potentials: The atoms Ga–Kr and In–Xe. *J. Chem. Phys.* **2001,** *114* (8), 3408-3420.
9. Hay, P. J.; Wadt, W. R., Ab initio effective core potentials for molecular calculations. Potentials for K to Au including the outermost core orbitals. *J. Chem. Phys.* **1985,** *82* (1), 299-310.
10. Ditchfield, R.; Hehre, W. J.; Pople, J. A., Self-Consistent Molecular-Orbital Methods. IX. An Extended Gaussian-Type Basis for Molecular-Orbital Studies of Organic Molecules. *J. Chem. Phys.* **1971,** *54* (2), 724-728.
11. Miertuš, S.; Scrocco, E.; Tomasi, J., Electrostatic interaction of a solute with a continuum. A direct utilizaion of AB initio molecular potentials for the prevision of solvent effects. *Chem. Phys.* **1981,** *55* (1), 117-129.
12. Bauernschmitt, R.; Ahlrichs, R., Treatment of electronic excitations within the adiabatic approximation of time dependent density functional theory. *Chem. Phys. Lett.* **1996,** *256* (4–5), 454-464.
13. Frisch, M. J.; Trucks, G. W.; Schlegel, H. B.; Scuseria, G. E.; Robb, M. A.; Cheeseman, J. R.; Scalmani, G.; Barone, V.; Mennucci, B.; Petersson, G. A.; Nakatsuji, H.; Caricato, M.; Li, X.; Hratchian, H. P.; Izmaylov, A. F.; Bloino, J.; Zheng, G.; Sonnenberg, J. L.; Hada, M.; Ehara, M.; Toyota, K.; Fukuda, R.; Hasegawa, J.; Ishida, M.; Nakajima, T.; Honda, Y.; Kitao, O.; Nakai, H.; Vreven, T.; Montgomery Jr., J. A.; Peralta, J. E.; Ogliaro, F.; Bearpark, M. J.; Heyd, J.; Brothers, E. N.; Kudin, K. N.; Staroverov, V. N.; Kobayashi, R.; Normand, J.; Raghavachari, K.; Rendell, A. P.; Burant, J. C.; Iyengar, S. S.; Tomasi, J.; Cossi, M.; Rega, N.; Millam, N. J.; Klene, M.; Knox, J. E.; Cross, J. B.; Bakken, V.; Adamo, C.; Jaramillo, J.; Gomperts, R.; Stratmann, R. E.; Yazyev, O.; Austin, A. J.; Cammi, R.; Pomelli, C.; Ochterski, J. W.; Martin, R. L.; Morokuma, K.; Zakrzewski, V. G.; Voth, G. A.; Salvador, P.; Dannenberg, J. J.; Dapprich, S.; Daniels, A. D.; Farkas, Ö.; Foresman, J. B.; Ortiz, J. V.; Cioslowski, J.; Fox, D. J. *Gaussian 09*, Gaussian, Inc.: Wallingford, CT, USA, 2009.

14.   O'Boyle, N. M.; Tenderholt, A. L.; Langner, K. M., cclib: A library for package-independent computational chemistry algorithms. *J. Comput. Chem.* **2008,** *29* (5), 839-845.

Chapter IV
Amide containing ligand design for enhancing the chromaphores of ruthenium based dyes.

Introduction

In the previous two chapters the complexes examined were all based on carboxylate substituted picolinic acid. What was discovered was that those complexes can exist in both a Ru^{IV} oxidation state as dichlorides and Ru^{III} as both dichloride and chloroaqua species. However, the complexes performed poorly as dyes, with absorption being limited to the high-energy-visible and UV regions of the spectrum. In order for us to further understand the factors which affect the performance of ruthenium-based dye sensitisers, better absorbing dyes with similar properties to the picolinic acid complexes must be produced.

The object of this chapter was to survey a series of anionic ligands to examine if they held any promise for the development and understanding of ruthenium based dyes for use in heterogeneous water oxidation processes. The goal was, therefore, to develop a simple synthetic route for a series of complexes derived from commonly available ruthenium precursors. If such a procedure could be possible, the synthesised complexes could be compared to the earlier work on the picolinic acid complexes. In addition, these complexes could act as a framework not only to investigate the properties of ruthenium-based sensitiser dyes but to also develop cheaper alternatives to the more expensive bipyridine- and terpyridine-based dyes.

In order to build on the work of the previous chapters, it was decided to develop the picolinic acid moiety, as it allows for comparison with the previous work and would be easily modified in the future. The problem that immediately arises is that in order to have the same range of substitution patterns as in the dipicolinic acid based dyes, modification must either be of the ruthenium coordinated chlorides or on the picolinic acid itself.
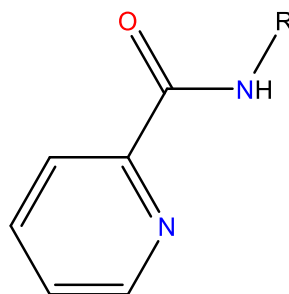
Figure 4.1 Picolinamide moiety.

While exchange of the chlorides would be the easiest option to take, it has been shown in chapter 3, where an aqua group replaced a chloride, that such an exchange does not significantly enhance the absorption profile. The picolinic acid is alternately difficult to modify as any modification to the acid group would render the group neutral rather than anionic, thus making comparison with the previous examples tenuous at best. The option that was taken was to replace the coordinating oxygen in the acid with nitrogen, allowing for further modification while maintaining the ligand as anionic (Figure 4.1). While this does distance the subsequently synthesised ligands from the dipicolinic acids it is the option most likely to preserve the primary characteristics of those complexes.

The first three ligands to be explored were based on picolinic acid with three different linkers. The linkers were ethane, benzene and benzoic acid (Figure 4.2). The ethylene and ortho-phenylene bridged ligands are known in the literature.[1-2] The ethylene linked ligand is the simplest of the three and most similar to picolinic acid. Its two sp^3 hybridised carbons do not enhance electron delocalisation while both the ortho-phenylene and carboxyl substituted ortho-phenylene bridged ligands will.
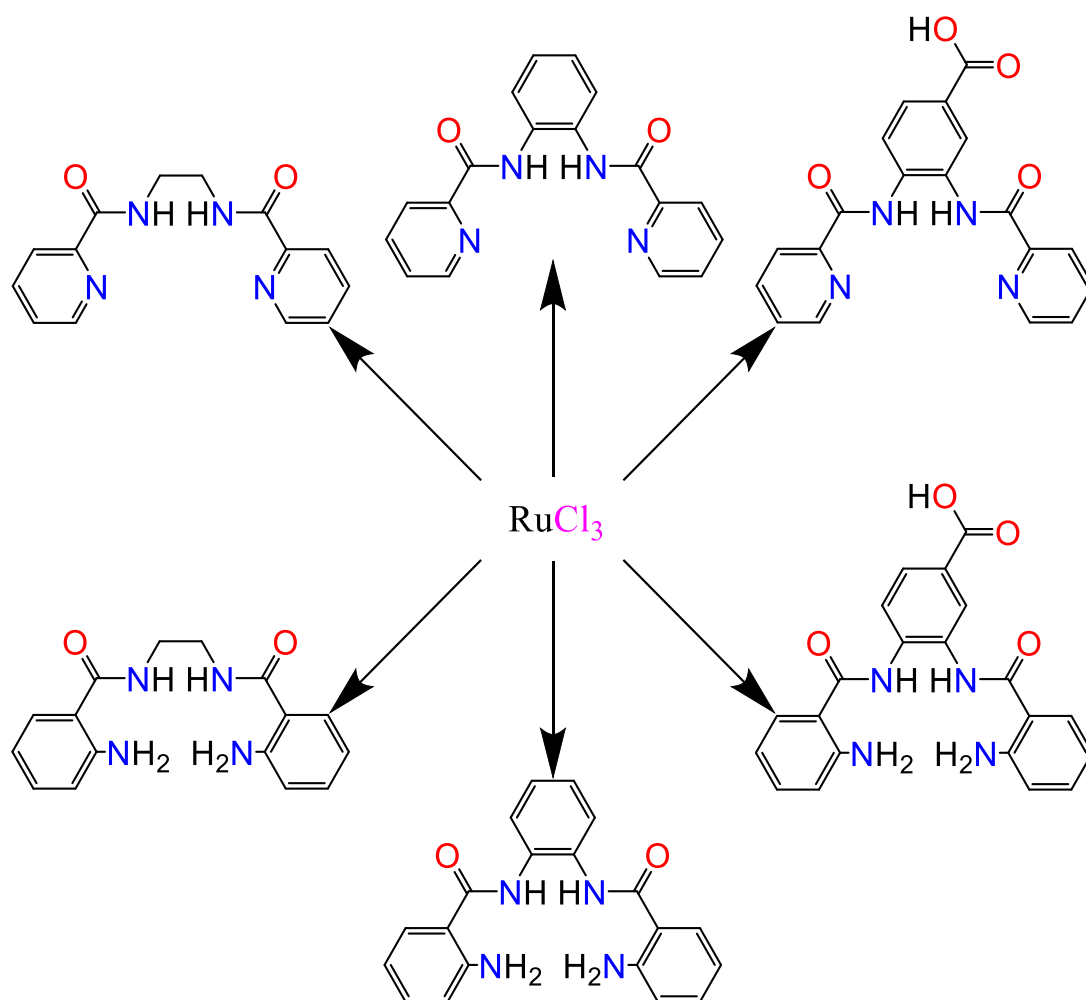
Figure 4.2 Acid amide ligands.

In addition, the aromatic nature of the aryl group allows for the ligand to undergo redox activity itself (Figure 4.3). As was demonstrated by Wieghardt et al in 2000, the greater delocalised nature of this ligand means that it is able to stabilise higher oxidation state metal centres such as iron (IV).[3] The stabilisation of higher oxidation state Ru^{IV} complexes would be advantageous as the TDDFT spectra of the Ru^{IV} complexes, discussed in Chapter 3, showed increased absorption in the visible region compared to the Ru^{III} complexes. Ru^{III} complexes derived from these ligands should also experience increased absorption due to the lowering of the ligand centred π^* orbitals compared to the orbitals located on the metal. A benzoic acid bridging group was included in this survey as it would test for effects of an anchoring group on the expanded, delocalised π orbitals.
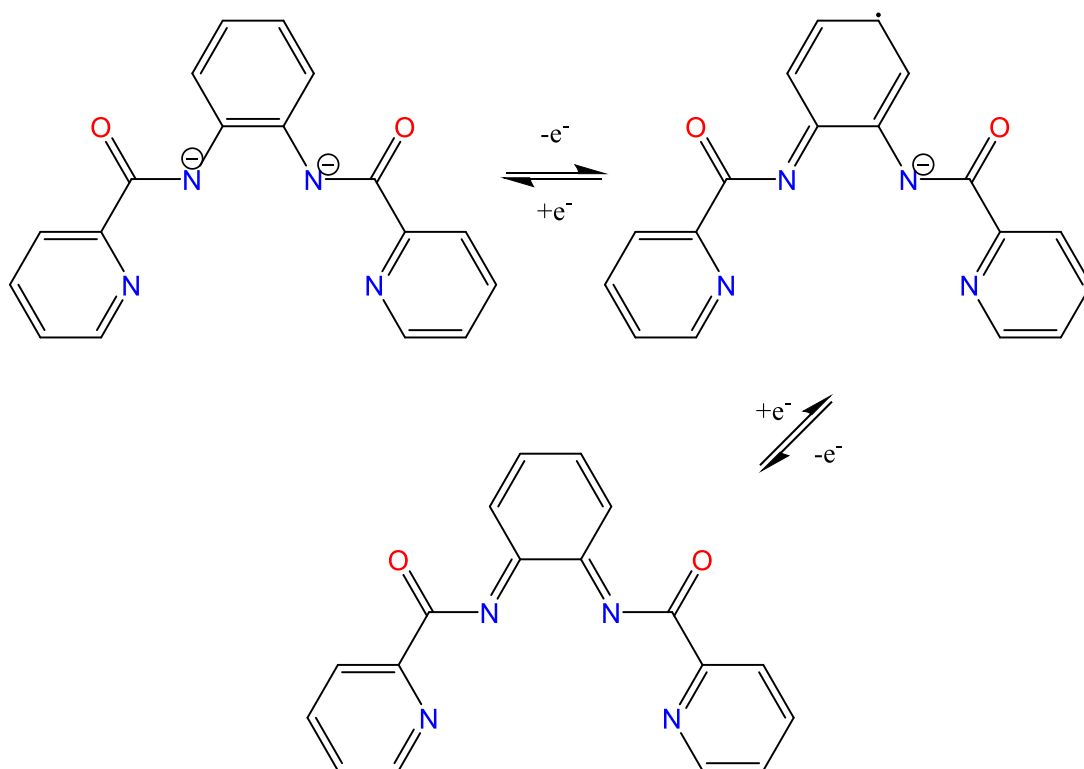
Figure 4.3 Redox activity of deprotonated H$_2$bpb.

These picolinamide ligands have been used in transition metal chemistry since the 1970s with the `most studied being the aryl bridged 1,2-bis(pyridine-2-carboxamide)benzene known as H$_2$bpb.[2] Metal complexes of this ligand are significantly more studied when compared to those of 1,2-bis(pyridine-2-carboxamide)ethane (H$_2$bpe) and 3,4-bis(pyridine-2-carboxamide)benzoic acid (H$_3$bpba).[3-6] The preference of H$_2$bpb over the ethane bridged amide is that the rigidity of the aryl ring forces the two amide nitrogens to orientate in the same direction and, therefore, to the same metal. In contrast, the ethane bridged amide can form dendritic coordination systems due to its greater flexibility. Ruthenium complexes, as with the majority of the picolinamide metal species, are dominated by H$_2$bpb within the literature. Of the H$_2$bpb derived complexes the majority of species contain strong π-accepting ligand such as carbonyl and nitrosyl groups. The interest in these complexes is driven by the photolability of these π-accepting groups when coordinated to the ruthenium centre. Of the dichloride structures there exists one known mononuclear and two dinuclear complexes (Figure 4.4) as well as the 4-methyl pyridine complex mentioned in Chapter 1 (Figure 1.23).[7-9]
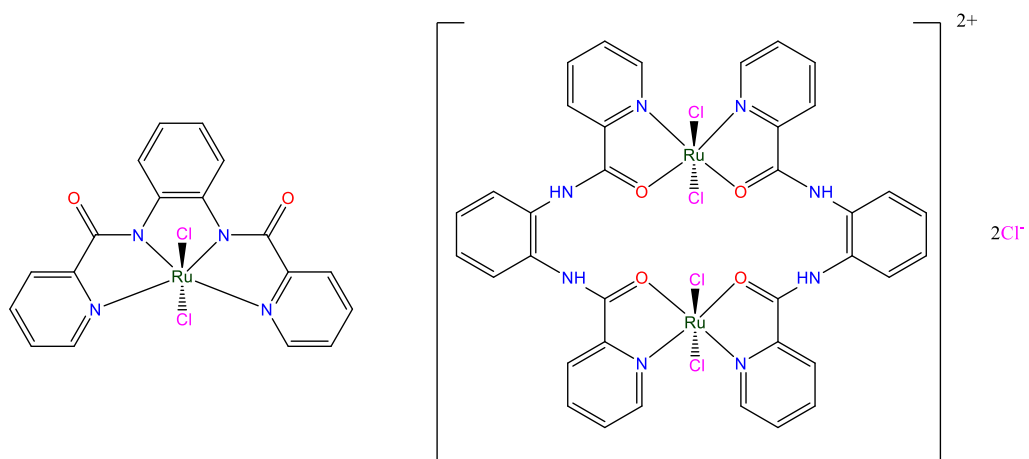
Figure 4.4 Left: mononuclear ruthenium complex derived from H$_2$bpb. Right: proposed structure of dinuclear complex derived from H$_2$bpb.

Of the ruthenium complexes of H$_2$bpe only one has been reported with a dichloride configuration but in a dinuclear rather than a mononuclear complex, although this was unsupported with crystallographic data.

Results and Discussion
Picolinamides

The pyridine containing ligands were synthesised by two methods, first by the conversion of picolinic acid into an acid chloride using thionyl chloride before bridging with the nucleophilic primary amine. The second was via the use of the triphenyl phosphite coupling in neat pyridine.[1]
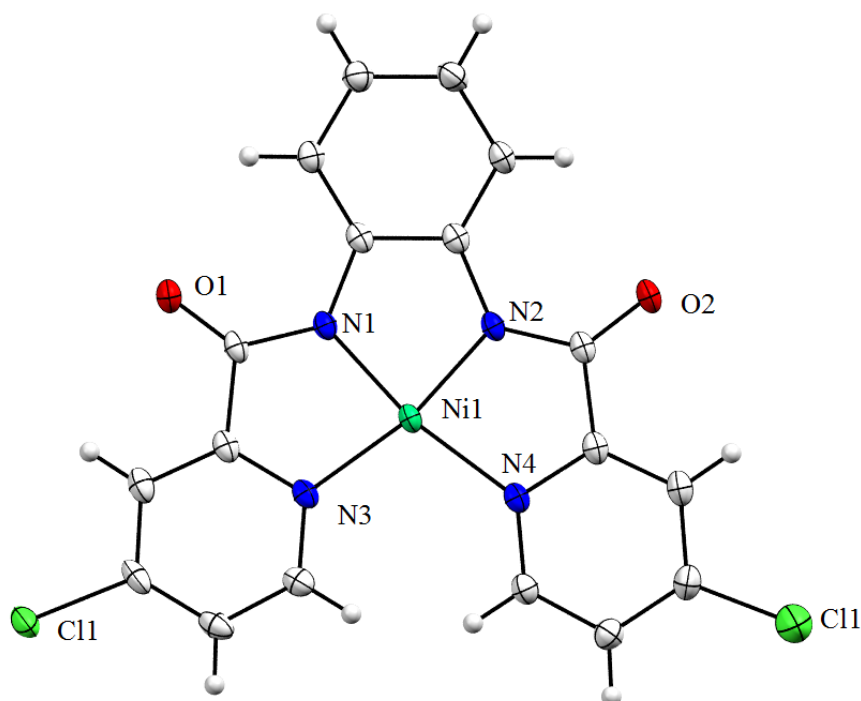
Figure 4.5 X-ray structure of chlorine substituted Nibpb; chlorines possess 50% occupancy. Ellipsoids shown at 50% probability.

Of the two methods the second was preferred, as additional chlorination of the pyridyl ring was observed when using the acid chloride method - as shown in the nickel complex of H_2bpb derived from this method (Figure 4.5). The nickel complex was synthesised to determine the viability of the ligand synthesis as the nickel complex is known in the literature and both forms and crystallises easily.[10] The chlorination was only observed on the para position from the pyridyl nitrogen so may be used in the future as a route into functionalising that position. The chlorination was not total as the nickel structure shown has one chlorine distributed over the two sites, with occupancies of 50%. Longer or more extreme reaction conditions when preparing the

acid chloride would be required to form the chlorine substituted ring in analytically pure yields.
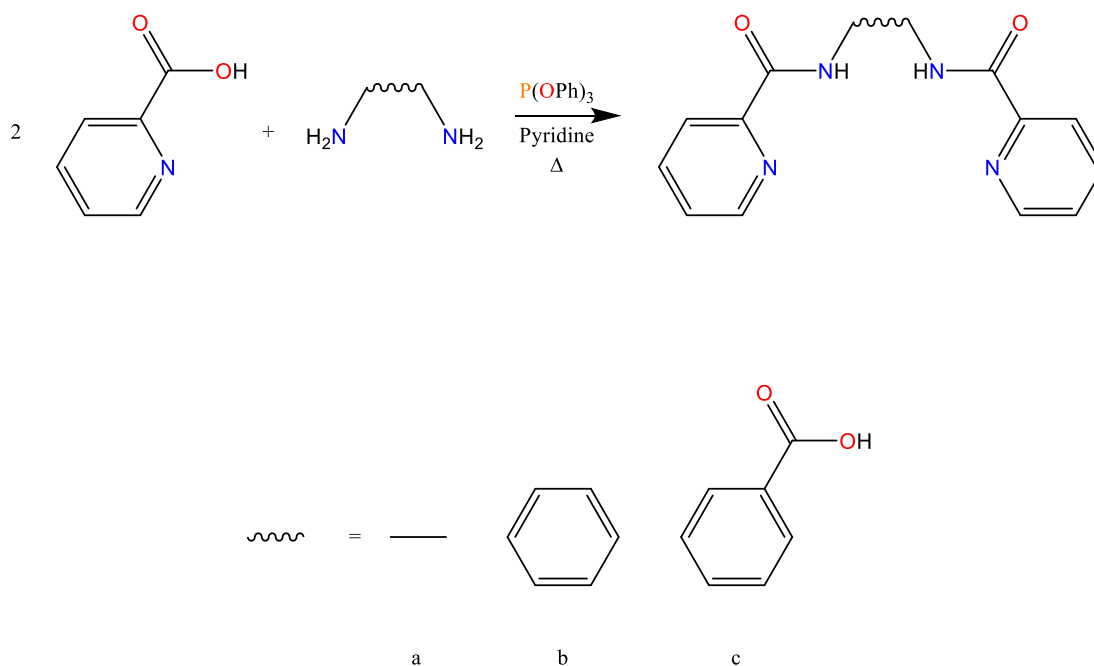
Scheme 4.1 Synthesis of picolinamide ligands.

The triphenyl phosphite coupling (Scheme 4.1) was not the initially preferred method as it was thought that a coupling reaction might occur between the acid group and the amines in the synthesis of the benzoic acid bridged ligand.[11] Luckily this coupling was not observed, most likely due to the phosphite-picolinate intermediate forming first and being more reactive towards nucleophilic attack from the aryl amines of the 3,4-diaminobenzoic acid than from exchange with its acid group.

Crystal structures were obtained for H_2bpb and H_2bpe (Figures 4.6 and 4.7).
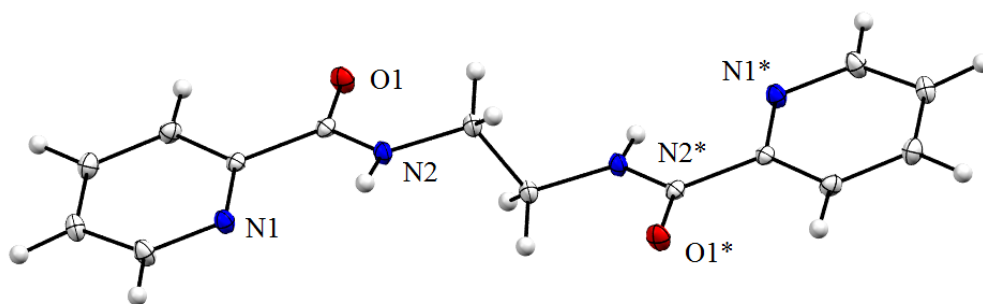
Figure 4.6 X-ray structure of N,N'-(ethane-1,2-diyl)dipicolinamide (H_2bpe). Ellipsoids shown at 50% probability. Symmetry operators to generate equivalent atoms: (*) -x+1, -y+1, -z+1 .
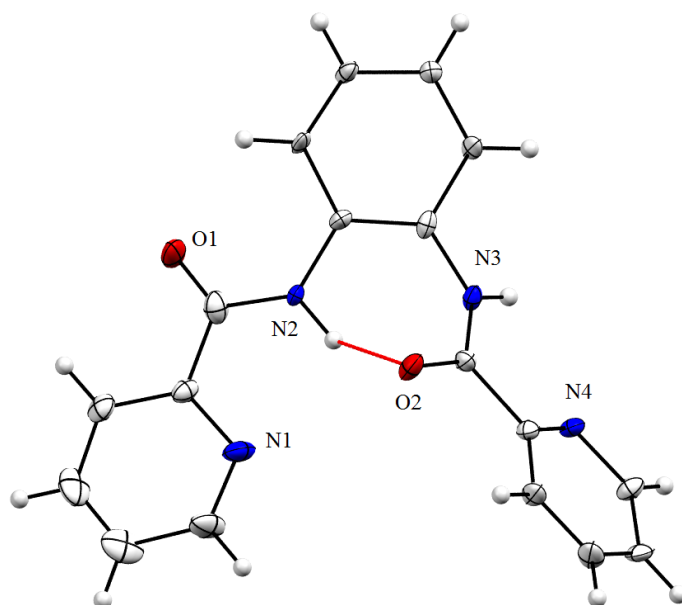
Figure 4.7 X-ray structure of N,N'-(1,2-phenylene)dipicolinamide (H₂bpb). Intramolecular hydrogen bond represented by a dashed red line. Ellipsoids shown at 50% probability.

These structures showed agreement with previously reported structures.[12] The H₂bpb structure containing a hydrogen bond between one of the amide protons and the opposing amide oxygen. Although a crystal structure of the benzoic acid bridged H₂bpba was not obtained, its formation was confirmed via mass spectrometry, NMR and elemental microanalysis. The ease of the preparatory method and purification of these ligands would indicate that they would make suitable candidates to develop as ruthenium based dyes.

Following a similar preparatory method to that of the picolinic acid complexes, the ligands were refluxed with ruthenium trichloride in light alcohols to form the desired complexes. However, unlike the dipicolinic acids, the resulting compounds were significantly more difficult to synthesise in a pure form and, more problematically, had a considerably lower aqueous solubility. For the complexes of H₂bpe and H₂bpb, mass spectrometry revealed that the complexes were indeed forming as the desired dichloride complexes (405.04 m/e and 488.73 m/e respectively). However, the elemental microanalysis revealed that the formed compounds were impure, with the H₂bpe complexes' microanalysis indicating that a third chloride was present. Attempts at purification via recrystallization and column chromatography were unsuccessful with the resulting yields frequently displaying poorer elemental analysis than before. The analysis showed lowered CHN values indicating either the presence of additional

heavy elements such as ruthenium and/or chloride, or the loss of carbon, hydrogen and nitrogen from the structure.

The difficulty in purifying the complexes and the lack of any X-ray structures meant that the protic nature of the amides could not be determined. It was therefore not possible to deduce if the ligands were coordinating to the ruthenium in a charge carrying manner or as a neutral ligand. The addition of a base to the reaction mixture has been reported to increase yields for similar compounds based on amides; however, while this was explored it did not appear to have any significant increase in yield. [13-14]

Turning to the literature for answers to the synthetic problems of these complexes it was found that there exists only one previous study on the ruthenium +4 dichloride complex of H_2bpb.[8] Synthesised by Srivastava *et al*, the complex showed the ruthenium with both amides being charge carrying. However, as has been shown in Chapter 2, ruthenium compounds of this type, bearing four anionic ligands, can exist in both +4 and +3 oxidation states with little structural difference between them. The preparatory method for Srivastava's complex involves the commercially unavailable precursor *mer*-RuCl₃(TMSO)₃ from which the crystal structure in Figure 4.8 was obtained. However, the paper does not make reference to the instability and difficulty purifying said compound.
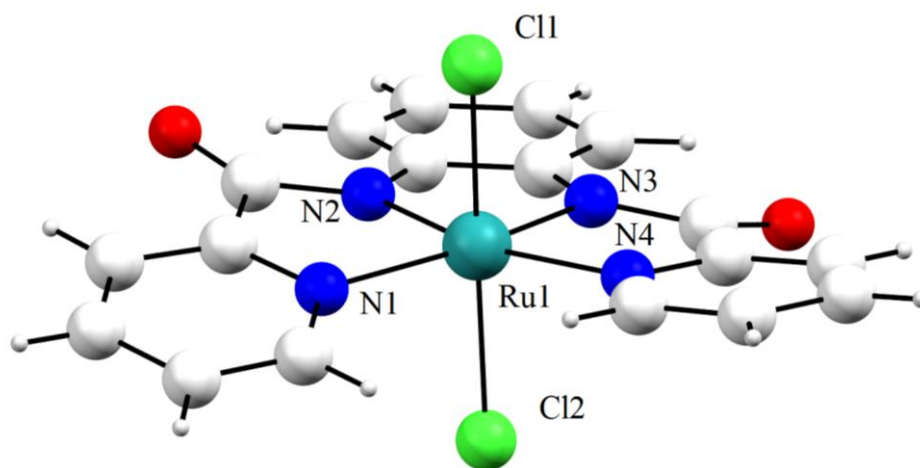
Figure 4.8 X-ray structure of RubpbCl₂ reported by Srivastava *et al*.

Decomposition of ruthenium picolinamide based complexes is not unknown. The Ru[II] dipicoline complex mentioned in Chapter 1, despite being described as both air and moisture stable, displayed decomposition into an aqua/carbonyl complex when

exposed to an oxidising environment.[7] The stability as a Ru[II] species but not as a Ru[III] or Ru[IV] suggest that these Rubpb species may be fundamentally unstable when in higher oxidation states.

It should be noted that the dichloride iron, cobalt, chromium and vanadium based complexes are known and have been synthesised from their simple chloride salts without the level of difficulty experienced for the ruthenium complexes.[15-18] This indicates that the ruthenium dichlorides may simply be inherently unstable or form an unstable intermediate during formation - a theory which is supported by the only observed dihalogen complex of this class of ligand beyond the first row of the transition metals being Srivastava's complex. Examination of the related iron compounds shows a possible reason for the poor microanalysis. The iron dichloride complexes form an anionic Fe[III] species, with H_2bpb derived ligands (which is the case for all the first row transition metal dichlorides) as the Fe[IV] centre described by Wieghardt was formed electrochemically in situ. These iron dichloride complexes are known to be moisture sensitive with one of the chlorides being replaced by an aqua group to make a neutral species. However, an alternate pathway has also been observed where the anionic complex reprotonates one of the amides and becomes a dimer complex (Figure 4.9).[19] In this transformation the ligand coordinates to one of the carbonyls on the ligand in a similar manner to that observed in the ruthenium H_2bae complex (*vide infra*).
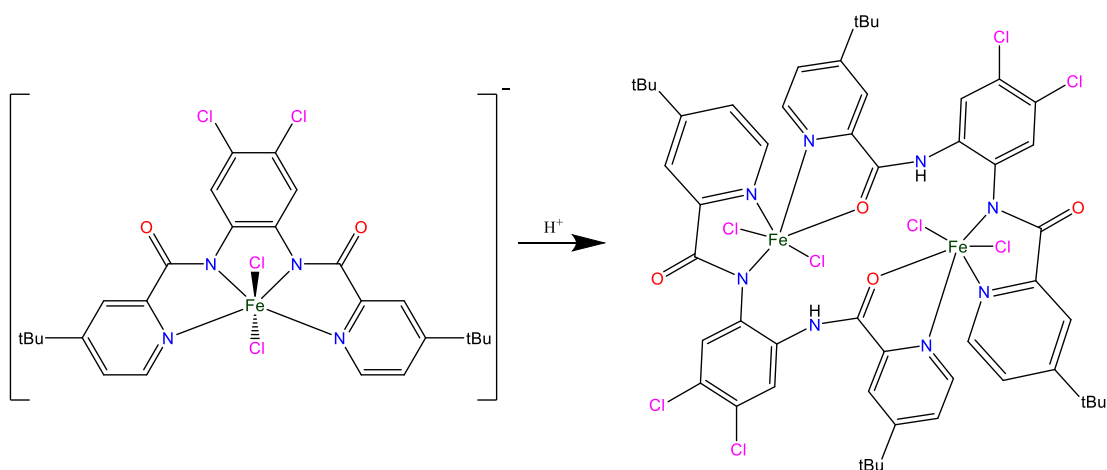
Figure 4.9 Conversion of mononuclear, anionic, iron dichloride structure to neutral iron dichloride dimer.

Linking this transformation with the information derived from Chapter 2 and 3 on the oxidation state of ruthenium dichloride species allows for a proposed decomposition

pathway for the ruthenium amide dichloride complexes. The earlier chapters showed that ruthenium dichloride complexes have the tendency to stabilise in +3 oxidation state even when formed in +4 oxidation state. If such a transition from the Ru[IV] complex to the Ru[III] complex were to occur, it would weaken the ruthenium amide bond and make it susceptible to protonation in the same manner as that observed in the iron dichloride complex above.

In an effort to find a similar but stable ligand moiety a second series of ligands was surveyed. While the pyridine based donor systems hold the most promise for understanding how the substitution pattern of anchoring groups affects the properties of derived photoactive dyes, the difficulty in being able to synthesise the pure compounds limits the ability to probe those properties further. In order to investigate a route into the synthesis of stable pyridine based dyes bearing amide linkers, corresponding ligands containing primary amines rather than pyridines were synthesised. The concept was that the amine would allow for protonation and deprotonation, possibly stabilising the ruthenium centre as protonation of the amines, while not ideal, would not allow for rearrangement of the complex as protonation of the amide. The replacement of pyridyl groups for amido groups will also change the size of the potential coordination sphere of the metal complex as the primary amines shrink the volume which the ruthenium can occupy while being coordinated to all four nitrogens. Similar complexes based on group 15 elements have been synthesised using phosphines instead of amines; however, the requirement of phosphines having large bulky groups (e.g. phenyl) contorts the derived ruthenium dichloride structure resulting in chlorides being cis rather than trans (Figure 4.10).[20] Palladium, platinum and nickel structures of the same ligand showed distorted square planar structures which indicate that if the steric bulk surrounding the metal is reduced then the ligand coordinates in a meridional rather than face sitting manner.[21-23] A ligand with primary amines rather than the tertiary phosphines would be expected to adopt a structure similar to salen and salophen based complexes.
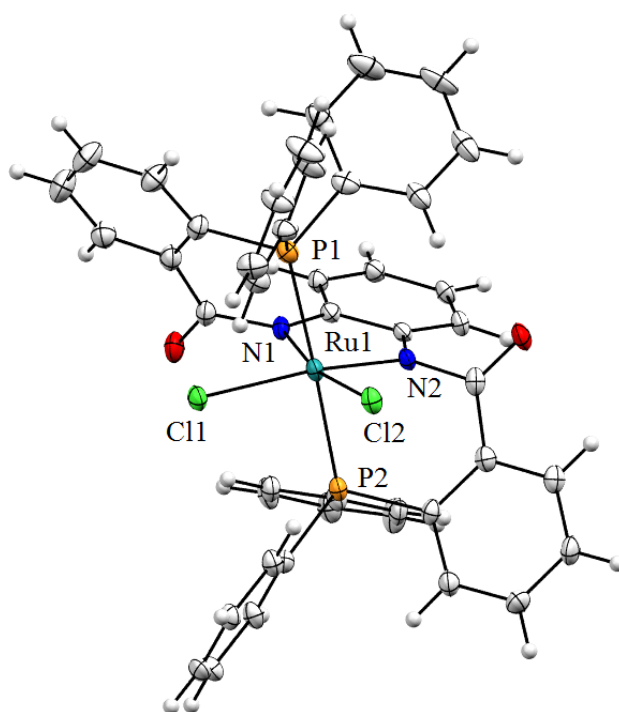
Figure 4.10 X-ray structure of [(1,2-bis-N-[2′(diphenylphosphanyl)benzoyl]diaminobenzene)Ru(Cl)₂] showing chlorides in the cis configuration. Ellipsoids shown at 50% probability.

The comparison to salen based complexes extends beyond simple geometry with both sets of ligands being dianionic and with an sp^2 carbon between the aromatic ring and the common nitrogen donors, allowing for delocalised molecular orbitals across two or more donor atoms. Salen-based complexes have been examined for mononuclear water oxidation with ruthenium and for dye sensitisation with other metals.[24-25] It is, however, feared that as with other Schiff bases, the hydrolysis of the carbon-nitrogen bond would make such derived complexes decompose in aqueous environments.[26] Decomposition occurs due to metal coordination of the nitrogen drawing electron density from the carbon making it susceptible to nucleophilic attack from water or other nucleophiles. Research in a separate area showed that tripodal Schiff base complexes based on tris(2-aminoethyl)amine can both undergo hydrolysis and rearrangement due to this weakness of the imine bond (*vide infra*). The use of Schiff bases with a phenyl backbone is further complicated by the tendency of the ligands to form benzimidazoles (particularly from the pyridine based ligands) before complexation can occur (Figure 4.11).[27] The use of amides rather than imines does reduce these problems but does not eliminate them. Protonation of the oxygen can lead

to the carbon becoming a target for nucleophilic attack once more but at a significantly lower rate than that of the imines.
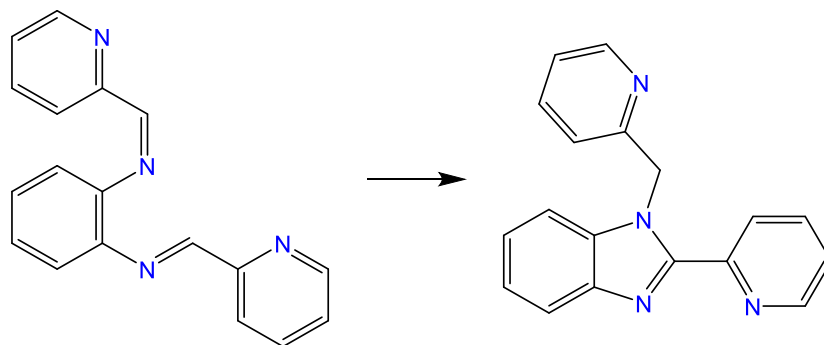
Figure 4.11 Conversion of Schiff base to benzimidazole.

Aminobenzamides

The synthesis of the aniline based ligands was significantly simpler compared to that of pyridine based ligands (Scheme 4.2). The synthesis used isatoic anhydride, which undergoes nucleophilic attack on the ring bound sp^2 carbon from the primary amine of either ethylene diamine or o-pheneylene diamine to yield the desired tetradentate ligand as a white powder.[28] Attempts to replicate the reaction with 3,4 diaminobenzoic acid yielded similar white powder but analysis showed mixed products most likely due to the protic oxygen of the acid nucleophilically attacking unreacted isatoic anhydride. This would be more favoured in the later stages of the reaction when one of the amines on the benzoic acid had already formed its amide. The newly attached aniline group would sterically hinder the second amine on the benzoic acid resulting in the acid group being favoured, despite oxygen being the weaker nucleophile. The presence of such large quantities of side products mean that this route is not suitable for the synthesis of the benzoic acid bridged species. Formation of the ethyl ester before reaction with isatoic anhydride yielded similar results to the benzoic acid species indicating that the oxygen of the ester is still too nucleophilic. Both the ethane and phenyl bridged ligands yielded crystals in similar fashion to the picolinamide ligands (Figures 4.12 and 4.13).
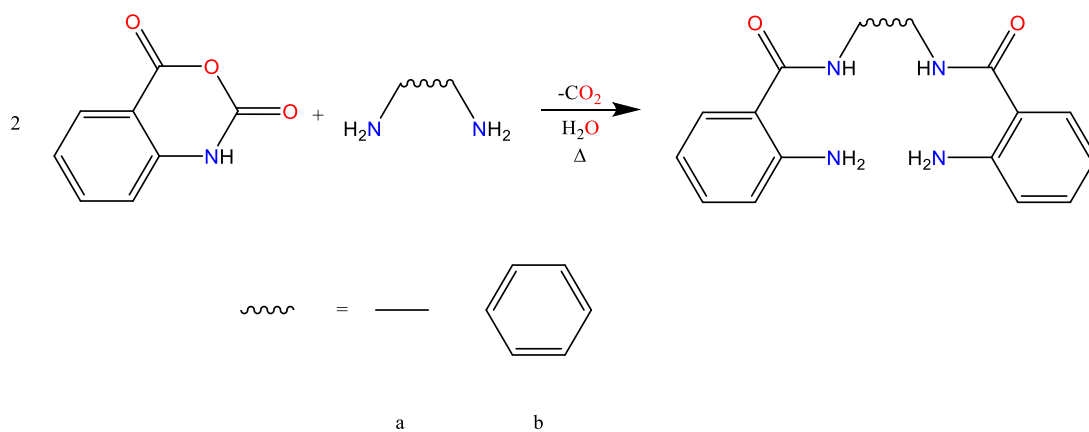
Scheme 4.2 Synthesis of aniloamide ligands.

Compared to the pyridine based ligands the aniline based species display increased hydrogen bonding within their own structures due to the availability of the protons on the primary amines for hydrogen bonding with the amide oxygen. Both the ethane and phenyl bridged ligands orientate the amine nitrogen and amide oxygen in the same direction due to the hydrogen bond between them. The directionality of these two prospective donors over that of the amine/amide might prove to be problematic as it would favour the coordination of the oxygen before the amide.
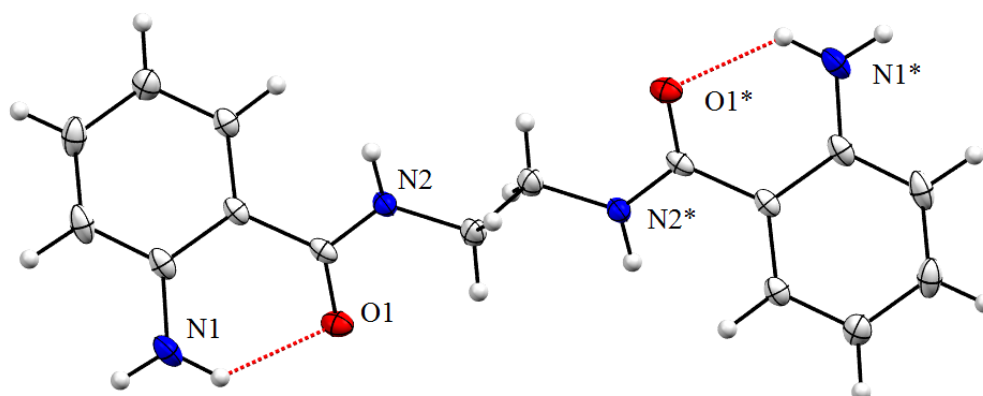
Figure 4.12 X-ray structure of N,N'-(ethane-1,2-diyl)bis(2-aminobenzamide) (H$_2$bae). Intramolecular hydrogen bond represented by a dashed red line. Ellipsoids shown at 50% probability. Symmetry operators to generate equivalent atoms: (*) -x+1, -y+2, -z+1 .
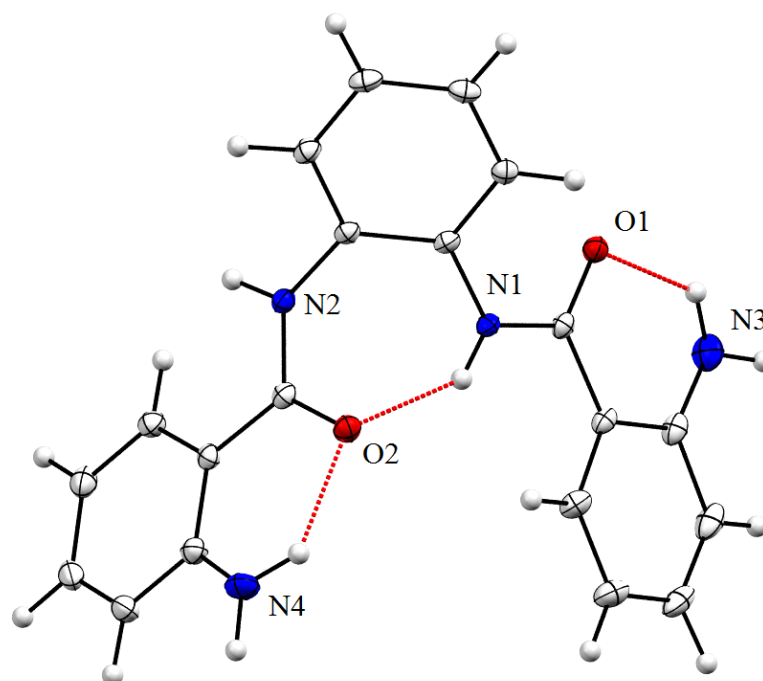
Figure 4.13 X-ray structure of N,N'-(1,2-phenylene)bis(2-aminobenzamide) (H$_2$bab). Intramolecular hydrogen bond represented by a dashed red line. Ellipsoids shown at 50% probability.

In comparison to the pyridine based ligands the aniline based ligands are relatively unexplored. Of the benzene-bridged ligand only one metal containing structure is known (rhenium) and of the ethane-bridged there are no examples.[29] In the rhenium structure one of the aniloamide groups has been severed upon complexation to yield a monoanionic ligand containing two primary amines and one amide (Figure 4.14).
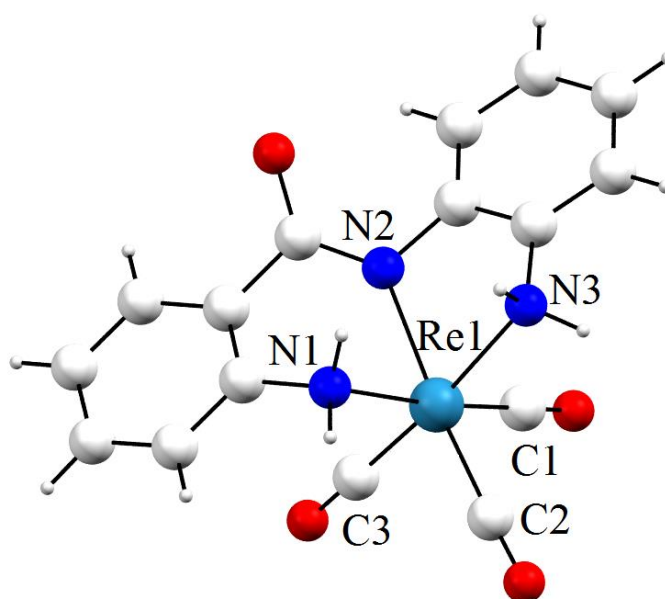
Figure 4.14 X-ray structure of [Re(CO)$_3$(daa)] reported by Booysen *et al.*

Attempts at synthesising ruthenium complexes displayed similar problems to the pyridine based ligands in that purification was extremely difficult, although, as with the pyridine based complexes, mass spectroscopy showed that the complexes were indeed forming. Recrystallisation was partially successful in that the compounds purity could be improved; however, elemental microanalysis revealed this purity was batch-dependant, with recrystallised samples frequently being less pure as much as more. The samples exhibited loss of carbon, nitrogen and hydrogen as a percentage of total mass. This indicates either the presence of heavy elements such as ruthenium or chlorine in greater abundance than our understanding of the compounds allows or with the loss of parts of the ligand to either oxidation or simply cleavage of the amide bond. This is in keeping with the results for the pyridine-based ligands, indicating that these compounds are not stable and are decomposing when in solution. Reduction of initial reaction times did not alleviate this issue, as the compounds were forming in an impure form and requiring of a recrystallisation step to remove impurities; but also decomposing in the recrystallisation step to yield yet more impurities. The rhenium compound mentioned above shows that decomposition of the ligand can occur upon complexation to a metal centre - it is, therefore, hypothesised that another decomposition pathway exists: that the decomposition pathway for these species is through severing of the amide carbon-nitrogen bond.

Of particular note is that the majority of ruthenium species bearing the pyridine based ligands such as H_2bpb do so in lower oxidation states and with stronger π-accepting ligands such as carbonyl, nitrosyl or picoline.[6-7,14,30] This indicates that the presence of higher oxidation states made available via the absence of these groups may be playing a hand in the decomposition of these particular ruthenium species.

The decomposition of these species is not limited to those complexes derived from aromatic bridged ligands but also those containing an ethane bridge. The complex formed from ruthenium trichloride and H_2bae has been reported in the literature before where the synthesis used sodium hydroxide to deprotonate the amide groups and the structure was reported as having the amide groups coordinated.[31] In the single crystals yielded from our similar reaction, without such a base, the amide groups did not

coordinate, but rather remained protonated and coordination was effected though both aromatic amines and one of the amide oxygens.
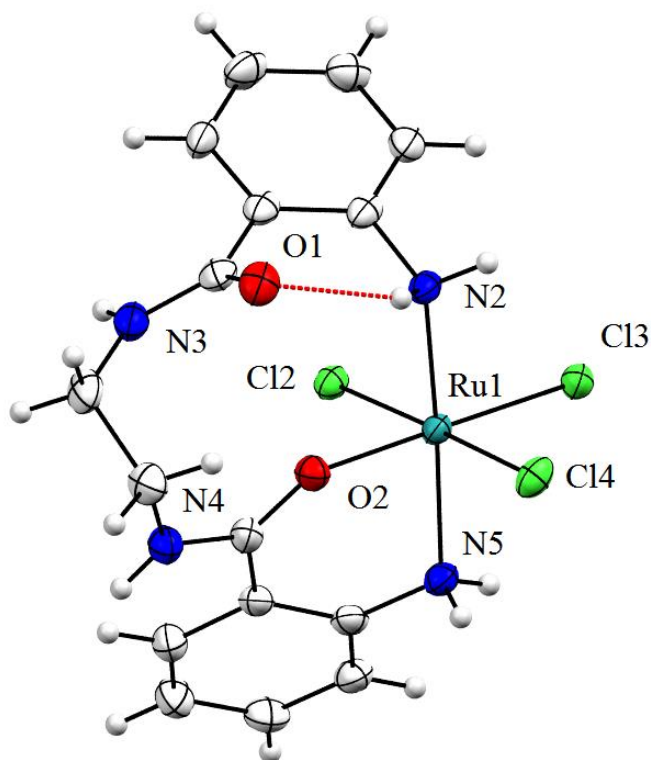
Figure 4.15 The X-ray crystal structure of RuH$_2$baeCl$_3$ showing coordination of amide oxygen rather than nitrogen. Intramolecular hydrogen bond represented by a dashed red line. Ellipsoids shown at 50% probability.

The crystal structure of RuH$_2$baeCl$_3$ (Figure 4.15) displayed the ruthenium in a +3 oxidation state, with the ligand contorted in bow type configuration with the two coordinated amines trans from one another, and with the coordinated oxygen sitting cis to both. The chlorides remain coordinated along the opposing meridonal plane. There remains an intramolecular hydrogen bond between the uncoordinated oxygen and protons on the closest of the coordinated amines. As shown in Table 4.1, the shortest of the ruthenium H$_2$bae bonds is that with the amide carbonyl oxygen (2.043 Å) followed by the amines (2.103 - 2.145 Å) and the chlorides (2.342 - 2.357 Å).

196

Table 4.1 Bond lengths of coordination sphere of adduct of ruthenium trichloride and H_2bae.

Bond	Bond Length (Å)
Ru-O_2	2.0426(16)
Ru-N_2	2.1441(19)
Ru-N_5	2.1039(18)
Ru-Cl_2	2.3564(6)
Ru-Cl_3	2.3425(6)
Ru-Cl_4	2.3490(6)

This crystal structure shows that in the ligands with more flexible backbones alternate coordination modes may be available. The flexibility of the ethane bridged ligands also indicates that in situ rearrangement of the complexes may be possible depending on the pH: a change in pH could deprotonate the uncoordinated amide nitrogen triggering rearrangement. In contrast, in a highly protic environment the reverse reaction may also be possible in the ruthenium complexes. This bears remarkable similarity to the rearrangement of the iron complexes based of H_2bpb, as seen in Figure 4.9, and further emphasises the sensitivity of these compounds in protic environments.

Tripodal Schiff bases

The aniline amide ligands bear similarity to additional work that was conducted based on tripodal, nitrogen containing, ligands using first row transition metals. Those species contain comparable sp^2 carbon and nitrogen moieties to those of the amide described above. These species exhibited both decomposition and rearrangement around these two atoms and examination of them shed some light on the possible decomposition of these species.
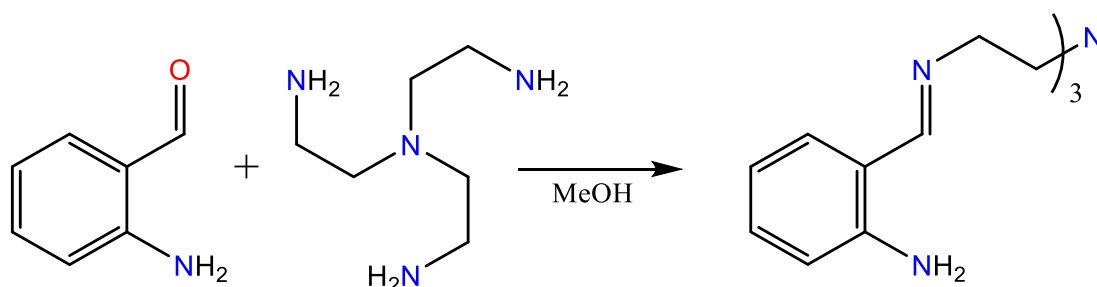
Scheme 4.3 Synthesis of TrenAb.

The first of these tripodal ligands was the Schiff base referred to here as TrenAb, prepared from tris(aminoethyl)amine and o-amino-benzaldehyde (Scheme 4.3). It was isolated as a white crystalline solid, which could be recrystallised from chloroform-

methanol (Figure 4.16). Consistent with Garcia et al., structural analysis of TrenAb reveals that the three anilino groups are folded inwards from the apical nitrogen such that the three aryl rings are placed in close proximity to one another.[32] The anilino hydrogens are also directed towards the Schiff base nitrogens thus forming a network of three internal hydrogen bonds. The hydrogen bonding is analogous to that found in the aniline-containing amides but without the amide oxygen.
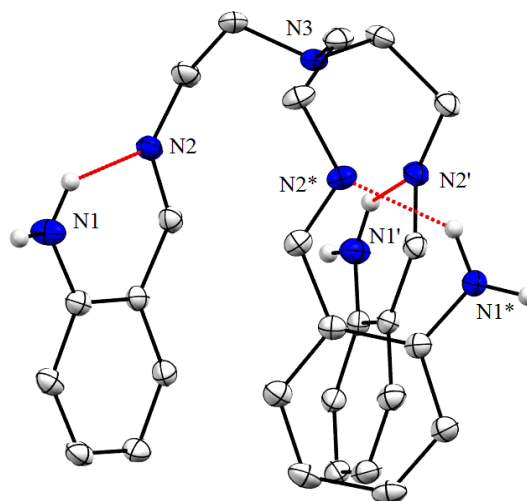
Figure 4.16 The X-ray crystal structure of tris-((2-aminobenzylidene)-aminoethylamine. Hydrogens omitted for clarity. Non-amine protons omitted for clarity. Intramolecular hydrogen bond represented by a dashed red line. Ellipsoids shown at 50% probability. Symmetry operators to generate equivalent atoms: (*) -x+y+1, -x+1, z (') -y+1, x-y, z .

The halides of nickel, copper and zinc were treated with TrenAb under conditions typically employed (methanol ~65 °C for 2 hrs.) for the formation of the related salicylaldehyde Schiff base species (TrenSal) and similar to those of the Ruthenium amide complexes.[33-34] The mass spectra of the isolated complexes (referred to as NiTrenAb, CuTrenAb and ZnTrenAb) are dominated by ions associated with the parent species (MTrenAb, M = Ni, Cu, Zn) and their fragmentation/recombination products. No evidence was found to support the formation of multimetallic species at this juncture (c.f. $M_3(TrenSal)_2$, M = Ni, Zn; $Cu_4(TrenSal)_2$).[33] Vibrational spectroscopy of the three complexes (coincident amide, imine and aromatic bands) indicates that the structures of these products are of high symmetry and related. It was possible to record the ^{1}H NMR spectrum of the ZnTrenAb which shows that there are three imine environments (δ7.00, δ7.01, δ6.91). However, the chemical shift difference is not sufficient to suggest that any of these remain uncoordinated. The region assigned to tren is broad but indistinguishable, indicating that the primary

amines are all coordinated and chemically similar. Thus it can be proposed that ZnTrenAb is a six-coordinate species similar to $Zn_3(Tren5BrSal)_2$ as shown in Figure 4.17.[33]
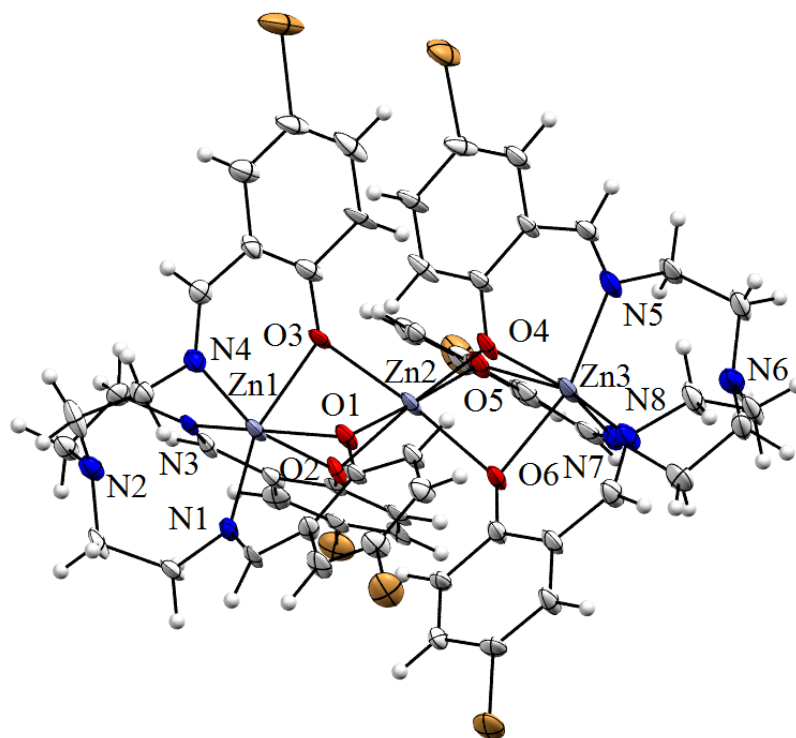
Figure 4.17 The X-ray crystal structure of $Zn_3(Tren5BrSal)_2$. Ellipsoids shown at 50% probability.
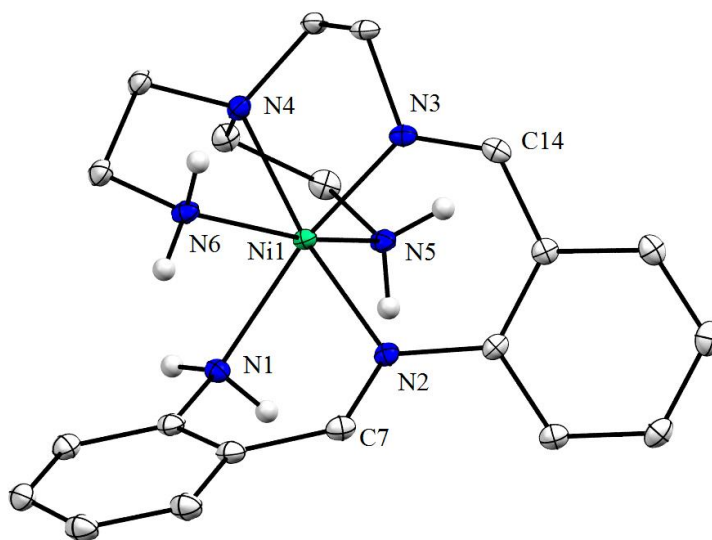
Figure 4.18 The X-ray crystal structure of the isolated dicationic adduct of nickel iodide and TrenAb. The structure is presented to clearly show the fused aniline moieties which results from Schiff base cleavage/migration. Non-amine protons and iodide counter ions omitted for clarity. Ellipsoids shown at 50% probability.

Table 4.2 Bond lengths of coordination sphere of dicationic adduct of nickel iodide and TrenAb.

Bond	Bond Length (Å)
Ni-N$_1$	2.186(3)
Ni-N$_2$	2.087(3)
Ni-N$_3$	2.018(3)
Ni-N$_4$	2.121(3)
Ni-N$_5$	2.093(3)
Ni-N$_6$	2.123(3)

Previous studies clearly show that it is difficult to predict the absolute structures of the metal complexes of heptadentate ligands such as those discussed here. Thus, in an effort to gain greater insight into the structure of these MTrenAb species the scope of the study was extended to a range of salts. From the reactions with nickel iodide suitable crystals were possible to obtain for analysis by diffraction methods (Figure 4.18). The structure obtained is, however, not consistent with that expected for a simple MTrenAb complex. It would seem that the protracted crystallisation process (over a week) allowed the ligand to both hydrolyse and re-arrange. Not only is one of the aniline units lost completely but also a second is transferred to an adjacent aniline group, probably via an intramolecular reaction, giving rise to the formation of a coordinated aniline-methylidene-aniline moiety. The resulting perturbation of the number (seven to six), and positioning of the aniline donors, facilitates the movement of the nickel into the coordinating environment of all four donors on tren.[35-36] Migrations and rearrangements of this type go some way to explaining the behaviour of the parent species in the mass spectrometer, where ions with masses consistent with the gain and loss of aniline units are freely seen. Although not as prominent, a similar degradation process has been reported for the nickel salts of TrenSal where the phenolate arms are lost.[33] Consistent with that observation here, the reaction reported takes time to come to completion. Linking what we know from the decomposition of the amide ligands (particularly the rhenium structure) it becomes clear that metal coordination to an sp^2 nitrogen, which is bound to an aromatic group through an sp^2 carbon, weakens the carbon-nitrogen bond, allowing for hydrolysis and either decomposition or rearrangement.

In the reactions involving zinc chloride a second product crystallised directly from the cooling mother liquors (Figure 4.19). Examination of the crystal structure revealed that the ligand (TrenAb) had re-arranged within the lifetime of the crystallisation

process. Consistent with the nickel example above (Figure 4.18), an intermolecular migration has occurred whereby the aniline group migrates to replace the nitrogen of tren in the Schiff base linkage. However, in this instance a second coupling takes place and in-so-doing forms a tetracyclic ring system fused to a nitrogen donor on tren (N4, Figure 4.19). As the reaction proceeds, the zinc migrates deep into the tren moiety maintaining a coordination number of 5. This more complex rearrangement is most likely a result of the increased Lewis acidity of zinc. This rearrangement reinforces the concept that the ruthenium amides are decomposing throughout the crystallisation process and explains why purification through recrystallisation could yield poorer elemental microanalysis results that before recrystallisation.
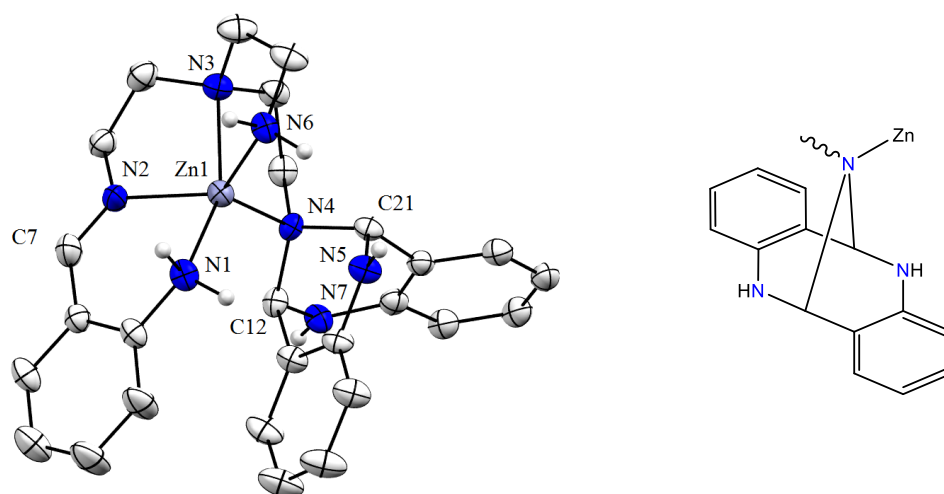
Figure 4.19 Left: The X-ray crystal structure of the isolated dicationoic adduct of zinc chloride and TrenAb. The structure is presented to clearly show the fused tetracyclic component of the ligand which results from Schiff base cleavage/migration. Non-amine protons and $[ZnCl_4]^{2-}$ counter ion have been omitted for clarity. Ellipsoids shown at 50% probability. Right: A schematic representation of the fused aniline moieties.

Table 4.3 Bond lengths of coordination sphere of dicationic adduct of zinc chloride and TrenAb.

Bond	Bond Length (Å)
Zn-N$_1$	2.120(5)
Zn-N$_2$	2.067(6)
Zn-N$_3$	2.213(5)
Zn-N$_4$	2.102(4)
Zn-N$_6$	2.066(5)

In both instances (nickel and zinc) mass spectrometry provides evidence that the primary complex (MTrenAb) is forming with ease. Structural analysis of the ligand itself (Figure 4.16, Table 4.3) clearly shows that the components are positioned in line

with the expected condensation reaction. Thus, migration must be occurring as a result of the placement of the Lewis acid at the various donors. The hypothesis is that nickel, by virtue of its preferred higher coordination number, only facilitates the coupling of two aniline groups. Zinc however is both a slightly stronger Lewis acid and has a lower coordination number. As the rearrangement in the zinc structure would require the cleavage of multiple zinc-nitrogen bonds and the presence of a lower coordination number zinc transition state it is unlikely that this rearrangement would be favoured in the nickel-containing complex. This variance in the rearrangement pathway for zinc raises the prospect of a more aggressive ring closure reaction and one which has the capacity to encompass further aniline units.

Although the Schiff base linkage remains an integral part of many ligand designs, researchers tend to dismiss (or fail to consider) the reactivity of the imine function in the long term, or, as is shown here, the short term. Our previous attempts to generate the heptadentate N_4S_3 ligand system based on tren and 2-(*tert*-butylthio)benzaldehyde were curtailed due to the limited stability of the imine group within the metal complexes studied.[26] The salicylidene-tren systems are more robust but even these, when metallated (e.g. nickel) have demonstrated a tendency to degrade albeit over a prolonged time period.[33] In retrospect, it is thus unsurprising that the nitrogen donor systems reported here display behaviour intermediate between that observed for the phenolates and thio-ethers.

The general absence of a tren based polyamine system in the literature has always presented itself as a curious omission especially as the tetradentate systems have been known for many years and that studies on high denticity salicylaldehyde species were also reported over fifty years ago.[37] The study here finally shows that it is possible to generate these species. While their primary coordination chemistry is in line with previous studies, regrettably their stability is poor. The placement of an amine adjacent to a Schiff base linkage was, in retrospect, expected to give rise to intra-molecular chemistry. The amides, supposedly more stable than the Schiff bases, clearly suffer from similar complications to their coordination chemistry. As mentioned above, the higher attainable oxidation states of the ruthenium complexes appear to have an aggravating effect on these decompositions.

In conclusion while it does appear possible to derive ruthenium complexes from pyridyl and anilino acid amides, the poor stability of the derived compounds makes them unsuitable for further exploration. The two primary weaknesses in these complexes is postulated to be the flexible backbone of the ethane-derived complexes and the susceptibility of the amide nitrogen to protonation. While the flexible backbone can be remedied by either the addition of sterically bulky directing groups, the protonation of the amides is not as easily solved, and at this point is considered to be a block to further exploration of this area, as any dyes containing this amide moiety would be unable to tolerate the highly acidic conditions found at the anode of any water oxidation cell.

Experimental

All experiments were carried out using standard apparatus and commercially available chemicals. NMR analysis was carried out on a Bruker AMX 400 operating at 400 MHz for ^{1}H and 100 MHz for ^{13}C. Mass spectra were recorded in house on a Thermo Finnigan LCQDuo by electrospray ion trap, 4.5kV, 200°C and a Kratos-Shimadzu Axima-CFR MALDI-TOF using an N_2 laser operating at 337nm. Elemental microanalysis was carried out in house on a Perkin Elmer 2400 CHN Analyser. Crystals were coated in mineral oil and mounted on glass fibres or loops. X-Ray measurements were conducted using either an Oxford Diffraction Gemini CCD diffractometer at 123 K using graphite monochromated Mo-Kα radiation or an Oxford Diffraction Gemini CCD diffractometer at 123 K using graphite monochromated Mo-Kα or Cu-Kα radiation.

Synthesis of N,N'-(ethane-1,2-diyl)-bis(2-pyridine-carboxamide) (H₂bpe):

Triphenylphosphite (10.7 mL, 40.6 mmol) was added dropwise to a cold, stirred solution of picolinic acid (5.00 g, 40.6 mmol) in pyridine (20 mL). 1,2-ethylenediamine (1.22 g, 20.3 mmol) was then added and the solution heated to 70 °C for 17 hours. The pyridine was removed *in vacuo* to give a brown sticky solid which was washed with cold H_2O/MeOH(1:1) and Et_2O to give an brown solid. The solid was refluxed in methanol (20 ml) with decolourising charcoal for 5 minutes, after which the volume was reduced to 5 ml and the solution cooled to yield the product as pure white needles (3.79 g, 69%). Single crystals were grown via evaporation of methanolic solutions. ^{1}H NMR (400 MHz, DMSO-d$_6$):δ = 8.97 (br, 2 H), 8.64 (ddd, *J* = 4.75, 1.67, 0.97 Hz, 2 H), 8.04 (dt, *J* = 7.84, 1.22 Hz, 2 H), 7.98 (td, *J* = 3.89, 1.69 Hz, 2 H), 7.60 (ddd, *J* = 7.40, 4.76, 1.48 Hz, 2 H), 3.54 (s, 4 H); ^{13}C NMR(100 MHz, DMSO-d$_6$): δ = 164.2, 149.9, 148.3, 137.7, 126.4, 121.8, 37.5; (MALDI) Calcd. for $C_{14}H_{14}N_4O_2$ [M]$^+$: 270.29; found: 270.85; Anal. Found: C, 60.11; H, 4.81; N, 18.47 % Calcd. for $C_{14}H_{14}N_4O_2 \cdot CH_3OH$: C, 59.59; H, 6.00; N, 18.53 %.

Synthesis of N,N'-(1,2-phenylene)-bis(2-pyridine-carboxamide) (H₂bpb):

Triphenylphosphite (10.7 mL, 40.6 mmol) was added dropwise to a stirred solution of picolinic acid (5.00 g, 40.6 mmol) in pyridine (20 mL). After stirring for 15 minutes, 1,2-phenylenediamine (2.20 g, 20.3 mmol) was added and the solution heated to 70 °C for 17 hours. The pyridine was removed *in vacuo* to give a brown sticky solid which was washed with cold H_2O/MeOH(1:1) and Et_2O to give an off white solid. Recrystallisation from hot methanolic solution yielded the product as pure white needles (5.23 g, 81%). Single crystals were grown via cooling of methanolic solutions. ^{1}H NMR (400 MHz, DMSO-d₆):δ = 10.73 (br, 2 H), 8.64 (ddd, J = 4.76, 1.64, 0.87 Hz, 2 H), 8.17 (dt, J = 7.78, 1.01 Hz, 2 H), 8.04 (td, J = 3.88, 1.76 Hz, 2 H), 7.79 (dd, J = 5.89, 3.64 Hz, 2 H), 7.64 (ddd, J = 7.53, 4.75, 1.28 Hz, 2 H), 7.30 (dd, J = 5.90, 3.64 Hz, 2 H); ^{13}C NMR(100 MHz, DMSO-d₆): δ = 162.7, 149.4, 148.5, 138.1, 131.0, 127.0, 125.6, 125.2, 122.4; (MALDI) Calcd. for $C_{18}H_{14}N_4O_2$ [M]$^+$: 318.11; found: 318.80; Anal. Found: C, 64.39; H, 4.52; N, 16.93 % Calcd. for $C_{18}H_{14}N_4O_2 \cdot H_2O$: C, 64.28; H, 4.79; N, 16.66 %.

Synthesis of N,N'-(3,4-benzoic acid)-bis(2-pyridine-carboxamide) (H₂bpba):

3,4-diaminobenzoic acid was purified by refluxing in decolourising charcoal before use. Triphenylphosphite (10.7 mL, 40.6 mmol) was added dropwise to a cold, stirred solution of picolinic acid (5.00 g, 40.6 mmol) in pyridine (20 mL). 3,4-diaminobenzoic acid (3.09 g, 20.3 mmol) was then added and the solution heated to 70 °C for 17 hours. The pyridine was removed *in vacuo* to give a dark brown sticky solid which was washed with cold H_2O/MeOH(1:1) and Et_2O to give a dark brown solid. The solid was refluxed in methanol (50 ml) with decolourising charcoal for 25 minutes, after which the volume was reduced to 5 ml and the solution cooled to yield the product as an off white powder (4.19 g, 57 %). ^{1}H NMR (400 MHz, DMSO-d₆):δ = 10.86 (br, 2 H), 8.69 (d, J = 3.84 Hz, 1 H), 8.61 (d, J = 3.68 Hz, 1 H), 8.27 (td, J = 6.48, 1.83 Hz, 1 H), 8.18 (dd, J = 7.84, 3.32 Hz, 2 H), 8.1-8.03 (m, 3 H), 7.89 (dd, J = 8.42, 1.90 Hz, 1 H), 7.70-7.64 (m, 2 H); (MALDI) Calcd. for $C_{19}H_{14}N_4O_4$ [M+Na$^+$]$^+$: 385.33, [M]$^+$: 362.35; found: 384.90, 362.93; Anal. Found: C, 60.64; H, 3.5; N, 14.96 % Calcd. for $C_{19}H_{14}N_4O_4 \cdot H_2O$: C, 60.00; H, 4.24; N, 14.73 %.

Synthesis of N,N'-(ethane-1,2-diyl)-bis(2-aminobenzamide) (H₂bae):

Isatoic anhydride (6.04g, 37 mmol) was added portion-wise over 30 minutes to a stirred, aqueous solution (50 ml) of 1,2-diaminoethane (1.11 g, 18.5 mmol) at 50°C. Once the addition was complete, the reaction was heated to 80° for 8 hr. The reaction mixture was cooled to room temperature and the resulting white solid was vacuum-filtered and washed with cold MeOH/Et$_2$O and vacuum-dried to yield the product as a white powder. (4.08 g, 74 %). Single crystals were grown via cooling of hot methanolic solutions. ^{1}H NMR (400 MHz, DMSO-d$_6$):δ = 8.31 (br, 2 H), 7.51 (dd, J = 7.98, 1.38 Hz, 2 H), 7.15 (td, J = 7.66, 1.48 Hz, 2 H), 6.71 (dd, J = 8.22, 1.02 Hz, 2 H), 6.53 (td, J = 7.49, 1.10 Hz, 2 H), 6.39 (br, 4 H), 3.42 (s, 4 H); ^{13}C NMR(100 MHz, DMSO-d$_6$): δ = 169.2, 149.5, 131.6, 128.1, 116.3, 114.8, 114.6, 39.3; (MALDI) Calcd. for C$_{16}$H$_{18}$N$_4$O$_2$ [M]$^+$: 298.35; found: 297.96; Anal. Found: C, 64.63; H, 6.04; N, 18.77 % Calcd. for C$_{16}$H$_{18}$N$_4$O$_2$: C, 64.41; H, 6.08; N, 18.78 %.

Synthesis of N,N'-(1,2-phenylene)-bis(2-aminobenzamide) (H₂bab):

Isatoic anhydride (6.04g, 37 mmol) was added portion-wise over 30 minutes to a stirred, aqueous solution (50 ml) of 1,2-diaminoethane (2.0 g, 18.5 mmol) at 50°. Once the addition was complete, the reaction was heated to 80°C for 8 hr. The reaction mixture was cooled to room temperature and the resulting solid, brown lump was removed and vacuum dried. The solid was ground into powder and stirred in cold methanol for 5 minutes before being collected via filtration and washed with cold MeOH/Et$_2$O. Recrystallisation from hot methanol yielded the product as white needles. (5.38 g, 84 %). ^{1}H NMR (400 MHz, DMSO-d$_6$):δ = 9.72 (br, 2 H), 7.62-7.58 (m, 4 H), 7.25 (dd, J = 6.02, 3.51 Hz, 2 H), 7.19 (td, J = 7.65, 1.51 Hz, 2 H), 6.75 (dd, J = 8.28, 1.00 Hz, 2 H), 6.55 (td, J = 7.53, 1.00 Hz, 2 H), 6.43 (br, 4 H); ^{13}C NMR(100 MHz, DMSO-d$_6$): δ = 167.8, 150.1, 132.4, 131.4, 128.2, 125.8, 125.2, 116.7, 115.8, 114.0; (MALDI) Calcd. for C$_{20}$H$_{18}$N$_4$O$_2$ [M]$^+$: 346.38; found: 346.9; Anal. Found: C, 69.15; H, 5.19; N, 15.90 % Calcd. for C$_{20}$H$_{18}$N$_4$O$_2$: C, 69.35; H, 5.24; N, 16.17 %.

Synthesis of Ru(H₂bpe)Cl₃:

RuCl$_3$.3H$_2$O (0.082 g, 0.31 mmol) was added to a methanolic solution (25 mL) containing H$_2$bpe (0.085 g, 0.31 mmol). The reaction mixture was refluxed for 24 h and reduced to 5 ml to precipitate the compound as a dark solid. The solid was vacuum-filtered, washed with cold MeOH/Et$_2$O and vacuum-dried. Recrystallisation from MeCN and diethyl ether afforded the product as a brown powder. (61 mg, 35%). (MALDI) Calcd. for C$_{14}$H$_{12}$N$_4$O$_2$Ru$_1$Cl$_2$ [M-Cl]$^+$: 404.97, [M]$^+$: 439.94; found: 405.04, 440.02; Anal. Found: C, 29.16; H, 2.87; N, 9.74 % Calcd. for C$_{14}$H$_{22}$N$_4$O$_2$Cl$_3$Ru$_1$.4(H$_2$O): C, 30.59; H, 4.03; N, 10.19 %.

Synthesis of Ru(bpb)Cl₂:

RuCl$_3$.3H$_2$O (0.082 g, 0.31 mmol) was added to a methanolic solution (25 mL) containing H$_2$bpb (0.1 g, 0.31 mmol). The reaction mixture was refluxed for 48 h and reduced to 5 ml to precipitate the compound as a dark solid. The solid was vacuum filtered, washed with cold MeOH/Et$_2$O and vacuum dried. Recrystallisation from MeCN and diethyl ether afforded the product as a black/brown/red powder. (76 mg, 49%). (ESI) Calcd. for C$_{18}$H$_{12}$N$_4$O$_2$Ru$_1$Cl$_2$ [M]$^+$: 488.29; found: 488.73; Anal. Found: C, 43.16; H, 3.98; N, 10.83 % Calcd. for C$_{18}$H$_{22}$N$_4$O$_2$Cl$_2$Ru$_1$: C, 44.28; H, 3.98; N, 10.83 %.

Synthesis of Ru(bpba)Cl₃:

RuCl$_3$.3H$_2$O (0.082 g, 0.31 mmol) was added to a methanolic solution (25 mL) containing H$_2$bpba (0.112 g, 0.31 mmol). The reaction mixture was refluxed for 24 h and reduced to 5 ml to precipitate the compound as a dark solid. The solid was vacuum filtered, washed with cold MeOH/Et$_2$O and vacuum dried. Recrystallisation from MeOH and diethyl ether afforded the product as a dark brown powder. (53 mg, 28%). (MALDI) Calcd. for C$_{19}$H$_{12}$N$_4$O$_4$Ru$_1$Cl$_1$ [M]$^+$: 496.96, [M-Cl]$^+$:461.99 ; found: 497.05, 462.09; Anal. Found: C, 36.59; H, 2.29; N, 8.94 % Calcd. for C$_{19}$H$_{22}$N$_4$O$_4$Cl$_3$Ru$_1$.2H$_2$O: C, 37.80; H, 2.67; N, 9.28 %.

Synthesis of Ru(H₂bae)Cl₃:

RuCl₃.3H₂O (0.082 g, 0.31 mmol) was added to a methanolic solution (25 mL) containing H₂bae (0.092 g, 0.31 mmol). The reaction mixture was refluxed for 24 h and reduced to 5 ml and diethyl ether (10 ml) added to precipitate the compound as a dark green solid. The solid was vacuum filtered, washed with cold MeOH/Et₂O and vacuum dried. Recrystallisation from DMF and diethyl ether afforded the product as a dark green powder. (61 mg, 39%). Single crystals were grown via diethyl ether diffusion into DMF solutions. (ESI) Calcd. for $C_{16}H_{18}N_4O_2Ru_1Cl_2$ [M]$^+$: 469.99; found: 470.08; Anal. Found: C, 38.34; H, 3.87; N, 10.48 % Calcd. for $C_{16}H_{18}N_4O_2Ru_1Cl_3$: C, 38.00; H, 3.59; N, 11.08 %.

Synthesis of Ru(bab)Cl₂:

RuCl₃.3H₂O (0.082 g, 0.31 mmol) was added to a methanolic solution (25 mL) containing H₂bpb (0.107 g, 0.31 mmol). The reaction mixture was refluxed for 24 h and reduced to 5 ml and diethyl ether (10 ml) added to precipitate the compound as a dark green/blue solid. The solid was vacuum filtered, washed with cold MeOH/Et₂O and vacuum dried. Recrystallisation from MeCN and diethyl ether afforded the product as a dark green/blue powder. (36 mg, 20%). (MALDI) Calcd. for $C_{20}H_{16}N_4O_4Ru_1Cl_1$ [M]$^+$: 480.39; found: 479.02; Anal. Found: C, 42.88; H, 4.85; N, 11.44 % Calcd. for $C_{20}H_{16}N_4O_4Ru_1Cl_3$: C, 43.38; H, 3.28; N, 10.12 %.

Synthesis of tris-((2-aminobenzylidene)-aminoethylamine (TrenAb):

o-amino-benzaldehyde (0.66 g, 5.5 mmol) was refluxed with tris(2-aminoethyl)amine (0.3 g, 2.0 mmol) in methanol (50 ml) for 90 minutes. The pale yellow solution produced was reduced in volume to 10ml. Diethyl-ether (20 ml) was added to obtain a white solid which was suction filtered and dried. The solid was recrystallised from chloroform and methanol by vapour diffusion. Yield 67%. ^{1}H NMR (400 MHz, CDCl₃):δ: 8.2 (s, 1H, -HC=N), 7.1 (t, 1H, arom); 6.8 (d, 1H, arom); 6.6 (m, 2H, arom); 6.3 (br s, 2H, -NH₂); 3.6 (t, 2H, -CH₂-); 3.5 (s, MeOH); 2.8 (t, 2H, -CH₂-). ^{13}C NMR (100 MHz CDCl₃):δ: 165, 148, 134, 131, 118, 116, 115, 60, 56. ν/cm^{-1}: 3231 (NH), 1639 (C=N), 1588 (C=C), 753 (arom). (ESI) Calcd. for $C_{27}H_{33}N_7$ [M]$^+$: 455.28; found: 456, Anal. Found: C, 70.26; H, 8.18; N, 20.92 % Calcd. for $C_{27}H_{33}N_7.1/2CH_3OH$: C, 70.03; H, 7.48; N, 20.78 %.

Synthesis of nickel, copper and zinc complexes of TrenAb:

TrenAb (0.05 g, 0.11 mmol) dissolved in methanol (15 ml) was treated with 2 mole equivalents of the relevant metal halide. The mixture was stirred at $50^{\circ}C$ for 15 minutes, allowed to cool and filtered.

[NiTrenAb]$^{2+}$ 2Cl$^-$:

FTIR [(ν/cm-1 (KBr)]: 2925 (-NH$_2$), 1610 (-C=N), 1500 (C=C), 760 (arom). (ESI) Calcd. for C$_{27}$H$_{33}$N$_7$Ni$_1$: [M-H]$^+$ 512 (25%), [M+R+H]$^+$ 615 (25%) [M+2R+H]$^+$ 718 (100%), [M+3R+H]$^+$ 823 (10%), [M-R+H]$^+$ 409 (10%) [M-2R+H]$^+$ 306 (25%), R = anilino group. These are observed to migrate during the mass spectroscopic analysis Anal. Found: C, 52.79; H, 6.08; N, 15.41% Calcd. for C$_{27}$H$_{33}$N$_7$NiCl$_2$.2H$_2$O: C, 52.21; H, 6.00; N, 15.78 %.

[NiTrenAb]$^{2+}$ 2I$^-$:

FTIR [(ν/cm-1 (KBr)]: 2925 (-NH$_2$), 1610 (-C=N), 1500 (C=C), 760 (arom). (ESI) Calcd. for C$_{27}$H$_{33}$N$_7$Ni$_1$: [M-H]$^+$ 512 (10%), [M+3Na-2H]$^+$ 581 (35%) [M+R-2H]$^+$ 684 (15%), [M+2R-2H]$^+$ 787 (100%). R = anilino group. These are observed to migrate during the mass spectroscopic analysis Anal. Found: C, 46.07; H, 5.25; N, 14.06 % Calcd. for C$_{27}$H$_{33}$N$_7$ I$_2$Ni: C, 42.22; H, 5.25; N, 12.76 %.

Crystals suitable for X-ray diffraction were obtained from the very slow evaporation of a methanol solution of [(TrenAb)Ni]$^{2+}$2[I]$^-$. The crystals were taken from an oily residue in the base of the flask which mitigated against further analysis.

[CuTrenAb]$^{2+}$ 2Cl$^-$:

FTIR [(ν/cm^{-1} (KBr)]: 2925 (-NH$_2$), 1615 (-C=N), 1505 (C=C), 760 (arom). (ESI) Calcd. for C$_{27}$H$_{33}$N$_7$Cu$_1$: [M-H]$^+$ 517 (25%), [M+2R-H]$^+$ 723 (45%) [M-2R+2H]$^+$ 310 (100%), λmax = 595 (solid) Anal. Found: C, 53.15; H, 5.98; N, 15.49% Calcd. for C$_{27}$H$_{33}$N$_7$CuCl$_2$.H$_2$O: C, 53.33; H, 5.80; N, 16.12 %.

[ZnTrenAb]$^{2+}$ [ZnCl$_4$]$^{2-}$:

FTIR [(ν/cm^{-1} (ATR)]: 2800-3200 (-NH$_2$), 1610 (-C=N), 1495 (C=C), 760 (arom). (ESI) Calcd. for C$_{27}$H$_{33}$N$_7$Zn$_1$: [M-H]$^+$ 518 (35%), [M-R-H]$^+$ 415 (30%) Anal. Found: C, 42.51; H, 4.98; N, 12.60 % Calcd. for C$_{27}$H$_{33}$N$_7$Zn$_2$Cl$_4$.2H$_2$O: C, 42.43; H,4.87; N,12.83 %. Crystals were grown by slow evaporation of the mother liquors over 24 hours leading to a ligand rearrangement.

Crystal Data

	H$_2$bpe	H$_2$bpb	H$_2$bae	H$_2$bab	RubaeCl$_3$
Formula	C$_{56}$H$_{56}$N$_{16}$O$_8$	C$_{36}$H$_{28}$N$_8$O$_4$	C$_{16}$H$_{18}$N$_4$O$_2$	C$_{20}$H$_{18}$N$_4$O$_2$	C$_{13.54}$H$_{19.69}$C$_{11.85}$N$_{3.69}$O$_{2.46}$Ru$_{0.62}$
FW	1081.06	636.66	298.34	346.38	401.20
Crystal System	Orthorhombic	Orthorhombic	Monoclinic	Monoclinic	Orthorhombic
Space Group	Pbca	Pb 2$_1$/a	P 2$_1$/c	P 2$_1$/n	P b c a
a/Å	9.6490(3)	22.3839(8)	15.348(3)	8.7110(2)	14.4690(10)
b/Å	8.8089(3)	24.4262(10)	5.3418(5)	14.3450(4)	17.2011(12)
c/Å	14.8111(5)	5.5610(2)	9.3815(12)	13.5451(4)	22.1110(16
α/°	90.00	90.00	90.00	90.00	90
β/°	90.00	90.00	106.300(17)	97.062(2)	90
γ/°	90.00	90.00	90.00	90.00	90
Z	4	4	2	4	13
V/Å^3	1258.90(10)	3040.5(2)	738.2(4)	1679.8(2)	5503.0(7)
Radiation type	MoK\a	MoK\a	MoK\a	MoK\a	MoK\a
Radiation wavelength / Å	0.71073	0.71073	0.71073	0.71073	0.71073
μ$_{calc}$/mm^{-1}	0.099	0.094	0.092	0.821	0.901
No. reflections measured	10890	14891	6090	63603	29110
No. unique reflections	4065	6330	1708	6598	6263
No. parameters	119	449	136	347	327
R$_w$^{a} (1>2σ(l))	0.0472	0.1285	0.0642	0.0219	0.0307
R$_w$^{b} (all reflections)	0.1034	0.3588	0.1501	0.0526	0.0918
GOF	1.064	1.381	1.066	1.049	1.086

	TrenAb	"NiTrenAb" H_3O^+ 3I	"ZnTrenAb" $[ZnCl_4]^{2-}$
Formula	$C_{27}H_{35}N_7O$	$C_{21}H_{35}I_3N_6NiO_2$	$C_{27}H_{36}Cl_4N_7O_{1.50}Zn_2$
FW	473.62	842.96	755.17
Crystal System	trigonal	Triclinic	Monoclinic
Space Group	R-3	P-1	P21/n
a/Å	12.9828(4)	9.8973(3)	9.4360(6)
b/Å	12.9828(4)	10.8803(5)	16.0009(8)
c/Å	26.1704(10)	14.5836(6)	20.7248(11)
α/°	90.00	69.044(4)	90.00
β/°	90.00	79.799(3)	98.967(2)
γ/°	120.00	89.366(3)	90.00
Z	6	2	4
V/Å^3	3820.1(2)	1441.05(10)	3090.9(3)
Radiation type	MoK\a	MoK\a	MoK\a
Radiation wavelength / Å	0.71073	0.71073	0.71073
μ_{calc}/mm^{-1}	0.079	3.915	1.935
No. reflections measured	9712	13150	11637
No. unique reflections	1854	6889	6060
No. parameters	122	329	399
R_w^a (1>2σ(l))	0.1338	0.072	0.1410
R_w^b (all reflections)	0.0513	0.028	0.0634
GOF	1.083	1.063	1.038

Citations

1. Barnes, D. J.; Chapman, R. L.; Vagg, R. S.; Watton, E. C., Synthesis of novel bis(amides) by means of triphenyl phosphite intermediates. *J. Chem. Eng. Data* **1978,** *23* (4), 349-350.

2. Chapman, R. L.; Vagg, R. S., Studies on the metal-amide bond. I. Metal complexes of the bis-amide tetradentate ligand N,N′-bis(2′-pyridinecarboxamide)-1,2-benzene. *Inorg. Chim. Acta* **1979,** *33* (1919), 227-234.

3. Patra, A. K.; Ray, M.; Mukherjee, R., Synthesis and characterization of pyridine amide cation radical complexes of iron: Stabilization due to coordination with low-spin iron(III) center. *Inorg. Chem.* **2000,** *39* (III), 652-657.

4. Patra, A. K.; Mukherjee, R., Synthesis and properties of a monomeric and a m - oxo-bridged dimeric iron (III) complex with a tetradentate pyridine amide in-plane ligand . X-ray structure of [Fe(bpc)Cl(DMF)] [H₂bpc 5 4, 5-dichloro-1,2-bis (pyridine-2-carboxamido)benzene. *Polyhedron* **1999,** *18*, 1317-1322.

5. Jain, S. L.; Bhattacharyya, P.; Milton, H. L.; Slawin, A. M. Z.; Crayston, J. a.; Woollins, J. D., New pyridine carboxamide ligands and their complexation to copper(II). X-Ray crystal structures of mono-, di, tri- and tetranuclear copper complexes. *Dalton Trans.* **2004,** (di), 862-871.

6. Ramachandran, R.; Viswanathamurthi, P., Ruthenium(II) carbonyl complexes containing pyridine carboxamide ligands and PPh₃/AsPh₃/Py coligands: Synthesis, spectral characterization, catalytic and antioxidant studies. *Spectrochim. Acta Mol. Biomol. Spectrosc.* **2013,** *103*, 53-61.

7. Kärkäs, M. D.; Åkermark, T.; Chen, H.; Sun, J.; Åkermark, B., A tailor-made molecular ruthenium catalyst for the oxidation of water and its deactivation through poisoning by carbon monoxide. *Angew. Chem. Int. Ed.* **2013,** *52*, 4189-4193.

8. Srivastava, R. S.; Fronczek, F. R.; Perkins, R. S.; Fukuyama, T.; Xu, W., Anticancer activities of the ruthenium carboxylato, amido and pyridine complexes. *Int. J. Oncol.* **2010,** *36* (6), 1591-1598.

9. Upadhyay, M. J.; Bhattacharya, P. K.; Ganeshpure, P. a.; Satish, S., Synthesis of binuclear amide complexes of Ru(III) and study of their catalytic activity in epoxidation of alkenes. *J. Mol. Catal.* **1994,** *88*, 287-294.

10. Stephens, F. S.; Vagg, R. S., Studies on the metal-amide bond. XIX. A comparison of molecular distortions in the crystal structures of [N,N′-bis(2′-pyridinecarboxamido)-1,2-benzene] nickel(II) with its 6′-methyl-substituted Analogue. *Inorg. Chim. Acta* **1986** *120* (2) 165-171

11. Higashi, F.; Mochizuki, A., Direct polycondensation reaction with triphenyl phosphite initiated by tertiary amine hydrochlorides. *J. Polym. Sci. A Polym. Chem.* **1983,** *21* (11), 3337-3340.

12. Lin, J.; Zhang, J.-Y.; Xu, Y.; Ke, X.-K.; Guo, Z., N,N'-(1,2-phenylene)bis(pyridine-2-carboxamide) and N,N'-(1,2-cyclohexanediyl)bis(pyridine-2-carboxamide) toluene hemisolvate. *Acta Crystallogr. Sect. C-Cryst. Struct. Commun.* **2001** *57* 192-194.

13. Ko, P.-H.; Chen, T.-Y.; Zhu, J.; Cheng, K.-F.; Peng, S.-M.; Che, C.-M., Synthesis, crystal structure and catalytic activities of [Ru^III(bbpc)(PPh₃)Cl][H₂bbpc = 1,2-bis(4-tert-butylpyridine-2-carboxamido)-4,5-dichlorobenzene] *J. Chem. Soc., Dalton Trans.* **1995** (13) 2215-2219

14. Patra, A. K.; Rose, M. J.; Murphy, K. A.; Olmstead, M. M.; Mascharak, P. K., Photolabile ruthenium nitrosyls with planar dicarboxamide tetradentate N(4) ligands: effects of in-plane and axial ligand strength on NO release. *Inorg. Chem.* **2004,** *43* (14), 4487-4495.

15. Yang, Y.; Diederich, F.; Valentine, J. S., Lewis acidic catalysts for olefin epoxidation by iodosylbenzene. *J. Am. Chem. Soc.* **1991,** *113* (19), 7195-7205.

16. Seo, J. S.; Ryu, J. Y.; Lee, J. Y.; Lee, J. S.; Jang, H. G.; Kim, C.; Kim, Y., Crystal Structure of Tetraethylammonium Dichloro[1,2-bis(2-pyridine-2-carboxamido)benzene]cobalt(III) Monohydrate. *Anal. Sci.: X-Ray Struct. Anal. Online* **2004,** *20*, x123-x124.

17. Choi, Y. W.; Kim, S. H.; Lee, D. N.; Kim, C.; Kim, Y., Tetraethylammonium dichloro[N,N'-(4,5-dichloro-1,2-phenylene)bis(pyridine-2-carboxamidato)]chromate(III). *Acta Crystallogr., Sect. E: Struct. Rep. Online* **2006,** *62* (10), m2715-m2716.

18. T. Vlahos, A.; A. Kabanos, T.; P. Raptopoulou, C.; Terzis, A., Novel vanadium(III/IV) compounds with the diamidate ligand 1,2-bis(2-pyridinecarboxamide)benzene (H$_2$bpb). *Chem. Commun.* **1997,** (3), 269-270.

19. Yang, L.; Wei, R.-N.; Li, R.; Zhou, X.-G.; Zuo, J.-L., Epoxidation catalyzed by iron(III) and manganese(III) pyridine-2-carboxamido complexes. *J. Mol. Catal. A: Chem.* **2007,** *266* (1–2), 284-289.

20. Fry, N. L.; Rose, M. J.; Nyitray, C.; Mascharak, P. K., Facile Ligand Oxidation and Ring Nitration in Ruthenium Complexes Derived from a Ligand with Dicarboxamide-N and Phosphine-P Donors. *Inorg. Chem.* **2008,** *47* (24), 11604-11610.

21. Chahen, L.; Karmazin-Brelot, L.; Süss-Fink, G., Double HCl elimination and configuration change in the square-planar palladium complex trans-[{(Ph$_2$PC$_6$H$_4$CONH)$_2$C$_6$H$_4$}PdCl$_2$] under Suzuki conditions: Isolation and molecular structure of cis-[{(Ph$_2$PC$_6$H$_4$CON)$_2$C$_6$H$_4$}Pd]. *Inorg. Chem. Commun.* **2006,** *9* (12), 1151-1154.

22. Burger, S.; Therrien, B.; Süss-Fink, G., 1,2-Bis-N-[2′-(diphenylphosphanyl)benzoyl]diaminobenzene, a New Chelating Ligand with Versatile Coordination Properties. *Eur. J. Inorg. Chem.* **2003,** *2003* (17), 3099-3103.

23. Huh, D. N.; Gibbons, J. B.; Haywood, R. S.; Moore, C. E.; Rheingold, A. L.; Ferguson, M. J.; Daley, C. J. A., Metal-amidato complexes: Synthesis, characterization, and reactivity of a diamidato-bis(phosphine) nickel(II) complex. *Inorg. Chim. Acta* **2014,** *423, Part A*, 290-297.

24. Leung, W. H.; Che, C. M., Oxidation chemistry of ruthenium-salen complexes. *Inorg. Chem.* **1989,** *28* (26), 4619-4622.

25. Jia, Y.; Gou, F.; Fang, R.; Jing, H.; Zhu, Z., SalenZn-bridged D-π-A Dyes For Dye-Sensitized Solar Cells. *Chin. J. Chem.* **2014,** *32* (6), 513-520.

26. Steel, G.; Mustapha, A.; Reglinski, J.; Kennedy, A. R., The nickel, copper and zinc complexes of potentially heptadentate nitrogen–sulfur donor ligands. *Polyhedron* **2014,** *67*, 360-367.

27. Gupta Atyam, V. S. S. S.; Sarva Raidu, C.; Nannapaneni, D. T.; Reddy, M. I., Synthesis, Characterization, and Biological Evaluation of Benzimidazole Derivatives as Potential Anxiolytics. *J. Young. Pharm.* **2010,** *2* (3), 273-279.

28. Swamy, S. J.; Suresh, K.; Someshwar, P.; Nagaraju, D., Synthesis of novel Schiff's bases containing pyridine rings. *Synth. Commun.* **2004,** *34* (May 2014), 1847-1853.

29. Booysen, I.; Gerber, T. I. A.; Hosten, E.; Mayer, P., Formation of a six-coordinate fac-[Re(CO)$_3$]$^+$ complex by the N-C bond cleavage of a potentially tetradentate ligand. *J. Iran. Chem. Soc. 5* (4), 689-693.

30. Fry, N. L.; Rose, M. J.; Rogow, D. L.; Nyitray, C.; Kaur, M.; Mascharak, P. K., Ruthenium nitrosyls derived from tetradentate ligands containing carboxamido-N and phenolato-O donors: Syntheses, structures, photolability, and time dependent density functional theory studies. *Inorg. Chem.* **2010,** *49* (17), 1487-1495.

31. Kumar, B. K.; Ravinder, V.; Swamy, G. B.; Swamy, S. J., Synthesis and characterization of iron(III), cobalt(II), nickel(II), copper(II), ruthenium(II,III), rhodium(III) and palladium(II) complexes with n-(2-carboxyphenyl)- and 2-amino-n-(2-carboxyphenyl)-benzamides. *Indian J. Chem., Sect A* **1994,** *33* (2), 136-142.

32. Elizondo García, M.; Bernès, S.; Pérez Rodríguez, N.; Elizondo Martínez, P., Tris{2-[(2-amino-benzyl-idene)amino]-ethyl}amine. *Acta Crystallogr., Sect. E: Struct. Rep. Online* **2010,** *66* (Pt 12), o3054-o3055.

33. Mustapha, A.; Busch, K.; Patykiewicz, M.; Apedaile, A.; Reglinski, J.; Kennedy, A. R.; Prior, T. J., Multidentate ligands for the synthesis of multi-metallic complexes. *Polyhedron* **2008,** *27* (2), 868-878.

34. Mustapha, A.; Reglinski, J.; Kennedy, A. R.; Armstrong, D. R.; Sassmannshausen, J.; Murrie, M., Multidentate Ligands for the Synthesis of Multimetallic Complexes. 2. Formation of a Planar Cu$_4$OH Motif. *Inorg. Chem.* **2010,** *49* (12), 5350-5352.

35. Mustapha, A.; Reglinski, J.; Kennedy, A. R., The use of hydrogenated Schiff base ligands in the synthesis of multi-metallic compounds. *Inorg. Chim. Acta* **2009,** *362* (4), 1267-1274.

36. Mustapha, A.; Busche, C.; Reglinski, J.; Kennedy, A. R., The use of hydrogenated Schiff base ligands in the synthesis of multi-metallic compounds II. *Polyhedron* **2011,** *30* (9), 1530-1537.

37. Dwyer, F. P.; Gill, N. S.; Gyarfas, E. C.; Lions, F., Sexadentate Chelate Compounds. VIII1. *J. Am. Chem. Soc.* **1957**, *79* (6), 1269-1273.

Chapter V

Final Conclusions

Final Conclusions

The water oxidation reaction remains one of the most challenging problems within chemistry and will continue to receive significant attention as the search for renewable fuels and chemical feed stocks becomes an ever more pressing issue for the modern world. Dye sensitisation of heterogeneous catalytic substrates is a key part of this process. The work detailed in this thesis explored the concept of anchoring position dependence on the performance of the ruthenium dyes based on pyridyl-containing ligands. The primary ligands studied are the carboxylate- substituted picolinic acids. These ligands displayed strong coordination to the ruthenium atom and with the chlorides able to form charge-neutral ruthenium +4 complexes.
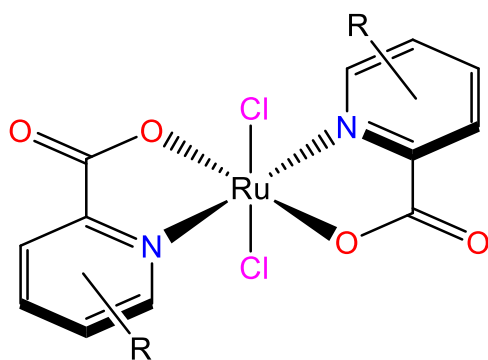
Figure 5.1: General structure of ruthenium picolinate dichlorides. R=ethylcarboxylate.

The complexes successfully formed with the coordinated pyridyl rings trans to one another across the ruthenium centre and, for the majority of the complexes, with the rings lying in the same plane. The coordinating pyridyl ring in the ruthenium picolinate complex, where the anchoring group is para to the coordinating nitrogen, exhibited 90° rotation around the axis of the ruthenium nitrogen bonds. This is not observed in any of the other complexes of any oxidation state. Computational analysis of the Ru^{IV} complexes using DFT methods determined that the in-plane orientation is the preferred geometry and that the Ru^{IV} dichlorides exist in a triplet, rather than singlet, ground state.

The ruthenium complexes exhibited variation in absorption, electrochemistry and performance as dye sensitisers for heterogeneous water oxidation. The electrochemistry in particular showed the clearest differences between the species with the redox potential for the $Ru^{III/IV}$ couple varying between species (1492-2140 mV).

Both the Ru$^{III/IV}$ and the Ru$^{II/III}$ exhibited dependence on the position of the anchoring group on the coordinated pyridyl ring with the anchoring carboxylate closer to the coordinated acid group exhibiting the greater potential. The variation in the optical properties of the complexes is less pronounced, with absorption being limited to the UV and high energy visual spectrum. The variation in these characteristics with the position of the anchoring group allowed us to conclude that the substitution position of the anchoring group on the aromatic ring of the ligand does affect the characteristics of the complex as a dye, and offers a possible method for improving dye selection for dye sensitisation - even though the complexes themselves are poor dyes. However, catalytic testing of the complexes on heterogeneous substrates displayed little variation in the effectiveness of the complexes as dye sensitisers. Crystallisation of the complexes from aqueous rather than ethanolic solutions revealed several of the complexes in the Ru^{III} oxidation state as both dichlorides and chloraqua species. The reduction of the ruthenium and the following exchange of one of the chlorides, allowed for comparison of the structural changes within the complexes as they cycle oxidation state.

Using DFT, it is determined that for the majority of species, the isomers where the anchoring group is situated closest to the ruthenium are the highest in energy and therefore the least stable. In the simulations of the chloroaqua species, those isomers are lowered in energy, compared to the other isomers, due to the presence of intramolecular hydrogen bonding. Comparing the solution absorption spectra of the complexes to those produced with the use of TDDFT it is determined that the complexes existed in a +3 rather than a +4 oxidation state when in solution. This reduction is attributed to the complexes acting as water-oxidation agents due to the high oxidation potential of their Ru$^{III/IV}$ couples in comparison to that of the water oxidation reaction.

The development of amide-based light-harvesting complexes based on these ruthenium picolinates proved to be extremely difficult as, although the ligands can be readily synthesised, the complexes cannot. The complexes formed proved to be unstable with several weaknesses focusing around the sp^2 hybridised carbon and nitrogen of the amide. Similar weaknesses have been observed in the similarly

hybridised linkages of the tripodal Schiff bases based on tren when complexed to transitions metals. This proved to be a currently unresolvable restriction to research in this area.

There still remains great scope for the improvement and exploration of ruthenium-based dye-sensitisers through a more discerning selection process regarding how improvements can be made - the ruthenium picolinate complexes demonstrated how the variation in such a simple thing as substitution pattern can have a marked effect on certain characteristics such as electrochemical potential. It is this author's opinion that the next step would be the inclusion of the dipicolinic acid into existing dye sensitisers where the variation in substitution pattern can be more easily observed in other characteristics. Given the observed decomposition of the amide linkages, it would be prudent for these sensitisers to be aromatic in nature, such as pyridine or pyrrole. A comprehensive study into the effect that small variations in ligand design, such as substitution pattern, will undoubtedly result in a more fundamental understanding of these dyes and allow for the design of superior dyes in the future.

Figures and Tables List

Figures and Tables List

Chapter 1

pg

Chapter 2

Chapter 3

Chapter 4

233

Chapter 5